Annular flows and their interaction with a cylindrical probe

Thesis submitted for the degree of
Doctor of Philosophy
at the University of Leicester

by

ADEBAYO, David Shina
Department of Engineering
University of Leicester

2012

Supervisors:
Professor Abdelwahab Aroussi
Dr. Aldo Rona

Annular flows and their interaction with a cylindrical probe

ADEBAYO, David Shina
Department of Engineering
University of Leicester
Leicester, LE1 7RH, UK.

Abstract

A numerical and experimental study is presented of the flow in the gap between concentric rotating cylinders and of its interactions with a cylindrical probe. The radius ratio η of the cylinders is 0.53, 0.44, and 0.35 corresponding to an aspect ratio Γ of 11.36, 7.81 and 5.32. The test cases covered the Taylor number range $2.35 \times 10^6 \leq Ta \leq 17.520 \times 10^6$, which is above the first critical Taylor number. The cylinders are laid horizontal with the inner cylinder rotating clockwise. The cylindrical probe, which is used to test the intrusiveness of an endoscopic probe on the ensued Taylor vortex flow, is 0.01m in diameter and 0.6m long into the annular region. To the author's best knowledge, no published study has analysed the intrusivity of a cylindrical probe on the flow in concentric rotating cylinders. The flow is herein analysed in the meridional and azimuthal planes.

The results from this study further confirm that η, Γ, Ta, and the end-wall conditions are all important parameters that determine the flow regime in the annular gap between concentric cylinders. The results also show wavy vortex flow with aspect ratio $\Gamma < 25$ at high Taylor numbers, well beyond the published Taylor number for transition to turbulent flow. In this flow, the vortex centres shift toward the outer cylinder as the centrifugal force due to the rotation of the inner cylinder is greater than the pressure gradient due to the stationary outer cylinder wall. As the η increases, the vortex centres displace more towards the outer cylinder wall.

Introducing the cylindrical probe changes the Taylor flow structure. It shifts and distorts the vortices from their original axial position, reduces and elongates the size of the vortices, and reduces the strength of the vortices located between the rotating inner cylinder and the stationary outer cylinder.

Acknowledgements

I would like to express my appreciation and gratitude to Professor Abdelwahab Aroussi for his supports, motivation, encouragement, and for funding this research work.

I would like to express my profound appreciation and gratitude to Dr. Aldo Rona who was exceptional in his support, advice, and guidance, whose untiring efforts allowed the realisation of this thesis. I would like to thank Emeritus Professor J.P. Gostelow for his continued support, tremendous inspiration and encouragement throughout the period of my stay at the University of Leicester.

I thank all my colleagues, Neet, Lanre, Nora, Farid Mohammed, Ivan, Davide, Pietro and Manuele for all their support, the relationship established and their encouragement during this research.

I would like to thank Paul Williams, whose experience and expert knowledge was of tremendous benefit during the building and development of the experimental rig. I would like to thank Dipak Raval for all his assistance in the installation of the instrumentation during the experimental investigation. I would like to thank Alan Wale and Simon Millward for their support in the construction of the experimental rig. I would like to thank all the Mechanical and Electrical Engineering workshop staffs, Barry Chester, Ian Bromley, Pete Barwel, Luigi Alessandro and Tom Robotham for all their support.

This project has been supported by a Specific Targeted Research Project of the European Community's Sixth Framework Programme under project number 32669 (PROVAEN).

Most importantly, I am grateful to my wonderful wife, my beloved children and the other members of my family for their continued support in prayers, motivation, patience, encouragement, and endurance throughout the period I spent on this work.

Finally, I thank God the almighty for the grace, sustainance, strength and the knowledge given to me to complete this work.

Table of Contents

Nomenclature

C_d	Drag coefficient
D_H	Hydraulic diameter $D_H = D_o - D_i$
D_i	Diameter of the inner cylinder
D_o	Diameter of the outer cylinder
D_p	Diameter of the cylindrical probe
d	Gap width between the cylinders
E	Wall constant (= 9.793)
I	Identity unit diagonal matrix
k	Axial wavenumber (m^{-1})
κ	von Kármán constant (= 0.4187)
k	Turbulent kinetic energy (m^2/s^2)
L	The length of the cylinders
ℓ	Length scale
m	azimuthal wave number
N	Number of samples
p	Pressure (pa)
q	Growth rate
r	Radial co-ordinate
Re_{in}	$\Omega_i R_i d/\nu$ = Reynolds number of the inner cylinder
Re_{out}	$\Omega_o R_o d/\nu$ = Reynolds number of the outer cylinder
Re_c	Critical Reynolds numbers
Re_T	Transition Reynolds numbers
R_i	Inner cylinder radius
R_o	Outer cylinder radius
St	Strouhal number
S^2	Variance
s	Strain tensor
S	Closed surface
Ta	Taylor numbers
Ta_c	Taylor critical number
TI	Turbulent intensity
u_x	Velocity in the axial direction, m/sec
u_y	Velocity in the flow-normal direction, m/sec
u_z	Velocity in the spanwise direction, m/sec
u_r	Velocity in the radial direction, m/sec
u_θ	Velocity in the tangential direction, m/sec

u_∞ Free stream velocity (m/s)

u' Velocity fluctuation

$\mathbf{v}$ Velocity vector

$\overline{\mathbf{v}}$ Mean for the velocity vector

$\mathbf{v}'$ Fluctuation for the velocity vector

X Axial co-ordinate

x Distance along the wall from the starting point of the boundary layer

x_i The i^{th} data point

$\bar{x}$ The mean (average) of the data points

Y Flow-normal co-ordinate

y_p Distance to the wall from the adjacent cell centroid

Z Spanwise co-ordinate

Greek letters

Γ L/d = Aspect ratio

Γ The angular momentum of a fluid element per unit mass

Δu_x Axial velocity contour spacing

Δu_r Radial velocity contour spacing

Δu_θ Tangential velocity contour spacing

ε Turbulent dissipation rate (m^2/s^3)

η R_i/R_o

θ Circumferential co-ordinate (rad/s)

λ Wavelength

μ Dynamic viscosity of the fluid (kg/m.s)

μ_t Turbulent or eddy viscosity

ν Fluid kinematic viscosity (m^2/s)

ν_t Kinematic turbulent or eddy viscosity (μ_t/ρ)

π Pi

ρ Density of the fluid (kg/m^3)

σ Standard deviation

σ_k Turbulent Prandtl number for kinetic energy

σ_ε Turbulent Prandtl number for dissipation rate

τ_w Wall shear stress

ϕ Scalar quantity

$\overline{\phi}$ Mean of the scalar quantity

ϕ' Fluctuation for the scalar quantity

ψ Ω_o/Ω_i

Ω_i Inner cylinder rotational speed

Ω_o Outer cylinder rotational speed

Subscripts

D Drag

c Critical

T Transition

t Turbulent

i/in Inner

o/out Outer

∞ Free stream condition

Superscripts

′ Fluctuating component

Accents

- Short-time average variable

˜ Time mean component

^ Roe averaged variable

< > Favre averaged variable

Chapter One: Introduction

1.1 Background and motivation for the present work

Laser Doppler Anemometers (LDA) and Phase Doppler Anemometers (PDA) are well-established measurement techniques that have been widely used by researchers (Albrecht et al., 2003; Bates and Banerjee, 1978; Goldstein and Kreid, 1967; Jensen, 2004; Sommerfeld and Qiu, 1993) to obtain instantaneous velocity measurements in flows. These techniques allow the measurement of the instantaneous velocity by using a light beam thereby avoiding the necessity of introducing probes into the measuring region. Hence, these techniques do not perturb the flow in the measuring volume. Both LDA and PDA are a single-point measurement technique, which means one can only measure the velocity components of the flow at one single point at a time. This makes these techniques the proper choice when one would like to accurately determine the flow statistics, such as the mean flow velocity and the turbulent intensity, which require large numbers of samples recorded over extended periods of time (Adrian and Westerweel, 2011). The shortcoming of these techniques is that it is not possible to simultaneously determine the velocity components at several points in a flow.

In the early eighties, Particle Image Velocimetry (PIV) was developed (Adrian, 1984; Pickering and Halliwell, 1984), which produces spatially resolved velocity field measurements simultaneously at several points in the flow. Using the PIV technique it is possible to obtain instantaneous velocity flow field information, which is important for probing the time-dependent structure of turbulent flow fields (Meinhart and Adrian, 1995; Westerweel et al., 1996). From the time of this development, the contribution made by Particle Image Velocimetry (PIV) to the study of gas and liquid flows is substantial. The application of PIV in a controlled laboratory environment is well-established (Adrian, 1988; 1991; Hesselink, 1988; Hopkins et al., 2000; Keane and Adrian, 1990; 1992; Liu et al., 1991; McCluskey, 1992; Westerweel et al., 1996; Westerweel, 2000), while its application in hostile environments or to flows with poor optical access is less established. In the past, such environments have caused scientists and researchers accuracy problems in some of their measurements. Most of the commercially available PIV systems are incapable of operating in confined spaces or in environments with limited optical access. This is because they require large, expensive, complex, and delicate laboratory

instruments. This has been a serious concern for manufacturers of aerospace, turbomachinery, and chemical products.

The need to access confined environments to obtain PIV velocity measurements is a major challenge, as in most cases the areas are inaccessible due to the hostility and harshness of the local environment. For example, the deployment of conventional PIV measurements in internal combustion aero-engines, bearing chamber, rotating tube heat exchangers, turbomachinery or pumps usually requires the manufacturing of expensive prototypes with large glass windows. This is because the PIV technique requires optical access for a light sheet as well as for a camera, as illustrated in Figure 1.1, where a Nd:YAG laser-based PIV system was used in a single-stage 50.8cm diameter transonic axial compressor at NASA Lewis.

Figure 1.1: Measurements in a transonic axial compressor (Wernet, 1997).

To overcome these problems, a single-stem PIV endoscope was developed and patented by Aroussi and Menacer (2003). Figure 1.2 shows an early example of the PIV endoscope. This is a conventional rigid bore endoscopic probe with an embedded laser light and image optics for PIV measurement. The tool comprises of two separate probes, one for the light sheet optics and another for the imaging optics, which relay a light sheet and imaging optics through endoscopes or boroscopes to a planar position (the focal plane of the endoscope viewing window) within the desired flow regime. Thus, this single-stem endoscopic probe allows for flow visualisation and for PIV measurement via small bore holes in a confined environment, where a conventional PIV system cannot be easily used.

The PIV endoscope in Figure 1.2 has been produced for commercial purposes by Olympus Keymed and partners.

In order to widen the use of this PIV endoscope, the European Community's Sixth Framework Programme under project number 32669 (PROVAEN) released funds to a consortium including University of Leicester to further assess this new invention. The single-stem PIV endoscope nonetheless has some shortcomings in the sense that the probe induces disturbances in the flow, altering the flow field characteristics. Thus, the measured velocity could be significantly different from that of an undisturbed flow. The University of Leicester was tasked to conduct research on the intrusive effects of the endoscope on selected flows. This researcher's work for the consortium is on the flow regime in an annular rig and in a pneumatic particle laden rig, which are examples of enclosed flows where the single-stem PIV endoscope is likely to be used. These flows were selected based on the industrial requirement of exploring the use of the single-stem PIV endoscope in enclosed flow regimes as agreed by the consortium. For the purpose of the PhD, the work on the annular flow regime is presented.

This thesis is motivated by the need of Olympus Keymed and partners to commercialise the single-stem PIV endoscopic probe for industrial and academic use.

Figure 1.2: Semi-intrusive PIV endoscope (Courtesy of Keymed, 2007).

1.2 Aims and objectives

A typical example of an enclosed environment where the single-stem PIV endoscope in Figure 1.2 can be used is in the gap between rotating coaxial cylinders. The annular flow between rotating coaxial cylinders is often characterised with respect to the Taylor number, Ta, which expresses in non-dimensional form the importance of the centripetal acceleration in a rotating flow relative to the viscous forces. In this study, where only the inner cylinder is rotating, the Taylor number Ta is defined as

$$Ta = \frac{2\eta^2 d^4}{1-\eta^2}\left(\frac{\Omega}{\nu}\right)^2 \qquad 1.1$$

consistently with the definition of Barcilon and Brindley (1984), Burkhalter and Koschmieder (1973), Jones et al. (1973), Eagles (1974), Koschmieder (1979), Donnelly (1963), Schwarz et al.(1964), and Robert (1965). In equation 1.1, $\eta = R_i/R_o$ is the radius ratio, where R_i and R_o are the radii of the inner and outer cylinder respectively, $d = R_o - R_i$ is the gap width, Ω is the rotational speed of the inner cylinder, and ν is the fluid kinematic viscosity.

The study of the flow developing between coaxial rotating cylinders is an established interest of the academic community. Many aspects of the flow physics are yet to be fully detailed and, to the author's best knowledge, the interaction of this flow with a cylindrical PIV probe is not documented in the open literature. The extent of this interaction is best assessed in the context of back to back measurements of the flow with and without the cylindrical probe in the flow.

Therefore, the first aim of this research is to provide further details on the flow features in the annulus between coaxial cylinders. The second aim is to investigate the intrusive effects of inserting a cylindrical probe, representing a PIV endoscope, on the ensued flow, so that the manufacturer of the single-stem PIV endoscope can use the knowledge from this research to develop and test alternative probe geometries for lower flow disturbance.

Towards these aims, the first objective of this study is to investigate numerically and experimentally the axial, radial and tangential velocity as well as the pressure distributions across the full annular region of a coaxial cylinder assembly without probe. The influence of the gap width between the inner and the outer cylinder on the flow field will also be examined.

It has been established in the literature (Andereck et al., 1986; Coles, 1965; Koschmieder, 1979; Taylor, 1923) that the flow regime in the annular region of coaxial rotating cylinders changes with the Taylor number. The second objective of this study is, therefore, to investigate whether the stated threshold Taylor numbers for the regime change are absolute or whether it is possible to observe non-turbulent flow at a high Taylor number.

The third objective is to investigate the extent to which other parameters, in addition to the Taylor number, determine the flow pattern in the rotating coaxial cylinders. The effects of the end-walls on the flow pattern in the coaxial rotating cylinder will be investigated in

details and measurements will be presented of flows beyond the ranges of radius ratios and of normalized gap widths reported in the open literature.

The fourth objective of this study is to investigate the intrusive effects of inserting a cylindrical probe representing a PIV endoscope between coaxial rotating cylinders on the ensued flow.

1.3 Methodology

In order to achieve the research objectives stated in section 1.2, four main activities are identified. The first activity is to conduct Computational Fluid Dynamics (CFD) modelling of the flow in the concentric rotating cylinders at various aspect ratios and Taylor numbers. The second activity is to develop an experimental rig of concentric rotating cylinders to study the flow at the same aspect ratios and Taylor numbers as in CFD. The third activity is to validate the numerical model using the experimental data. The fourth activity is to determine by experiment the intrusive effects of a cylindrical probe model on the ensued flow by comparing the flow fields without and with the cylindrical probe model in the annular region of the coaxial cylinder.

CFD and PIV have been selected for this study because the two approaches will supplement and complement one another. For example, the CFD approach will allow a better insight into the flow field in three-dimensions. The PIV approach on the other hand will allow the measurement of the instantaneous velocities of the flow field.

1.4 Thesis layout

This thesis is organized into nine chapters.

Chapter one is the introductory chapter and is intended to summarize the background and the motivation for which this research study was carried out, the aims and objectives of this present research, the research methodology as well as an outline of the structure of the thesis.

Chapter two provides a concise literature review of the available research to date on the flow regimes as well as documentation on the theories of fluid instability in concentric rotating cylinders. This chapter also reviews the flow around circular cylinders and a brief discussion on the drag reduction techniques applicable to cylindrical probes. The flow features around cylindrical objects, such as the flow separation near wake, and formation of von-karman vortices are discussed.

Chapter three starts by giving an overview of current CFD modelling techniques including the basic principles of CFD. The numerical methodology, including the numerical scheme, the governing equations (continuity and momentum equations), and convergence criteria employed for this study are discussed. The turbulence modelling and the boundary condition options available for this study are documented.

Chapter four discusses the evolution of the design of concentric rotating cylinders test rig. The rig as built is detailed.

Chapter five gives an overview of the working principles of PIV. It then presents the specific objectives of PIV in this experiment, the specific PIV experimental layout and the rig instrumentation. The rest of chapter five covers the PIV image acquisition and procedure, the data processing and analysis as well as on the experimental equipment set-up procedure.

Chapter six describes the CFD modelling of the air-flow between rotating coaxial cylinders. This chapter then details the CFD geometry and problem formulation, the mesh generation, the turbulence model selection, the boundary and initial conditions, the convergence criteria as well as the numerical accuracy estimates. The second parts of this chapter presents and discusses the results from the CFD predictions for the annular flow between coaxial cylinders of aspect ratio $\Gamma = L/d = 11.36$ and $\Gamma = 7.81$, where L is the axial length of the cylinders.

Chapter seven documents the experimental investigation of the flow between concentric cylinders without the cylindrical probe. The first section of this chapter covers the convergence of the PIV data. The second section discusses the results obtained from test cases with aspect ratio $\Gamma = 11.36$ and $\Gamma = 7.81$, and compare them with the corresponding CFD predictions. The third and the final section in this chapter documents the results obtained from test case with aspect ratio $\Gamma = 5.32$.

Chapter eight focuses on the interaction and the intrusive effects of a cylindrical probe on the Taylor vortex flow. The emphasis is on the experimental investigation of flow between concentric cylinders with aspect ratio $\Gamma = 11.36$ with a cylindrical probe inserted through the left end-wall. Data are analysed and the intrusive effects of the cylindrical probe are quantified and discussed.

Chapter nine discusses the current study and what was learnt from it. Conclusions are drawn on the research work in this thesis, specifically, on what new knowledge has been exposed. From the conclusions, recommendations for further work are made.

Chapter Two: Literature review

2.1 Introduction

Improving the efficiency of turbomachines requires the understanding of the flow field occurring within rotating machinery in which the inner and outer cylinders co-rotate or counter-rotate as well as the scenario of one rotating while the other is stationary. This chapter gives a review of flows in coaxial annular cylinders in which either both cylinders rotate or one of the cylinders rotates and the other is at rest.

2.2 Review of flows in concentric rotating cylinders

The study of the flow regimes that exist between concentric independently rotating cylinders has attracted great attention over the years. This is attributed to its many areas of scientific and engineering application. Examples are found in secondary air passages for turbine disk cooling, rotating tube heat exchangers, electric motors, propulsion, chemical mixing filtration, bearing chambers, flotation cells and extractors, pumps for the oil and water industries as well as in the drilling of oil wells, where mud flows between the drilling rod and the well casing, to remove the cuttings.

2.2.1 The geometry of concentric rotating cylinders

The rotating cylinder experiment has become fundamental research tool since it was first designed by Couette (1890) for the study of the instability and non-linear flow behaviour. Thus, concentric rotating cylinders have been a popular geometry for research studies due to the simplicity of the assembly and the fact that it represents a classical fluid dynamic problem. According to Owen and Rogers (1996), as quoted by Rashaida (2005), this flow geometry is also a subject of widespread practical interest in connection with pumps, steam and gas turbines as well as other rotating fluid devices. The flow concept from this apparatus has also been used to investigate the heat and mass transfer characteristics of Newtonian and non-Newtonian fluids (Hansford and Litt, 1968; Kawase and Ulbrecht, 1983; Mishra and Singh, 1978).

The commonly used apparatus for studying the flow in an enclosed rotating system consists of two concentric cylinders of different diameter, one or both of which are rotating at constant speed along their common axis. The cylinders can co-rotate in the same direction or counter-rotate in opposite directions about a vertical or a horizontal axis,

as illustrated in Figure 2.1. Normally, there is a fluid (gas or liquid) in the annular gap between the rotating cylinders.

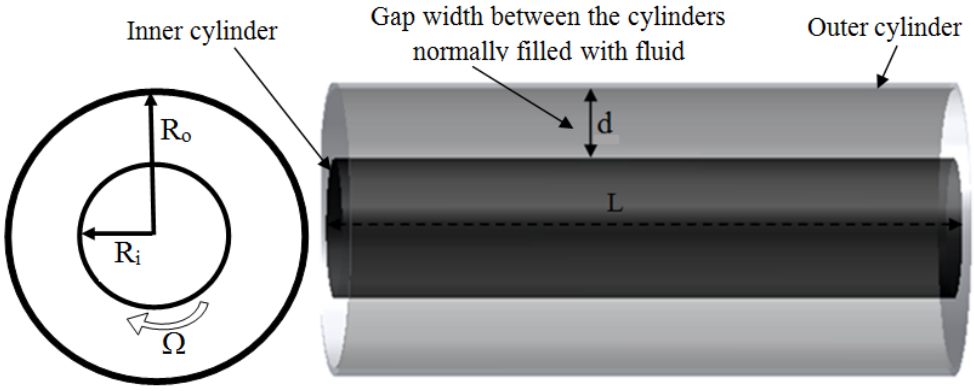

Figure 2.1: Schematic drawing of a typical concentric rotating cylinder apparatus.

2.2.2 The Taylor-Couette flow

The study of the flow pattern that develops in the annulus of coaxial cylinders dates back to 1888 and 1890 when Mallock (1888) and Couette (1890) conducted independent experiments using concentric rotating cylinders. The former conducted his experiment by rotating the inner cylinder while the outer cylinder was kept fixed. The aim of his experiment was to determine the constant of viscosity of water. The experimental result of Mallock revealed anomalous behaviour because Taylor vortices occurred. Mallock (1896) concluded that the vortices arise from the shear flow between a rotating inner cylinder and a concentric, fixed outer cylinder. Couette (1890), in his own experiment, kept the inner cylinder fixed while the outer cylinder was rotated. His experiment is the basis for the modern viscometer. He avoided any vortical structure and obtained an accurate measurement of the viscosity of various fluids. The result of the Mallock (1888) and Couette (1890) experiments started the academic research on the flow pattern and flow instability in concentric rotating cylinders.

The understanding of the flow regime prevailing in an annular enclosure in which the inner and outer cylinders co-rotate or counter-rotate, as well as the scenario of one rotating while the other is stationary is reasonably well established in the literature. As the inner cylinder rotates, it induces a centrifugal force that moves the fluid radially outward. This motion is resisted by the radial pressure gradient due to the stationary outer cylinder wall. At equilibrium, when the angular speed of the inner cylinder is moderate, the centrifugal force is balanced by the radial pressure gradient and the resulting swirling flow pattern

between the two concentric rotating cylinders is the laminar two-dimensional flow known as the Couette Flow (CF). If the inner cylinder is rotated fast enough, the centrifugal forces overcome the radial pressure gradient and the system makes a transition from the two-dimensional flow regime to more complex flow regime. The initial two-dimensional Couette flow develops into an axisymmetric flow pattern in the form of toroidal vortices, which are characterized by axisymmetric cells of alternating positive and negative circulation, stacked axially between the cylinders, known as a Taylor Vortex Flow (TVF), from Taylor (1923).

Figure 2.2(a) and Figure 2.2(b) show the schematic drawing and a flow visualisation of the counter-rotating vortex pattern that forms in the gap between the rotating coaxial cylinders. These vortices are generated at the surface of the inner cylinder and extend into the gap between the cylinders, depending on the flow regimes and the boundary conditions. Studies by Andereck et al. (1986), Coles (1965), Mallock (1896), and Taylor (1923) have shown that the stability or otherwise of the resulting flow pattern is highly dependent on the rotational speed of the inner cylinder, Ω_i, on the rotational speed of the outer cylinder, Ω_o, and on the gap d between the cylinders.

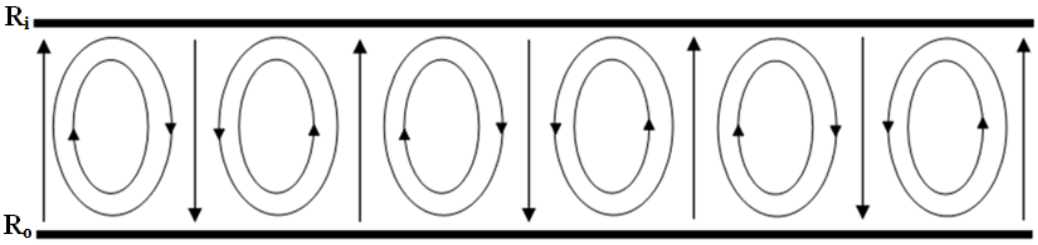

(a)

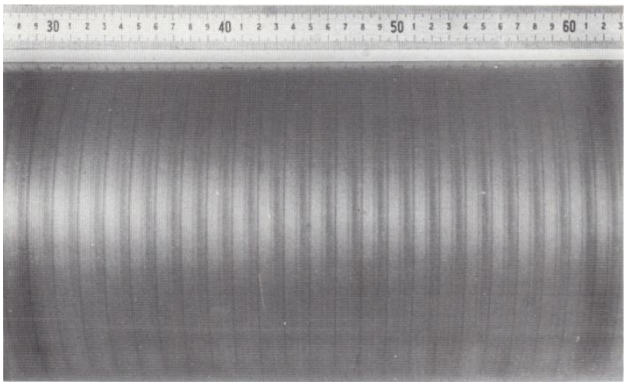

(b)

Figure 2.2: Counter-rotating flow pattern that forms in the gap between the cylinders (a) schematic drawing and (b) flow visualisation with aluminium powder of axisymmetric Taylor vortices between a rotating inner and stationary outer cylinder at $Ta = 1.16Ta_c$ for $\eta = 0.896$ and $\Gamma = 122$ (Koschmieder, 1993).

2.2.3 Flow regime transition in concentric rotating cylinders

The Taylor-Couette system of shear flow in the gap between concentric cylinders provides a great insight into the centrifugal stability of rotating flows, as a result it is now commonly used for quantitative comparison between theory and experiment (Macumber, 2005).

The Couette apparatus designed by Couette (1890), as quoted by Deng (2007), consists of two long coaxial cylinders, the inner one being fixed and the outer cylinder rotating about the common axis with the annular gap between the two cylinders filled with water. The aim of his experiment was to determine the viscosity of water by measuring the torque exerted by water on the inner cylinder rather than to study the fluid stability. He observed that, when the angular velocity was moderate, the flow was laminar and the torque was proportional to the angular velocity. He also discovered that when the angular velocity was increased to a large value, the water flow became unstable and the slope of torque versus speed line plot increased. He attributed this phenomenon to the development of some form of turbulent motion. Subsequently, authors like Mallock (1896) developed a similar apparatus to investigate the moment transmitted by fluid viscosity across the annular space between two concentric independently rotating cylinders. His objective was to examine the limits between which the motion of the fluid in the annulus was stable and the manner in which this stability broke down. Mallock (1896) tested three different configurations: (1) the outer cylinder rotating while the inner one is fixed; (2) the inner cylinder rotating with the outer one fixed, and (3) the outer cylinder rotating while the inner cylinder is fixed and the width of the annulus is varied. He discovered from his experiment that, at all of the rotational speeds tested, the flow instability occurred at a lower angular speed when the inner cylinder rotates and the outer one was stationary. The instability also occurred when the outer cylinder rotated and the inner one was at rest at a large angular velocity. Neither Couette nor Mallock established a definite criterion for the hydrodynamic stability of the fluids. This led Rayleigh (1917) to investigate the conditions that promote the stability or instability of inviscid fluid motion between two concentric rotating cylinders. He was the first to publish a criterion for the hydrodynamic stability of inviscid fluid between two concentric rotating cylinders. He concluded that the inviscid flow remains stable only if the square of the circulation Γ increases with the increasing radius and proposed the first stability criterion for the case when both cylinders are rotating.

The work of Taylor (1923) provides experimental and analytical explanations for the appearance and the development of flow instabilities between rotating concentric cylinders. The aim of Taylor's experiment was to obtain a stability threshold for flow between two rotating cylinders by measuring the torque. Taylor's experiment showed that, when the angular velocity of the inner cylinder is increased above a certain threshold, the Couette flow becomes unstable. He then used linear stability analysis to predict the threshold analytically and succeeded in obtaining quantitative agreement between theoretical and experimental results for the flow instability between two concentric rotating cylinders. His results were compared with Rayleigh's work. He further remarked that the experiments done by Couette (1890) and Mallock (1896) were not suitable for confirming the correctness of Rayleigh's criterion, since they were concerned with estimating the value of viscosity of water. He demonstrated that the Rayleigh's criterion is only approximately satisfied in a viscous fluid. Taylor attributed the stability of the viscous flow to the viscous forces which damp small disturbances and thus stabilize the flow.

Taylor (1923) theoretically expressed the threshold at which the flow in coaxially rotating cylinders becomes unstable as:

$$\mathrm{Ta_c} = \frac{\pi^4(1 + \mathrm{d}/2\mathrm{R_i})}{0.057(1 - 0.652\mathrm{d}/\mathrm{R_i}) + 0.00056(1 - 0.652\mathrm{d}/\mathrm{R_i})^{-1}} = 1706 \qquad 2.1$$

In equation 2.1, the term $0.652\mathrm{d}/\mathrm{R_i}$ is a correction factor due to the fact that d, the distance between the cylinders, is not negligible compared with $\mathrm{R_i}$. This correction allows neglecting higher-order terms of the ratio $\mathrm{d}/\mathrm{R_i}$ and may be expected to hold until $\mathrm{d}/\mathrm{R_i}$ exceeds one third.

This resulting value of 1706 in equation 2.1 is now referred to as the first critical Taylor number $\mathrm{Ta_c}$. The first critical Taylor number, $\mathrm{Ta_c}$ is defined by Deshmukh et al. (2007) and Batten et al. (2002a) as the Taylor number at which the first transition occurs from Couette Flow (CF) to Taylor Vortex Flow (TVF). Taylor (1923) established that, below the first critical Taylor number, the flow is stable with no vortical structure. When the Taylor number (Ta) of the flow exceeds the first critical Taylor number ($\mathrm{Ta} > \mathrm{Ta_c}$), the flow is unstable and forms axisymmetric toroidal vortices.

The mathematical description of the vortex instability by Taylor (1923) is based on the assumption that the distance between the inner and the outer cylinder is small compared to the inner cylinder radius, $\mathrm{R_i}$, so that $\eta \rightarrow 1$. From the time Taylor (1923) established the

Ta_c threshold, further investigations have been conducted by both analytical and numerical methods on the Taylor instability of the flow between rotating cylinders. These include the contributions from Jeffreys (1928), Chandrasekhar (1954; 1961), and Di Prima (1961). Jeffreys (1928) was the first to propose an alternative solution approach for the linear perturbation model by Taylor. He reduces the equations of linear theory of Taylor instability to a single sixth-order differential equation for the case of a narrow gap d/R_i. Jeffreys (1928) shows the value of the first critical Taylor number to be approximately equal 1709 for the case $\Omega_o/\Omega_i \rightarrow 1$, where Ω_o/Ω_i is the ratio of the rotation rates of the outer and inner cylinders. This value, which is derived from an asymptotic analysis of the governing equations, is in good agreement with the value of 1706 obtained by Taylor using a linear approximation, from equation 2.1.

Chandrasekhar (1954) and Di Prima (1961) derived another expression for the first critical Taylor number as a function of the gap width d and the inner cylinder radius R_i, when d is much smaller than R_i. This expression is given as:

$$Ta_c = 1695\left(1 + \frac{d}{2R_i}\right) \qquad 2.2$$

Chandrasekhar (1961) obtained two simple equations for the computation of the critical Taylor number depending on the value of ψ as:

$$Ta_c = \frac{3416}{1+\psi}\left[1 - 7.61 * 10^{-3}\left(\frac{1-\psi}{1+\psi}\right)^2\right] \quad (\psi \longrightarrow 1, \eta \longrightarrow 1) \qquad 2.3$$

$$Ta_c = Ta_{co}(1-\psi)^4 \quad (\psi \longrightarrow \infty, \eta \longrightarrow 1) \qquad 2.4$$

where $Ta_{co} = 1182$ and $\psi = \Omega_o/\Omega_i$.

The case of wide gaps ($\eta < 1$) when $\Omega_o = 0$ was studied numerically by Roberts (1965) who found the critical Taylor number to vary with the gap d as:

$$Ta_c = 4931\eta^2 - 10087\eta + 6895.2 \qquad 2.5$$

as reported by Deshmukh et al. (2007). Roberts (1965) and Recktenwald et al. (1993) determined the first critical Taylor number for various radius ratios η. The values from Roberts (1965) and Recktenwald et al. (1993) are reported in Table 2-1 and Table 2-2 respectively. As each value of Taylor number can be linked to a corresponding value of Reynolds number by equation 2.9, table 2-1 reports the critical Reynolds number values,

Re_c corresponding to Ta_c. The critical Taylor number increases with the decrease of the radius ratio η as shown in Table 2-1 and Table 2-2.

Table 2-1: Critical parameters for the onset of Taylor vortices for various values of η (Roberts, 1965).

Radius ratio, $\eta = R_i/R_o$.	Critical Taylor number, Ta_c.	Equivalent critical Reynolds number, Re_c.
0.975	1723.89	260.95
0.9625	1737.55	213.23
0.950	1754.76	184.98
0.925	1787.93	151.48
0.900	1823.37	131.61
0.875	1861.48	118.16
0.850	1902.4	108.31
0.750	2102.17	85.78
0.650	2383.96	74.96
0.50	3099.57	68.19
0.36	4551.60	69.54
0.28	6344.89	75.10
0.20	10355.30	88.13

Table 2-2: Critical parameters for the onset of Taylor vortices for various values of η (Recktenwald et al., 1993).

Radius ratio, $\eta = R_i/R_o$.	Critical Taylor number, Ta_c.	Equivalent critical Reynolds number, Re_c.
0.975	1723.89	260.95
0.900	1823.37	131.61
0.80	1992.91	94.7
0.70	2230.68	79.5
0.60	2570.45	71.7
0.50	3099.57	68.19

Deshmukh et al. (2007) and Batten et al. (2002a) reported the value of Ta_c as 1701. This value is in good agreement with the value reported by Taylor (1923) in equation 2.1. Other estimates of the first critical Taylor number are given by Parker and Merati (1996), Batten et al. (2004), Shiomi et al. (2000), and more can be found in the literature.

Based on these analytical results, several researchers have employed both experimental and computational techniques to understand the flow field that occurs in the gap between rotating cylinders. Such researchers include Chandrasekhar (1958), Donnelly (1958),

Brewsteret al. (1959), and Di Prima (1959). These researchers noted that the hydro-dynamic instability and the transition between different flow regimes where both cylinders were rotating or when only one cylinder is rotating can be determined as functions of different non-dimensional parameters.

The flow with both cylinders rotating is characterised by certain geometric parameters of the system. These parameters have a crucial influence on the nature of the flow dynamics and scaling of the system as well as the transition threshold. The main factors influencing the formation of different transition regimes of Taylor-Couette flow include:

(a) The Reynolds numbers. This is the classical parameter for distinguishing between different flow regimes and for estimating whether a flow is stable or unstable. The hydrodynamic instability and the transition between different flow regimes where both cylinders are rotating are determined by the inner and outer cylinder Reynolds numbers Re_{in} and Re_{out} respectively. These Reynolds numbers are defined as:

$$\mathrm{Re_{in}} = \frac{\Omega_i R_i d}{\nu} \qquad 2.6$$

$$\mathrm{Re_{out}} = \frac{\Omega_o R_o d}{\nu} \qquad 2.7$$

Re_{in} and Re_{out} are functions of the gap width $d = (R_o - R_i)$, which is the distance between the outer radius of the inner cylinder R_i and the inner radius of the outer cylinder R_o. The rotational speed of the inner and the outer cylinders are Ω_i and Ω_o respectively, and the ν is the fluid kinematic viscosity. For low angular velocities of the inner cylinder, measured by the Reynolds number (Re), the flow is steady. When the angular velocity increases above a certain Re threshold, the first critical Reynolds number, the initial steady Couette flow changes to a Taylor vortex flow (Taylor, 1923). By further increasing the angular speed of the inner cylinder, the system undergoes a progression of instabilities and, beyond a certain Re, there is the onset of turbulence.

(b) The radius ratio $\eta = R_i/R_o$.

(c) The aspect ratio $\Gamma = L/(R_o - R_i) = L/d$, where *L* is the length or height of the cylinders.

(d) The Taylor number. The Taylor number Ta is defined in section 1.2. For the case where both cylinders are rotating, the Taylor and Reynolds numbers are related by:

$$Ta = 2Re^2 \left[1 - \frac{\psi}{\eta^2}\right]\left[\frac{1-\eta}{1+\eta}\right] \qquad 2.8$$

where ψ is defined in equation 2.3 and $Re = \Omega_i R_i d/\nu$. For $\psi < 0$, corresponding to the cylinders rotating in opposite directions, only the region near the inner cylinder is unstable. This is because the azimuthal velocity profile changes sign at some point in the gap between the two cylinders, due to the opposite rotation of the cylinders.

For the case where only the inner cylinder is rotating, such as the case in this research work, the flow is likewise characterised by Re, η, Γ, and Ta.

Xiao et al. (2002) conducted an investigation on the effects of radius ratio on the "Second Taylor Vortex Flow" in concentric rotating cylinders when the inner cylinder is subject to some critical acceleration. They described their "Second Taylor Vortex Flow" as a special type of flow regime in which Taylor vortices are axisymmetric and do not display any wavy motion, even though the regime is located inside the wavy flow regime under quasi-steady condition. They concluded from their results that the "Second Taylor Vortex Flow" is sensitive to the gap size between the two cylinders and does not exist for some radius ratio.

In the experimental investigation conducted by Xiao et al. (2002), they showed that the existence of the "Second Taylor Vortex Flow" regime is also sensitive to changes in the aspect ratio. That is, a reduction in the aspect ratio leads to an increase in the Reynolds number range characterised by the "Second Taylor Vortex Flow". For example, at low aspect ratios of 20 and 15, their experiment shows that the Reynolds number range for "Second Taylor Vortex Flow" expanded and merged with the Taylor vortex flow range.

For the case where only the inner cylinder is rotating, equation 2.8 reduces to:

$$Ta = 2Re^2\left[\frac{1-\eta}{1+\eta}\right] \qquad 2.9$$

or

$$Ta = Re^2\frac{\mathrm{d}}{\mathrm{R_i}} \qquad 2.10$$

Based on the four parameters (Re, η, Γ, and Ta), several flow regimes that exist in an incompressible fluid between two concentric independently rotating cylinders have been identified. For example, the experimental investigation by Taylor (1923) observed that further increasing the angular velocity of the inner cylinder beyond the first critical Taylor number results in a progression of instabilities that lead to states with greater spatio-temporal complexity, to form a new state known as wavy vortex flow (WVF). For the case where the two cylinders are rotating in opposite directions, Taylor observed a state known

as spiral vortex flow (SVF). He also observed that increasing the inner cylinder angular speed beyond a certain Reynolds number leads to the onset of turbulence with the formation of turbulent Taylor vortex flow (TTVF). Gollub and Swinney (1975) and Fenstermacher et al. (1979) studied the temporal properties of the flow field for increasing Reynolds numbers beyond the first critical Reynolds number by using an optical heterodyne technique to measure the time dependence of the radial component of velocity at a fixed point. The power spectra obtained from the Fourier transform of the velocity records show (i) a transition from Couette flow to steady Taylor vortex flow, (ii) a transition from Taylor vortex flow to periodic wavy vortex flow (one time frequency), (iii) a transition to a quasi-periodic flow with two frequencies, with the new frequency disappearing at a larger value of the Reynolds number, and (iv) a transition to chaotic flow with a continuous spectrum. Walden and Donnelly (1979) have observed the same transitions in power spectra obtained by a different technique. In addition, for large aspect ratios and at large Reynolds numbers, Walden and Donnelly (1979) observed another frequency component.

Andereck et al. (1986) conducted an experimental investigation in which both cylinders were rotated in different directions and both cylinders were rotated in the same direction. They observed several flow regimes, including Taylor vortex flow, wavy vortex flow, Modulated Wavy Vortex Flow (MWVF), Laminar Spirals Flow (LSF), interpenetrating spirals, spiral turbulence, turbulent Taylor vortex flow, and various combinations of these flows. These flow regimes are shown in Figure 2.3.

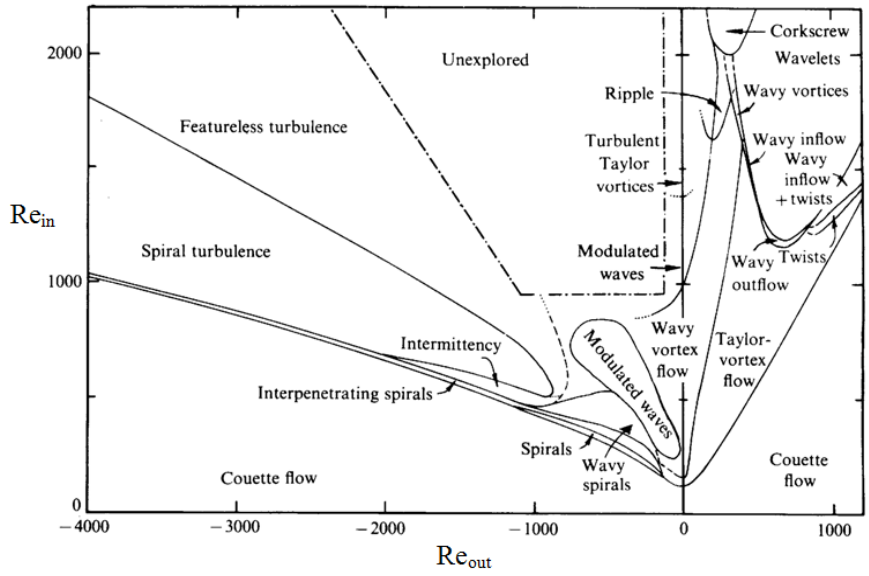

Figure 2.3: Flow regimes between independently rotating concentric cylinders (Andereck et al., 1986).

Recently, Liao et al. (1999) conducted numerical simulations and established three regimes of the Couette-Taylor system, namely the steady circular Couette flow, the steady axisymmetric Taylor vortex flow, and the periodic spiral vortex flow. They validated their computational results using the experimental observations of Andereck et al. (1986). They concluded that this system exhibits a rich diversity of steady and chaotic flow patterns (hydrodynamic instability) that are complex in nature and may arise as a result of small perturbations.

For the case in which the inner cylinder is rotating, as many as 20 to 25 different states have been observed at a given rotational speed by Coles (1965). Each state is defined by the number of Taylor vortices and the number of tangential waves. The flow regimes identified include the Taylor vortex flow, the wavy vortex flow, the modulated wavy vortex flow, and the turbulent Taylor vortex flow. Baier and Graham (1998) investigated the centrifugal instability of a pair of radially stratified immiscible liquids in the annular gap between concentric co-rotating cylinders. The aim of their paper was to show that two-fluid Taylor-Couette flow can be achieved by centrifugally stratifying two immiscible fluids between coaxial co-rotating cylinders. They used an aqueous solution of water and glycerine and an organic solution of white mineral oil and kerosene as the working fluids for their experiment. At a high inner cylinder rotation rate relative to the outer cylinder rotation rate, there is emulsification between the two fluids. For their final results, the inner cylinder rotation rate, Ω_i, was kept constant at 12.5 rev/s and the outer cylinder rotation rate, Ω_o, was varied from 7.5 rev/s to 12.5 rev/s. Lower values of Ω_o less than 7.5 rev/s were not pursued in their experiment in order to avoid emulsification. Their experimental results show two-layer of counter-rotating Taylor vortices, one layer for each phase, with a well-defined interface separating the two-layers. Their results show that such a two-fluid system with counter-rotating vortices lying side-by-side across the interface can be made stable or unstable, depending on the co-rotation or counter rotation rates of the cylinders. The Taylor-Couette flow pattern that forms as result of using two immiscible fluids within the annular cylinder geometry is schematically shown in Figure 2.4.

Serre et al. (2001) observed different instabilities in the boundary layers in the annulus between stationary and rotating discs using three-dimensional direct numerical simulations. The influence of curvature and confinement was studied using two geometrical configurations; (i) a cylindrical cavity including the rotation axis and (ii) an annular cavity radially confined by a shaft and a shroud. The results of their investigation

show a basic stationary axisymmetric steady flow, followed by three-dimensional structures at a critical rotational rate. At higher rotation rates, transition to unsteady flow was observed.

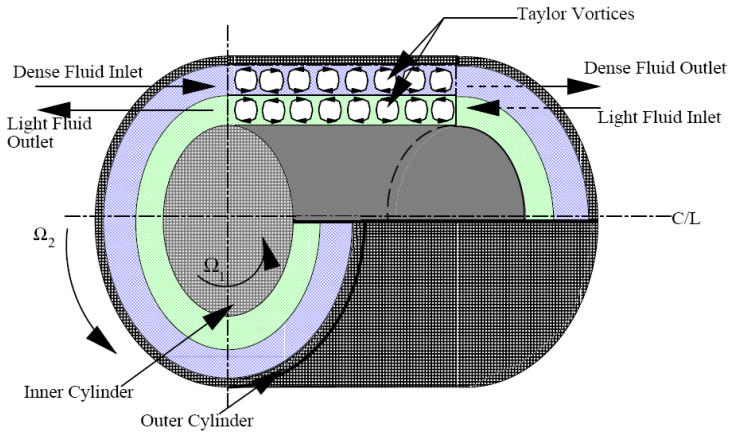

Figure 2.4: Schematic of a two-fluid Taylor-Couette extractor (Baier and Graham, 1998).

Czarny et al. (2002) performed a direct numerical simulation using a three dimensional spectral method of a short finite-length annular flow driven by counter-rotating cylinders. The numerical model predicted two different flow regimes, wavy vortices and interpenetrating spirals.

Di Prima (1960) and Stuart (1958) reported that the flow is relatively stable when the outer cylinder is rotating; consequently the Re_c, is larger and pressure loss is smaller than when the inner cylinder is rotating. Lathrop et al. (1992) examines the behaviour of the Couette-Taylor system over the Reynolds number range $800 \leq Re \leq 1.23 \times 10^6$ using high-precision torque measurements, local wall shear stress measurements, and flow visualisation. They found that, above a non-hysteretic transition Reynolds number, $Re_T = 1.3 \times 10^4$, the closed system behaves like open wall-bounded shear flows (pipe flow, duct flow and flow over a flat plate) at high Reynolds numbers.

Recently, Kim et al. (2007) conducted an experimental study on the Taylor vortex flow of non-Newtonian fluids in a concentric annulus in which the outer cylinder was stationary and the inner cylinder was rotating. Their results showed that the Re_c decreases as the rotational speed increases. They concluded that the rotation of the inner cylinder promotes the onset of transition due to the excitation of the Taylor vortices. An investigation on the Taylor vortices formed in a mineral oil between a rotating inner cylinder and a stationary outer cylinder with a wide gap (radius ratio $\eta \approx 0.613$) and a short liquid column (aspect ratio $\Gamma \approx 5.17$) was conducted by Deng et al. (2005) using both experimental and

computational methods. Their results show that the transition to wavy vortex flow occurs at a very high Reynolds number compared to the flow in an infinitely long column.

End-wall effects have been identified as one of the major factors affecting the type of flow regime in concentric rotating cylinders. Taylor in his original work recognised the important role end-walls play in his experiments. The presence of end-walls destroys the translation invariance characteristic of the infinite length L model. As a result, the bifurcation scenario is qualitatively different in the finite length L case. In their paper on the anomalous modes in the Taylor experiment, Benjamin and Mullin (1981) outlined the importance of end-wall effects. The discontinuous nature of the boundary conditions, where the inner cylinder meets the end-walls, generates weak circulation cells adjacent to the end-walls. As the Reynolds number is increased, the cellular pattern propagates towards the centre of the apparatus until it fills the column. They concluded that the transition to Taylor vortex flow is not the result of a bifurcation but of a continuous process. In the case when $\Gamma = 10$, the cellular pattern with ten cells is smoothly connected to the basic flow as $Re \rightarrow 0$. The importance of the boundary conditions was explained by Benjamin and Mullin (1981) in relation to the flow governing equations. Since the equations of fluid motion are elliptical, this in practice means that effects from the boundaries are felt over the entire domain.

2.2.4 The main flow regimes in concentric rotating cylinders

This section gives a concise review of the most common flow regimes in concentric rotating cylinders and their characteristics as identified by various researchers. This review is limited to the cases in which the inner cylinder is rotating while the outer cylinder is stationary.

Taylor Vortex Flow (TVF)

The Taylor vortex flow is a steady axisymmetric vortex flow, in which toroidal vortices encircle the inner cylinder and are stacked in the axial direction. The radial motion of the flow between two adjacent vortices is shown by upward and downward arrows in Figure 2.2(a). The boundaries between neighbouring vortices are flat and perpendicular to the cylinder axis. The flow pattern is shown by the flow visualisation in Figure 2.2(b). The vortical motion of the TVF grows as the Reynolds number increases. The upper limit of the TVF regime is marked by the appearance of azimuthal travelling waves on these vortices.

Wavy Vortex Flow (WVF)

At larger Taylor and Reynolds numbers, the axisymmetric time-independent Taylor vortex flow that is developed in the annular region of concentric cylinders changes to that of non-axisymmetric unsteady time-dependent wavy Taylor vortices. This wavy vortex flow is characterized by travelling azimuthal waves that are superimposed on the Taylor vortices. The azimuthal waves rotate around the inner cylinder at some wave speed as shown in Figure 2.5. The wavy vortices have a defined azimuthal wavenumber and move with a finite wave velocity in the azimuthal direction. The waves travel around the annulus at a speed that is 30% to 50% of the surface speed of the inner cylinder, depending on the Taylor number and other conditions (King et al., 1984)**.** The whole wave pattern rotates as a rigid body about the cylinder axis, hence the pattern is at rest for an observer fixed in a reference frame that rotates with the waves. The wavy vortex flow is also time-periodic and breaks the continuous rotational symmetry of the Taylor vortex flow.

At any given Reynolds number in the wavy vortex flow regime, several flow states are possible, each characterized by a different axial wavelength and azimuthal wave number *m*. This attribute makes wavy vortex flow a complicated and non-unique flow regime. An interesting property of the waves is the absence of dispersion. The state of the system depends on the Reynolds number history and other factors, but each state, once established, is stable over a range of Reynolds number (Coles, 1965). At any given Reynolds number, the wave speed is essentially independent of *m* (Shaw et al., 1982). In wavy vortex flow, the wave pattern has an *m*-fold rotational symmetry. Both the inflow and outflow vortex boundaries in wavy vortex flow are wavy and are S-shaped (Gorman and Swinney, 1982).

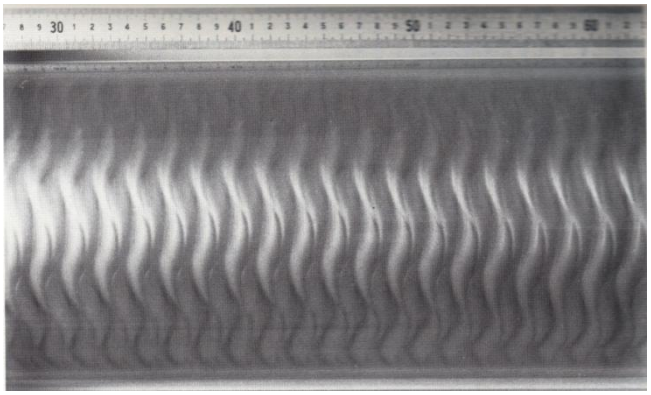

Figure 2.5: Flow visualisation with aluminium powder of wavy Taylor vortices between a rotating inner and stationary outer cylinder at $Ta = 8.49Ta_c$, $\eta = 0.896$, and $\Gamma = 122$ (Koschmieder, 1993).

The travelling azimuthal waves on the inflow and outflow boundaries are shifted in azimuthal phase angle in wavy vortex flow. This is shown by the flow visualisation in Figure 2.5 and further investigated experimentally by Akonur and Lueptow (2003), as illustrated in Figure 2.6. Akonur and Lueptow (2003) demonstrated that the distortion of the azimuthal velocity contours is directly dependent on the phase of the wave. Figure 2.6 shows the azimuthal velocity contours normalised by the inner cylinder rotational speed ΩR_i, that corresponds to the wave speed throughout one wave at a Reynolds number $Re = 1.48Re_c$. In other words, the fluid at each contour is moving at precisely the same speed as the azimuthal wave. Figure 2.6(a) shows five contours uniformly sampled in time through the first half of the wave, while Figure 2.6(b) shows the second half of the wave. According to Akonur and Lueptow (2003), if the contours were animated, they would move according to the arrows shown in Figure 2.6(a) and (b) as time progresses. The bold contours, which are identical in Figure 2.6(a) and (b), indicate the beginning and end of the half-phase. The bulges in the contours result from the radial transport of azimuthal momentum by the vortices. The inflow regions correspond to leftward maxima in the contours while outflow regions correspond to rightward maxima in the contours.

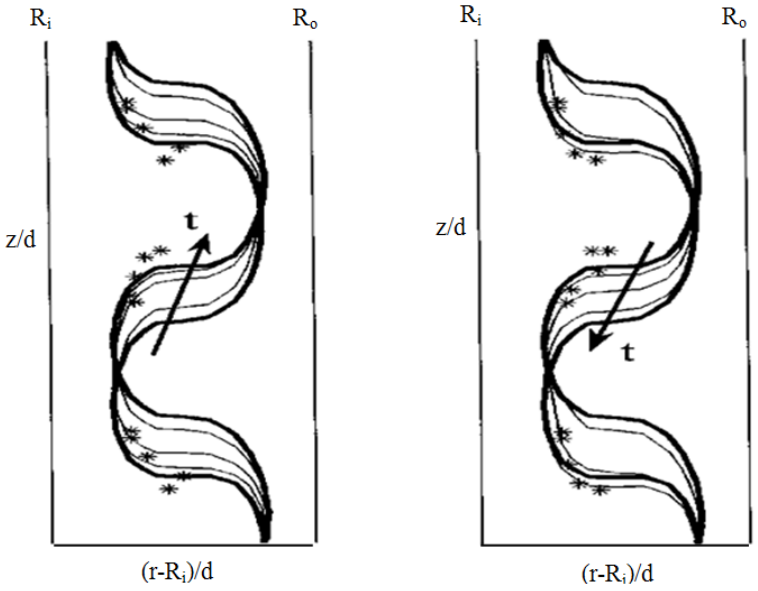

(a) (b)

Figure 2.6: Azimuthal velocity contour corresponding to the wave speed at Re =1.48Re_c. (a) up-cycle and (b) down-cycle. The limit contours at each half-cycle are bold and the (*) is the vortex centres, Akonur and Lueptow (2003).

Akonur and Lueptow (2003) explained that an animation of these figures show that not only do the bulges oscillate up and down with the azimuthal wave, they subtly change in axial extent and that these changes are not sinusoidal. They also show that, at certain

points in the phase, the axial extent of the bulges changes more quickly than at other points in the phase. The asterisks in Figure 2.6 indicate the instantaneous position of the vortex centres, which moves radially as well as axially, even though the wave speed contour remains essentially centered in the annulus. The vortex centre remains fairly close to the wave speed contour, but is in the region of fluid that is just slightly faster than the wave speed.

Akonur and Lueptow (2003) also show that the character of these contours changes substantially with the Reynolds number, as indicated in Figure 2.7. At the lower two Reynolds numbers (Re = $0.28Re_c$ and Re = $1.48Re_c$), the leftward inflow and rightward outflow bulges are similar in size. The outflow is much stronger at the higher Reynolds number (Re = $5.03Re_c$), resulting in a broadening of the outflow bulge and a narrowing of the inflow bulge. In this case, the inflow bulge is only about one-third as wide as the outflow bulge. The strength of the outflow also results in this contour shifting radially outward. The fluid to the left of the contour is moving faster than the wave speed, while the fluid to the right is moving more slowly.

At the highest Reynolds number, Figure 2.7 shows that a very large proportion of the fluid moves faster than the wave speed. At the lower Reynolds numbers about half the fluid moves faster than the wave speed and half moves slower. The axial transport between vortices is also evident in the contour at the highest Reynolds number. The narrow bulge to the left is tilted downward because of the net downward axial flow at this point in the phase.

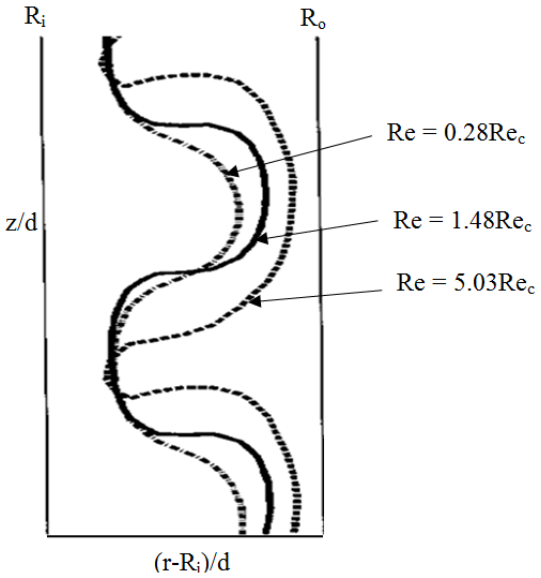

Figure 2.7: Azimuthal velocity contour corresponding to the wave speed at approximately the same phase of the wave for Re = $0.28Re_c$, $1.48Re_c$, and $5.03Re_c$ (Akonur and Lueptow, 2003).

For the Reynolds numbers in the range from the onset of wavy vortex flow up to Re/Re_c = 10.1, velocity power spectra show that the wavy vortex flow is characterized by a single frequency, as shown in Figure 2.8(a). In Figure 2.8, it is evident that wavy vortex flow is purely periodic in nature with the amplitude of the fundamental more than 5 orders of magnitude above the instrumental noise level. The single frequency is found experimentally to equal to the frequency of travelling azimuthal waves passing a point of observation in the annulus.

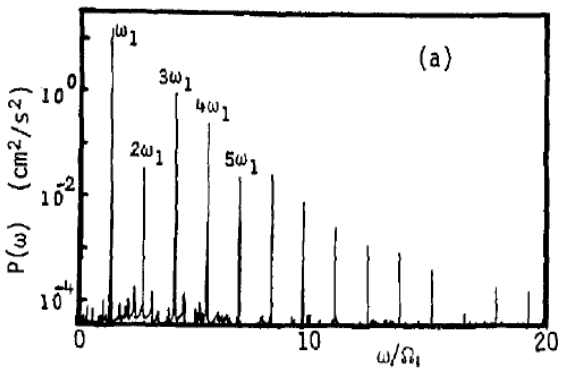

(a)

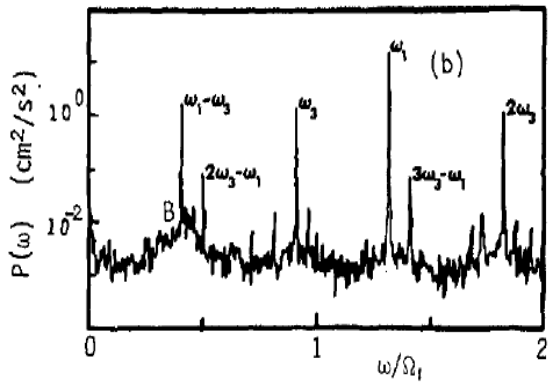

(b)

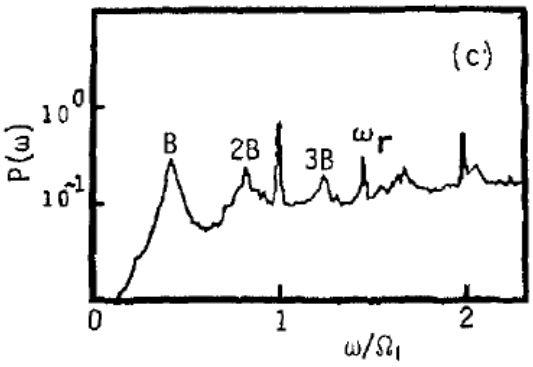

(c)

Notes:
(a) Periodic flow at Re/Re_c = 5.6. All components are harmonically related to ω_1; the first 5 harmonics are labelled.

(b) Weakly turbulent flow at Re/Re_c = 15.1. This flow is characterised by two discrete fundamental frequencies, ω_1 and ω_3, and a broadband component.

(c) Weakly turbulent flow at Re/Re_c = 28.0. This flow is characterised by the broadband component B and a discrete component ω_r, the component at ω/Ω_1=1 and 2 are instrumental artifacts. In (a) and (b), the aspect ratio is 20; in (c) it is 80.

Figure 2.8: Power spectra for time-dependent Taylor vortex flow (Di Prima and Swinney, 1981).

Davey et al. (1968) show that, with increasing Reynolds number, a second critical Reynolds number that depends on radius ratio, η, is reached. This critical Reynolds number corresponds to the second critical Taylor number, at which there is the onset of wavy vortex flow. At the second critical Taylor number, the Taylor vortices become unstable, leading to the first transition from Taylor vortex flow to wavy vortex flow, which is characterised by azimuthal waves superimposed on the Taylor vortices. Davey et

al. (1968) have shown that the Taylor number at which the onset of wavy vortex occurs is between 8% to 20% above the Taylor number at which the Taylor vortex flow first appears.

The Taylor number for the transition from axisymmetric toroidal Taylor vortices to non-axisymmetric wavy vortices is not firmly established, theoretical and experimental results show that the critical Taylor number at which wavy vortex flow starts depends on:

(1) Radius ratio: The transition to onset of wavy vortex flow was theoretically predicted by Eagles (1971) and Snyder and Lambert (1966) to occur at a Taylor number over the range $1.05Ta_c$ to $1.1Ta_c$ for a radius ratio $0.85 \leq \eta \leq 0.95$ in infinitely long cylinders. Eagles (1971) calculated the stability of the Taylor vortex flow using fifth-order terms in amplitude and found that the onset of the wavy vortex flow is at a Taylor number about 10% above the first critical Taylor number for $\eta = 0.95$. Experiments by Serre et al. (2008) indicate a range of higher Taylor number values for the onset of the wavy vortex flow to be between $1.14Ta_c$ and $1.31Ta_c$ over the range $0.85 \leq \eta \leq 0.95$ depending on the experimental conditions. This value is much larger than $10Ta_c$, for the radius ratio $\eta = 0.5$ (Debler et al., 1968; Snyder and Lambert, 1966; Snyder, 1969b).

Schwarz et al. (1964) observed that the critical Taylor number for the onset of wavy vortices was 5% to 8% above the critical Taylor number for the onset of Taylor vortices for radius ratio $\eta = 0.95$. In the experimental investigation conducted by Donnelly (1963), the Taylor number for the onset of wavy vortex flow was found to be 15% above the first critical Taylor number, for radius ratio $\eta = 0.95$. In the experiment conducted by Coles (1965) using an apparatus with a radius ratio $\eta = 0.874$ and aspect ratio $\Gamma = 27.9$, the critical Taylor number for the onset of wavy vortex flow is estimated to be about 55% above which the Taylor vortex flow first occurs. In the experimental investigation conduct by Coles (1965), the wavy nature of the Taylor vortex and the numbers of vortices was determined to be dependent on the way in which the rotational speed of the cylinders is varied and on the method used to increase or decrease the speed.

(2) Aspect ratio: Cole (1976) presented experimental results on the effect of the annulus length on the critical speeds at which Taylor vortices and, subsequently, wavy vortices are formed, by torque measurements and visual observations. He observed that only the onset of wavy vortices is significantly affected by the reduction of the annulus length. Cole (1976) further observed that aspect ratio values greater than 40 are required before the second critical Taylor number is within a few percent of the theoretical value calculated

for infinite cylinders (Di Prima and Swinney, 1981). He concluded that the aspect ratio affects the formation of wavy vortex flow whereas the value of the critical Taylor number at which Taylor vortex flow occurs is insensitive to annulus length. Walden and Donnelly (1979) and Walden (1978) have also found that the Taylor numbers for some higher mode transitions depend on the aspect ratio.

Walden and Donnelly (1979), Takeda (1999) and, recently, Wang et al. (2005) observed the possibility for re-emergence of wavy modes above the turbulent vortex transition for a sufficiently large aspect ratio, greater than 25, and the influence of end effects in short devices.

Many researchers have conducted numerical investigations to address the physical mechanism responsible for the azimuthal waviness in a circular Couette system. Marcus (1984) investigated numerically the Taylor vortex flow and wavy vortex flow. The results of his computation suggested that a local inviscid centrifugal instability of the strong radial motion at the outflow boundaries between vortices is responsible for the azimuthal waviness. He also indicated that the waviness results in fluid being mixed between adjacent vortices. Jones (1985) noted that the radial outflow jet results in strong azimuthal jets at the outflow region as it carries high azimuthal momentum outward. He suggested that it is the azimuthal jets, which are stronger than the radial jets, which destabilise the axisymmetric flow and make the vortices wavy. He concluded that the onset of wavy vortices occurs close to the onset of axisymmetric vortices for narrow gaps. Coughlin and Marcus (1992) conducted numerical simulations on a Taylor-Couette flow and concluded that the important features related to waviness are at the outflow jet, where both the radial and azimuthal velocities as well as the axial gradient of the azimuthal velocity are greatest. Wereley and Lueptow (1998) conducted experimental investigations using a PIV technique to measure the axial and radial velocities in a meridional plane for non-wavy and wavy Taylor-Couette flow in the annulus between a rotating inner cylinder and a fixed outer cylinder with fixed end conditions. The experimental results for the Taylor vortex flow indicate that, as the inner cylinder Reynolds number increases, the vortices become stronger and the outflow between pairs of vortices becomes increasingly jet-like. They concluded that the waviness of the boundary is directly related to the degree of fluid transfer between vortices.

Akonur and Lueptow (2003) used a PIV technique to measure the azimuthal and radial velocities in azimuthal planes perpendicular to the axis of rotation. Their study was conducted for a wavy vortex flow in the annulus between a rotating inner cylinder and a

fixed outer cylinder with fixed end conditions. Their measurements were matched with previous measurement by Wereley and Lueptow (1998), resulting in a time-resolved three-dimensional field of all three velocity components for wavy vortex flow. The results of their experiment show that waviness is related to the motion of the vortex centres. Because their results show a relatively strong shear layer in the azimuthal velocity compared to the radial inflow and outflow shear layers between the vortices, they concluded that the azimuthal waviness is more likely related to an instability in the azimuthal velocity profile, as proposed by Jones (1985).

Modulated Wavy Vortex Flow (MWVF)

At higher Taylor numbers, the wavy vortices transition to rotating waves that appear to be modulated. At this flow regime, two fundamental frequencies in the coaxial cylindrical flow appear in the power spectrum (see labelled ω_3 in Figure 2.8) with no hysteresis observed. This was first discovered by Gollub and Swinney (1975). This type of flow is termed quasi-periodic because it has approximate but not exact recurrence. As *Re* is increased still further, the amplitude of the azimuthal waves begins to vary with time, giving rise to quasi-periodic regimes known as modulated wavy vortex flow (MWVF) and chaotic wavy flow (CWF) (Takeda, 1999). The latter flow regimes are distinguished by the absence or presence, respectively, of a broad peak in the velocity power spectra. When the flow changes to MWVF, the flow pattern changes from the S-shape to a slight flattening of the wavy vortex outflow boundary. All the waves in the axial direction are modulated in phase, while, in the azimuthal direction, the wave modulation can have the same phase, or the modulation phase can vary with angle (Gorman and Swinney, 1982).

In MWVF, there are two rotating waves superimposed on the Taylor vortices with different frequencies and in general, different azimuthal wave-numbers. The modulated wavy vortex flow is time-periodic. The transition to a MWVF is most easily detected from the spectral analysis of the velocity or of the reflected light measured at a single point in the flow. The WVF has a single peak at a frequency related to the passage of the azimuthal wave. The MWVF introduces a second spectral peak at a lower frequency related to the modulation. Investigations has been conducted on MWVF by many researchers like Gorman and Swinney (1982) and Shaw et al. (1982).

At still higher Taylor numbers, the waviness gives way to turbulence that raises the spectral amplitude level at all frequencies. The vortices are still axisymmetric but the flow is turbulent at small scales. The MWVF is the final pre-turbulent flow regime.

Turbulent Taylor Vortex Flow (TTVF)

As the Reynolds number is further increased above $Re/Re_c = 13$, a weak broad component appears in the velocity spectrum (Figure 2.8(b) labelled B). The flow can no longer be described by a small number of well-defined characteristic frequencies. The flow can only be described as chaotic or turbulent (Di Prima and Swinney, 1981). Cole (1965) observed this type of flow regime and concluded that the discrete spectrum changes gradually and reversibly to a continuous one by the broadening of the initially sharp spectral lines.

Upon further increasing *Re*, azimuthal waves disappear altogether, marking the onset of "weakly turbulent" or "soft turbulent" flow, although the axial periodicity associated with the Taylor vortices remains. This turbulent Taylor vortex flow (TTVF) becomes increasingly complex as the Taylor number ratio increases beyond 5×10^5 until the vortex structures themselves eventually become indiscernible (Smith and Townsend, 1982). Koschmieder (1993) stated that order emerges from chaotic flow that leads to turbulent flow when $Ta \approx 1000Ta_c$. In the case of the inner cylinder rotating and the outer cylinder fixed, increasing the Taylor number above the critical Taylor number results in higher instabilities than in the case of the outer cylinder rotating. In this flow, the vortical structure is retained, but the vortices are modified. Figure 2.9 shows the of turbulent Taylor flow pattern at $Ta = 1625Ta_c$ for $\eta = 0.896$ and $\Gamma = 122$ from Koschmieder (1993).

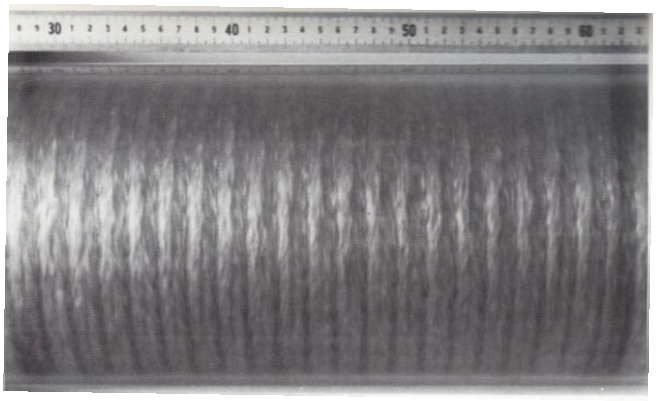

Figure 2.9: Flow visualisation with aluminium powder of turbulent Taylor vortices between a rotating inner and stationary outer cylinder at $Ta = 1625Ta_c$ for $\eta = 0.896$ and $\Gamma = 122$ (Koschmieder, 1993).

2.2.5 Theories of fluid instability in concentric cylinders

In this section, some of the known theories of fluid instability in concentric cylinders are reviewed. Since the work of Taylor on instability, theories predicting the growth of the Taylor vortices and the mechanism of flow instability with further increase of speed were proposed by many investigators. These theories include (i) the linear stability theory, (ii)

the energy method, and (iii) the weak nonlinear stability theory by Stuart (1958) and Davey (1962).

Rayleigh criterion for instability

Neither Couette nor Mallock was able to establish a definite criterion for the hydrodynamic stability of the fluid in the gap between rotating cylinders. The first hydrodynamic stability criterion for inviscid fluids was derived by Rayleigh (1917) who formulated a stability criterion for the mean viscous flow between two concentric rotating cylinders which was based on the inviscid perturbation equations. Rayleigh considered a basic swirling flow of an inviscid fluid which moves with angular velocity Ω about the axis of rotation. The equations of motion allow Ω to be an arbitrary function of the distance r from the axis, provided the velocities in the radial and axial directions are zero. Rayleigh did not establish his criterion for stability by an analytical discussion of the relevant perturbation equations but by a simple physical argument.

The kinetic energy of the fluid contained in two elemental rings with r = R_1, and r = R_2, with equal volumes dV can be expressed as:

$$\frac{1}{2}\rho(\Gamma_1^2 R_1^{-2} + \Gamma_2^2 R_2^{-2})dV \qquad 2.11$$

where Γ (= ru_θ) is the angular momentum of a fluid element per unit mass.

Assuming the fluids contained in the two elementary rings are interchanged, as the angular momentum of an element of the inviscid fluid is constant, the resulting kinetic energy is:

$$\frac{1}{2}\rho(\Gamma_1^2 R_2^{-2} + \Gamma_2^2 R_1^{-2})dV \qquad 2.12$$

The change in the kinetic energy as a result of the interchange is:

$$\tfrac{1}{2}\rho(\Gamma_1^2 R_2^{-2} + \Gamma_2^2 R_1^{-2})dV - \tfrac{1}{2}\rho(\Gamma_1^2 R_1^{-2} + \Gamma_2^2 R_2^{-2})dV \qquad 2.13$$

The change in the kinetic energy is therefore proportional to:

$$(\Gamma_2^2 - \Gamma_1^2)(R_1^{-2} - R_2^{-2}) \qquad 2.14$$

Suppose that $R_2 > R_1$, then the change in kinetic energy is negative provided $\Gamma_2^2 > \Gamma_1^2$ and positive if $\Gamma_2^2 < \Gamma_1^2$. Thus, if Γ^2 decreases with r anywhere, this would increase the kinetic energy and would imply instability. On the other hand, if Γ^2 increases with r, this would lower the kinetic energy and would imply stability. This is simply Rayleigh's criterion

which states that the necessary and sufficient condition for a distribution of angular velocity Ω(r) to be stable (to axisymmetric disturbances) is when the condition

$$\frac{d}{dr}(r^2\Omega)^2 > 0 \qquad 2.15$$

is satisfied everywhere in the flow field and that the distribution of angular velocity Ω(r) is unstable if $(r^2\Omega)^2$ decreases with increasing r anywhere inside the flow field.

However, Rayleigh's stability criterion can only be applied to the case of inviscid flow or when the effect of viscosity is assumed not to affect the onset of instability. In addition, Rayleigh's physical arguments were based on axisymmetric disturbances to the flow. At a low rotational speed, viscosity damps the perturbations, thereby preventing the formation of vortices. For such a case, the flow develops as a basic Couette flow for the case of a fluid between two concentric rotating cylinders. This implies that another theory is needed to deal with viscous fluid flow. This gives rise (drove) to the development of a linear instability theory where transition to instability is governed by the critical Taylor number, depending on the radius ratio of the cylinders and on the rotational speeds.

Linear theory of instability

Taylor (1923) was the first to successfully apply linear stability theory to a specific incompressible fluid dynamic problem and succeeded in obtaining quantitative agreement between theory and experimental results for the onset of the flow instability between two concentric rotating cylinders. In contrast to Rayleigh's analysis, Taylor considered an incompressible viscous fluid in steady motion between two infinitely long concentric cylinders, which are rotated about a common axis with constant angular velocity Ω_1 at r = R_i and Ω_2 at r = R_o where $R_o > R_i$. One of the aims was to determine the velocity distribution within the annulus.

Taylor (1923) assumed a Bessel function series solution for the streamwise velocity perturbation u_1 as:

$$u_1 = \sum_{m=1}^{\infty} a_m B_1(k_m r) \qquad 2.16$$

where $B_1(k_m r)$ is a Bessel function of order 1 and k_m is the m^{th} wavenumber. This satisfies the conditions $u_1 = 0$ at R_i and R_o. Taylor substituted the solution of equation 2.16 into the momentum perturbation equations to obtain the complete solution for v_1 and w_1.

A system of linear homogenous equations in a_m, $1 \leq m \leq \infty$, was obtained by Taylor after the application of the boundary conditions $u_1 = v_1 = w_1 = 0$ at $r = R_i$ and $r = R_o$ Taylor was able to eliminate all the unknowns from the equations of disturbed motion since the number of the unknowns is the same as that of the equations. The resulting equation takes the form of an infinite determinant equating to zero, which can be regarded as an equation to determine the growth rate q of a given initial harmonic type disturbance. Taylor used the solution as a criterion for the stability of a given initial disturbance and concluded that if the value of q is real, then the motion is stable or unstable according as whether q is negative or positive. Similarly, if q is complex, the motion is unstable, if the real part of q is positive. The motion is then an oscillation of increasing amplitude.

After Taylor's first success in the calculation of the critical Taylor number by using linear stability theory, many authors such as Jeffreys (1928), Chandrasekhar (1961), Di Prima (1960), Di Prima and Swinney (1981), and Sparrow (1964) have made significant improvements to the linear stability theory both analytically and numerically.

The linear stability theory has become a useful tool in analysing the stability or otherwise of flow regimes. As such, researchers such as Renardy and Joseph (1985), Joseph et al. (1984) have employed linear stability theory to the flow of two immiscible fluids lying between concentric cylinders when the outer cylinder is fixed and the inner cylinder rotates, with the interface assumed to be concentric with the cylinders, and the gravitational effects neglected. The effects of different viscosities, densities and surface tension on the linear stability of the Couette flow were studied numerically. Their results indicate that, with the surface tension, a thin layer of the less viscous fluid next to either cylinder is linearly stable and that it is possible to have stability with less dense fluid lying outside. The study also revealed that the stable configuration with less viscous fluid next to the inner cylinder is more stable than the one with the less viscous fluid next to the outer cylinder. They concluded that the onset of Taylor instability for one fluid may be delayed by the addition of a thin layer of less viscous fluid on the inner wall and promoted by a thin layer of more viscous fluid on the inner wall.

This theory agrees well with experimental data for Taylor-Couette flow and Rayleigh-Bernard convective problem. However, the theory fails when used for wall bounded parallel flows such as plane Couette flow, plane Poiseuille flow, and pipe Poiseuille flow.

Energy theory of instability

The energy theory method helps to understand the physical processes that lead from a linear instability to a non-linear instability in flows (Criminale(Jr) et al., 2003). The energy theory method has been used in the study of flow instabilities by Schmid and Henningson (2001), Betchov and Criminale (Jr) (1967), Lin (1955), Joseph (1976), and Drazin and Reid (2004). This method involves observing the rate of increment of the disturbance energy of the flow system with time. The critical condition is determined by the maximum Reynolds number at which the disturbance energy in the system monotonically decreases with time (Dou, 2006). Dou (2006) observed that the critical Reynolds number obtained using the energy method by Betchov and Criminale (Jr) (1967), Drazin and Reid (2004), and Schmid and Henningson (2001) is much lower than that obtained in experiment.

In the flow system, it is considered that turbulent shear stresses interact with the velocity gradient and a flow disturbance gets energy from mean flow in such a way. Thus, a small flow disturbance can be amplified by the large energy gradient. When disturbances are amplified, they suppress the mean flow energy, when disturbances are decaying, the mean flow internal energy increases (Criminale(Jr) et al., 2003).

Although it is possible to understand the transition process from the energy theory method, the mechanism is still not fully understood and the agreement with the experimental data is still not satisfying. As such, Dou (2006) proposed another mechanism for flow instability and transition to turbulence in wall-bounded shear flows (which include the plane Poiseuille flow, the pipe Poiseuille flow, and the plane Couette flow). This mechanism suggests that the energy gradient in the transverse direction plays a role in the amplification of a disturbance, whereas the energy loss in streamline direction serves the function of damping the disturbance. The related analysis obtains consistent agreement with the experimental data at the critical condition for wall-bounded shear flows.

Recently, Dou et al. (2008) utilised the new energy gradient theory mechanism to study the instability of Taylor-Couette flow between concentric cylinders. The aim of their investigation was to demonstrate that the mechanism of instability in the Taylor-Couette flow can be explained via the energy gradient concept. They gave detailed derivation for the calculation of the energy gradient parameter in the flow between concentric rotating cylinders. Their calculated results for the critical condition of primary instability (with semi-empirical treatment) are found to be in very good agreement with the experiments in

the literature. Their results also show that a mechanism of spiral turbulence generation observed for counter-rotation of two cylinders can be explained using the energy gradient theory and that the energy gradient theory can serve to relate the condition of transition in Taylor–Couette flow to that in plane Couette flow.

Weakly non-linear theory

The linear theory only considered the infinitesimal disturbances in the flow. As such, only the initial growth of the disturbance can be determined. The linear theory of hydrodynamic stability can easily predict correctly the critical Taylor number, but it cannot predict the establishment of a new equilibrium flow, the Taylor vortex flow, above the critical Taylor number. The exponential growth of the disturbances considered in linear theory cannot be sustained long in time and, in a real flow, the growth rate is suppressed by viscous effects. Therefore, it is necessary to solve the nonlinear equations, which means that the higher order terms cannot be neglected (Deng, 2007).

Stuart (1958) extended the linear theory to larger amplitude disturbances by studying the mechanics of disturbance growth taking the non-linearity of the hydrodynamic system into account. Davey (1962) made use of a weakly non-linear approach to obtain a Landau-type equation that describes the time evolution of the vortex velocity field. A good agreement was found between Davey's result and the one obtained by Donnelly (1958) over the range of the Taylor numbers above the critical value for which the perturbation theory is expected to be valid.

Non-linear theory

Jones (1981) proposed an approach that is valid near the stability boundary for the onset of wavy vortex flow for two radius ratios, $\eta = 0.8757$ and $\eta \rightarrow 1$ at a large Taylor numbers. They employed the Galerkin method for the solution of the partial differential equations in two spatial variables with prescribed boundary values. In the Galerkin method, the stability problem is solved by finding the eigen-values of the matrices related to the differential equations. They applied their techniques only for the case where the inner cylinder is rotating and the outer cylinder is at rest. The results obtained using their method show agreement with the results of Zarti and Mobbs (1979).

2.3 Review of flow around cylinders

This section is concerned with the review of the flow around cylinders, which are bluff bodies. Bluff bodies are structures with shapes that disturb the flow around them. The geometry of the PIV endoscopic probe in Figure 1.2 is similar to that of a cylinder. In this thesis, a cylinder is used to test by experiment the intrusivity of this probe, by inserting it in the test rig annular gap. As such, the author thought it wise to briefly review the aerodynamics behind bluff body configurations.

Over the years, several attempts have been made to study the flow field around circular cylinders. There are many reasons for the continuing interest in the study around this geometry. Firstly, there are huge amount of experimental data on cylindrical flows to validate analytical and numerical flow models. Secondly, the associated flow field displays fundamental flow phenomena that form the building blocks of more complex flows. Thirdly, it is a good problem for testing methods for modelling flows past other bodies of practical importance.

The flow field around cylinders has been studied extensively through experimental and computational methods. For example, the flow field over and behind a circular cylinder with its axis aligned with the free stream was investigated experimentally by Higuchi et al. (2006) using PIV technique to study the behaviour of the leading edge separating shear layer and its effect on the wake. These authors discovered that the shear layer reattaches with subsequent boundary layer growth for large length to diameter ratio (L/D), whereas the shear layer remains detached for a shorter length diameter ratio. Higuchi et al. (2006) also investigated and analysed the flow structures of the separating and reattaching shear layer and of the wake behind a sting-mounted cylinder with the Proper Orthogonal Decomposition (POD), using both flow visualisation and PIV technique. POD is a technique to capture the overall behaviour of a dynamic system by generating an eigenvector matrix that captures the non-linearity of the input system. The result of the experiment and anlyseis revealed that the wake of a supporting strut was found to influence the cross-sectional velocity profile downstream. The Turbulence properties in unsteady flows around a circular cylinder wake at high Reynolds numbers with a low aspect ratio and high blockage coefficient was studied by Braza et al. (2006) using PIV techniques. Adaramola et al. (2006) experimentally studied the turbulent wake of a finite length circular cylinder mounted normal to a wall and partially immersed in a turbulent boundary layer using two-component thermal anemometry in a low-speed wind tunnel.

The flow along a circular cylinder involves a leading edge separation that reattaches on the side surface, depending on the length of the cylinder. The phenomenon of flow separation has been a subject of research studies, for example, Kiya (1991) studied flow separation from the shoulder of the cylinder and its reattachments and found a cellular structure in the reattachment region.

The turbulent wake of flow across a circular cylinder over a wide range of Reynolds number develops a von-Karman vortex street. The flow characteristics across a circular cylinder are determined by the Reynolds number, Re, which is the ratio of inertia forces to the viscous force. Mathematically, this is defined by:

$$Re = \frac{\rho \mathrm{v} D}{\mu} \qquad 2.17$$

where ρ is the density (kg/m^3) of the fluid, v is the free-stream velocity (m/s), D is the diameter of cylinder (m), and μ = dynamic viscosity of air (kg/ms).

Different flow regimes display different flow characteristics. Flows that display similar characteristics over a range of Reynolds numbers are grouped together and described by certain flow regimes. Table 2-3 shows the different regimes of flow across a cylinder at different Reynolds numbers. Included in the table are the lists of representative experiments for each flow regime.

At a Reynolds number less than approximately 40, the flow is steady and laminar. The separation of the boundary layer on the surface of the cylinder occurs at a Reynolds number between 3.2 and 5 (Nisi and Porter, 1923; Taneda, 1956) and a pair of steady symmetric vortices form behind the cylinder. At Reynolds numbers between 10 and 40, the velocity profiles in the wake are self-similar past 10 diameters downstream of the cylinder. The length of the recirculation zone behind the cylinder grows linearly with Reynolds number and the velocity distributions across the rear symmetry axis in the recirculation zone at different Reynolds numbers exhibit streamwise similarity (Nishioka and Sato, 1974).

Experiments have shown that, the steady flow for the circular cylinder becomes unstable at Re $\geq$ 40 and starts to shed vortices. A characteristics frequency, expressed in non-dimensional form as Strouhal number, is associated with the wake at this Reynolds number. The Strouhal number is defined as:

$$St = \frac{fD}{v} \qquad 2.18$$

where f is the frequency of the vortex shedding and D and v are defined in equation 2.17.

The critical Reynolds numbers at which shedding first occurs was quoted at Re = 30 by Taneda (1956), whereas Kovasznay (1949) and Roshko (1954b) found that vortex shedding starts at Re = 40. Monkewitz (1988) applied linear parallel stability theory to the cylinder wake and established that the flow becomes absolutely unstable at Re = 25. The concept of global instability was used by Chomaz et al. (1988) to show that global oscillations of a shear flow will occur only once a critical sub-volume of the flow is absolutely unstable.

For Re < 150, the flow remains laminar (Bloor, 1964; Roshko, 1954a), the shed vorticity decays as it convects downstream, and the Strouhal number increases with the Reynolds number. At Re = 80, transition to a three-dimensional near wake occurs and this is signalled by two discontinuities in the Strouhal-Reynolds number relation. The first discontinuity, at around Re = 180, arises from the generation of vortex loops evolving into pairs of counter-rotating streamwise vortices in the wake. The second discontinuity comes from a transition to fine scale streamwise vorticity over the range $230 \leq Re \leq 260$ (Beaudan and Moin, 1994).

The sub-critical range regimes cover the range $300 \leq Re \leq 2 \times 10^5$. Over this Reynolds number range, the flow around the entire cylinder is laminar and transition to turbulence occurs in the separated free shear layers (Cardell, 1993). At Re = 300, the wake becomes fully turbulent between 40 and 50 cylinder diameters downstream of the cylinder (Uberoi and Freymuth, 1969), after which distance the regular vortices have completely decayed. When $Re > 10^4$, transition in the shear layers occurs very close to the separation points, and the base pressure coefficient C_{pb}, drag coefficient C_d, and Strouhal number St are approximately constant at values of 1.1, 1.2 and 0.2 respectively (Roshko and Fiszdon, 1969). The mean aerodynamic properties of the cylinder are sensitive to free stream disturbances in the sub-critical Reynolds number range. These disturbances, as well as the cylinder surface roughness, the blockage ratio, and other geometric parameters, have been shown by Norberg (1987) to influence the transition to turbulence in the free shear layer, as well as the mixing and entrainment in the wake region for sub-critical and critical Reynolds numbers up to 3×10^5. Over the range $2 \times 10^5 \leq Re \leq 3.5 \times 10^6$, which is referred to as the critical Reynolds number transition range, two transitions of drag coefficient named by Roshko (1961) as lower and upper transitions are identified. The results of the experiment by Roshko (1961) show that the drag coefficient drops abruptly from 1.2 to about 0.3 over the lower transition range $2 \times 10^5 \leq Re \leq 5 \times 10^5$.

Table 2-3: Flow regimes over a cylinder.

Regime	Reynolds number	Flow characteristics	Experiments
Steady	$0 \leq Re \leq 5$	Attached boundary layer.	Kovasznay (1949) Coutanceau and Bouard (1977) Tritton (1959; 1971)
	~5	Flow convectively unstable.	
	$5 \leq Re \leq 40$	Symmetric, attached twin vortices.	
	~25	Flow absolutely unstable (parallel stability theory).	
Unsteady laminar	$40 \leq Re \leq 150$	Stable vortex street, decaying downstream.	
	~ 90	Oblique vortex shedding.	
Transitional	$150 \leq Re \leq 300$	Transitional to turbulence in the wake. Fully turbulent wake in 40 at 50D downstream.	Williamson (1989)
Sub-critical	$300 \leq Re \leq 2 \times 10^5$	Transition in the free shear layers.	Cantwell and Coles (1983) Roshko (1954)
	$Re \geq 10^4$	Most of the shear layers is turbulent; Base pressure coefficient insensitive to Re.	
Critical	$2 \times 10^5 \leq Re \leq 5 \times 10^5$	Lower transition in C_d from ≈ 1.2 to ≈ 0.3; Near wake width decreases to less than 1D; Separation moves to rear of cylinder; Laminar separation, transition, reattachment and turbulent separation of boundary layer.	Achenbach (1968) Norberg (1987) Delaney and Sorensen (1953)
	$5 \times 10^5 \leq Re \leq 3.5 \times 10^6$	Upper transition in C_d from; Near wake width increases (stays less than 1D); Separation point moves forward.	
Post-critical	$\geq 3.5 \times 10^6$	Turbulent cylinder boundary layer; Regular vortex shedding ($St \approx 0.27$), $C_d \approx 0.7$; Transition precedes separation, no reattachment.	Roshko (1961) Shih et al. (1992)

It was discovered that a laminar separation of the boundary layer is followed by transition to turbulence, reattachment and a final turbulent separation. The separation point moves from the front to the downstream side of the cylinder and the width of the near wake decreases to less than 1 diameter. Over the upper transition range $5 \times 10^5 \leq Re \leq 3.5 \times 10^6$, the base pressure coefficient C_{pb}, which is the pressure coefficient on the leeward side of the cylinder (Ackerman et al., 2009), decreases monotonically from approximately -0.2 to -0.5, while the drag coefficient C_d increases from 0.3 to 0.7 and remains at this value for Reynolds numbers up to 10^7. When the Reynolds number is increased further, the separation point moves forward but remains on the downstream side of the cylinder. At the same time, the wake width increases but stays smaller than one cylinder diameter.

In the post-critical regime, at $Re > 3.5 \times 10^6$, the boundary layer on the cylinder surface becomes turbulent before it separates. The separation-reattachment bubble present in the critical region disappears. The base pressure coefficient C_{pb} continues its monotonic decrease started at $Re = 5 \times 10^6$ reaching -0.6 at $Re = 8 \times 10^6$. The drag coefficient C_d is constant at around 0.7 and vortices are shed regularly at an approximately constant St = 0.27 (Roshko, 1961).

With the advent of high-speed computers and time resolved experimental techniques, complex flow phenomena about a circular cylinder have been discovered at both low and high Reynolds numbers. This has helped to resolve the flow features around this geometry in great details and provided answers to questions on the asymptotic development of the recirculation region (wake bubble), drag, separation point location, vorticity, and of the pressure distribution. All of these flow phenomena are relevant to the understanding of high-Reynolds number flows. Fornberg (1980; 1985) numerically obtained predictions of the steady viscous flow past a circular cylinder at Reynolds numbers up to 600. The aim of his study was to provide further information on the limiting properties of the steady flow at increasing Reynolds numbers on the development of the recirculation region (wake bubble), drag, separation point location, vorticity, and pressure distribution. The results obtained show some new trends in the predicted flow shortly before Re = 300. As vorticity starts to recirculate back from the end of the wake region, this region becomes wider and shorter. He also noticed that other flow quantities, like the position of the separation point, drag, pressure and vorticity distributions on the body surface, appear to be quite unaffected by this reversal of trends.

Kalro and Tezduyar (1997) presented a parallel three-dimensional (3D) finite-element computation of an unsteady incompressible flow around a circular cylinder over the range

$300 \leq Re \leq 1.0 \times 10^5$. They employed stabilised finite-element formulations to solve the Navier-Stokes equations on a CM-5 supercomputer to resolve the flow features around the cylinder in great detail by capturing the strongly 3D character of the circular cylinder.

Figure 2.10 shows the variation of the drag coefficient of cylinders and spheres with their Reynolds number**.** An enlarged view of a section of Figure 2.10 with the corresponding flow patterns is shown Figure 2.11**.** As the Reynolds number increases, the variation in the drag coefficient C_d (based on the front cross-sectional area) decreases and, over the range $10^3 \leq Re \leq$ and 10^5, C_d is nearly constant.

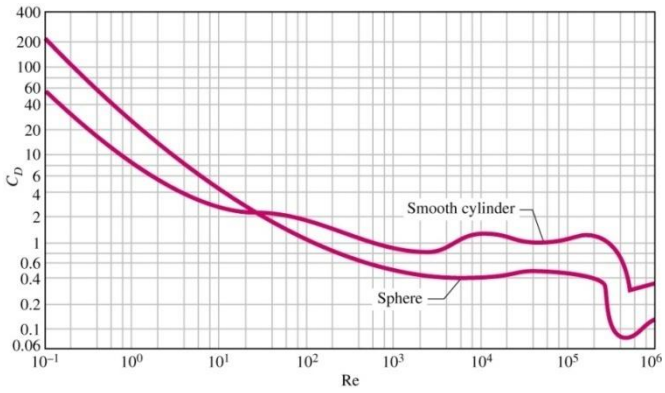

Figure 2.10: Variation of the drag coefficient of a smooth cylinder and of a sphere with Reynolds number (Acheson, 1995).

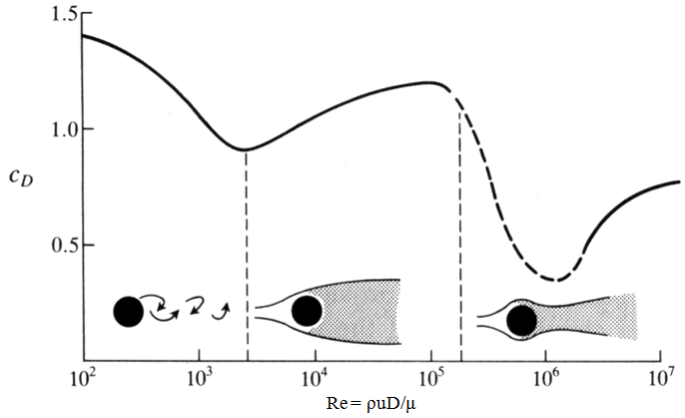

Figure 2.11: Variation of the cylinder drag coefficient with Reynolds number and corresponding flow patterns (Acheson, 1995).

Over the range $10^5 \leq Re \leq 10^6$, the drag coefficient C_d takes a sudden dip. The dip indicates that the pressure drag has suddenly become smaller. The dip in the drag coefficient C_d occurs at the point where the circular cylinder boundary layer changes from laminar to turbulent. When the flow is laminar ($Re < 10^5$), separation starts very near the

shoulder of the cylinder and a large wake forms. Whereas, when the flow is turbulent ($Re > 10^6$), separation is delayed and the wake is correspondingly smaller. The Reynolds number at which the flow changes with a sudden decrease in the drag is termed as the critical Reynolds number, Re_c.

2.3.1 Flow and drag reduction techniques

When the Reynolds number is very low, the flow over a bluff body is highly viscous with skin friction attributed for the force exerted on the body. At a higher Reynolds number, beyond the critical value, vortex shedding occurs in the wake, resulting in a significant pressure drop on the rear surface of the body. The vortex shedding is responsible for serious structural vibrations, acoustic noise and resonance, enhanced mixing, and a significant increases in the drag and lift fluctuations (Choi et al., 2008).

Flow control aims at controlling the different parameters of the flow around a bluff body to achieve desired flow characteristics. The main objectives of most of the flow control techniques to manipulate the wake flows behind circular cylinder are outlined by Kuo and Chen (2009). These are; (i) to reduce the form drag (Tokumaru and Dimotakis, 1991), (ii) to suppress vortex shedding, and (iii) to change the heat transfer characteristics (Lange et al., 1998).

Drag reduction has been a major area of research for decades. Increasing environmental awareness (global warming crisis) has further intensified the need to investigate such technology. Drag reduction is closely related to energy saving and extensive efforts have been made to reduce the drag acting on moving bluff bodies (Lim and Lee, 2003). This research is limited by the assessment of the drag experienced by a cylindrical probe in an annular flow. The implementation of an effective flow control method to reduce the probe drag is left as future work and is beyond the scope of this PhD.

Chapter Three: Computational Fluid Dynamic technique

3.1 Introduction

Computational Fluid Dynamics (CFD) has been employed in this present research study to complement an experimental investigation of the annular flow between rotating cylinders because of its cost effectiveness, easy accessibility and ability to render three-dimensional flow maps. The modelling in this research study was carried out using the commercial software ANSYS FLUENT, version 6.3. This chapter gives a detailed overview of the specific application of ANSYS FLUENT to the modelling of the annular flow. The basic principles and governing equations that ANSYS FLUENT uses to solve an incompressible fluid dynamic problem are presented. The realisable k-ε turbulence model proposed by Shih et al. (1995) and its application to the annular flow is also discussed.

3.2 Basic principles of CFD

There are three main elements in a CFD simulation. These are: (1) pre-processing, (2) processing (solver), and (3) post-processing.

The pre-processing comprises of the definition and discretisation of the geometry to be analysed. Specifically, the geometry or flow domain is divided up into a number of discrete elements by a grid or mesh. The geometry describes the shape of the problem to be analysed. There are various ways of creating the geometry, depending on the complexity of the flow domain. This study used Gambit, version 2.4.6. This is a commercial mesh generator that is part of the ANSYS FLUENT software license package. The design and construction of a good quality grid is crucial to the success of the CFD analysis. The computational cells within the flow domain define an assembly of unit control volumes. The flow problem is solved in each cell. The cell shape and size has a significant impact on the rate of convergence, solution accuracy, and the CPU time required. Many different cell elements and grid types are available. A mesh can be coarse, medium, or fine. The appropriate choice of the mesh depends on complexity of the geometry on flow field, and on the cell types that are supported by the solver. Triangular and quadrilateral cells are commonly used for two-dimensional (2D) problems, in which the flow depends only on two spatial coordinates. The pre-processing aspect is important, as over 50% of the time spent in industry on a CFD project is devoted to the definition of the domain geometry and grid generation (Versteeg and Malalasekera, 1995).

The processing stage (solver) involves the selection of an appropriate physical model for the flow that needs to be modelled, the specification of the fluid properties inside the domain, the definition of appropriate boundary and operating conditions as well as of thermodynamic properties of the flow. This stage involves the discretisation of the governing equation (Navier-Stokes equations) of the system so that they can be solved iteratively. Versteeg and Malalasekera (1995) identified four major numerical solution techniques commonly used for discretised problems in commercial CFD. These solution techniques are: (1) the finite difference method, (2) the finite element method, (3) the finite volume method, and (4) the spectral method. In this work, the finite volume approach is followed, which is discussed in section 0. The advantages of this method over the others are also discussed in section 0.

Post-processing is the process of displaying and visualising the CFD results through the manipulation of the numerical output. In ANSYS FLUENT, some post-processing tools are incorporated into the academic license package to visualise the flow, extract, and manipulate CFD data. Flow properties such as the static pressure, velocity magnitude, turbulent kinetic energy, and velocity vectors are computed and plotted from the flow state output of the flow solver. An adequate analysis of the variation of the flow properties at any point in the medium can be performed using ANSYS FLUENT's graphical interface. Several other features like 2D and 3D surface plots, particle tracking, view manipulations (translation, rotation and scaling) and colour postscript output can be displayed. A key functionality of the post-processing software is the ability to visualize complex flows.

In the ANSYS FLUENT software, it is possible to export the geometry and the flow data to other post-processing software, such as Tecplot and Matlab. Tecplot offers a greater level of sophistication in the geometry and flow rendering tool, aiding the visualisation and the interpretation of the predicted flow pattern. Matlab has been used in this thesis to complement the analysis of the results by the Tecplot. While Matlab does not offer the body fitted (curvilinear) geometry render of Tecplot, it can perform spectral analysis in frequency or wavenumber of the predicted flow, using its signal processing toolbox.

Numerical method

There are three fundamental principles that govern physical aspects of any continuous flow, including turbulent ones (Anderson, 1995; Versteeg and Malalasekera, 1995). These three fundamental principles are:

- The conservation of mass.

- Newton's second law for the conservation of momentum.
- The first law of thermodynamics for the conservation of energy.

The governing equations

The above three fundamental principles can be expressed in terms of basic mathematical equations, the continuity equation, the momentum equations, and the energy equation which, in their most general form, are either integral or partial differential equations. These governing equations are solved subject to boundary conditions describing the physical state of the flow at the computational domain boundaries. The behaviour of the fluid properties is generally described in terms of macroscopic intensive properties such as velocity, pressure, density, temperature, and specific energy. Anderson (1995) identified three important principles that are helpful for obtaining the basic equations of fluid motion as:

- Choosing of appropriate set from any of the law of physics described earlier.
- Application of this set to a suitable model of the flow.
- Obtaining an equation which represents the set.

In this study, all the CFD simulations assume an isothermal, viscous, and incompressible fluid condition. For an incompressible flow, the density is constant. As such the energy equation becomes uncoupled from the continuity and momentum equations. Therefore, all the discussions in this section will only focus on the continuity and momentum (Navier-Stokes) equations. The summary of these equations are presented in this thesis, while the detailed derivations of these equations can be found in Versteeg and Malalasekera (1995), Anderson (1995), and in other fluid mechanics text books.

The continuity equation

The law of conservation of mass can be applied to any fluid flow in a control volume, so that the change of mass in the control volume is equal to the mass that enters through its faces minus the total mass leaving its faces. The unsteady, three-dimensional continuity equation can be written in conservative form as:

$$\frac{\partial \rho}{\partial t} + \nabla \cdot (\rho \mathbf{v}) = 0 \qquad 3.1$$

The first term on the left hand side of equation 3.1 is the rate of change in time of the density (mass per unit volume). The second term describes the net mass flux across the boundaries of an element control volume and it is called the convective term.
For an incompressible flow, the density, ρ is constant, hence the continuity equation 3.1 simplifies to:

$$\nabla \cdot \mathbf{v} = 0 \qquad 3.2$$

The momentum or Navier-Stokes equations

When Newton's second law of motion is applied to the fluid flow in a moving control volume, the rate of change of momentum of a fluid particle equals to the sum of the forces acting on the particle (*F = ma*). There are two types of forces acting on a fluid particle, namely, surface forces and body forces. Surface forces act directly on the surface of the fluid element. They are due to only two forces: (a) the thermodynamic pressure distribution acting on the surface, imposed by the outside fluid surrounding the fluid element, and (b) the shear and normal viscous stresses acting on the surface, also imposed by the outside fluid "tugging" or "pushing" on the surface by means of friction (Anderson, 1995). The body forces act directly on the volumetric mass of the fluid element. These forces "act at a distance". Examples are gravitational, centrifugal, Coriolis, and electromagnetic forces (Anderson, 1995).
The Navier-Stokes equations applied to a fixed control volume are represented in vector form by:

$$\rho \frac{\partial \mathbf{v}}{\partial t} + \rho \mathbf{v} \cdot \nabla \mathbf{v} = -\nabla p + \mu \nabla^2 \mathbf{v} \qquad 3.3$$

This vector equation involves four basic quantities: Local acceleration, convective acceleration, the pressure gradient and viscous forces. The viscous forces are the normal and shear stress distributions acting on the surface. These are modelled in equation 3.3 assuming a Newtonian fluid. In the momentum equation, it is a common practice to highlight the contribution due to the surface forces as separate terms and to include the effects of the body forces as source terms. Therefore, the conservative form of the linear vector momentum equation 3.3 expressed in terms of surface (pressure and viscous stresses) and including the body forces is given as:

$$\rho \frac{\partial \mathbf{v}}{\partial t} + \rho \mathbf{v} \cdot \nabla \mathbf{v} = -\nabla p + \nabla \cdot \tau + \boldsymbol{\mathcal{S}} \qquad 3.4$$

Neglecting the effects of the body forces as source terms, equation 3.4 becomes

$$\frac{\partial \rho \mathbf{v}}{\partial t} + \nabla \cdot \rho \mathbf{v}\mathbf{v} = -\nabla \mathrm{p} + \nabla \cdot \tau \qquad 3.5$$

The continuity equation 3.2 and momentum equation 3.3 can be re-cast into an integral form by integrating them over an arbitrary volume **V** bounded by a close surface **S**. This gives:

$$\int_{\mathrm{V}} \nabla \cdot \mathbf{v} \mathrm{dV} = 0 \qquad 3.6$$

$$\rho \int_{\mathrm{V}} \frac{d\mathbf{v}}{dt} d\mathrm{V} + \rho \int_{\mathrm{V}} \mathbf{v} \cdot \nabla \mathbf{v} \mathrm{dV} = - \int_{\mathrm{V}} \nabla \mathrm{p} \mathrm{dV} + \mu \int_{\mathrm{V}} \nabla^2 \mathbf{v} \mathrm{dV} \qquad 3.7$$

By the application of the Gauss divergence theorem, these become:

$$\int_{\mathrm{S}} \mathbf{v} \cdot \mathrm{d}\mathbf{S} = 0 \qquad 3.8$$

$$\rho \frac{d}{dt} \int_{\mathrm{V}} \mathbf{v}\, \mathrm{dV} + \rho \int_{\mathrm{s}} \mathbf{v}\mathbf{v} \cdot d\mathbf{S} = - \int_{\mathrm{s}} \mathrm{p}\mathbf{I} . d\mathbf{S} + \mu \int_{\mathrm{s}} \nabla \mathbf{v} \cdot d\mathbf{S} = \qquad 3.9$$

where **I** is the identity unit diagonal matrix.

In flows of simple geometry, the continuity and Navier-Stokes equations can be solved analytically, while more complex flows can be tackled numerically with CFD techniques, such as the finite volume method, without additional approximations at low and moderate Reynolds numbers (Versteeg and Malalasekera, 1995). The ease with which solutions can be obtained and the complexity of the resulting flows often depend on which quantities are important for a given flow.

Numerical scheme

The CFD software package ANSYS FLUENT used in this research work is a finite volume code. The computational domain is divided into unit control volumes. To solve the flow governing equations numerically in each control volume, they have to be transformed into algebraic expressions. The process of transforming these equations into solvable algebraic expressions is known as discretisation. The finite volume approach in ANSYS FLUENT involves the integration of the flow governing differential equations over all the

control volumes of the solution domain to yield a volume averaged estimate of the flow state at each cell. The discretisation using the finite volume method involves the substitution of piece-wise constant approximations for the terms in the integral equation representing flow processes such as convection, diffusion, and sources terms. This converts the integral equations into a system of linear algebraic equations (Versteeg and Malalasekera, 1995). These linear algebraic equations are solved iteratively over the control volumes to compute the flow state until convergence. The accuracy of a converged solution is dependent on the physical models, on the grid resolution, as well as on the problem setup (FLUENT, 2006). The advantages of finite volume method over all other techniques as outlined in ANSYS FLUENT 6.3 user's guide (2006) include:

- Flexibility in terms of its usage on either a structured or unstructured mesh.
- Its economical use of computer memory and speed for very large problems, higher speed flows, turbulent flows, and source term dominated flows.
- Easy programming in terms of CFD code development.

There are two numerical solution techniques provided by ANSYS FLUENT (2006). These are:

- A pressure based solver (segregated and coupled algorithms).
- A density based solver.

In both methods, the velocity field is obtained from the momentum equations. The integral form of the governing equations for the conservation of mass and momentum are solved using either method. Both methods use a control-volume-based technique and the discretisation process for the two numerical methods is the finite-volume one. The two methods differ in the approach used to linearize and solve the discretised equations.

The pressure based solver is formulated either as a segregated or a coupled algorithm. In this thesis, the pressure based segregated solver has been used. In this solver, each discrete governing equation is linearised implicity with respect to the conservative variable of that equation. That is, the conservative variables in the governing flow equations are solved implicitly by considering all cells one after another in a sequential manner. This results in a system of linear equations with one equation for each cell in the domain. The reason for selecting the pressure based segregated solver is that this is computer memory efficient, since the discretized equations need only be stored in the memory one at a time. The pressure based segregated solver requires about 1.5 to 2.0 times less computer memory than the pressure based coupled solver. The general solution procedure for the pressure

based segregated and coupled algorithms as well as the density based solvers is fully described in ANSYS FLUENT (2006).

3.2.1 Spatial discretisation

In all CFD simulations involving finite volume method, the computational domain is divided into a finite number of elements or cells. The cell is the control volume into which the physical domain is broken down by the regular and irregular arrangement of nodes to construct the mesh. The flow problem is solved in the cell that is defined around grid points or nodes. The cell averaged flow state is determined at these nodes, so that the flow can be described mathematically by specifying the cell averaged flow state at all grid points in space and time. The accuracy and stability of the numerical computation is dependent on the quality of the mesh. The attributes associated with mesh quality outlined in ANSYS FLUENT (2006) are the node point distribution, the smoothers, the cell skewness and the cell aspect ratio.

The node point distribution determines the degree to which shear layers, separated regions, shock waves, and boundary layers are resolved. Poor node density and node distribution in critical regions leads to poor resolution, which adversely affects the flow predictions. To achieve a good resolution of the boundary layer for a laminar flow, the grid adjacent to the wall should satisfy the condition

$$y_p \sqrt{\frac{\rho u_\infty}{\mu x}} \leq 1 \qquad 3.10$$

where y_p is the distance to the wall from the adjacent cell centroid, u_∞ is the free stream velocity, ρ is density of the fluid, μ is the dynamic viscosity of the fluid, and x is the distance along the wall from the starting point of the boundary layer. Equation 3.10 places the first grid point within the lower quarter of the boundary layer thickness. The resolution of the laminar boundary layer plays a significant role in the accuracy of the computed wall shear stress.

The numerical results for the turbulent flows tend to be more susceptible to grid dependency than those for a laminar flow, due to the interaction of the mean flow and turbulence. The mesh resolution required at the near-wall region depends on the turbulence closure model being used.

Smoothness in the computational mesh reduces the truncation error of the numerical solution. The smoothness of the mesh can be improved by refining the mesh based on the change in cell volume or the gradient of the cell volumes along computational mesh lines.

The cell skewness is the difference between the shape of the cell and the shape of an equilateral cell of equivalent volume. Highly skewed cells can decrease the solution accuracy and de-stabilise the solution procedure. For a good unstructured mesh, the skewness should always be below 0.98 (FLUENT, 2006).

The cell aspect ratio is a measure of the stretching of the cell. It is defined as the ratio of the maximum distance between the cell centroid and face centroid to the minimum distance between the nodes of the cell. A general rule of thumb is to avoid aspect ratios in excess of 5:1 (FLUENT, 2006).

The three major types of mesh that are generally used in CFD simulation are the single-block structured, single-block unstructured, and multi-block structured meshes. The choice of the type of mesh depends on the problem and the solver capabilities.

A structured mesh is typically restricted to topologically rectangular computational domains and is hexahedral in shape. This type of mesh is preferred for analysis of rectangular shapes and of simple cuboid geometries. An unstructured mesh, on the other hand, is typically a mesh with irregular spacing between grid points that are joined to form a tetrahedral mesh. This type of mesh is designed for more complex geometries as nodes can be placed within the computational domain depending on the shape of the body. In other word, the grid can acquire a shape more closely matching a body surface.

Multi-block structured meshes combine the lower computing cost associated with a structured mesh and the flexibility associated with an unstructured mesh. In this type of mesh, the computational domain is subdivided into different blocks that can be structured meshed. An unstructured mesh has been used in this study.

Equation discretisation

There is the need to solve the integral form of the governing partial differential equations 3.6 and 3.7 by the CFD solver. The flow governing equations are solved for each control volume iteratively in discrete form. The discretisation process results in a set of algebraic equations that resolve the variables using a pseudo-time integration method at a specified finite number of points within the control volumes. The flow field within the whole

domain is then obtained (Fokeer, 2006). The semi-discrete form of the governing equations is given by:

$$\sum_{i=1}^{N} \mathbf{v} \cdot \Delta \mathbf{S} = 0 \qquad 3.11$$

$$\rho \frac{\partial}{\partial t} < \mathbf{v} > + \rho \sum_{i=1}^{N} \mathbf{v}\mathbf{v} \cdot \Delta \mathbf{S} = - \sum_{i=1}^{N} \mathrm{p} \Delta \mathbf{S} + \mu \sum_{i=1}^{N} \nabla \mathbf{v} \cdot \Delta \mathbf{S} \qquad 3.12$$

where

$$< \mathbf{v} >= \int_{\mathrm{V}} \mathbf{v} \mathrm{dV}$$

and $\Delta \mathbf{S}$ is the *i*-th facet of each control volume V, which is fully enclosed by *N* facets. The equations solved by ANSYS FLUENT are defined at the control volumes generated by the unstructured computational grid. The discrete variable values such as pressure, velocities and specific turbulent kinetic energy are calculated and stored at the cell centres by ANSYS FLUENT. Using the finite volume method, the integral conservation laws are approximately satisfied over the control volume. That is, the net flux through the control volume boundary is the sum of integrals over the different control volume faces as the control volumes do not overlap. At the control volume faces, the values of the integrand are required for the convection terms of the turbulence closure model. This can only be determined by interpolation from the cell-averaged flow state. This is accomplished by using an upwind scheme to determine the values at the faces. The up-winding is the process of deriving the cell face values of the state variables from quantities in the cell upstream, relative to the direction of the mean velocity.

The finite-volume discretisation method and formulae are further explained with relevant examples in Blazek (2001) and Versteeg and Malalasekera (1995).

3.2.2 Upwind integration schemes

Four upwind schemes are available in ANSYS FLUENT (2006). These four upwind schemes are first-order upwind, second-order upwind, power law, and the QUICK scheme. The first-order upwind and the second-order upwind schemes used in this research are briefly discussed. The detailed description of these schemes can be found in ANSYS FLUENT (2006) and are also treated by Versteeg and Malalasekera (1995) and Blazek (2001).

First-order upwind scheme

This is the simplest numerical scheme available in ANSYS FLUENT. In this scheme, quantities at the cell faces are determined by assuming that, for any variable throughout the entire cell, the face values are identical to the cell average. Hence, when the first-order upwind scheme is selected, the face value of a variable is set equal to the cell average value of the variable in the upstream cell (Versteeg and Malalasekera, 1995).

The main advantages of this scheme are:

- Easy to implement resulting in very stable calculations.
- Can yield better convergence.
- Can be applied without any significant loss of accuracy when the flow is aligned with the grid, especially for a quadrilateral or hexahedral grid, so that numerical diffusion is naturally low.
- Can be used as a starter to perform first a few iterations for any numerical simulation that involves complex flows.

The disadvantage is that this scheme is prone to numerical discretisation errors (numerical diffusion) in a tetrahedral mesh and it will yield less accurate results than on a hexahedral mesh.

Second-order upwind scheme

This scheme is more appropriate than a first order scheme for triangular and tetrahedral grids where the flow is never aligned with the grid. The scheme is more accurate than the first-upwind scheme because it applies a reconstruction of the state variable gradient inside each cell. In this scheme, quantities at cell faces are computed using a multidimensional linear reconstruction approach, whereby higher-order accuracy is achieved at cell faces through a Taylor series expansion of the cell-centred solution about the cell centroid. Hence the face value of a variable is computed by averaging the cell values in the two cells adjacent to the face using a gradient method. The main disadvantage of this scheme is that it can result in face values that are outside of the range of cell values in regions with strong gradients. In such case, it is then necessary to apply limiters to the predicted face values to achieve accuracy and stability. The Green-Gauss node based method is applied as the limiter for the computation of the gradients in the cell centers. The Green-Gauss node based method computes the arithmetic average of the

nodal values on the face. The nodal values are computed from the weighted average of the cell values surrounding the nodes of the face.

3.2.3 Numerical scheme for pressure

The conservative variables in the vector momentum equation are stated in the form of convection-diffusion terms, except for pressure. Pressure appears as a source term in the integral momentum equation 3.7, thus, the pressure field needs to be calculated at the computational cell boundaries in order to solve these equations. Therefore, an interpolation scheme is required to compute the face values of pressure from the cell values.

Pressure interpolation schemes

This scheme computes the face values of pressure from the cell values. The standard scheme method that is available in ANSYS FLUENT (2006) has been used in this thesis. This scheme interpolates the pressure values at the faces using momentum equation coefficients and is only applicable when the pressure variation between cell centres is smooth. The detailed descriptions of the standard pressure interpolation scheme can be found in ANSYS FLUENT (2006).

Pressure-velocity coupling

In an incompressible flow model, the density is constant and hence it is not linked to pressure. As there is no governing partial differential equation for pressure, a constraint is therefore introduced in the coupling between pressure and velocity on the solution of the flow field. The continuity equation can only be satisfied for the velocity field if the correct pressure field is applied to the momentum equations. To achieve this, a pressure-velocity coupling algorithm adds a correction factor to the face flux, so that the corrected face flux satisfies the continuity equation (FLUENT, 2006).

The Semi-Implicit Method for Pressure Linked Equations (SIMPLE) algorithm that uses a relationship between velocity and pressure corrections to enforce mass conservation and to obtain the pressure field has been employed in this work. This algorithm substitutes the flux correction equations into the discrete continuity equation to obtain a discrete equation for the pressure correction in the cell. The SIMPLE algorithm is recommended for steady-state calculations.

3.2.4 Convergence criteria

In all CFD simulations, the governing equations must be transformed to algebraic expressions that are solved iteratively. To obtain a solution, there is the need to specify the information that is required to control the numerical solution algorithm. During the process of CFD simulation, there are integration errors in the discretised equations, summed over all control volumes, which may lead to inaccuracy in the flow solution. The solution to the numerical equations can be used to evaluate such errors. These measures of error, which are generally known as residual errors or residuals, can be used as a guide to see if a solution process is converging or not. The residual is the imbalance of the conservation equation for either mass or momentum summed over all the computational cells. The residual of the solutions can also be used to monitor the performance of a simulation. Progress towards a converged solution can be greatly assisted by the careful selection of the settings of various under-relaxation factors (FLUENT, 2006). Each Under-Relaxation Factor (URF) is adjusted *ad hoc* for its respective conservative variable in order to improve the convergence rate. As the solution process progresses from iteration to iteration, the residual errors from each equation should reduce. Low residuals suggest a solution that converges and the simulation can be considered stable if the residuals keep decreasing in magnitude monotonically with further iterations. That is, solutions of CFD problems are considered to converge when the flow field and the scalar fields are no longer changing.

In many applications, the momentum and continuity residuals are monitored to measure the error in the solution. When the value of each residual is between three to four orders of magnitude below its initial value, the solution is said to achieve convergence to an acceptable level (FLUENT, 2006), depending on the level of accuracy required. At the completion of every flow solver iteration, the sum of the residual squared of each conserved variable is computed and stored to a data file or displayed on terminal screen, where the convergence history is visualised. This enables a quick check on the progress of the solution to be made. Low residuals do not however guarantee that the converged solution is correct. Additional reports of integrated quantities at surfaces and boundaries are often used to judge convergence. A physical variable of the solution flow field therefore needs to be monitored to ensure the convergence of the computation to a physically correct solution. This convergence is reached when the physical variable remains constant for a sufficient number of iterations and the residuals have reached a pre-determined reduction. Mass imbalance is also often used to monitor convergence. This is a

report of the mass flow rates at the inlet and outlet flow boundaries, which should add to zero for a converged solution (Fokeer, 2006).

3.3 Turbulence modelling techniques

Turbulence modelling is an important consideration in CFD. Most flows of engineering importance are turbulent. As such, there is the need to have access to viable tools capable of representing the effects of turbulence on the mean flow. Turbulent flows are characterised by fluctuations in the velocity fields. These fluctuations mix transported quantities such as momentum, and cause the transported quantities to diffuse in the mean flow. Simulating these small scale and high frequency fluctuations directly in practical engineering calculations is often too computationally expensive. Instead, the instantaneous (exact) governing equations can be time averaged, ensemble averaged, or otherwise manipulated to remove the small scales, resulting in a modified set of equations that are computationally less expensive to solve. However, the modified equations contain additional unknown variables such as, the Reynolds stresses, and turbulence models are needed to determine these variables in terms of known quantities. A turbulence model is therefore a computational procedure to close the system of mean flow equations so that a range of turbulent flow problems can be modelled. The purpose of a turbulence model is to provide numerical values for the additional stresses (the Reynolds stresses) due to velocity fluctuations at each point in the flow. The objective is to represent the Reynolds stresses and the turbulent scalar transport terms as realistically as possible, while maintaining a low level of complexity. The effects of the turbulence on the mean flow are modelled so that the details of the turbulent fluctuations are not required to predict the mean flow (FLUENT, 2006). The choice of the turbulence model depends on considerations such as the flow physics, the established practice for a specific class of problems, the level of accuracy required, the available computational resources, and the amount of time available for the simulation. The most important aspect is to ensure that the selected turbulence model is suited to the particular flow being considered. A wide range of models are available and understanding the limitations and advantages of the selected one is required if useful flow predictions are to be obtained with minimum computational cost. It should be noted that no single turbulence model is universally accepted as being superior for all classes of problems.

3.3.1 Reynolds averaged flow equations

The Reynolds-Averaged Navier-Stokes (RANS) equations govern the transport of the averaged flow quantities, with the whole range of the scales of turbulence being modelled. The process of Reynolds-averaging involves the decomposition of each flow variable in the instantaneous (exact) Navier-Stokes equations into its mean (time averaged) and fluctuation components. The velocity vector is represented by equation 3.13 while the pressure and other scalar quantities are represented by equation 3.14.

$$\mathbf{v} = \bar{\mathbf{v}} + \mathbf{v}' \qquad 3.13$$

$$\phi = \bar{\phi} + \phi' \qquad 3.14$$

where $\mathbf{v}$ is the velocity vector,

$\bar{\mathbf{v}}$ and $\mathbf{v}'$ are the mean and fluctuation for the velocity vector,

ϕ denotes a scalar quantity such as pressure, specific energy etc,

$\bar{\phi}$ and ϕ' are the mean and fluctuation for the scalar quantity.

Substituting expressions of this form for the flow variables into the instantaneous continuity and momentum equations and taking a time average (and dropping the overbar on the mean velocity $\bar{\mathbf{v}}$) gives the Reynolds averaged continuity and Navier-Stokes equations for incompressible flow. These can be written in vector form as:

$$\nabla \cdot \mathbf{v} = 0 \qquad 3.15$$

$$\rho \frac{\partial \mathbf{v}}{\partial t} + \rho \mathbf{v} \cdot \nabla \mathbf{v} = -\nabla p + \mu \nabla^2 \mathbf{v} - \nabla \cdot \rho \overline{\mathbf{v}'\mathbf{v}'} \qquad 3.16$$

The above equations have the same general form as the instantaneous Navier-Stokes equations, with the velocities and other solution variables now representing time-averaged values. In equation 3.16, additional terms appear that represent the effects of turbulence. These Reynolds stresses, $-\rho\overline{\mathbf{v}'\mathbf{v}'}$, must be modelled in order to close the system of equation 3.15 and equation 3.16.

Many of the turbulence models are based on the assumption that there exists an analogy between the action of viscous stresses and Reynolds stresses on the mean flow. Both stresses appear on the right hand side of the momentum equations. It has been shown from Newton's law of viscosity that the viscous stresses are proportional to the rate of deformation of a fluid element. For an incompressible fluid, this is represented by:

$$\tau = 2\mu s \qquad 3.17$$

where the strain tensor s is given as:

$$s = \frac{1}{2}(\nabla \mathbf{v} + (\nabla \mathbf{v})^T) \qquad 3.18$$

It was experimentally discovered that turbulence decays unless there is shear in isothermal incompressible flows. Turbulence stresses are found to increase as the mean rate of deformation increases. Boussinesq (1877) proposed the hypothesis that the Reynolds stresses could be taken as proportional to the mean rate of deformation. This is represented by:

$$\rho\overline{\mathbf{v}'\mathbf{v}'} = 2\mu_t s \qquad 3.19$$

Equation 3.17 and equation 3.19 show that the constant of proportionality between τ and $-\rho\overline{\mathbf{v}'\mathbf{v}'}$ is the turbulent or eddy viscosity, μ_t which has the same units as that of molecular viscosity, Pa.s. It is possible to also define a kinematic turbulent or eddy viscosity, $\nu_t = \mu_t/\rho$ with units m^2/s. The turbulent or eddy viscosity is in-homogenous, but it is assumed to be isotropic. This assumption is valid for many flows except for flows with strong separation or swirl. Using this assumption allows to simplify the problem from determining the n^2 components of the Reynolds stress tensor τ in an n-dimensional problem to determining just one scalar field variable μ_t. The turbulent viscosity is used to close the momentum equations.

The rest of this section presents brief overview of the turbulence model for the CFD solutions used in this thesis. The mathematical details of this model can be found in most CFD text books.

The Realizable *k*-*ε* model

The eddy viscosity μ_t distribution in the computational domain can be evaluated using the realizable *k*-*ε* model. The realizable *k*-*ε* model by Shih et al. (1995) belongs to the family of *k*-*ε* models proposed by Launder and Spalding (1972). Since then, it has become the most widely used two equations turbulence model in practical engineering flow calculations (FLUENT, 2006). It is a semi-empirical model based on the transport equations for the Reynolds averaged turbulence kinetic energy *k* and its dissipation rate *ε*. The model transport equation for *k* is derived directly from the Navier-Stokes equations, while the model transport equation for *ε* was obtained using physical reasoning. In this

model, the solution of two separate transport equations allows the turbulent kinetic energy and its length scale to be independently determined. This two-equation model estimate k and ε. The turbulent (or eddy) viscosity μ_t, is computed by combining k and ε algebraically, using dimensional analysis:

$$\mu_t = \rho C_\mu \frac{k^2}{\varepsilon} \qquad 3.20$$

where ρ is the density of the fluid and C_μ is the model closure constant.

The realizable k-ε model by Shih et al. (1995) is a relatively recent model and differs from the standard k-ε model in that it contains a new formulation for the turbulent viscosity. Secondly, the derivation of a new transport equation for the dissipation rate ε has been obtained from an exact equation for the transport of the mean-square vorticity fluctuation. This model satisfies certain mathematical constraints on the Reynolds stresses, consistent with the physics of turbulent flows.

For this model, the transport equations for the turbulent kinetic energy k and its rate of dissipation ε are given respectively in ANSYS FLUENT (2006) as:

$$\frac{\partial}{\partial t}(\rho k) + \nabla \cdot \rho k \mathbf{v} = \nabla \cdot \left(\mu + \frac{\mu_t}{\sigma_k}\right) \nabla k + G_k + G_b - \rho\varepsilon - Y_M \qquad 3.21$$

and

$$\frac{\partial}{\partial t}(\rho\varepsilon) + \nabla \cdot \rho\varepsilon \mathbf{v} = \nabla \cdot (\mu + \frac{\mu_t}{\sigma_\varepsilon})\nabla\varepsilon + \rho C_1 S\varepsilon - \rho C_2 \frac{\varepsilon^2}{k + \sqrt{\nu\varepsilon}} + C_{1\varepsilon}\frac{\varepsilon}{\kappa} C_{3\varepsilon} G_b \qquad 3.22$$

G_k represent the generation of turbulent kinetic energy due to the mean velocity gradients, G_b is the generation of turbulent kinetic energy due to buoyancy. Y_M represent the contribution of the fluctuating dilatation in compressible turbulence to the overall dissipation rate (this is normally neglected in the modelling of incompressible flows). C_1, C_2, $C_{1\varepsilon}$, and $C_{3\varepsilon}$ are constants while σ_k and σ_ε are the turbulent Prandtl numbers for k and ε respectively.

Neglecting the generation of turbulent kinetic energy due to buoyancy G_b and the contribution of the fluctuating dilatation Y_M, equations 3.21 and 3.22 can be rewritten respectively as:

$$\frac{\partial}{\partial t}(\rho k) + \nabla \cdot \rho k \mathbf{v} = \nabla \cdot (\mu + \frac{\mu_t}{\sigma_k})\nabla k + G_k - \rho\varepsilon \qquad 3.23$$

and

$$\frac{\partial}{\partial t}(\rho\varepsilon) + \nabla \cdot \rho\varepsilon\mathbf{v} = \nabla \cdot (\mu + \frac{\mu_t}{\sigma_\varepsilon})\nabla\varepsilon + \rho C_1 S\varepsilon - \rho C_2 \frac{\varepsilon^2}{k + \sqrt{\nu\varepsilon}} \qquad 3.24$$

G_k is modelled from the exact equation for the transport of k as:

$$G_k = -\rho\overline{\mathbf{v}'\mathbf{v}'}:\nabla\mathbf{v} \qquad 3.25$$

Equation 3.25 can be re-written in a manner consistent with the Boussinesq hypothesis as:

$$G_k = \mu_t S^2 \qquad 3.26$$

where

$$C_1 = max\left[0.43, \frac{\eta}{\eta + 5}\right];\ \ \eta = S\frac{k}{\varepsilon};\ \ S = |2s|$$

In ANSYS FLUENT (2006), the values of the model closure constants are: $C_{\varepsilon 1}$ = 1.44, C_2 = 1.9, σ_k = 1.0, σ_ε = 1.2.

The second term on the left hand side of equations 3.23 and 3.24 is the convection term, the first term on the right hand side of both equations is diffusion term, the second term on the right hand side of both equations is the production term while the third term on the right hand side of both equations is the destruction term.

The k equation for the realizable model by Shih et al. (1995) is the same as that in the standard k-ε model and in the Renormalization Group (RNG) k-ε model by Yakhot and Orszag (1986) except for the model constants. The only difference among these models is in the ε equation. The production term in the ε-equation of the realisable k-ε model (the second term on the right hand side of equation 3.24) does not involve the production of k, which makes the model a better representation of the spectral energy transfer. Another difference is the fact that the C_μ is not a constant in this model, but it is a function of the mean strain and rotation rates, the angular velocity of the system rotation, and the turbulence fields (k and ε). The relationship between these parameters is:

$$C_\mu = \frac{1}{A_0 + A_S\frac{kU^*}{\varepsilon}} \qquad 3.27$$

where

$$U^* = |\mathrm{s}|^2 + |\bar{\Omega}|^2 \qquad 3.28$$

and

$$\bar{\Omega} = \nabla \mathbf{v} - (\nabla \mathbf{v})^T \qquad 3.29$$

where $\bar{\Omega}$ is the mean rate of the rotation tensor. The model constant A_0 and A_S are given by:

$$A_0 = 4.04, \qquad A_S = \sqrt{6} cos\, \phi \qquad 3.30$$

where

$$\phi = \frac{1}{3} cos^{-1}\left(\sqrt{6} W\right), \qquad W = \frac{s \cdot s \cdot s}{\tilde{S}^3}, \qquad \tilde{S} = |s| \qquad 3.31$$

One benefit of the realizable *k-ε* model is that it predicts the spreading rate of both planar and round jets more accurately than the standard *k-ε* model (FLUENT, 2006). It is also likely to provide superior performance for flows involving rotation, boundary layers under strong adverse pressure gradients, separation, and recirculation (FLUENT, 2006). The realizable *k-ε* model has shown substantial improvements over the standard *k-ε* model where the flow features include strong streamline curvature, vortices, and rotation. One limitation of the realizable *k-ε* model is that it produces non-physical turbulent viscosity in situations in which the computational domain contains both rotating and stationary fluid zones, such as with multiple reference frames and with rotating and sliding meshes (FLUENT, 2006). This is not the case in any of the simuations in this thesis.

3.4 Boundary conditions

In the annular flow between co-rotating cylinders, the walls are the main source of mean vorticity and turbulence. Therefore, the wall model is likely to have significant impact on the numerical solution. In the near-wall region, the solution variables have large gradients. The momentum and other scalar transports occur most vigorously in the near wall regions. Viscous damping reduces the tangential velocity fluctuations, while kinematic blocking reduces the normal fluctuations very close to the wall. The boundary condition at a stationary wall is usually specified as no-slip. In order to satisfy this, the mean velocity at the wall has to be zero, thereby creating a steep velocity gradient starting as highest at the inner cylindrical wall and decreasing at increasing wall-normal distance. The rate of decrement depends on the computational domain. Therefore, the accurate representation of the flow in the near-wall region is a necessary requirement for the successful prediction of

any wall-bounded laminar/turbulent flows. The turbulent flow in the near-wall region is subdivided into three layers (FLUENT, 2006; Schlichting, 1979):

- The innermost layer, which is called the "viscous sub-layer", is a region where the flow is almost laminar and the (molecular) viscosity plays a dominant role in the momentum and mass transfer.
- The outer layer is usually called the mixing layer. In this region, the Reynolds stresses play a major role.
- Finally, there is an overlap region between the viscous sub-layer and the mixing layer, where the effects of molecular viscosity and turbulence are equally important.

The three sub-divisions of a turbulent boundary layer are illustrated in Figure 3.1. This diagram specifically refers to a fully developed turbulent boundary layer flow under zero stream-wise pressure gradient at a Reynolds number $Re_x = \rho v x/\mu \geq 200$, where x is the streamwise distance from the flat plate leading edge and ρ, v, and μ are defined as in equation 2.17. The boundary layer mean velocity profile exhibits in this case a logarithmic overlap region.

A higher mesh density and special wall modelling procedures are required to resolve the velocity gradient and better predict the flow behaviour in the near-wall region. ANSYS FLUENT (2006) identifies two alternative approaches, which are the wall function method and the near-wall modelling method. These are discussed briefly in sections 3.4.1 and 3.4.2.

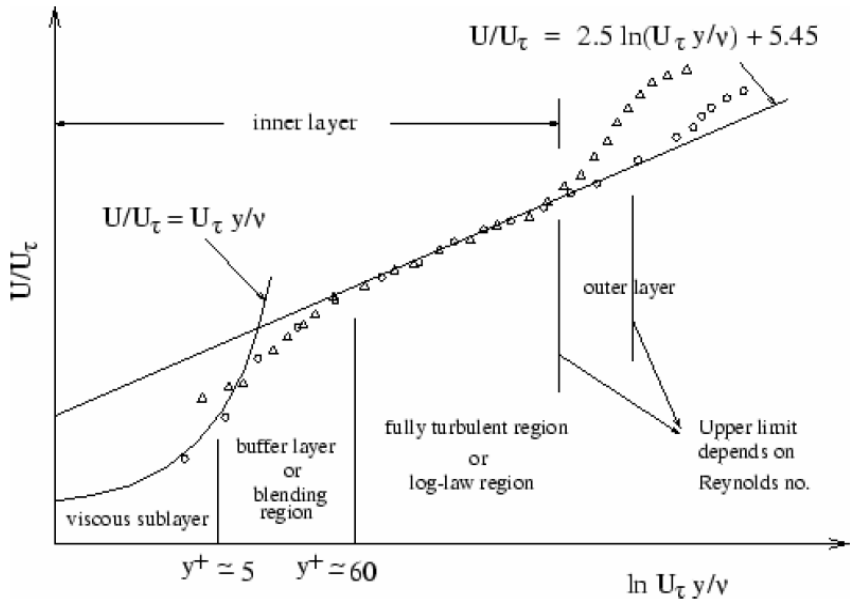

Figure 3.1: Subdivisions of the near-wall region (FLUENT, 2006).

3.4.1 The wall function approach

In modelling the near wall region, the viscosity-affected inner region (viscous sub-layer and buffer layer), where the solution variables change most rapidly, is not resolved. As such, there is the need to model the effects of the unresolved inner layer on the resolved outer layer. This is done by using semi-empirical formulas known as wall functions. The wall functions comprise of the von-Karman law of the wall for the mean velocity and algebraic formulae for the near-wall turbulent quantities. The use of the wall function particularly in high Reynolds number flows eliminates the need to modify the turbulence models to account for the presence of the wall and saves computational resources. This method is being used because it is economical, robust, and reasonably accurate and, as such, it is the best practical option for the near-wall treatment of industrial flow simulations. However, this method is not suitable for situations where low-Reynolds number effects are pervasive in the flow.

3.4.2 Near-wall modelling approach

In the near-wall modelling approach, turbulence models are modified to enable the viscosity-affected region to be resolved with a mesh all the way to the wall, including the viscous sub-layer. This method is suitable for situations where the low-Reynolds number effects are pervasive in the flow domain. In addition, the near-wall modelling approach combined with adequate mesh resolution in the near-wall region can be used for situations where there is transpiration through the wall, where there is a severe pressure gradient leading to boundary layer separations, where there are strong body forces like in the flow over a rotating disk and finally where there is high three-dimensionality in the near-wall region (FLUENT, 2006). The near-wall modelling approach can be used with the realisable k-ε model with the standard wall function option.

3.4.3 Near-wall treatment

Four different methods are available in ANSYS FLUENT (FLUENT, 2006) for the modelling of the near wall region. These are standard wall function, enhanced wall treatment, non-equilibrium wall function, and user-defined wall function. The Standard wall function has been used in this thesis and this is briefly discussed.

Standard wall function

This function has been widely used for industrial flows and is based on a variant of the log-law proposed by Launder and Spalding (1974). The application of the wall function is based on the assumption that the production of the turbulent kinetic energy *k* and its dissipation rate *ε* is equal in the cells adjacent to the wall.

The logarithmic law of the wall for the mean velocity of the flow is expressed as:

$$U^* = \frac{1}{\kappa} ln(Ey^*) \qquad 3.32$$

where

$$U^* \equiv \frac{U_P C_\mu^{\frac{1}{4}} \kappa_P^{\frac{1}{2}}}{\frac{\tau_\omega}{\rho}} \qquad 3.33$$

$$y^* \equiv \frac{\rho C_\mu^{\frac{1}{4}} \kappa_P^{\frac{1}{2}} y_P}{\mu} \qquad 3.34$$

and κ = von Kármán constant (= 0.4187)

E = wall constant (= 9.793)

U_P = mean flow tangential velocity at point P

k_P = turbulent kinetic energy at point P

y_P = wall normal distance from point P to the wall

ρ = fluid density

μ = dynamic viscosity of the fluid

τ_w = wall shear stress

The logarithmic law for the mean flow velocity is known to be valid over the range $30 < y^* < 300$. However, in ANSYS FLUENT (2006), the log-law is employed for $y^* > 11.225$. Where the mesh at the wall-adjacent cells is such that $y^* < 11.225$, the laminar stress-strain relationship $U^* = y^*$ is used.

The standard wall function has been reported to give reasonably accurate predictions for the majority of high Reynolds number wall-bounded flows (FLUENT, 2006). The disadvantage of the standard wall function is that it becomes less reliable when the near-wall flows are subjected to severe pressure gradients. In such case, the non-equilibrium wall functions can improve the results (FLUENT, 2006). The full details on the near-wall function treatment can be found in ANSYS FLUENT (2006).

Rotational wall boundary

The rotational wall boundary is used for modelling the inner cylinder rotating surface. In this situation, the rotational option is enabled and the rotational speed is defined about a specific axis in ANSYS FLUENT. More information on the use of rotational wall boundary condition for two-dimensional and three-dimensional problems can be found in ANSYS FLUENT (2006).

Chapter Four: Experimental rig design

4.1 Introduction

Experimental rigs are the basic tools for conducting practical engineering investigations. The purpose of the investigation determines the configuration of the experimental rig to be designed and constructed. This research aims to provide further information on the flow pattern that develops in concentric rotating cylinders and to investigate the intrusive effects of the cylindrical probe model on the ensued flow features. This chapter details the design and the construction of an assembly of concentric rotating cylinders that targets this aim.

4.2 Rig specifications

A concentric rotating cylinder assembly is considered in this study as this is a common geometry in many engineering applications, examples of which are given in section 2.2.
The experimental test rig was designed to:

- Allow the physical simulation of the different flow regimes that exist within the annular region of concentric rotating cylinders in a laboratory environment.
- Help investigating the intrusive effect of a cylindrical probe model on the flow pattern between the rotating concentric cylinders.
- Allow the comparison of the experimental results with CFD predictions.

4.2.1 Design of the experimental rig

A feasibility study was conducted on building an annular concentric rig that would fit the aims of this research work. A conscious effort was made to achieve a flexible geometry of simple construction. The design constraints include making the gap between the inner cylinder and the outer cylinder wide enough to allow the insertion of a cylindrical probe. Secondly, the length of the cylinders was to be made long enough in order to obtain a large aspect ratio so as to eliminate the phenomenon of the ‘end effects’ that causes distortion/interference in spatially-periodic Taylor-Couette flow (Baier, 1999; Moser et al., 2000; Youd, 2005).

Air was selected as the working fluid to eliminate the complexity of a change in the refractive index when using optical measurement techniques and to avoid any leakage problem from getting the probe into the annular region had liquid been used. Air has been

used previously by other researchers as the working fluid in the annular region of concentric cylinders. For instance, an experimental and theoretical-numerical investigation was conducted by Kuehn and Goldstein (1976) within a horizontal annulus using water and air at atmospheric pressure with a ratio of gap width to inner-cylinder diameter of 0.8 to study the velocity and temperature distributions as well as the local heat-transfer coefficients for natural convection. Dyko et al. (1999) investigated by numerical and experimental methods the development of spiral flow in air-filled moderate-gap annuli, its interaction with the primary flow, and the factors influencing the number and size of the spiral vortex cells.

Based on this review of past concentric cylinder rigs, the experimental test rig was designed, built, and commissioned. The isometric drawing of the design of the concentric rotating cylinders is shown in Figure 4.1, while the final assembly based on this design is shown in Figure 4.2. The concentric rotating cylinder design went through a series of modifications to arrive at the final design shown in Figure 4.1. The experimental rig consists of two main parts: the drive system and the test section. The detailed drawings and the descriptions of the major components of this rig are shown in Figure A 1 to Figure A 3 of appendix A.

The drive system

The drive system consists of three parts: the adjustable speed motor controller, the motor, and the drive belts. The apparatus uses an adjustable speed controller. The controller on this rig is a solid-state reversing variable-speed drive with dynamic braking. The controller is suitable for permanent-magnet and shunt-wound motors up to 750W. The controller is used to adjust the speed of the motor and for controlling the rotation of the cylinders in the clockwise or anticlockwise directions. The speed of the DC motor is controlled by a potentiometer using a linear closed loop control. The minimum and maximum speeds are pre-settable by means of timer potentiometers mounted on the controller printed circuit board. There are two speed controllers on the rig. Each controller is connected to the DC motor that drives one of the cylinders as shown Figure 4.2. The speed indicator on the controller specifies a range between 0 and 10. The actual operating speed is measured and monitored during the experiment using a tachometer.

The two motors on the rig are the SD12C 220V (series DC) model made by Parvalux. Each of the motor is rated at 150Watts with a rated maximum speed of 4000RPM. The speed of each motor is controlled by the DC reversing speed controller.

For this apparatus, the motor shaft driving the inner cylinder is connected to the inner cylinder shaft by an adjustable belt coupling through a pulley system, as is the outer cylinder. The two motors that rotate both the inner and the outer cylinder are bolted directly to the metal steel base platform shown in Figure 4.2. Whereas the rig was designed to rotate the two cylinders independently, all the experimental results in this thesis are obtained with the outer cylinder not rotating.

The test section

The main structural component of the test section is a long shaft made of steel. This is shown in Figure A 1 of appendix A. This long shaft is being supported by two bearing blocks. The bearing blocks house the bearings through which the long shaft is connected to the two DC motors and the inner cylinder. Apart from giving supports, the bearing blocks serve as stabilizers for the whole assembly by reducing the shaft vibration as the inner cylinder rotates at speed. The inner cylinder is mounted on the steel shaft in the test section and is propelled by one of the two electric motors through the shaft and the bearings. The inner cylinder is made of PVC tube, it has an axial length of 500mm and an outer diameter of 50mm. The thickness of the cylinder is 3mm. The inner cylinder is coated in black to minimize the reflection from the impinging light sheet from the PIV laser, which is detailed in chapter five. As the PVC inner cylinder is push fitted over the steel shaft, this fabrication process helps to remove any camber and stenotic thickness extrusion error in the PVC.

An outer cylinder was mounted coaxially with the inner cylinder. The outer cylinder is a perspex transparent tube. The choice of the transparent tube is to enable optical access to the test section for PIV measurements, for flow visualisation, and to keep costs to a minimum. The outer cylinder has an axial length of 520mm, a 100mm outer diameter, and is 3mm thick. This gives the system a gap width of 22mm and a cylinder radius ratio η of 0.53. The accuracy of the diameter of the Perspex is within $\pm$1.5mm.The parameters for this apparatus are different from all of the previous research work on Taylor-Couette flow instability. The major difference is the use of a wide gap between the inner and outer cylinders so that it can accommodate a 10mm diameter cylindrical probe, which is representative of the single-stem endoscopic PIV probe in Lad (2011).

The difference of approximately 20mm in the axial length between the inner cylinder and the outer cylinder is the length occupied by the free end collars of the two bearings. The free collars are fitted with three stud spacers each that support the outer cylinder as shown in Figure 4.1 and Figure 4.2.

The free end collar allows the outer cylinder to rotate independently from the inner cylinder. At the rear end of the outer cylinder, the collar takes the form of a long outer shell boss. The long outer shell boss, the spacers and the free end collar are shown in Figure 4.1 and Figure 4.2. The rig details are presented in Figure A 2 of appendix A.

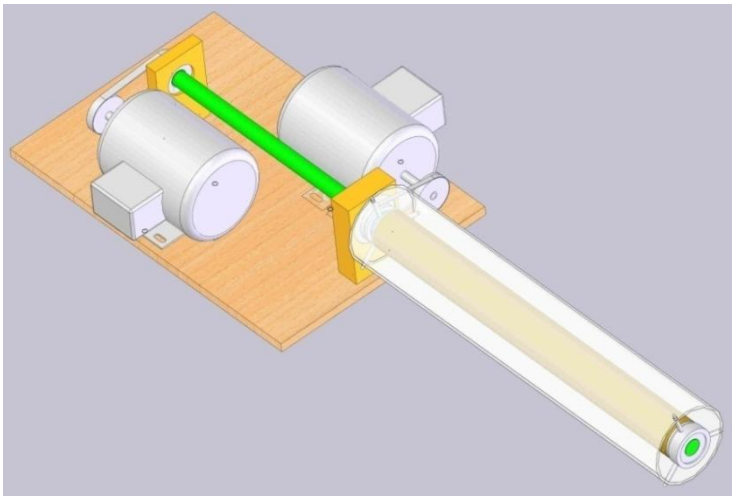

Figure 4.1: Isometric view of the concentric rotating cylinder assembly.

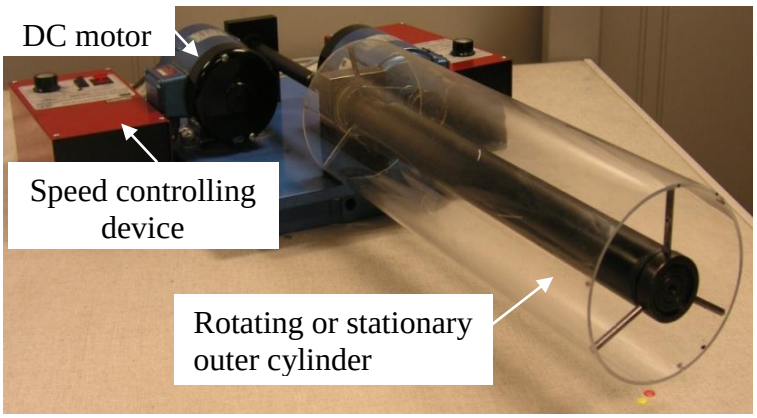

Figure 4.2: Concentric rotating cylinder test rig after assembly.

The stud spacers serve to support and balance the whole assembly, they allow the concentric positioning of the outer cylinder relative to the inner cylinder, and they reduce the vibration that develops by the apparatus as the inner cylinder rotates at speed. The stud spacers are prevented from influencing the flow by the use of end-walls. This is discussed in details in section 4.3. Further reductions in the vibration could have been achieved by simply supporting the free end of the non-rotating cantilevered outer cylinder. It was

preferred to keep the cantilever support arrangement to provide a consistent benchmark for future tests involving the rotation of the outer cylinder.

The entire rig is securely fitted on a thick metal steel base platform with a wider area in consideration of the load it has to support. The metal steel frame base allows all operational electrical components to be fitted conveniently around the rig. The whole rig is structured as an independent and complete stand-alone unit and can be easily relocated without dismantling it. A drawing of the steel platform with the concentric cylinders is shown in Figure A 4 of appendix A.

4.2.2 Further design modifications of the test rig for parametric study

As the research work progressed, further investigations required to further modify the test rig. One of the considerations for selecting the outer cylinder radius was the size of the probe to be inserted in the gap width between the cylinders. Reducing the size of the outer cylinder below 100mm would have reduced the clearance between the walls of the inner and of the outer cylinders and the cylindrical probe, creating excessive blockage. Therefore, the cylinder gap width ratio was varied in the experiment by increasing the diameter of the outer cylinder while the diameter of the inner cylinder remained fixed. This increased the gap width between the cylinders and created more clearance between the probe and the walls of the inner and of the outer cylinders. This modification allows a parametric study on the intrusivity of the cylindrical probe at different flow regimes in the annular region. It is expected that the flow regimes will change due to increase in the Reynolds number as a result of the increase in the gap width d. It is of interest to explore how the changes in radius ratio and aspect ratio affect the flow regime that develops in the annular region of the cylinders and the effect that these changes have on the interaction of the ensuing flow field with the cylindrical probe.

It is acknowledged that altering the Reynolds number by increasing the cylindrical gap width d may create more problems as already observed by Taylor (1923), who noted that end-wall effects due to the finite length of the cylinders will be significant and difficult to eliminate when the radius of the inner cylinder is much less than half of the outer cylinder radius. As a result, the flow pattern will cease to be the same as that between two infinitely long cylinders.

To conduct a parametric study on the gap width effect on the annular flow between coaxial cylinders, two more annular rigs of different radius ratio were built. Since there was no change in the other components of the apparatus apart from the outer cylinder, the

final design layout remained the same as that of Figure 4.1. This resulted in the three interchangeable layouts shown in Figure 4.3. The test assemblies shown in Figure 4.3 have a common inner cylinder outer diameter of 50mm, an outer cylinder inner diameter of (a) 100mm, (b) 120mm, and (c) 150mm, and a common outer cylinder thickness of 3mm.

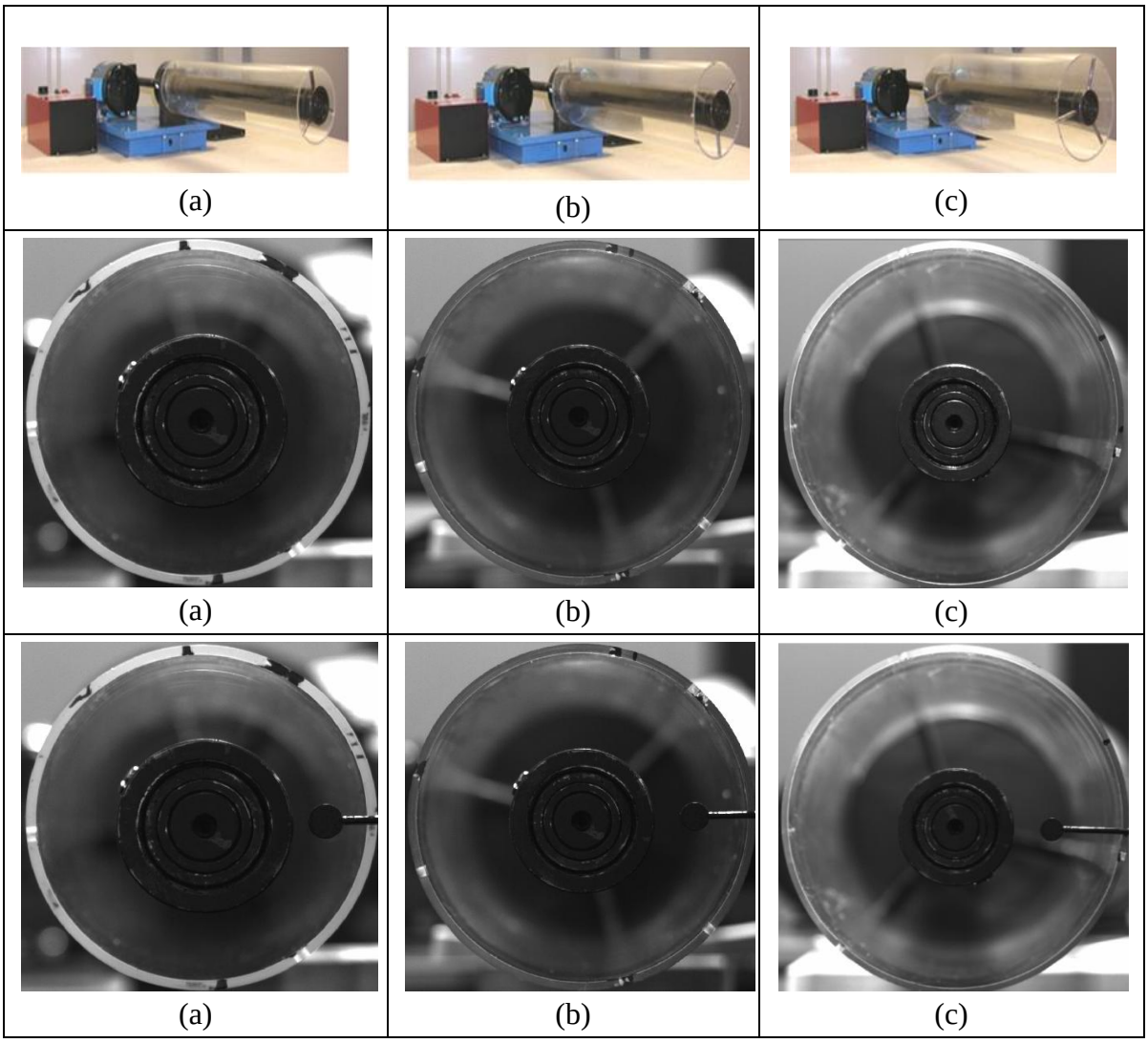

Figure 4.3: Assembly of concentric rotating cylinders with various aspect and radius ratios viewed in perspective and in the azimuthal plane without and with cylindrical probe. (a) test case 1, (b) test case 2, and (c) test case 3.

4.3 Concentric rotating apparatus with cylindrical probe

As the research work progressed, it was realised that there was a mismatch in the end-wall conditions between the experimental apparatus of Figure 4.3 and the CFD model geometry detailed in chapter six. It was thought that changing the boundary conditions of the CFD geometry would have led to a computationally more expensive simulation. It was therefore decided that modifying the end-walls of the experimental apparatus was the

more attractive option. As such, end-walls of the experimental apparatus at the left and right sides were changed to solid walls. This change in the boundary conditions of the experimental apparatus makes it easy to have the same visualisation area as the total geometry area of the CFD simulations, such that the geometries for the two techniques have the same aspect ratio and radius ratio. However, there is a slight difference in the boundary condition at the left end-wall. This is due to the fact that the light sheet from the laser during PIV measurement passes through the left end-wall.

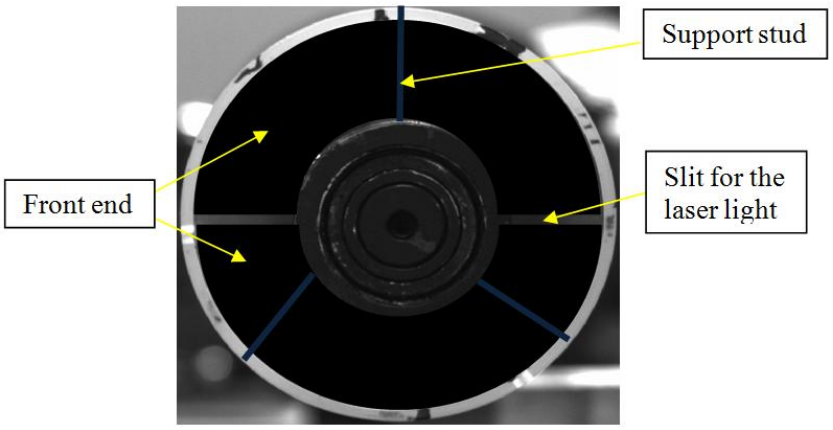

Figure 4.4: Azimuthal plane showing the left end-wall without the cylindrical probe.

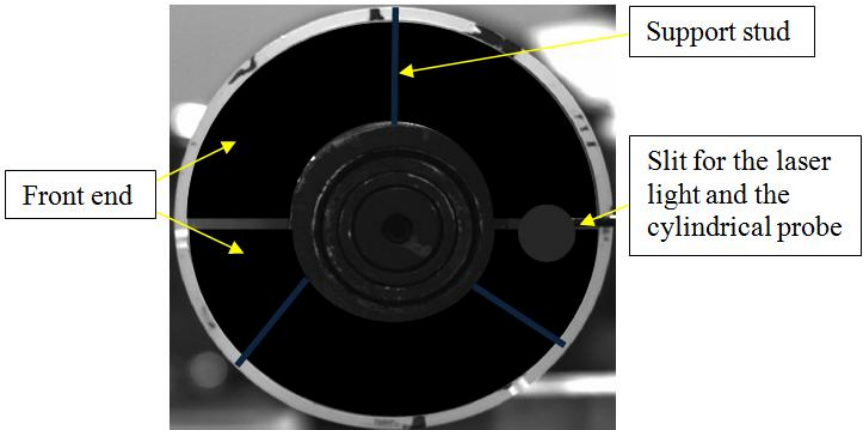

Figure 4.5: Azimuthal plane showing the left end-wall with the cylindrical probe.

An attempt was made to use a transparent end-wall at the left boundary for the passage of the light sheet from the laser. This attempt was discontinued due to the difficulty in getting the cylindrical probe and the seeding particles through to the annulus of the concentric cylinders. As such, a slit was created on the left end-wall to allow the passage of the light sheet. This was implemented by positioning a black perspex sheet with the slit at the left end-wall of the concentric cylinders. The front view of the modified apparatus is shown in Figure 4.4 and Figure 4.5 without and with the cylindrical probe in position respectively.

4.4 Particle feeder

The annular air gap between the two concentric cylinders in Figure 4.3 is seeded by liquid droplets for Particle Image Velocimetry using a particle feeder device. The particle feeder employed in this study is the high volume liquid seeding generator (10F03) shown in Figure 4.6. This seeding generator produces droplets designed for PIV and LDA measurements. It is Dantec's preferred seeding solution for medium to large size facilities.

Figure 4.6: High volume liquid seeding generator (10F03).

The seeding generator works by injecting air into a fluid, normally olive oil or other recommended products, at near sonic velocity via a number of Laskin nozzles. Each nozzle produces micro-bubbles with micro-droplets with a typical diameter of 1-5 micron. These bubbles reach the free oil surface and burst, releasing the micro-droplets. Internal baffles are used to remove unwanted large droplets that can be produced by the splash when a bubble bursts. The density of the micro-droplets is determined by the air flow rate through the nozzles and by the number of nozzles. It is important to have a large free surface where the bubbles burst to avoid foaming. This sets the upper limit of the micro-droplet production rate. Control of the micro-droplet production rate is provided by turning nozzles on and off and by adjusting the air supply pressure. This level of control tends to produce a fixed seed density at a variable flow rate. In order to provide control of the seed density and avoid the need for a mixing plenum in the experiment, dilution air can be admitted to the generator so that lower seed densities can be produced when required. Details of the seeding particle parameters and how the seeding generator is used to seed the annular air gap between the coaxial cylinders are further discussed in section 5.6.3.

Chapter Five: Instrumentation – Particle Image Velocimetry (PIV)

5.1 Introduction

This chapter is concerned with the instrumentation and the detailed description of the experimental techniques used to investigate the flow in the concentric rotating cylinders. The specific details of the experimental set-up and data acquisitions procedure, data processing and analysis are also discussed. Two sets of experimental investigations were conducted using the same PIV measuring technique. The two sets of experiments were conducted back to back. The first set of experiments was to investigate the different flow regimes that exist in the annular region of coaxial rotating cylinders with the inner cylinder rotating and the outer cylinder at rest at various aspect and radius ratios. The second set of experiments was to investigate the intrusive effect of inserting a cylindrical probe into the annular gap of the concentric rotating cylinders. This was achieved by comparing the results from the second set with the ones from the first set of experiments. The method and criteria employed for determining the PIV results convergence and accuracy are discussed in chapter seven.

5.2 Particle Image Velocimetry

PIV is an optical, non-intrusive measurement technique used to simultaneously determine the velocities at many points in a flow, thereby permitting spatially resolved velocity field measurements. PIV measures the velocity of a fluid element indirectly by means of the measurement of the velocity of tracer particles within the flow (Raffel et al., 2007). It allows to record spatially resolved flow images in a variety of applications in gaseous and liquid media and to extract instantaneous velocity fields out of these images. These features are unique to PIV, as most of the other techniques for velocity measurements only allow the measurement of the velocity of the flow at a single point (Adrian, 1991; Rostami et al., 2007).

PIV is a very important technique in research today because it provides spatially resolved velocity measurements instantaneously even in high speed flows with shocks or in boundary layers close to a wall, where the flow may be disturbed by the presence of the probes. It is capable of measuring a whole two-dimensional (2D) flow field at once with more than one velocity components. The 2D PIV data can also be used to compose a 3D

volume for the time mean statistics by combining several individual measurement planes. The results from PIV provide a reliable basis of experimental flow field data to complement and validate numerical and computational techniques (Adrian, 1991; Westerweel, 2000).

5.3 Principle of PIV

The general principle of PIV measurements is illustrated in Figure 5.1. PIV is based on the ability to accurately measure the position of small tracers suspended in the flow as a function of time. PIV measures the distance travelled by seeding particles that are entrained in the flow over a known time interval. The technique involves seeding the flow region of interest with tracer particles. A light sheet generated by a laser illuminates the flow field so that the tracer particles in the flow can be photographed. This light sheet is pulsed to produce a stroboscopic effect that freezes the movement of the particles. The principle is that the particles scatter light into a photographic lens located at 90° to the light sheet. The photographic lens is positioned so that its in-focus object plane coincides with the illuminated slice of fluid. The laser sheet is formed by opening up an axisymmetric laser beam by a cylindrical lens located between the laser head and the flow. Two images of the region of interest are captured in rapid succession on a Charge Coupled Device (CCD) camera. The camera is able to capture the light scatter from the tracer particles from each light sheet pulse in separate image frames. It is important that the duration of the illumination light pulse be short enough to freeze the motion of the particles during exposure in order to avoid the blurring of the image (Raffel et al., 2007). Each frame is time stamped by the illumination pulse time t, so that the time difference $\Delta t = t_1 - t_2$ of each pair of frames taken at time t_1 and t_2 in rapid succession is available for the data analysis. The images are subsequently transferred to a computer where appropriate software is installed for the data analysis. The digital images are used to determine the particle positions in the laser sheet. The images are divided into small sub-sections called interrogation areas. The objective of the image interrogation is to determine the displacement between two patterns of particle images. The interrogation areas are determined by calculating the average particle displacement. The interrogation areas from each image frame are cross-correlated with each other, pixel by pixel. For an accurate velocity measurement, an interrogation area should contain at least seven to ten particle pairs, where one pair refers to a particle imaged at both time t_1 and t_2 (Keane and Adrian, 1992). Raffel et al. (2007) showed that particle concentration influences the

probability of detecting the correct particle displacement as well as the particle displacement measurement uncertainty. Tests with changing particle concentration showed that the number of particles in each interrogation area should be higher than five.

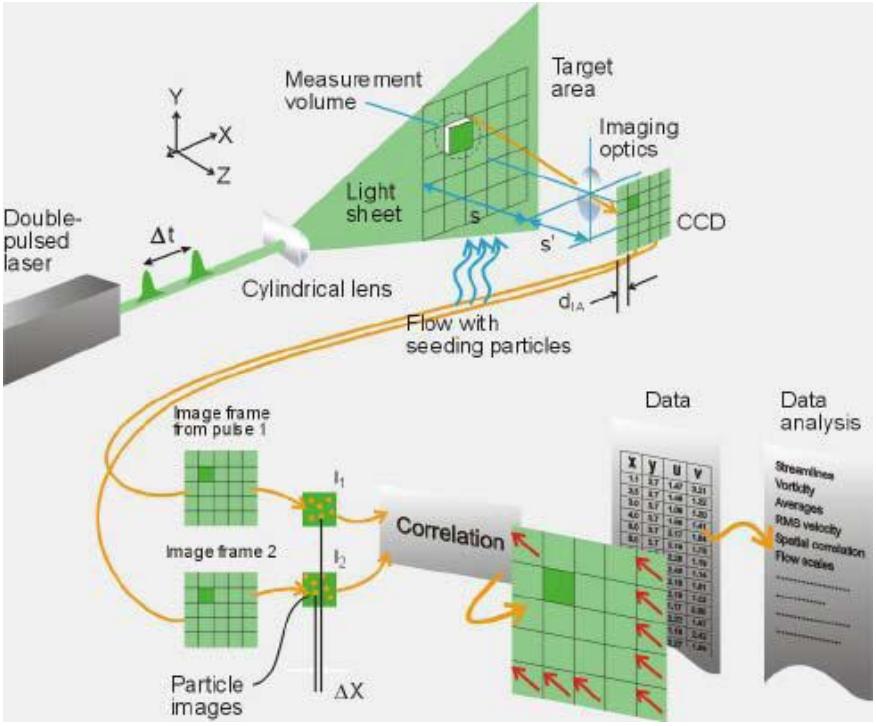

Figure 5.1: Principle of Particle Image Velocimetry (Dantec-Dynamics, 2006).

The cross-correlation between interrogation areas produces a signal peak, identifying the average particle displacement Δx in the interrogation area pair. A displacement vector map over the entire flow field area of interest is obtained by repeating the cross-correlation for each interrogation area over the two image frames captured by the CCD camera. Tests conducted by Raffel et al. (2007) to determine the influence of the particle displacement on the velocity measurement accuracy showed that the maximum particle displacement between two frames should be less than 50% of the interrogation area.

The velocity is estimated as a function of displacement and time as:

$$\text{Velocity } v = \frac{\Delta x}{\Delta t} \qquad 5.1$$

where Δx is the average displacement of the particles in the fluid over the time interval Δt = $t_2 - t_1$ between successive light pulses (Adrian, 1991). The time delay between the light pulses is set by the PIV user, based on the image magnification factor of the CCD camera and on an a priori estimate of the mean flow velocity.

5.4 Objectives of the PIV experimental investigations

The first objective of using PIV in this study is to provide information that will enhance the current understanding of the flow that develops in the annular region of concentric rotating cylinders at different radius and aspect ratios when the inner cylinder is rotated and the outer cylinder is at rest. The second objective is to investigate the intrusive effects of a circular probe inserted in the annular region between the concentric cylinders on the flow that was observed in the first set of experiments. The understanding of the flow phenomena and of the degree of the intrusiveness from the cylindrical probe will help the manufacturers of PIV endoscopic probes to design PIV probes that give a reduced flow interference. Finally, the data obtained from PIV will provide a reliable basis for direct comparison with numerical predictions of the flow.

5.5 PIV instrumentation set-up

A correct PIV set-up is vital to the success of any experimental investigation, as an inappropriate set-up of the instrumentation often leads to inaccurate results. In order to obtain results that can be compared with one another, all the set-up parameters of the PIV equipment are kept constant during each measurement. This implies using the same equipment and running conditions throughout the duration of the experiment.

5.5.1 PIV layout

The PIV system consists of several sub-systems. The standard layout of the PIV equipment used in this research is shown in Figure 5.2. The same layout has been used for all the test cases reported in chapter seven. This layout is made up of three sections; (1) the laser sheet creation section, (2) the test section, and (3) the image recording section.

5.5.2 Laser sheet creation section

The laser sheet creation section comprises of Litron Nano L laser and of the laser sheet optics. The laser provides the light source while the laser optics creates a light sheet to illuminate the tracer particles in the measurement plane. The high-power Litron Nano laser that generates a pulsed light sheet consists of a two-cavity double pulsed Nd:YAG (Neodymium Yurium Aluminium Garnet) laser with an infra-red radiation emission that is frequency-doubled to a wavelength of 532nm. The maximum pulse energy output of the laser is 400mJ. The pulse duration is 4ns. A pulse rate of 15Hz is used to generate the light

sheet. A cylindrical lens of approximately 5mm diameter is fixed at the output beam aperture of the laser head. A plano-convex spherical lens with an anti-reflective coating of focal length 0.35m is positioned between the laser and the test section as shown in Figure 5.2. The purpose of the lenses is to transform the beam into a sheet of light 1mm thick and they can also control the collimation, height and width of the light sheet.

The laser unit is mounted on a Dantec traverse system that is used to align the laser with the meridional plane of the concentric cylinders at the beginning of the experiment. The traverse system is controlled by the computer system, as such it is possible to move the laser in the horizontal (left and right) and also in the vertical (up and down) directions. The traverse system has four heavy duty locking caster wheels that provide a stable platform for the laser operation.

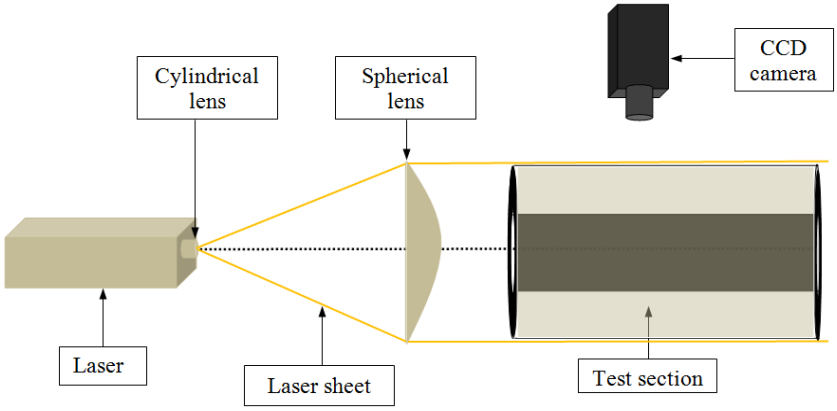

Figure 5.2: PIV experimental arrangement for the Taylor-Couette flow apparatus.

5.5.3 The test section

PIV measurements are taken in the annulus between a rotating inner cylinder and a concentric stationary outer cylinder over a test section 250mm in length. The detailed description of the materials and dimensions of the test rig used for this study are given in chapter four. The main test rig and field of view (test section) parameters are summarised in Table 5-1 and Table 5-2 respectively. The aspect ratio and the radius ratio are stated according to their definition in section 1.2 and section 1.4.

Table 5-1: Summary specifications for the three test rigs.

Description	Inner cylinder length (m)	Outer cylinder length (m)	Inner cylinder outer diameter (m)	Outer cylinder inner diameter (m)	Width gap d (m)
Test case 1	0.5	0.52	0.05	0.094	0.022
Test case 2	0.5	0.52	0.05	0.114	0.032
Test case 3	0.5	0.52	0.05	0.144	0.047

Table 5-2: Experimental field of view area.

Description	Axial length of the view area	Radial length of the view area	Aspect ratio $\Gamma = L/d$	Radius ratio $\eta = R_i/R_o$	Clearance ratio = d/R_i
Test case 1	$0 \leq X/R_i \leq 10$	$-1.88 \leq r/R_i \leq 1.88$	11.36	0.53	0.88
Test case 2	$0 \leq X/R_i \leq 10$	$-2.28 \leq r/R_i \leq 2.28$	7.81	0.44	1.28
Test case 3	$0 \leq X/R_i \leq 10$	$-2.88 \leq r/R_i \leq 2.88$	5.32	0.35	1.88

5.5.4 The image recorder

The PIV images are acquired using a Dantec DynamicStudio FlowSense 4M CCD camera with a resolution of 2048 x 2048 pixels with a 60mm AF Micro Nikon image lens, operated at a frequency of 4Hz. The camera encodes images with a 12 bit data resolution. The camera is mounted on a square steel stand and placed directly on top of the wooden sheet cover on which the experimental rig is mounted. This CCD camera is placed at a right angle to the light sheet for recording the PIV flow images. The camera lens has an aperture range of f/2.8 to f/32. An f/4 aperture is used in this study.

5.6 Equipment start-up and image acquisition procedure

5.6.1 Safety precautions

Operating the Nd:YAG laser requires extra care, as it is classified as Class 4 radiation hazards. For the safety and security of the operator, of other electronic operated equipment (CCD camera), as well as of any third party, it is very important before and during the experimental investigation to follow an appropriate safety protocol. Througout the duration of this study, appropriate protocols are followed to ensure the safety of the operator, of any third party, and of the equipment.

5.6.2 Calibration target

The camera needs to be calibrated so that tracer particle displacement in pixels on the CCD image can be converted into distance in millimetres (mm) on the cylinder meridional plane before any image can be processed. This calibration requires the user to focus the camera on an object of known size, acquire an image, and then select two points on the captured image from which the object to image size ratio is estimated. In this research study, the camera was calibrated by focussing the camera on a steel ruler positioned in the annular region of the concentric cylinders where the flow is to be measured, as shown in

Figure 5.3. It is important that the calibration target is aligned with the light sheet and installed at the centre of the camera field of view. In other words, the calibration target should be positioned at the actual location where the light sheet illuminates the flow being measured. In order to obtain a sharp image, the steel ruler needs to fall within the depth of field of the camera lens. This is the region in which the image is acceptably sharp. It is possible to calculate the magnification ratio since the camera has a fixed number of pixels in each direction. For this research study, the pixel matrix of the CCD camera is 2048 x 2048 and the field of view is 250mm, resulting in a magnification ratio of 0.122mm/pixel. The same magnification ratio applies in the axial and radial directions of the CCD camera view plane, due to the low optical distirtion through the outer cylinder from using air as the working fluid.

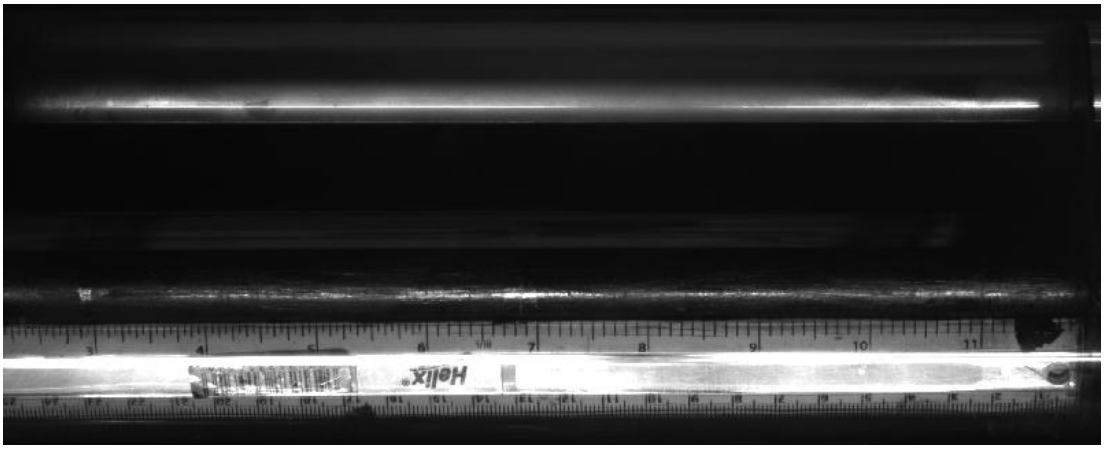

Figure 5.3: PIV calibration target.

5.6.3 Image acquisitions

In PIV, digital images of the flow with embedded particles are acquired to estimate the velocity of the fluid. Figure 5.2 shows the standard PIV arrangement used for the image acquisition in this study. The light sheet of approximately 1mm thickness is shone through the slit as shown in Figure 4.4 to illuminate the tracer particles in the measurement plane of the annular region. The pulsed light sheet and the camera are synchronised by a PIV processor that is installed with the PC running the Dynamic studio PIV software so that the particle positions are recorded together with each pulse/frame time. Inside the PIV processor, the synchronising unit provides a physical platform for communicating signals to and from the illuminating systems (comprising of the laser and the laser shutter), the camera and the trigger device.

Special care was taken to ensure that the time delay between the illumination pulses is long enough to accurately determine the displacement between the images of the tracer particles with sufficient resolution and short enough to avoid particles with an out of plane velocity component leaving the light sheet between subsequent illuminations. The out of plane motion was particularly significant in the choice of the time delay in this study, since the out of plane flow velocity is the dominant velocity component in this flow. The time delay between pulses is also chosen based on the mean flow velocity and on the image magnification factor of the CCD camera. The pulse settings are adjusted until reasonable results are achieved. The time interval between the two frames for an inner cylinder angular speed of 500 rpm is set to 10^{-3}s for all the three test cases reported in Table 5-2.

Measurements are taken as the inner cylinder rotates at an angular speed of 500rpm (52.36 rad/s) with the outer cylinder at rest. The rotating speed of the inner cylinder Ω = 52.36rad/s is the same for all the test cases. The start-up procedure for all the experiments in this study is a sudden start condition in which the desired rotating speed of the inner cylinder is reached within one second. The speed of the inner cylinder shaft is set and monitored by a handheld laser micro-processor tachometer. The tachometer is a CT6 series with a measurement range from 3rpm to 99,999rpm. It includes a standard optical/laser system that operates at a stand-off distance between 1 meter and 2 meters. The laser tachometer uses laser pulses to count rotations per minute of the spinning object and displays the result on the screen. This is achieved by pulsing a beam of light against the rotating inner cylinder on which a reflective device is attached and the tachometer measures the rate at which the light beam is reflected back. During the test, the speed was kept constant within ±1 rpm. The speed can be translated to the tangential velocity of the inner cylinder using $v = \Omega R_i$, where v is the velocity (m/s), Ω is the angular rotational speed (rad/s), and R_i is the radius of the inner cylinder (m). The tangential speed of the inner cylinder for all the test cases is therefore 1.31m/s.

The seeding generator model 10F03 from Dantec Dynamics Studio discussed in 4.4 is used to atomize a mixture of 20% polyethylene glycol (PEG600) and 80% water as seeding particles. The density and dynamic viscosity of polyethylene glycol is approximately 1125kg/m^3 and 0.14kg/ms respectively at room temperature, while the density and dynamic viscosity for water is 1000kg/m^3 and 0.001kg/ms respectively. The nominal diameter of the polyethylene glycol droplets is 1-5μm.

The seeding generator works by injecting air into the fluid, as discussed in section 4.4. In all the test cases, compressed air is supplied to the fluid in the seeding generator from the low pressure (100 psig) compressed air distribution rig of the Thermodynamics laboratory, University of Leicester. The air and seeding particle mist output from the seeding generator is then introduced into the annular region between the cylinders via a compressed gas hose in such a manner that it produces a region of uniformly seeded flow within the test section. The valve control unit on the seeding generator allows the rate of air and seeding particle mist output that goes into the annular region between the cylinders to be controlled. The air and seeding particle mist output from the seeding generator are introduced into the annular region of the experimental rig before starting the DC motor that rotates the inner cylinder. After the inner cylinder has reached the desired constant speed, the mist output is allowed to develop for between 2 to 5 minutes to ensure that the flow is uniformly distributed and fully developed before PIV measurements begin. As the cylinders are fitted with end-walls, the particles in the annular region take more than 20 minutes before they finally disappear from the test section, therefore no further seeding particle is added during the PIV image acquisition. The seeding particles generated are assumed small enough to follow the flow accurately because the Stokes number is far less than 0.14, which is the maximum Stokes number for which a particle can be assumed to accurately follow the flow, according to Dring (1982).

The temperature of the mist output in the apparatus is monitored to avoid large temperature fluctuations. Temperature is measured before and after each set of data acquisitions using a K-type thermocouple. This was found to be within $\pm 0.5^{o}C$ of the ambient temperature.

Raw particle images are captured by the image grabbing facility controlled by the Dynamic Studio software. The PIV recording method is the double frame-single exposure recording technique. This double pulsed system enables the light scattered by the particles to be recorded on two frames, to which different correlation algorithms are applied to obtain the particle displacement vectors.

Statistical convergence measurements were initially performed to test the number of images needed for an accurate result. During this initial testing, it was discovered that a minimum of 30 images are required to obtain reliable PIV output results. This is discussed in details in chapter seven. In all the PIV measurements in this study, the number of acquired image pairs for the ensemble average statistics was 100. The field of view covered 0.25m with stationary end-walls at both sides. During the testing for repeatability

of the experiment, the time interval between successive sets of experiments is more than one hour to avoid possible “memory effect” of the fluid (Xiao et al., 2002). The measured velocity profile was confirmed to be repeatable and statistically steady for the ensemble size of 100 images.

5.6.4 Image masking

Masking of the image is the first step in the PIV data processing. It follows the acquisition of the raw images by the CCD camera that is stored on the PIV computer hard disk. The purpose of masking is to remove from the image areas of no interest or areas that may produce bad vectors due to the presence of a wall or of a spurious source of light scatter, like a shiny edge. This process prevents spurious particle displacement vectors from interfering with the normal vectors in the flow.

5.6.5 Image interrogation

The subsequent data analysis sub-divides the area of the recorded image frames into small units called interrogation areas. The CCD camera, via the personality module, detects and transmits the images to the PIV processor in the PC that divides the camera images into interrogation areas to determine the displacement vectors in the flow. In the correlation software module, images from each pulse are correlated to produce an average displacement vector in each interrogation area.

Dividing each particle displacement by the known time between the captured images gives a raw velocity vector map. It is assumed that the tracer particles move with the local flow velocity between the two illuminations. Validation algorithms are applied to the raw velocity vector map so that erroneous vectors can be detected and removed to produce a validated vector map. The Dantec Dynamic Studio software stores the vector maps in a database in the computer. The database is also used to keep track of the data and of the corresponding data acquisition and analysis parameters.

Before the images are correlated, a background image is subtracted from the PIV images to produce digital images of a uniform gray background with particles. The particle image intensity is equalized and pixel noise is reduced by the Gaussian smoothing option available in the Dantec Dynamic Studio software.

Care was taken in the choice of the interrogation area as its inaccurate selection affects the quality of the results. As suggested by Raffel et al. (2007), the number of particles in each interrogation area should be higher than five and the maximum particle displacement

between two frames should be less than 50% of the interrogation area. In this study, a 16 x 16 pixels interrogation area was used to correlate the two frames with horizontal and vertical 50% overlaps. The average particle displacement was estimated to be approximately six pixels which is less than 50% of the interrogation area, in agreement with the PIV measurement best practice recommended by Raffel et al. (2007). The enable averaging of 100 vector maps detailed in section 5.6.6 compensates for the loss of vector field spatial resolution during the processing of individual image vectors.

5.6.6 Post-processing of data

This process involves the statistical processing of the ensemble of 100 instantaneous velocity fields, data validation, removal of erroneous data, replacement of removed data, and data smoothing. Various validation algorithms, such as range validation, and the moving average validation are embedded in the Dynamic Studio software for processing the data. In this study, the local displacement vector is determined for each interrogation area by means of an adaptive correlation. It is assumed that the tracer particles move with the local flow velocity between the two image frames. The adaptive correlation algorithm essentially calculates a displacement vector with an initial Interrogation Area (IA) of the size N time the size of the final IA and uses this intermediate result as information for defining the boundary of the next IA of smaller size, until the final IA is reached (Dynamics, 2006). The smaller interrogation area on the second frame is defined to be shifted from the first frame by the displacement vector estimated from the larger IA. The main benefits from using a shifted window is that particles which have left the interrogation area during the time between the two light pulses (in-plane dropout) can be identified and ignored, as they would otherwise result in erroneous vectors. Local validation algorithms are added to the adaptive correlation so that less bad vectors are generated and local interpolations (green vectors) are added as a realistic correction to the measured velocity field. This is illustrated in Figure 5.4 where the blue velocity vectors are shown as validated vectors and the green vectors are the realistic correction vectors generated automatically by the adaptive algorithm. The advantage of using the adaptive correlation is the ability to track well the motion of fluid in rotation, shear, and expansion.

Spurious vectors are replaced during the adaptive correlation by adding a local neighbourhood validation. The way the local neighbourhood validation works is by comparing among individual vectors in the neighbourhood vector area, with size set in this study as 3 x 3. If a spurious vector is detected, it is removed and replaced by a vector

calculated by a local interpolation of the vectors present in the 3 x 3 neighbourhood vector area. In this study, the interpolation is performed using a moving average, which compares each vector with the average of the vectors in a defined neighbourhood. An acceptance factor of 0.12 and three moving average iterations are employed in computing the estimated values. Any other spurious or outlying vector that is not removed by the adaptive correlation is eliminated using the range validation algorithm. This is achieved by fixing a velocity threshold (minimum or maximum) such that all the velocity vectors that exceed a prescribed threshold are eliminated. The thresholds are user-defined based on an assessment of the range of velocities that are physically possible in a given flow geometry. This means it is essential to have prior knowledge of the flow structure.

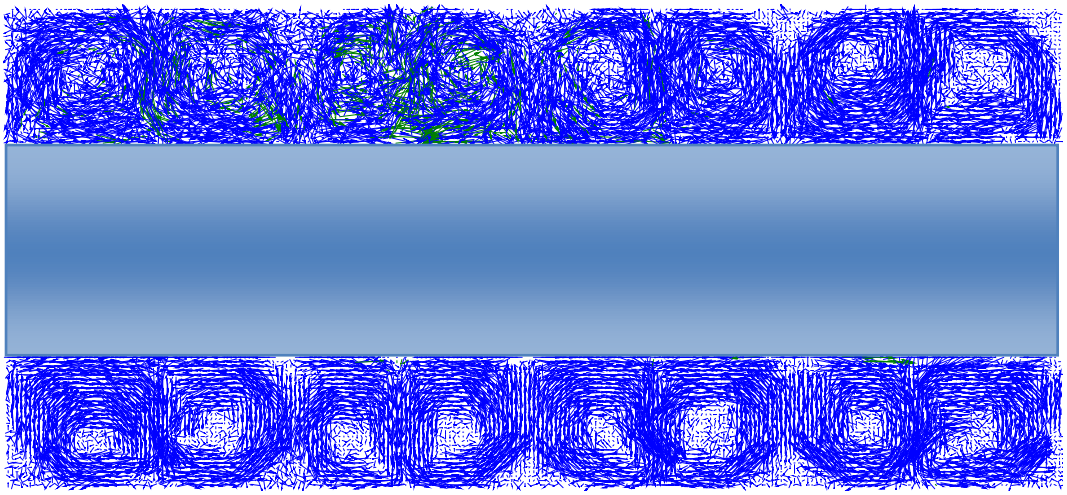

Figure 5.4: Typical instantaneous velocity vector map calculated by adaptive correlation with a 16 x 16 IA and 50% overlap. The green vectors are the correction to the velocity vector map from the local neighbourhood validation.

Following this experimental procedure, one set of 100 instantaneous velocity vector maps was acquired for each of the concentric cylinder test cases detailed in Table 5-2. These measurements are discussed in details in chapters seven and eight.

Chapter Six: Modelling of gas flows between coaxial rotating cylinders

6.1 Introduction

In this chapter, the CFD modelling of the air-flow in the annular gap between two concentric rotating cylinders is documented. The computational approach used in this work develops from past CFD studies on both axisymmetric and non-axisymmetric Taylor-Couette flows in coaxial rotating cylinders reported in the literature. For example, Wild et al. (1996) studied by experiment and computation the Taylor vortex flow in a centrifugal rotor using the standard k-ε, the Renormalisation Group (RNG), and the Reynolds Stress Model (RSM) for the turbulence closure of the Reynolds Averaged Navier-Stokes (RANS) equations. Batten et al. (2002a) studied the transition from axisymmetric vortex flow to non-axisymmetric wall-driven turbulence flow in the Taylor-Couette system in concentric rotating cylinders using the k-ω turbulence model simulation developed by Wild et al. (1996). The aim of their study was to examine the predicted velocity distribution in the viscous sub-layer at the cylindrical surfaces with respect to standard k-ε model prediction. Other researchers, such as Deshmukh et al. (2007) have also used CFD to investigate the flow pattern in concentric rotating cylinders using the Reynolds Stress Model (RSM). Marcus (1984) simulated numerically the stable axisymmetric Taylor-Couette flow and the stable non-axisymmetric wavy vortex flow with one travelling wave. The Reynolds Stress Model was used by Zhou et al. (2007) to study the characteristics of the turbulent Taylor vortex flow in concentric rotating cylinders.

This present work expands on the knowledge from previous computational studies in the available literature by modelling the air-flow in the annular gap between coaxial cylinders with different radius ratio using the commercial CFD package, ANSYS FLUENT 6.3.26 (2006). The results obtained are validated in chapter seven against PIV experimental results. The basic steps in the CFD simulation discussed in chapter three have been followed for all the CFD models described in this chapter.

Based on the results of earlier researchers such as Taylor (1923), the flow regimes in this study are in the parameter region above the critical Taylor number at which an axisymmetric counter-rotating Taylor vortex structure is formed. Therefore, the axisymmetric Taylor vortex flow that is contained in the gap between a rotating inner

cylinder and an outer stationary cylinder with fixed end-walls has been modelled as a steady incompressible three-dimensional flow. This study employed an implicit finite-volume RANS method coupled with the realisable *k-ε* turbulence model for turbulence closure. The advantages of this turbulence model for different flow regimes has been discussed in details in chapter three and more information can be found in the ANSYS FLUENT user's guide (2006).

6.2 Geometry and problem formulation

The geometries adopted for the investigation of flow instability in coaxial rotating cylinders are described in this section. The concentric rotating cylinders for the test cases 1 and 2 detailed in chapters four and five and reported in Table 5-1 and Table 5-2 are investigated computationally in this chapter. The two different geometries have been developed for the coaxial assembly to allow a parametric study of the Taylor vortex flow pattern, which exists in the annular region of the coaxial cylinders. The model aims to represent the experimental rig discussed in chapter four as closely as possible. However, modelling the whole experimental rig would have been too computationally intensive and would have required computational resources that were above what was available to the author. As such, only half of the total length of the experimental rig has been modelled, which is the total view area for the PIV experiment reported in Table 5-2.

The rotating speed of the inner cylinder Ω of 52.36 rad/s is constant in all test cases, giving an angular velocity ΩR_i = 1.31m/s. The Taylor number and the Reynolds number tabulated in Table 6-1 are calculated for each test case using equations 1.1 and 2.6 respectively.

Table 6-1: Flow parameters.

Description	Taylor number (Ta)	Reynolds number (Re)
Test case 1	2.35×10^6	1.97×10^3
Test case 2	6.47×10^6	2.87×10^3

6.3 Cylindrical reference system of the coaxial rotating cylinders

A three-dimensional (3D) numerical model has been chosen for the present work so that the flow details can be examined in more than one plane. Whilst a 3D model is more demanding both in terms of its development time and of the computational resources, it

has the potential to resolve the time-average of the localised flow disturbances induced by the rotation of the inner cylinder.

A cylindrical reference system is used for the CFD modelling as shown in Figure 6.1(a). The orthographic plan view of the geometry as seen by the PIV CCD camera in the experimental set up is shown in Figure 6.1(b). The cylinders are coaxial with the axis coinciding with the X-direction of a cylindrical reference system (r, θ, X). All the geometries of the concentric rotating cylinders modelled in this study are created in GAMBIT version 2.4.6.

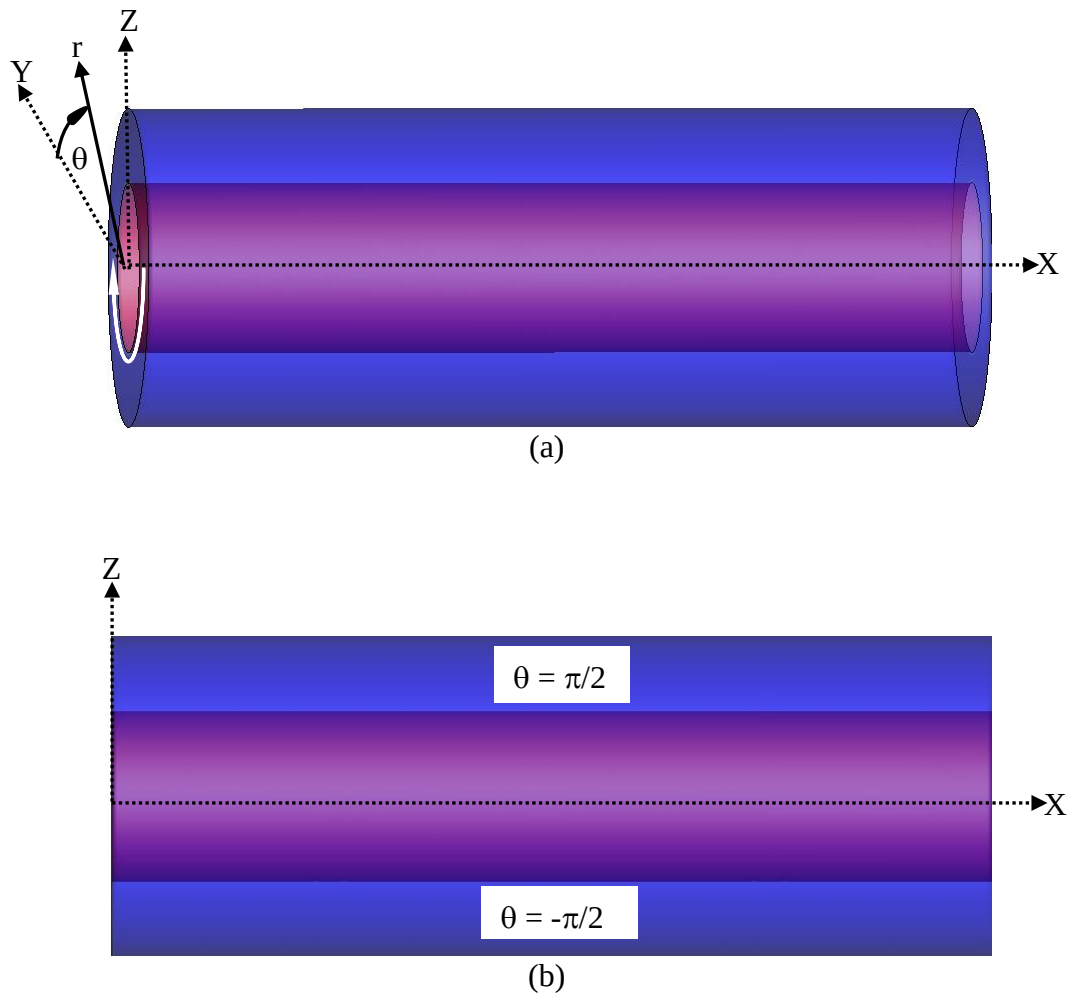

Figure 6.1: (a) Cylindrical reference system of the concentric cylinder assembly and (b) meridional plane.

6.4 Mesh generation

A numerical mesh was generated to create the control volumes inside the flow domain and the control surfaces at all computational domain boundaries in order to numerically solve the governing equations. The geometry of the domain and the areas of flow of interest

determine the way the mesh is built. For example, in areas where the gradients of the flow are high, a large number of unit control volumes are required to accurately predict the flow.

All the computational domains in this study were meshed using an unstructured meshing technique using the commercial mesh generation software package GAMBIT version 2.4.6. An unstructured meshing technique was selected for the simulations taking into consideration the degree of grid resolution required in each region of the domain and the capacity of the available computer memory.

6.4.1 Face and volume meshing

Two types of unstructured grid were initially tested for the meshing of the computational domain. These are: (1) a combination of quadrilateral/hexahedral-copper tools and (2) quadrilateral/tetrahedral cells. The latter produced the best results when compared with experiment. Therefore, the computational domain in the current work has been discretised using a combination of finite-volume quadrilateral cells on the wall faces and a tetrahedral unstructured mesh for the computational domain interior. The flow regime is expected to be dominated by a Taylor vortex pattern of characteristic size d. The Delaunay triangulation is designed to obtain a spatially isotropic mesh, which is appropriate for resolving the large-scale instability in a near-uniform mesh. This type of mesh was used by Wardle et al. (2006) and was found to be appropriate for successfully predicting the flow pattern in the annular region of concentric cylinders. It is therefore adopted in the current study.

The entire computational domain has four faces; the inner cylinder surface, the outer cylinder surface, the left and the right end-walls. Each face was first discretised before the computational domain interior. This was done so that the mesh density in each section of the faces could be controlled in such a way that a denser mesh could be created in regions of interest. The refinement of meshing around the inner cylinder surface was implemented by using the size functions tool available in GAMBIT 2.4.6. Size functions are used to smoothly control the growth of the mesh size over any particular region of the geometry. Size functions allow the direct control of cell size distribution in edges, faces and volumes directly for automatic meshing, thereby eliminating the need to pre-mesh these regions manually. Size functions are generally designed to grade meshes with tetrahedral grids, even though they can be used with a hexahedral mesh (FLUENT, 2006). Size functions require the specification of the type and each size function type requires the specification

of source entities, attachment, and size parameters. The type of size function dictates the criteria upon which the mesh will grow. For all the test cases in this work, the fixed type method was chosen, the sources entities are the faces while the attachment is the volume. The size function method used in this work employed a constant starting cell size of 1.0mm for all the test cases. This value was increased by 50% and 40% for growth rate and maximum cell size respectively for the test cases Γ = 11.36 and 7.81. The size function has been normalised by the inner cylinder radius R_i. The detailed normalised parameters of the size functions used for the final meshing of the coaxial rotating cylinder cases are shown in Table 6-2. A typical unstructured tetrahedral mesh for the computational domain is show in Figure 6.2.

Table 6-2: Size function parameters for the coaxial rotating cylinders.

Size function parameters	Aspect ratio Γ = 11.36	Aspect ratio Γ = 7.81
Starting cell size	0.04	0.04
Growth rate	0.06	0.056
Maximum cell size	0.06	0.056

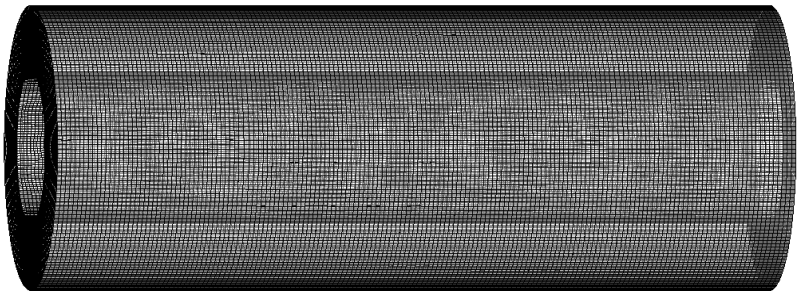

(a)

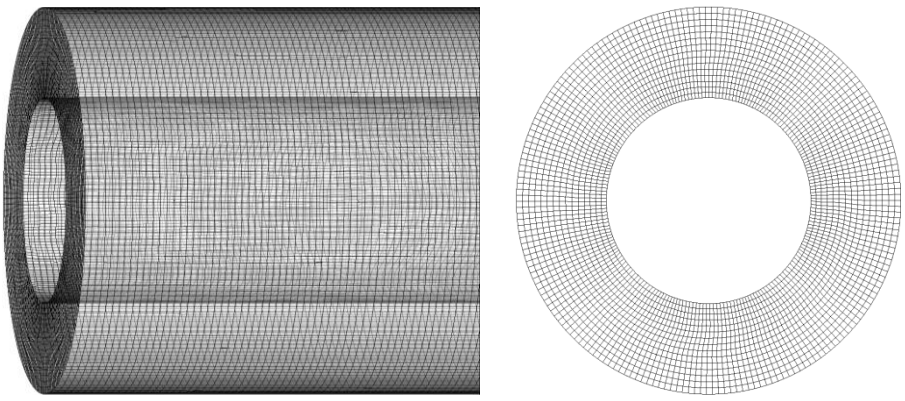

(b) (c)

Figure 6.2: (a) Tetrahedral computational mesh structure and (b, c) computational mesh detail at the left-end wall.

6.4.2 Meshing quality assessment

The tetrahedral cells are associated with an unstructured mesh that tends to have a large aspect ratio that affects the cell skewness, which can in turn reduce the accuracy and the convergence rate of the solution. Therefore, the mesh quality for all the geometries was assessed by evaluating the cell skewness throughout the computational domain, using Gambit 2.4.6. The skewness of a cell is defined as:

$$Q_{EAS} = \max\left[\frac{\theta_{max} - \theta_e}{180 - \theta_e}, \frac{\theta_e - \theta_{min}}{\theta_e}\right] \qquad 6.1$$

where θ_{max} = largest angle in degrees between faces or cells.

θ_{min} = smallest angle in degrees between faces or cells.

θ_e = angle in degrees for an equiangular cell. For a triangular cell, $\theta_e = 60^o$ and for a hexahedral cell, $\theta_e = 90^o$.

Q_{EAS} values range from 0 to 1. 0 is the the skewness of an equiangular cell, which is a cell with the lowest skewness for a given mesh element type, and 1 is the skewness of a highly skewed cell.

Based on the definition of skewness given in equation 6.1, the maximum cell skewness for all the test cases were found to be within the range 0.50 – 0.7. ANSYS FLUENT (2006) user's guide recommends that, for a good tetrahedral mesh, the skewness should always be below 0.90, which suggests that all the meshes in this work are of good quality. The volume statistics including minimum, maximum and total cell volume in m^3 was also checked in ANSYS FLUENT 6.3.26. The meshing result shows there was no negative value for the minimum volume, which indicates that all edges were properly connected. A negative minimum volume could have occurred due to the incorrect orientation of a face or due to large boundary surface curvature. Improperly connected edges may occur at the apex of geometry with large concavity, where two edges may intersect, creating a pinched surface. There was no such occurrence in this model.

6.5 Computational techniques and procedure

This section details the techniques and procedure used for all the CFD modelling in this work.

6.5.1 Procedure

After the completion of the meshing process and the checking of the mesh quality in Gambit 2.4.6, the models were imported into ANSYS FLUENT. In ANSYS FLUENT the

physical properties and the initial flow conditions are set as discussed in chapter three. The imported numerical mesh is checked against import errors, by checking the minimum and maximum cell size against the values reported by Gambit. In Gambit, the geometry was created in millimetres. In ANSYS FLUENT, the mesh is scaled to metres. The numerical solver, turbulence model and the initial flow conditions are selected as detailed in sub-sections 6.5.2 to 6.5.5. The computation was monitored for convergence as detailed in section 6.6. All the results presented in this work were post-processed using Tecplot 2010 and Matlab software.

6.5.2 Computational modelling

The computational domain consists of air-flow in the annular region between the inner rotating cylinder and the stationary outer cylinder, which is bounded at the left and the right by fixed end-walls with the cylindrical coordinates as defined in Figure 6.1. The flow needs to be simplified so that it can easily be solved numerically, as such, the flow is assumed isothermal, adiabatic, incompressible, and steady. Based on these assumptions, a steady state, segregated and pressure-based approach with absolute velocity formulation was defined for the model, since the segregated solver and pressure-based approach was developed specifically for incompressible flow (FLUENT, 2006). In the pressure-based segregated algorithm, the individual governing equations for the solution variables such as velocity, pressure, turbulent kinetic energy dissipation rate, turbulent kinetic energy are solved one after the other. The Green-Gauss node based scheme was used for the gradient option since the geometry was meshed with unstructured tetrahedral meshes. The advantage of this scheme over the default cell-based scheme has been discussed in chapter three. The standard wall function discussed in chapter three was chosen for the wall treatment for all the test cases.

6.5.3 Boundary and initial operational flow conditions

The internal flow between the two rotating cylinders is modelled as fully enclosed. At the start of the computation, zero flow conditions are imposed throughout the computational domain, using still air at constant density ρ =1.225 kg/m^3 and at ISA ground level ambient pressure p = 101325 N/m^2. The force of gravity is assumed negligible. No-slip stationary adiabatic wall boundary conditions are applied at the left and the right end-walls as well as at the outer cylindrical surface at R_o. The inner cylinder surface is modelled as a rotating adiabatic no-slip wall with a constant angular speed Ω_i = 52.36 rad/s in the clockwise

direction, as shown in Figure 6.1. These boundaries fully delimit the computational domain. The simulations were carried out with a sudden start of the inner cylinder at the specified angular speed. This approximates the experimental procedure detailed in chapters seven and eight, in which the target rotational speed of the inner cylinder is reached within one second from starting the electrical motor. An adequate match of the acceleration profile between experiment and computation was found to be important in this work. Specifically, initial CFD tests with different acceleration profiles led to a number of Taylor vortices that was different with respect to the experiment. This led to the practice of using a sudden start as the CFD initial condition. This is in agreement with the observation made by Koschmieder (1993) that the pattern of Taylor-Couette flow is strongly dependent on the start-up procedure. In addition, the results of the CFD simulation conducted by Deshmukh et al. (2008) show that start-up procedure influences the number of Taylor vortices at various speeds.

The turbulence level was specified in terms of the turbulence intensity and hydraulic diameter. Estimations of turbulence intensity, turbulent kinetic energy, and turbulent dissipation rate were calculated for all the CFD simulations and tabulated in Table 6-3, based on the following parameters:

$$\text{Turbulence intensity } (TI) = 0.16(Re_H)^{-0.125} \qquad 6.2$$

$$\text{Turbulent kinetic energy } (k) = 1.5\left(U_{avg} TI\right)^2 \qquad 6.3$$

$$\text{Turbulent dissipation rate}(\varepsilon) = C_\mu^{0.75} \text{ x } \frac{k^{1.5}}{\ell} \qquad 6.4$$

where $\ell = 0.07D_H$ is the pipe characteristic length scale, based on the hydraulic diameter of the cylindrical assembly D_H, and $C_\mu = 0.09$ is a constant. For the annular geometry delimited by cylinders with an inner diameter D_i and outer diameter D_o, the hydraulic diameter D_H is given as $D_o - D_i$.

The turbulence intensity levels in Table 6-3 are indicative of a turbulent flow in the annular region between the cylinders and are above typical values of 0.2% to 0.3% that are found in the test section of well-designed wind tunnels.

Table 6-3: Estimations of turbulence level.

Descriptions	Turbulence intensity *TI*	Turbulent kinetic energy *k*	Turbulent dissipation rate ε
Coaxial cylinder with aspect ratio $\Gamma = 11.36$	6%	$0.0093 m^2/s^2$	$0.0478 m^2/s^3$
Coaxial cylinder with aspect ratio $\Gamma = 7.81$	5%	$0.0064 m^2/s^2$	$0.0189 m^2/s^3$

6.5.4 Selection of turbulence modelling

Two turbulence models, the realisable k-ε and the RSM were evaluated for closing the Reynolds Averaged Navier-Stokes (RANS) equations. These models were used to run identical cases for each of the computational geometries. Figure 6.3(a) and Figure 6.3(b) show the radial velocity distributions obtained using the two turbulence closure models for the test cases $\Gamma = 11.36$ and $\Gamma = 7.81$ respectively. The radial velocity distributions of Figure 6.3(a) and Figure 6.3(b) are extracted at the gap mid-span $r = R_i + 0.5d$ of the lower channel $\theta = -\pi/2$ in the meridional plane over the range $0 \leq X/R_i \leq 10$. The radial velocity profiles in Figure 6.3 show alternating maxima and minima corresponding to upwell (inward flow) and downwell (outward flow) regions induced along the annulus by Taylor vortices. The radial velocity maxima in Figure 6.3(a) and Figure 6.3(b) are sharp and well-localised along the cylinder axis. This flow pattern is further detailed in sections 6.7.1, 6.7.3, 7.5.1, and 7.5.4 where results obtained are compared with experimental and computational studies in the open literature.

Figure 6.3(a) and Figure 6.3(b) show that the realisable k-ε model predicts higher radial velocity maxima and lower radial velocity minima than the RSM model. This indicates that stronger Taylor vortices are predicted with the realisable k-ε model.

Apart from the quantitative differences between the two models, the RSM took an extra 50% to 60% of CPU time to complete the simulations for all test cases.

Based on this preliminary test information, the recommendation from ANSYS FLUENT user's guide and the agreement between the CFD predictions and the experimental results, the realisable k-ε model was chosen for the simulation of the concentric cylinder with aspect ratios $\Gamma = 11.36$ and $\Gamma = 7.81$.

6.5.5 Selection of solution parameters

The discretised finite-volume form of the flow governing equations is solved numerically using ANSYS FLUENT's standard scheme for the pressure. A second-order upwind

approximation is used for the conservation of momentum, specific turbulent kinetic energy, and turbulent kinetic energy dissipation rate. The SIMPLE pressure-velocity coupling estimates the pressure field updates using an under-relaxation factor of 0.3 for pressure. The first-order scheme was employed to perform the first few iterations. This was later switched to the second-order scheme to continue the calculation to convergence as this scheme helps to reduce the effects of numerical diffusion on the solution. Double precision was used for all the calculations so that round-off errors are minimised.

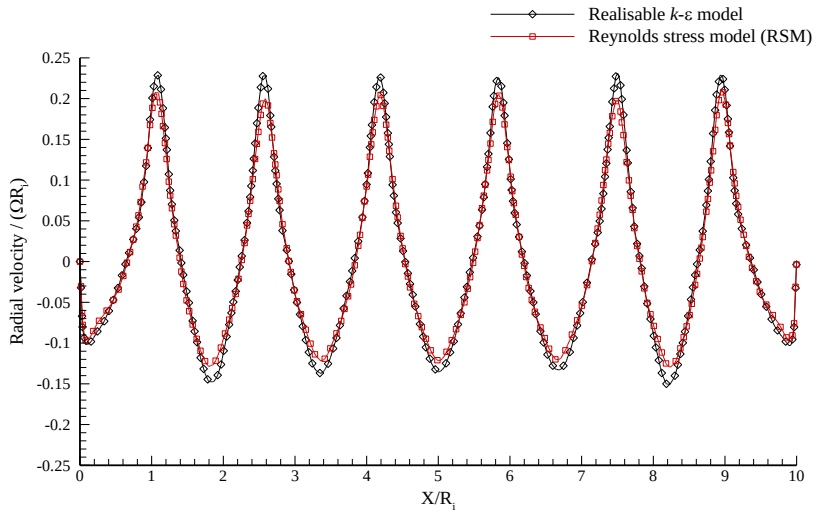

(a)

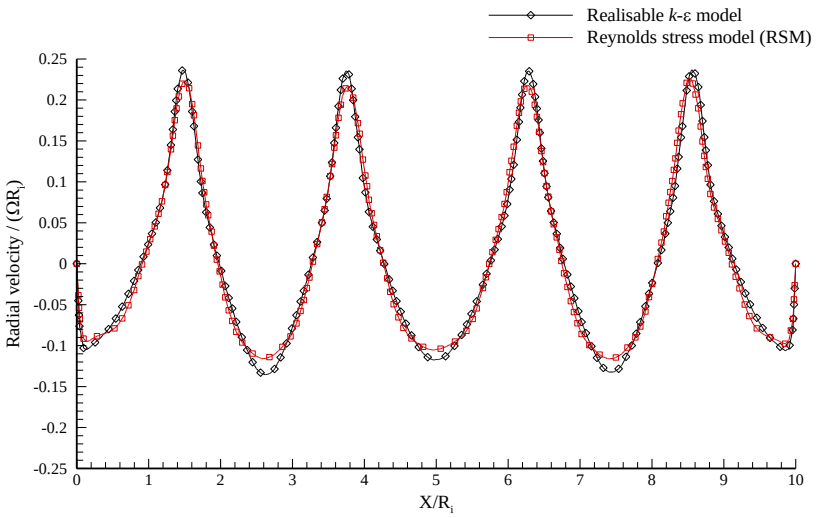

(b)

Figure 6.3: Radial velocity profiles at r = R_i + 0.5d with different turbulence models for the coaxial cylinders with (a) Γ = 11.36 (b) Γ = 7.81.

6.6 Convergence criteria and numerical accuracy

In computing the simulation, the discretised conservation equations are solved iteratively. For the solution to reach convergence, a number of iterations are set with the residuals

monitored to assess the convergence of the solution. Convergence is reached when changes in the solution variables from one iteration to the next one is negligible. The implicit scheme of section 3.2.3 is iterated to steady flow, based on the residual history of the momentum equations. The residual plot shows when the residual values reach a specific tolerance. For all the computations in this work, the solution is taken as converged when the momentum equation residuals reduce to 10^{-4} of their initial value. When convergence is reached, the overall conservation property of the solution is said to have been achieved. It should be noted that the accuracy of the converged solution is dependent on the appropriateness and accuracy of the physical models, the grid resolution and independence, as well as the problem setup. Each Under-Relaxation Factor (URF) is adjusted *ad hoc* for its corresponding conservative variable in order to improve the convergence rate. For momentum, pressure, turbulent kinetic energy and dissipation rate, the typical URFs vary between 0.3 and 0.8. During the simulation, the sum of the residual squared of each conserved variable is computed and stored in a data file at every iteration. Each conserved variable is also displayed on the terminal screen where the convergence history is visualised and a quick check on the progress of the solution is made. The same computational modelling procedure has been followed for all the test cases detailed in Table 6-1. Figure 6.4 shows typical scaled residuals from the test case $\Gamma = 11.36$.

The residuals of the velocity components in Figure 6.4 are shown in Cartesian coordinates rather than in the cylindrical coordinates of Figure 6.3, as this was the native output from ANSYS FLUENT (2006). As such, the on-screen residuals plot is reported in Cartesian coordinates. The cylindrical coordinate system support in ANSYS FLUENT 6.3.26 was found to work well only for 2D axisymmetric geometries. Therefore, the 3D geometry and the flow solution in this study were solved in Cartesian coordinates and then projected in cylindrical coordinates by post-processing. The Cartesian coordinate system is related to the cylindrical coordinate system of Figure 6.1 by

$$\begin{bmatrix} u_x \\ u_y \\ u_z \end{bmatrix} = [A] \begin{bmatrix} u_x \\ u_r \\ u_\theta \end{bmatrix} \qquad 6.5$$

where

$$A = \begin{bmatrix} 1 & 0 & 0 \\ 0 & \cos\theta & \sin\theta \\ 0 & -\sin\theta & \cos\theta \end{bmatrix} \begin{bmatrix} u_x \\ u_r \\ u_\theta \end{bmatrix}$$

All the results in the reminder of this thesis are therefore presented in cylindrical coordinates.

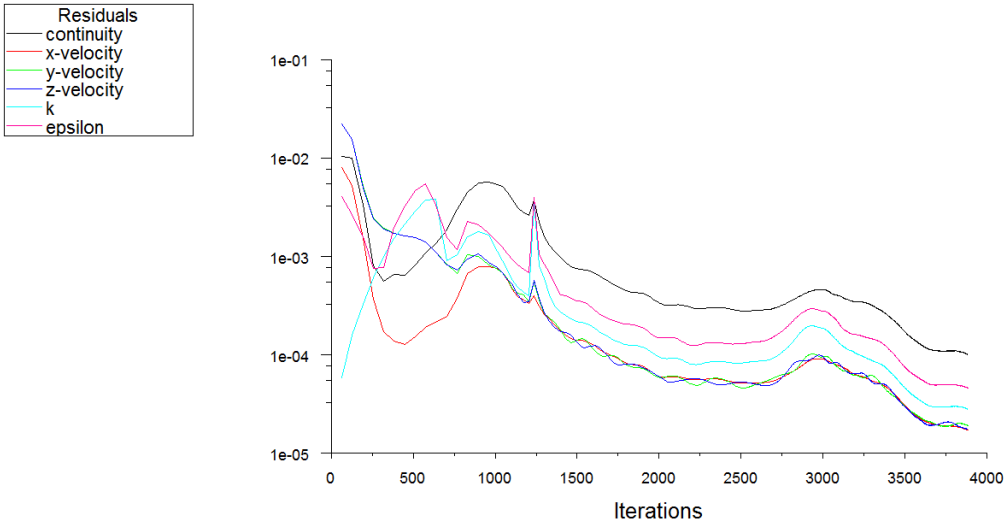

Figure 6.4: A typical plot of scaled residuals. Residuals are shown in dimensional form with units of kg/m^3, m/s, m^2/s^2, and m^2/s^3.

6.6.1 Grid independence tests

To test the dependence of the results upon the level of the spatial discretisation, there is the need to conduct a grid independence test. Grid independence simply means that the converged solution obtained from CFD prediction is independent of the grid density. Grid independence is achieved when further mesh refinement yields only very small and insignificant changes in the numerical results. There is tendency for numerical diffusion in the result if a coarse mesh is used. Numerical diffusion is due to truncation errors that are the result of representing the flow governing equations in an algebraic (discrete) form. The amount of numerical diffusion is inversely proportional to the resolution of the mesh, which means refining the mesh will reduce numerical diffusion. As such, three progressively finer meshes were tested for the coaxial cylinders with aspect ratios Γ = 11.36 and Γ = 7.81 as detailed in Table 6-4.

The CFD results at converged residuals for the different mesh types for the coaxial cylinders with aspect ratios Γ = 11.36 and Γ = 7.81 are presented in Table 6-5 and Table 6-6 respectively. The total number of vortices, the values for average static pressure, the axial velocity and radial velocity were used as monitoring parameters to establish the independence of the grid. The values presented in Table 6-5 and Table 6-6 are the absolute values of each parameter average over the entire annulus. The percentage difference between the finest refined grid and the other grids were calculated and are reported in

bracket in Table 6-5 and Table 6-6. The results show the percentage difference between the finest refined grid and the other two mesh types were all less than 5% for all the flow variables.

Table 6-4: Computational meshes.

Descriptions	Name	No of tetrahedral cells	No of nodes
Coaxial cylinder with aspect ratio Γ = 11.36	Mesh type 1	4,193,045	753,490
	Mesh type 2	6,081,984	908,563
	Mesh type 3	7,949,361	1,402,342
Coaxial cylinder with aspect ratio Γ = 7.81	Mesh type 1	4,869,311	857,514
	Mesh type 2	6,886,264	998,982
	Mesh type 3	8,678,719	1,587,213

Table 6-5: Grid independence results for the coaxial cylinders Γ = 11.36.

Mesh type	No of cells	No of vortices	Gauge static pressure magnitude (Pa)	Axial velocity magnitude (m/s)	Radial velocity magnitude (m/s)
Mesh type 1	4.2Millions	12	0.1169 (0%)	0.2413 (0.08%)	0.3139 (3.42%)
Mesh type 2	6.1Millions	12	0.1113 (4.8%)	0.2367 (1.99%)	0.3087 (1.71%)
Mesh type 3	7.9Millions	12	0.1169 (basis)	0.2415 (basis)	0.3035 (basis)

Table 6-6: Grid independence results for the coaxial cylinders Γ = 7.81.

Mesh type	No of cells	No of vortices	Gauge static pressure magnitude (Pa)	Axial velocity magnitude (m/s)	Radial velocity magnitude (m/s)
Mesh type 1	4.9Millions	8	0.1149 (0.53%)	0.2390 (1.19%)	0.3104 (4.58%)
Mesh type 2	6.9Millions	8	0.1095 (4.20%)	0.2342 (0.85%)	0.3042 (2.49%)
Mesh type 3	8.7Millions	8	0.1143 (basis)	0.2362 (basis)	0.2968 (basis)

The CFD flow predictions of the radial velocity profiles for the coaxial cylinders with aspect ratio Γ = 11.36 and Γ = 7.81 using different levels of computational mesh refinement, as defined in Table 6-5 and Table 6-6, are presented in Figure 6.5(a) and Figure 6.5(b) respectively. The radial velocity distributions of Figure 6.5 are extracted at

the same gap mid-span of the lower channel θ = -π/2 in the meridional plane of the annulus as in Figure 6.3. The radial velocity profiles in Figure 6.5 have the same trends as in Figure 6.3. The predicted flow characteristics are further detailed in sections 6.7.1 to 6.7.3, while the flow features for the experimental results at the same test conditions are discussed in sections 7.5.1 to 7.5.4. In these sections, the number of vortices is shown to be dependent on the experimental conditions and other flow parameters, as discussed in the literature review in chapter two.

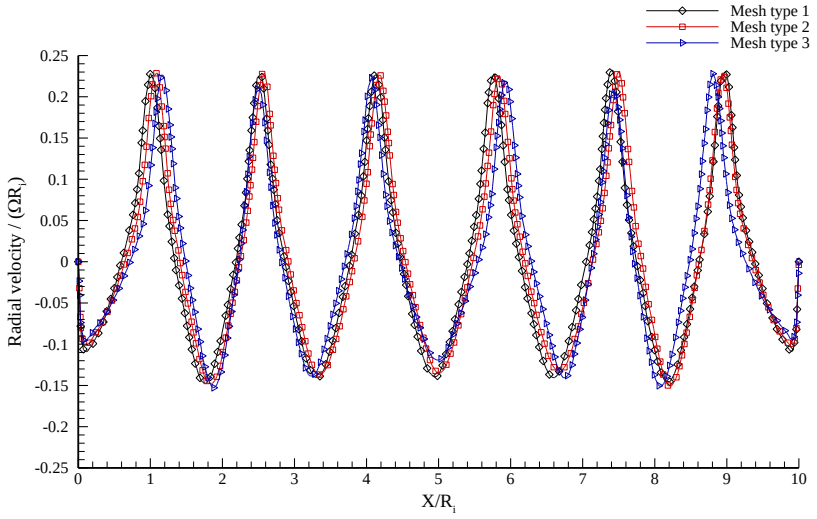

(a)

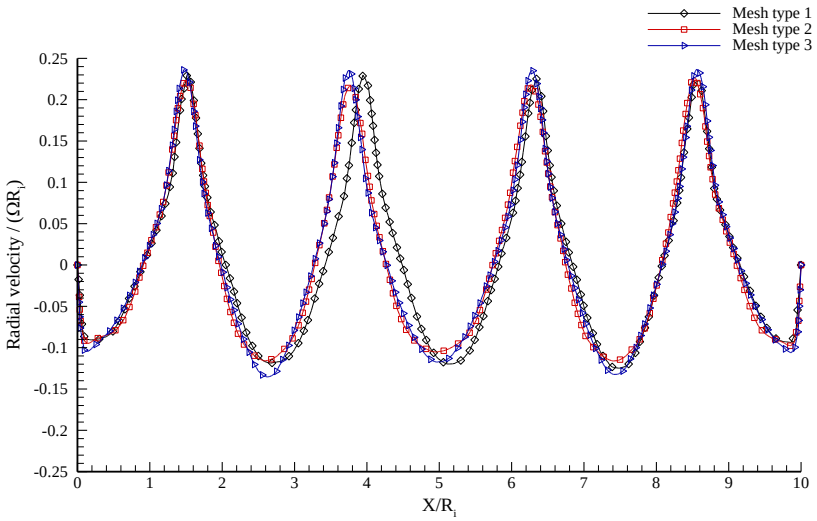

(b)

Figure 6.5: Radial velocity profiles for the different levels of computational mesh refinement at r = R_i + 0.5d for test cases (a) Γ = 11.36 and (b) Γ = 7.81.

Different levels of computational mesh refinement have little significant impact on the axial spacing of the Taylor vortices, as shown by the spacing between the maxima and minima reported in Figure 6.5(a) and Figure 6.5(b). Predictions obtained using mesh types

1 to 3 displays an appreciable overlap in radial velocity over the entire range $0 \leq X/R_i \leq 10$. These indicate that the numerical scheme is predicting the same Taylor vortex pattern at all the three levels of mesh refinement.

Computational mesh type 2 was chosen for the two test cases as sufficiently grid independent since the difference in static pressure, axial velocity and radial velocity values between refined grid case 3 and case 2 were less than 5%, as detailed in Table 6-5 and Table 6-6. Whereas the mesh convergence of the numerial model for the purposes of predicting the conventional Taylor vortex instability is adequate, the present work did not attempt to investigate whether the critical Taylor number for staging to wavy vortex flow was mesh independent. The mesh convergence claim is therefore limited to the specific flow regime of conventional Taylor vortex flow that results at one inner cylinder rotational speed. The behaviour of the model at increasing speeds, in particular for what concerns mode staging, is untested.

6.7 Numerical results and discussion for the coaxial cylinders $\Gamma = 11.36$ and $\Gamma = 7.81$

All the numerical results are based on the cylindrical reference system in which the cylinders are co-axial with the axis coinciding with the X-direction of the cylindrical reference system (r, θ, X) shown in Figure 6.1. The orthographic view of the meridional plane of the coaxial cylinders presented here is consistent with the plan view of the PIV experiment as seen from the top by the PIV CCD camera.

6.7.1 Flow pattern in the annulus of the coaxial cylinders

Figure 6.6(a) and Figure 6.6(b) show the predictions of the velocity vectors in the meridional plane for the test cases $\Gamma = 11.36$ and $\Gamma = 7.81$ respectively. The velocity vectors have been normalised by the inner cylinder angular speed, ΩR_i. The axial and radial positions are normalised by the inner cylinder radius R_i. This makes the normalised computational domain for the test cases $\Gamma = 11.36$ and $\Gamma = 7.81$ cover the ranges stated in Table 5-2. A typical Taylor vortex flow pattern is observed in the entire computational domain. Since the Taylor number for the test cases $\Gamma = 11.36$ and $\Gamma = 7.81$ is above the critical Taylor number, the steady viscous flow at the start of the computation becomes unstable and pairs of counter-rotating, axisymmetric toroidal vortices spaced periodically along the inner cylinder axis are established. The axisymmetric flow pattern of pairs of

counter-rotating vortices is repeated along the axial shaft with the consecutive cells moving the flow in the same direction at their meeting point. Along the axial direction of the computational domain, the velocity vectors of Figure 6.6(a) show twelve vortices for the test case Γ = 11.36, while Figure 6.6(b) shows eight vortices for the test case Γ = 7.81. The number of vortices in the computational domain for the test case Γ = 7.81 is less than the number of vortices obtained for the test case Γ = 11.36, due to the difference in the gap width d.

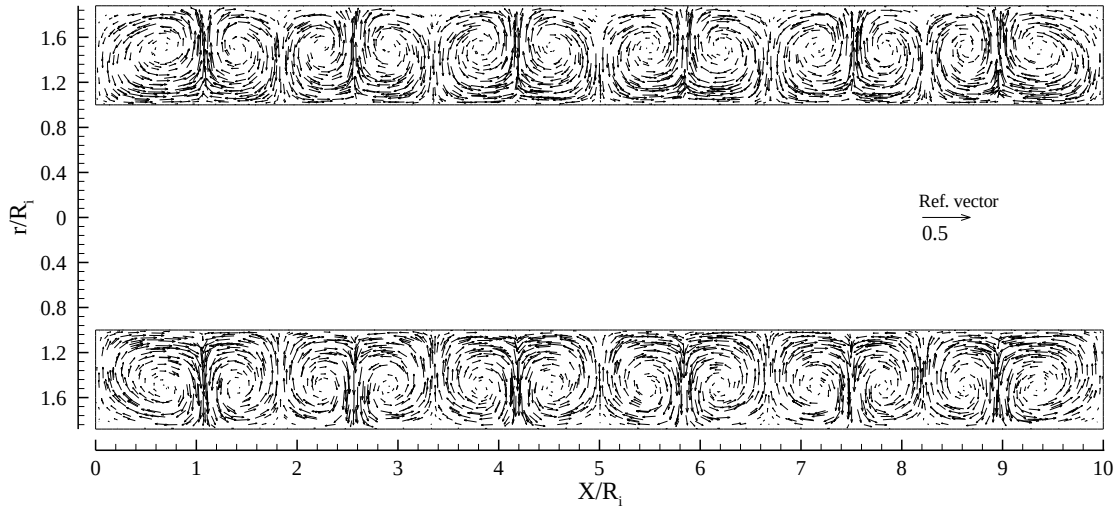

(a)

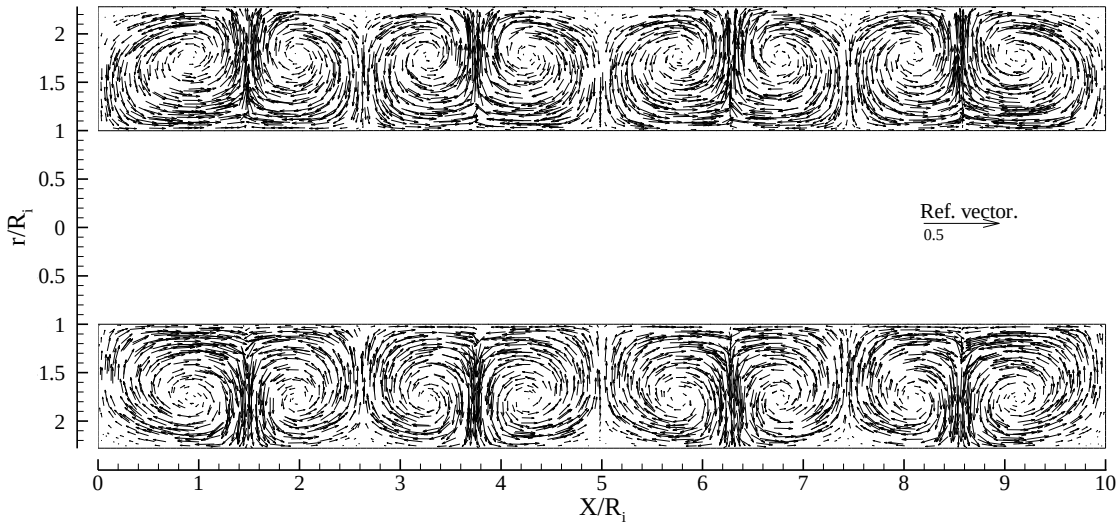

(b)

Figure 6.6: Normalised velocity vectors in the meridional plane of the annulus for test cases (a) Γ = 11.36 and (b) Γ = 7.81**.** The reference velocity vector is $0.5\Omega R_i$.

As the inner cylinder rotates, the fluid particles near the wall of the inner cylinder experience a higher centrifugal force and show a tendency of being propelled outwards. The radial velocity induced by the vortices convects the fluid with high tangential

momentum near the rotating inner cylinder radially outward, in the outflow regions between two adjacent pair of vortices, as indicated by the arrow A in the enlarged Figure 6.7. Symmetrically, low speed fluid from near the stationary outer cylinder is convected radially inward in the inflow (upwell at $\theta = -\pi/2$) regions between two adjacent vortices, as indicated by arrow B in the enlarged Figure 6.7. This redistributes the angular momentum of the fluid across the annulus. The consequent redistribution of mass flow across the annulus affects the inward flow and the outward flow velocity distribution. Thus, the radial outflow between the vortices is substantially stronger than the radial inflow, as evidenced by the magnitude of the vectors in Figure 6.6 and Figure 6.7, in agreement with experimental observation of Wereley and Lueptow (1998).

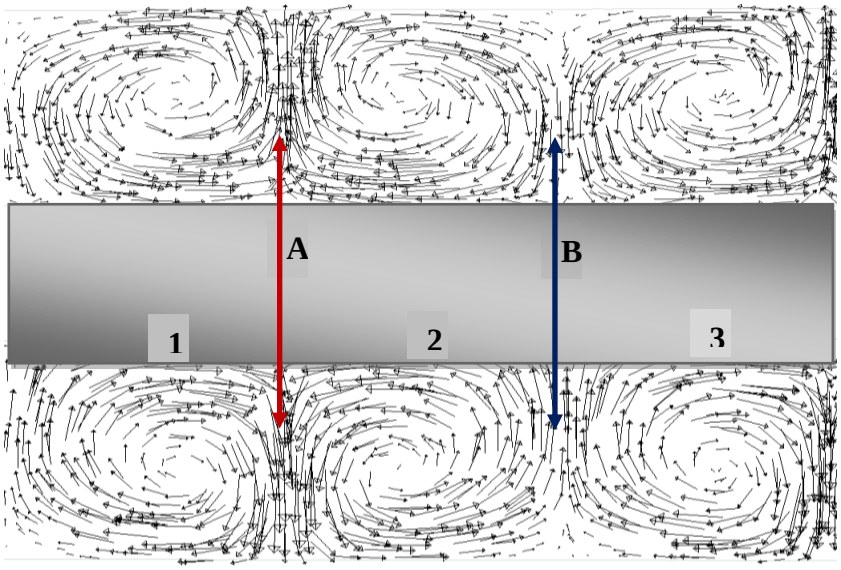

Figure 6.7: Enlarged normalised velocity vectors in section $1.84 \leq X/R_i \leq 4.19$ of Figure 6.6(a).

The two vortices near the left and right end-wall boundaries of the computational domain in Figure 6.6(a) and Figure 6.6(b) are elongated more than the remaining vortices in the central region of the annulus. This is due to the effects of the stationary end-walls. This flow pattern is consistent and in qualitative agreement with observation made in previous studies by Parker and Merati (1996), Haut et al. (2003), and Deshmukh et al. (2007). Neglecting the right and the left side vortices, a pair of counter-rotating vortices in the central region has a periodic length that is about twice the width, d, of the gap between the coaxial cylinders.

The weaker radial inflow at the end-walls of the vortices at $0 \leq X/R_i \leq 1.09$ and $8.95 \leq X/R_i \leq 10$ in Figure 6.6(a) for the test case $\Gamma = 11.36$ and at $0 \leq X/R_i \leq 1.47$ and $8.47 \leq X/R_i \leq 10$ in Figure 6.6(b) for the test case $\Gamma = 7.81$ is due to the end-walls being fixed to

the stationary outer cylinder. The no-slip boundary conditions imposed at the end-walls generate a boundary layer flow, driven by the discontinuity in velocity at the junctions between the rotating inner cylinder and the stationary end-walls. These end-walls cause an imbalance in the pressure gradient and in the centrifugal forces. As the centrifugal forces fall off towards the ends of the cylinders, there is an inward flow at the stationary end-walls. Thus, the presence of the end-walls determines the rotation of the vortices nearest to the end-walls. A vortex cell pattern propagates from the end-walls toward the centre until it fills the entire domain. The rotation of the other vortices in the central region is thus determined by the direction of the end-wall vortices. This is in agreement with the observations of Smieszek and Egbers (2005) and Deng et al. (2009). This flow pattern formation is also in agreement with the numerical results of Neitzel (1984) and the experimental results of Koschmieder (1979), where Taylor vortices were first observed to form at the end-walls. In addition, the discontinuity of the boundary conditions at the meeting point of the inner cylinder and the end-walls generates a weak circulation cell adjacent to each end-wall, as observed in Figure 6.6. A scenario whereby a radially outward boundary layer flow in a vortex cell pattern is obtained under anomalous conditions has been studied extensively by Benjamin and Mullin (1981) and Benjamin (1978).

A noticeable feature of the velocity vectors in Figure 6.6(a) and Figure 6.6(b) is the mixing and exchange of momentum at the meeting point of two adjacent vortices. At this meeting point, there is significant flow mixing between adjacent vortices, with each vortex adding to the mixing region at the centre of a vortex pair, close to the inner cylinder and then receiving fluid from this mixing region, close to the outer cylinder. A similar mixing process occurs at the inflow region, between neighbouring vortex pairs.

Another noticeable observation of the velocity vectors in Figure 6.6(a) and Figure 6.6(b) is the shifting of the vortex centres toward the outer cylinder. This is attributed to the high Reynolds number at which the flow regime is investigated. At a high Reynolds number, the centrifugal force due to the rotation of the inner cylinder is greater than the pressure gradient due to the stationary outer cylinder wall. This imbalance between these two forces causes the vortex centre to be shifted towards the wall of the outer cylinder. This is in qualitative agreement with the study conducted by Deng et al. (2009), in which they noticed that, when the Reynolds number is below 100, the radial positions of the vortex centres are located in the middle of the annulus, whereas, when the Reynolds number is increased, the vortex centres tend to shift toward the wall of the outer cylinder.

6.7.2 Flow field in the meridional plane of the coaxial cylinders

Figure 6.8, Figure 6.9, and Figure 6.10 show respectively the contour plots of axial velocity, radial velocity and tangential velocity in the meridional plane of the annulus for the test cases $\Gamma = 11.36$ and $\Gamma = 7.81$. All the velocity variables are normalised by the surface tangential speed of the inner cylinder ΩR_i. The axial and radial positions are normalised by the inner cylinder radius R_i, thus making the extent of the computational domain for the test cases $\Gamma = 11.36$ and $\Gamma = 7.81$ the same as those shown in Figure 6.6(a) and Figure 6.6(b) respectively. The contour lines in Figure 6.8 and Figure 6.9 have been evenly spaced with a contour spacing of $0.03\Omega R_i$.

Figure 6.8(a) and Figure 6.8(b) show the formation of an alternating pattern of axial velocity maxima and minima in the annulus at the same axial postion as the vortex centres for the test cases $\Gamma = 11.36$ and $\Gamma = 7.81$ respectively. This flow pattern is due to the high rotational speed of the inner cylinder, resulting in the transition between a steady Couette flow to a Taylor vortex flow, which is characterised by the formation of vortices spanning the gap between the inner cylinder and the outer cylinder.

These velocity maxima and minima are induced by the vortex motion and are aligned radially above and below each vortex core of Figure 6.6. The zero contour lines between the maxima and minima values of Figure 6.8 correspond to the radial positions of the centre core of the vortices in Figure 6.6. Figure 6.8 shows that each clockwise Taylor vortex induces axial velocity maxima radially below its core near the wall of the inner cylinder, and axial velocity minima radially above its core near the wall of the outer cylinder on the $\theta = -\pi/2$ plane.

The radial velocity contour plots for test cases $\Gamma = 11.36$ and $\Gamma = 7.81$ in Figure 6.9(a) and Figure 6.9(b) show an alternating pattern of radial velocity minima and maxima along the positive axial direction. The radial flow is due to the imbalance between the centrifugal forces exerted on the fluid due to the rotation of the inner cylinder and radial pressure gradients restoring radial momentum equilibrium in the flow. The magnitude of the alternating radial velocity maxima and minima are reported at the centre of their corresponding concentric contours in Figure 6.9(a) and Figure 6.9(b).

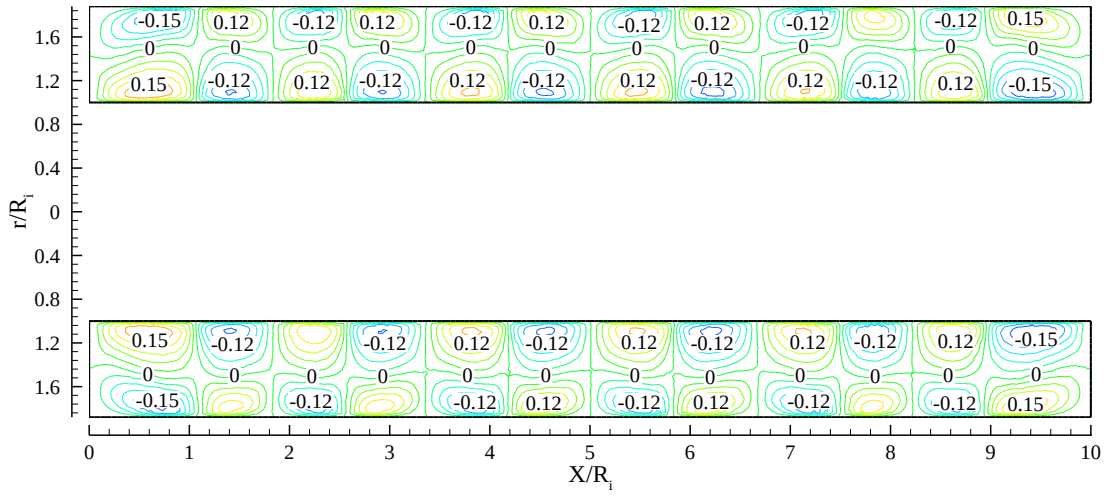

(a)

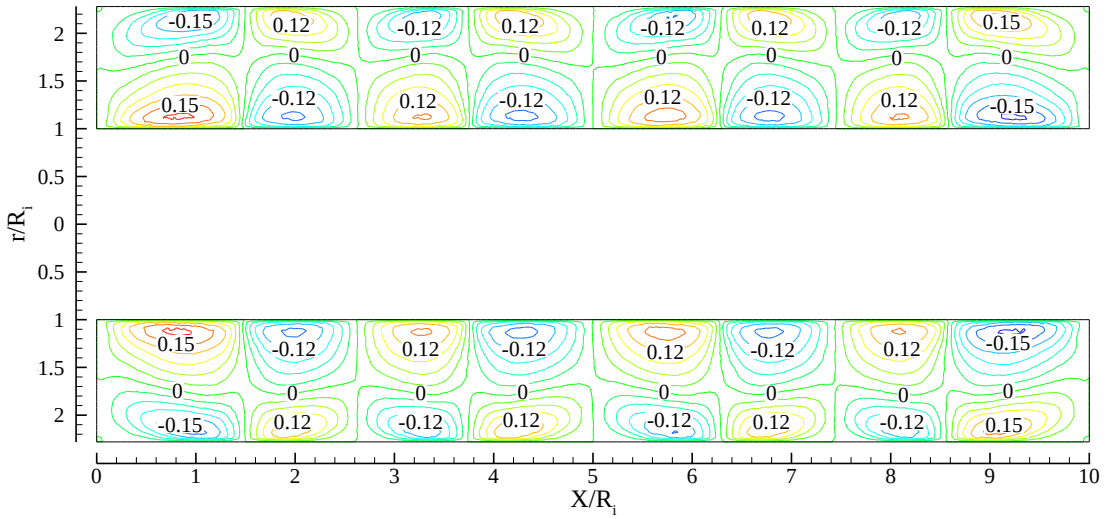

(b)

Figure 6.8: Contour plots of axial velocity in the meridional plane normalised by ΩR_i with contour spacing, $\Delta u_x = 0.03\Omega R_i$ for test cases (a) $\Gamma = 11.36$ and (b) $\Gamma = 7.81$.

The contour plot is colour coded such that the red colour corresponds to positive values of radial velocity and the blue colour corresponds to the negative values of radial velocity. The positive and negative values on these contour maps show the direction of rotation of the Taylor vortices. A red coloured contour cluster followed by a blue coloured contour cluster in the positive axial direction designates an anti-clockwise vortex on the $\theta = -\pi/2$ plane. Similarly, a blue coloured contour cluster followed by a red coloured contour cluster designates a clockwise Taylor vortex.

The negative and positive values on these contour clusters indicate inward flow regions (upwells) and outward flow regions (downwells) respectively at $\theta = -\pi/2$ at the meeting point of adjacent vortices of Figure 6.6(a) and Figure 6.6(b). The radial velocity maxima occur in the radial outward flow regions of Figure 6.6(a) and Figure 6.6(b), such as the

location identified by arrow A in Figure 6.7. The radial velocity minima occur in the radial inward flow regions of Figure 6.6(a) and Figure 6.6(b), such as the location identified by arrow B in Figure 6.7. The zero velocity contours corresponds to the centre position of the vortices in Figure 6.6(a) and Figure 6.6(b).

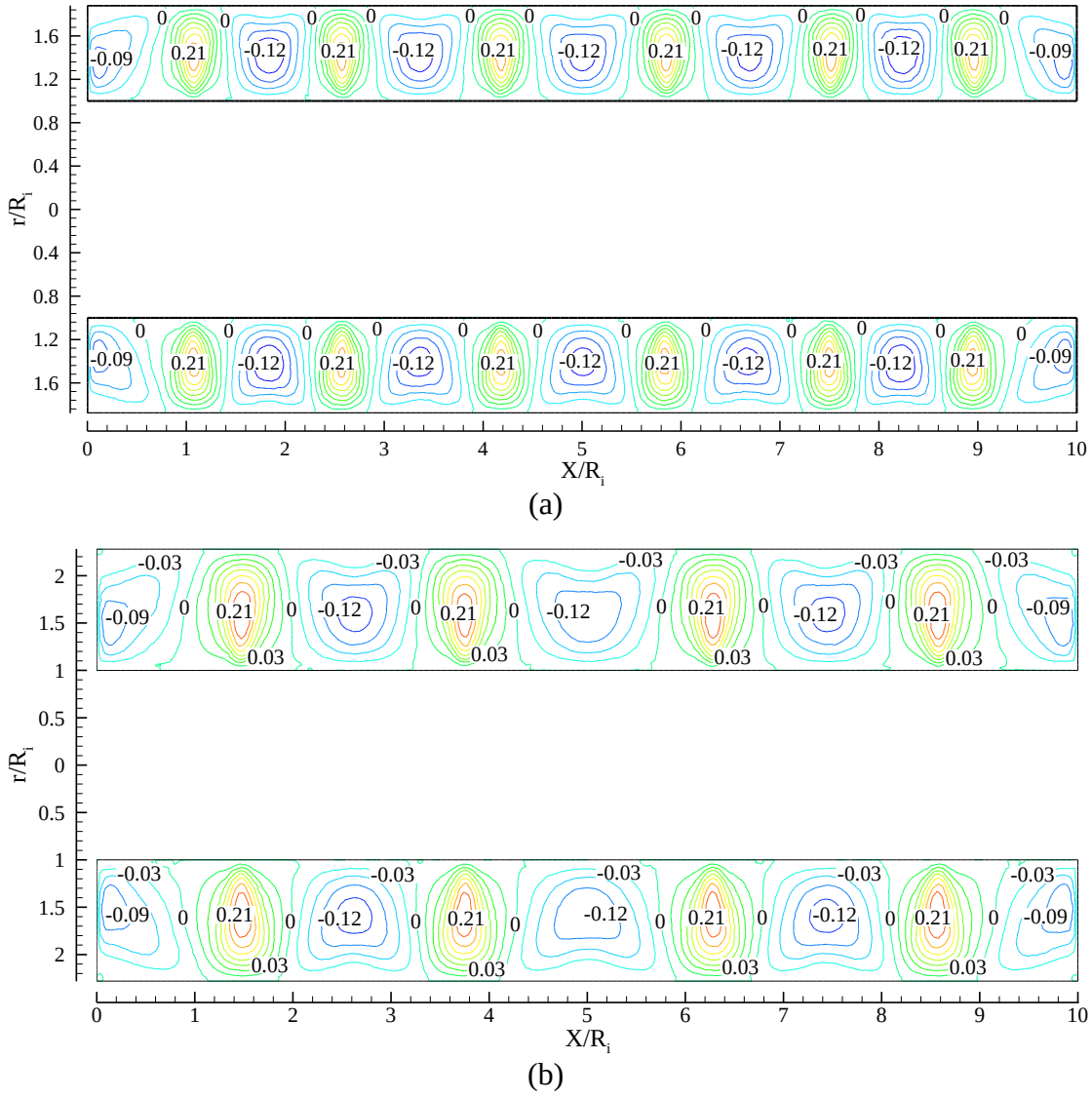

Figure 6.9: Contour plots of radial velocity in the meridional plane normalised by ΩR_i with contour spacing, $\Delta u_r = 0.03\Omega R_i$ for test cases (a) Γ =11.36 and (b) Γ = 7.81.

The flow pattern of alternating axial and radial velocity maxima and minima in Figure 6.8 and Figure 6.9 is consistent and is in qualitative agreement with past CFD study and experimental measurements by Deshmukh et al. (2007), Parker and Merati (1996), Deng et al. (2009) and Haut et al. (2003). For instance, Deng et al. (2009) show the radial velocity distribution along the mid-gap of two cylinders of aspect ratio 5.17 and radius ratio 0.613. Three velocity maxima are shown in a pattern of six vortices, corresponding to

one velocity maximum per vortex pair, which is the same pattern as in the current CFD predictions.

The radial velocity minima near the end-walls at $X/R_i = 0$ and $X/R_i = 10$ in Figure 6.9(a) and Figure 6.9(b) are lower than the corresponding values in the central region of the computational domain due to the use of side wall non-slip boundary conditions that constrained the development of the first Taylor vortex and of the last Taylor vortex, thereby reducing their strength.

The radial velocity contour plots in Figure 6.9(a) and Figure 6.9(b) show radial velocity extrema appearing before and after the centres of each vortex. It is observed that the number of the extrema does not correspond with the number of vortices. For example, the velocity vector maps in Figure 6.6(a) and Figure 6.6(b) show respectively twelve and eight vortices in the entire domain, whereas the radial velocity contours in Figure 6.9(a) and Figure 6.9(b) show the number of the extrema to be thirteen and nine for the corresponding test cases $\Gamma = 11.36$ and $\Gamma = 7.81$. The one additional minimum in Figure 6.9(a) and Figure 6.9(b) is attributed to the presence of the end-walls. The difference in the number of extrema between test case $\Gamma = 11.36$ and $\Gamma = 7.81$ in Figure 6.9(a) and Figure 6.9(b) is attributed to the diffenece in the gap width d.

The contour plots of the tangential velocity in Figure 6.10(a) and Figure 6.10(b) for the test cases $\Gamma = 11.36$ and $\Gamma = 7.81$ have been evenly spaced with a contour spacing of $0.1\Omega R_i$. These contour plots show a minimum tangential velocity near the wall of the inner cylinder and a maximum tangential velocity near the wall of the outer cylinder. The magnitude of the tangential velocity minimum is higher than that of the tangential velocity maximum. That is, the tangential flow speed is maximum near the inner cylinder in agreement with the direction of rotation of the inner cylinder that drives the flow by rotating at constant angular speed ΩR_i. This is expected since the convected fluid motion induced by the rotating inner cylinder rotates with the solid body with maximum angular velocity $u_\theta = \Omega R_i$ at the inner cylinder surface. The negative value of the tangential velocity observed near the wall of the inner cylinder is due to the direction of rotation of the inner cylinder based on the cylindrical reference system in Figure 6.1.

The fluid tangential velocity has two attributes: a magnitude (speed) and a direction. In this instance, the speed of the inner cylinder is constant at the inner cylinder outer surface, and the direction of the angular speed of the rotating inner cylinder has been specified as clockwise. The change in direction of the tangential velocity vectors in the azimuthal

plane gives rise to a net centripetal force which is directed toward the centre of the rotating cylinder. The clockwise inner cylinder rotation, based on the right handed cylindrical reference system shown in Figure 6.1, is responsible for the negative values of the tangential velocity in Figure 6.10(a) and Figure 6.10(b). Therefore, the red and the blue colour codes on the contour plots correspond respectively to minimum and maximum negative values of tangential velocity.

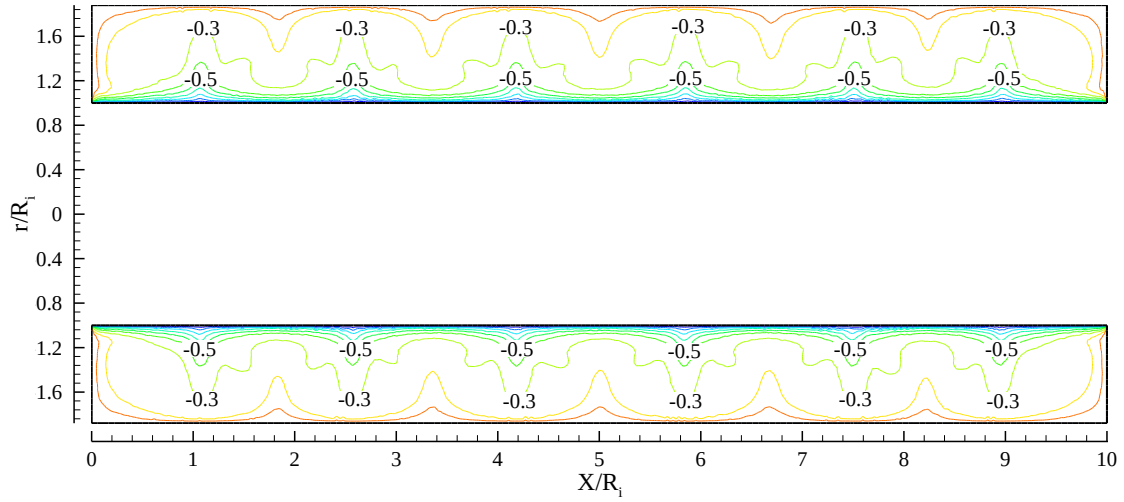

(a)

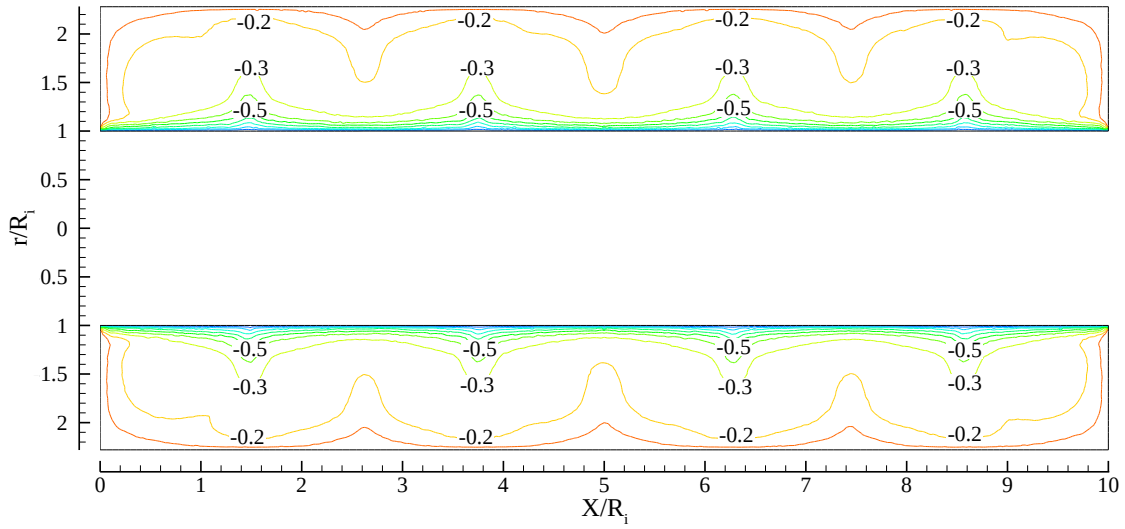

(b)

Figure 6.10: Contour plots of tangential velocity in the meridional plane normalised by ΩR_i with contour spacing, $\Delta u_\theta = 0.1\Omega R_i$ for test cases (a) Γ =11.36 and (b) Γ = 7.81.

In Figure 6.10(a) and Figure 6.10(b), the contours bulge outward in the radial outward flow regions as high tangential momentum fluid is transported by the Taylor vortices from near the inner rotating cylinder outwardly toward the stationary outer cylinder. The contours bulge radially inward in the inward flow regions as low momentum fluid is

transported by the Taylor vortices from near the wall of stationary outer cylinder inwardly toward the wall of rotating inner cylinder. The contour lines are more sharply curved in the outward flow regions than in the inward flow regions due to the shorter distance between the Taylor vortex centres and the outward flow saddle planes, which results in a greater outward flow radial velocity induced by the Taylor vortices in the outflow regions. This feature also indicates the strength of the induced velocity by the Taylor vortices in these regions.

The pressure distribution in the annulus of coaxial cylinders is a critical factor for journal bearing design. The study by Deng (2007) shows that the pressure distribution is significant for the formation of vortex cells and transition to different flow regimes (Taylor-Couette flow to Taylor vortex flow regimes) in the annulus of coaxial cylinders. The detailed pressure distribution in the gap between the coaxial cylinders for the test cases $\Gamma = 11.36$ and $\Gamma = 7.81$ is documented in this section.

In incompressible turbomachinery aerodynamics (Cumpsty, 2003; Gostelow, 1984), the relationship between the static and stagnation pressure is given as:

$$P + \frac{1}{2}\rho v^2 = P_o \qquad 6.6$$

where P = static pressure (Pa)

$0.5\rho v^2$ = dynamic pressure (Pa)

ρ = density of the fluid = $1.225 kg/m^3$

v = velocity of the flow (m/s)

P_o = stagnation pressure (Pa)

In the case of horizontal coaxial rotating cylinders with angular velocity $u_\theta = \Omega R$, equation 6.6 becomes:

$$P + \frac{1}{2}\rho R^2 \Omega^2 = P_o \qquad 6.7$$

Equation 6.7 shows that the pressure distribution is a function of radius. This means there will be no pressure variation in the axial direction as there is no gravitational force. The pressure distribution is determined by the balance between a radial pressure gradient and the centrifugal force associated with the circular motion. Figure 6.11 and Figure 6.12 show the contour plots of gauge static pressure and dynamic pressure in the meridional plane respectively. Pressure (static and dynamic) has been normalised by $0.5\rho R_i^2 \Omega^2$. The contour lines are evenly spaced with contour spacing of $0.01\rho R_i^2 \Omega^2$.

The contours of the gauge static pressure (pressure measured relative to the atmospheric pressure) in the meridional plane shown in Figure 6.11(a) and Figure 6.11(b) for the test cases Γ = 11.36 and Γ = 7.81 respectively show a pressure gradient along the radial direction in agreement with equation 6.7 with a gauge static pressure minimum near the wall of the inner cylinder and a gauge static pressure maximum near the wall of the outer cylinder.

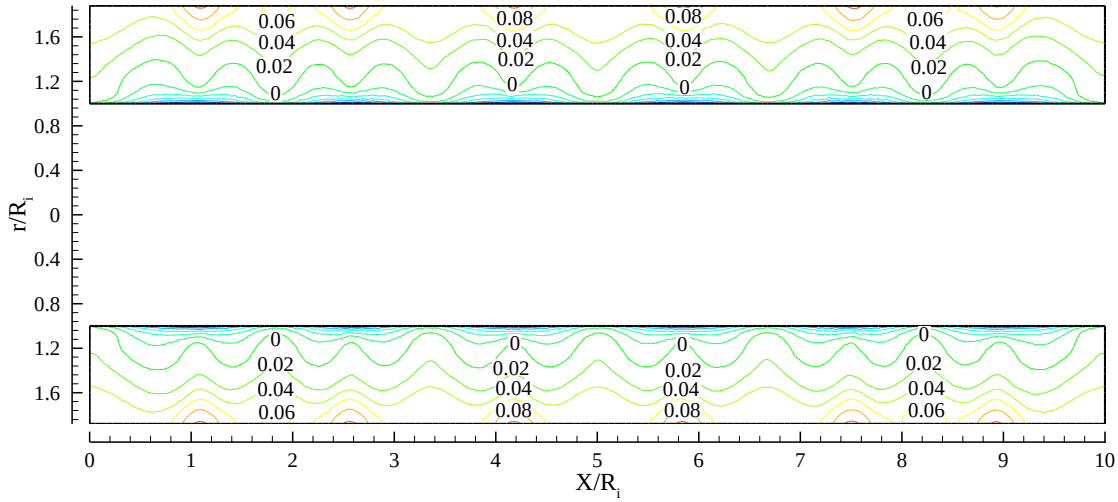

(a)

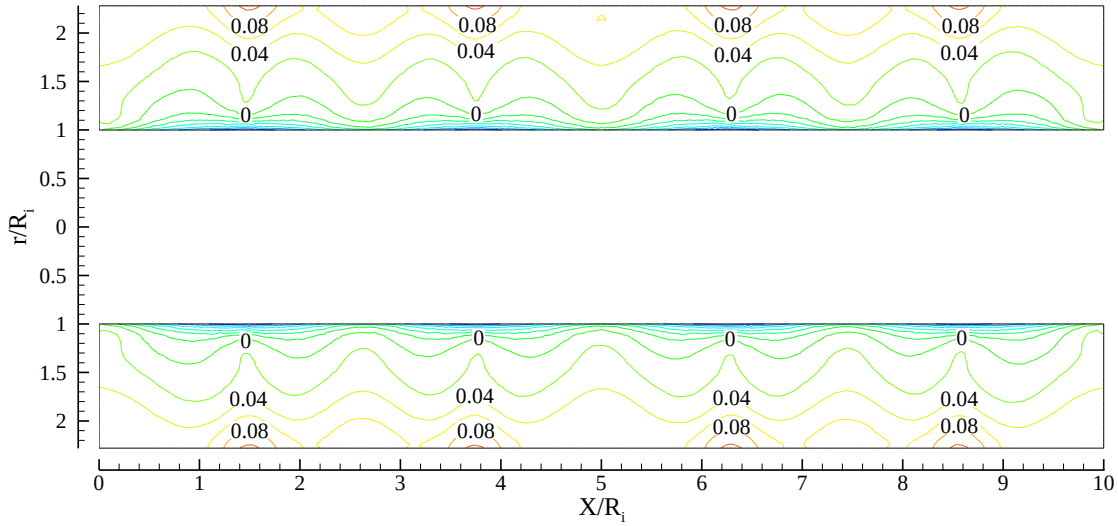

(b)

Figure 6.11: Contour plots of gauge static pressure in the meridional plane normalised by $0.5\rho R_i^2\Omega^2$ with contour spacing $\Delta p = 0.01\rho R_i^2\Omega^2$ for test cases (a) Γ =11.36 and (b) Γ = 7.81.

When the inner cylinder rotates, it causes all the particles of the fluid in direct contact with it to translate and rotate as a solid body, such that there is no relative motion between particles. Therefore, the fluid element is said to be in an equilibrium state. The rotating inner cylinder generates tangential shear stress acting on the fluid particles further away from its surface, due to the action of centrifugal force, and induce fluid to rotate along the

circumference of the cylinder. This results in the rotating fluid requiring a centripetal acceleration that is provided by the radial pressure gradient. The centripetal acceleration acting on the body of the rotating fluid results in higher pressure being exerted from the stationary outer cylinder towards the centre of rotation. This pressure balances the centripetal force to keep the fluid moving in a circular path, which explains the reduced gauge static pressure near the wall of the inner cylinder and the static pressure increase near the wall of the stationary outer cylinder.

The sharp curved contour lines in the outward flow regions in Figure 6.11 indicate the greater magnitude of the radial velocity induced by the Taylor vortices in these regions compared to the inward flow regions, as confirmed by the velocity vector map of Figure 6.6. The gauge static pressure flow pattern is in qualitative agreement with observation made in the CFD study by Zhou et al. (2007).

The contour plots in Figure 6.12(a) and Figure 6.12(b) show the distribution of dynamic pressure in the meridional plane for the test cases $\Gamma = 11.36$ and $\Gamma = 7.81$ respectively. The contour plots in Figure 6.12 show dynamic pressure maxima near the wall of the inner cylinder and dynamic pressure minima near the wall of the outer cylinder. This is expected as the rotating inner cylinder drives the tangential motion, resulting in a maximum flow tangential velocity, which is the dominant contribution to the dynamic pressure at the rotating inner cylinder surface. The flow tangential velocity gradually decreases toward the outer cylinder wall. As dynamic pressure is directly proportional to the fluid velocity, as the velocity of the fluid near the rotating inner cylinder decreases toward the outer stationary cylinder, the dynamic pressure also decreases.

Along the radial direction in Figure 6.12, the gradient of the dynamic pressure at the outward flow regions is high compared to the gradient at the inward flow regions. The contours bulge outward in the radial outward flow regions as high tangential momentum fluid is convected from near the inner rotating cylinder outwardly toward the stationary outer cylinder by the Taylor vortices. Similarly, the contours bulge radially inward in the inward flow regions as low momentum fluid is convected from near the wall of the stationary outer cylinder inwardly toward the wall of the rotating inner cylinder. The high tangential momentum fluid requires a greater adverse radial pressure gradient by the stationary outer cylinder to be maintained in a circular motion around the annulus. As in Figure 6.11, the contour lines in Figure 6.12 are more sharply curved in the outward flow regions than in the inward flow regions. This has been discussed in the contex of Figure 6.11.

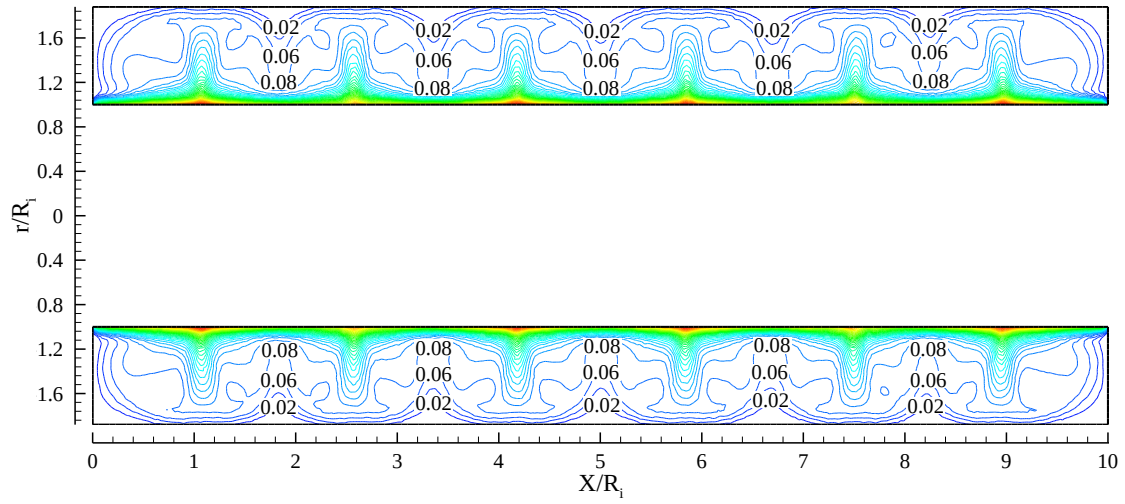

(a)

(b)

Figure 6.12: Contour plot of dynamic pressure in the meridional plane normalised by $0.5\rho R_i^2\Omega^2$ with contour spacing $\Delta p = 0.01\rho R_i^2\Omega^2$ for test cases (a) Γ =11.36 and (b) Γ = 7.81.

6.7.3 In-plane velocity profiles in the meridional plane

This section is concerned with the detailed quantitative discussion of the in-plane velocity profiles obtained from the predicted velocity vectors in the meridional plane of Figure 6.6(a) and Figure 6.6(b). To discuss in details the variation of the velocity distributions, profiles at three constant radial positions along the axial direction on the upper ($\theta = \pi/2$) and lower ($\theta = -\pi/2$) channels of the annulus have been extracted and plotted. The radial positions on the upper and the lower channels are $r = R_i + 0.95d$ (1mm away from the wall of the outer cylinder), $r = R_i + 0.5d$ (the mid-span gap of the annulus) and $r = R_i + 0.045d$ (1mm away from the wall of the inner cylinder) for the test case Γ = 11.36. The positions of the constant radial line where the profiles are extracted are illustrated and shown with

dotted lines in Figure 6.13. For the test case $\Gamma = 7.81$, the positions of the constant radial line where the profiles are extracted are taken at the same percentage gap width d as for test case $\Gamma = 11.36$. The velocity profiles have been normalised with respect to the inner cylinder surface speed ΩR_i.

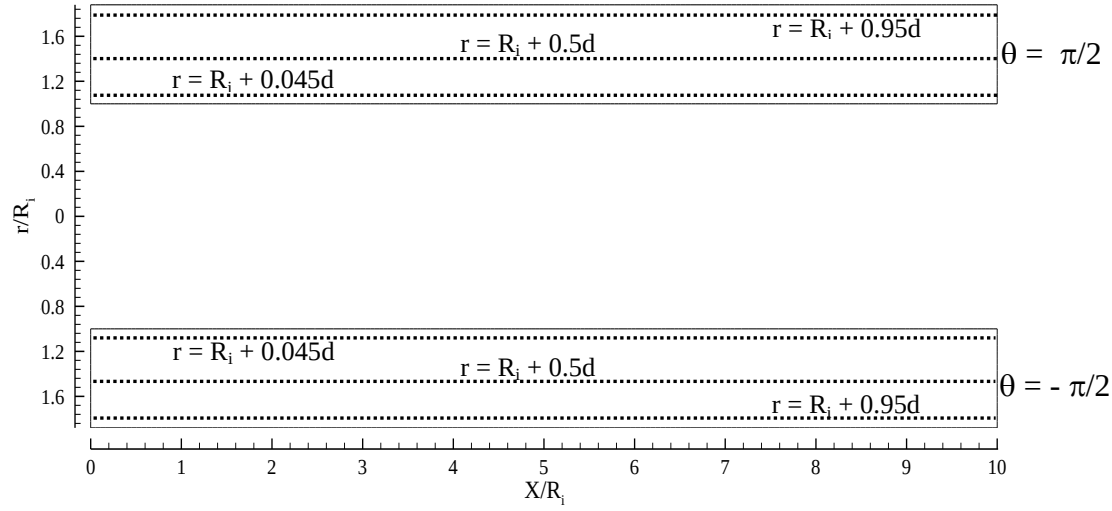

Figure 6.13: Location of velocity profiles at constant radial positions in the meridional plane along the axial direction.

Figure 6.14(a) and Figure 6.14(b) show the normalised axial velocity profiles at the three constant radial positions illustrated in Figure 6.13 on the lower and upper ($\theta = \pm\pi/2$) channels of the annulus for the test cases $\Gamma = 11.36$ and $\Gamma = 7.81$ respectively. The axial velocity profiles traverse through the inward and outward flow regions of Figure 6.6(a) for the test case $\Gamma = 11.36$ and Figure 6.6(b) for the test case $\Gamma = 7.81$. The centres of the inward and outward flows are saddle planes of axial velocity separating each Taylor vortex cell. The axial velocity profiles display alternating maxima and minima, with zero crossings in between, which is where the $r = R_i + 0.5d$ gap mid-span cylindrical surface intersects the saddle planes in the meridional plane. These positions are clearly shown and marked as zero on the contour lines in Figure 6.8(a) and Figure 6.8(b).

The axial velocity is observed to be relatively small compared with the surface speed of the inner cylinder. Each axial velocity maximum and minimum at $r = R_i + 0.045d$ and $r = R_i + 0.95d$ occours approximately at the same axial position of a vortex core. The axial velocity maxima occur radially below the cores of the clockwise vortices and the axial velocity minima occur radially below the cores of the anti-clockwise vortices for the profiles near the wall of the inner cylinder at $r = R_i + 0.045d$ and $\theta = -\pi/2$. For the profiles near the wall of the outer cylinder at $r = R_i + 0.95d$ and $\theta = -\pi/2$, the axial velocity

maxima occur radially above the cores of the anti-clockwise vortices and the axial velocity minima occur radially above the cores of the clockwise vortices. This trend reversal near the wall of the outer cylinder is due to the change in direction of the axial velocity induced by the Taylor vortices as the fluid approaches the wall of the outer cylinder. This is clearly shown in the velocity vectors of Figure 6.6(a) and Figure 6.6(b) for the test cases Γ = 11.36 and Γ = 7.81 respectively. The velocity maxima and minima at r = R_i + 0.045d and r = R_i + 0.95d occur almost at about the same axial location along X/R_i. Each velocity maximum and minimum pair is almost radially aligned. The axial velocity is driven by the Taylor vortex pattern. Each clockwise Taylor vortex induces an axial velocity maximum radially below its core at r = R_i + 0.045d and a minimum radially above its core at r = R_i + 0.95d. This is clearly shown in the contour plot of the axial velocity in Figure 6.8(a) and Figure 6.8(b) for the test cases Γ = 11.36 and Γ = 7.81 respectively.

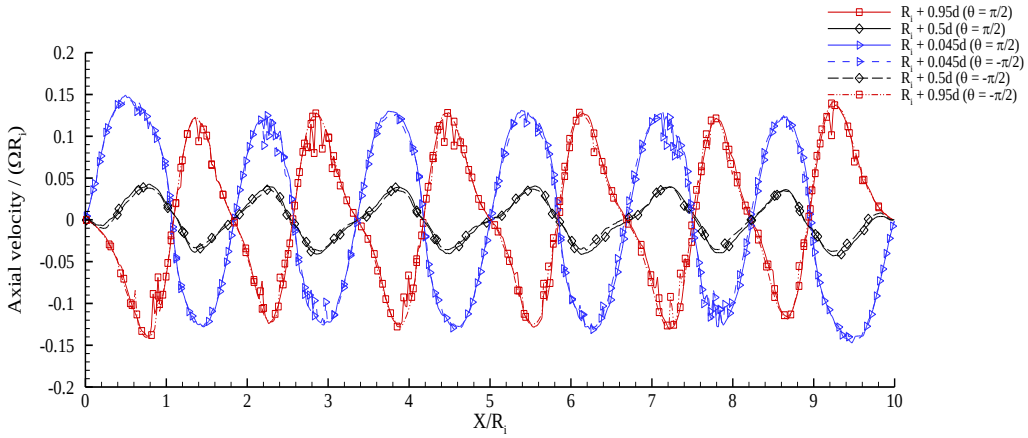

(a)

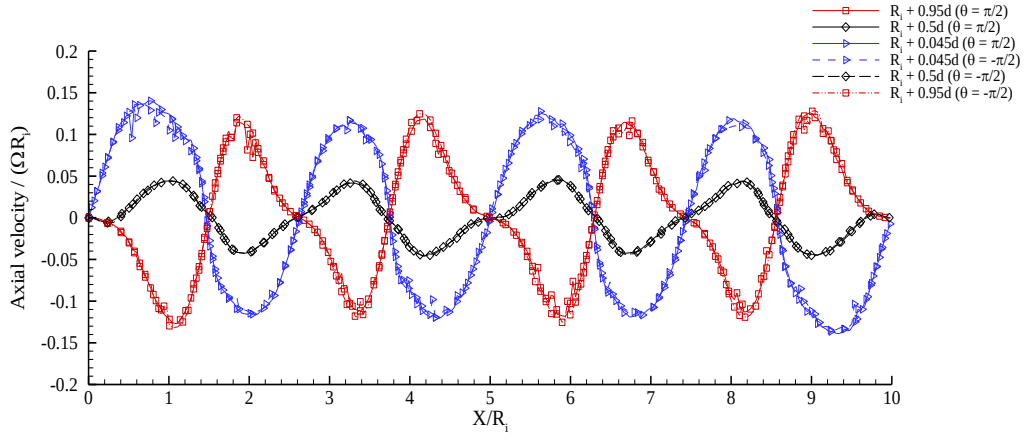

(b)

Figure 6.14: Normalised axial velocity profiles in the meridional plane at constant radial positions r = R_i + 0.045d, r = R_i + 0.5d, and r = R_i + 0.95d for the test cases (a) Γ = 11.36 and (b) Γ = 7.81.

The profiles in Figure 6.14 show almost the same amplitude of axial velocity maxima and minima near the inner cylinder wall at $r = R_i + 0.045d$ in the central region of the annulus at $1 \leq X/R_i \leq 9$ for the test case $\Gamma = 11.36$ and at $1.5 \leq X/R_i \leq 8.5$ for the test case $\Gamma = 7.81$. Similarly, the profiles show almost the same axial velocity maxima and minima near the outer cylinder wall, at $r = R_i + 0.95d$, at $1 \leq X/R_i \leq 9$ for the test case $\Gamma = 11.36$ and at $1.5 \leq X/R_i \leq 8.5$ for the test case $\Gamma = 7.81$. At the end-wall boundaries of the computational domain, the axial velocity maxima and minima at $r = R_i + 0.045d$ and $r = R_i + 0.95d$ are slightly higher in amplitude than along the central region at the same radial position.

At the radial position $r = R_i + 0.045d$ for the test case $\Gamma = 11.36$ in Figure 6.14(a), the axial velocity maxima and minima near the end-walls are approximately $0.15\Omega R_i$ and $-0.15\Omega R_i$ respectively, while the axial velocity maxima and minima at the central region of the computational domain are approximately $0.13\Omega R_i$ and $-0.13\Omega R_i$ respectively. These values correspond to approximately 15% and 13% of the speed of the inner cylinder respectively. At the radial position $r = R_i + 0.95d$ in Figure 6.14(a), the axial velocity maxima and minima near the end-walls are approximately $0.14\Omega R_i$ and $-0.14\Omega R_i$ respectively, while the axial velocity maxima and minima at the central region of the computational domain remain at $0.13\Omega R_i$ and $-0.13\Omega R_i$ respectively.

At the radial position $r = R_i + 0.045d$ for the test case $\Gamma = 7.81$ in Figure 6.14(b), the axial velocity maxima and minima near the end-walls are approximately $0.14\Omega R_i$ and $-0.14\Omega R_i$ respectively, while the axial velocity maxima and minima at the central region of the computational domain are approximately $0.12\Omega R_i$ and $-0.12\Omega R_i$ respectively. Similarly, at the radial position $r = R_i + 0.95d$ in Figure 6.14(b), the axial velocity maxima and minima near the end-walls are approximately $0.13\Omega R_i$ and $-0.13\Omega R_i$ respectively, while the axial velocity maxima and minima at the central region of the computational domain are approximately $0.12\Omega R_i$ and $-0.12\Omega R_i$ respectively. The agreement in the axial velocity maximum and axial velocity minimum values obtained at the same percentage gap width over the central region for the test cases $\Gamma = 11.36$ and $\Gamma = 7.81$ show a good consistency among the CFD simulations.

The variation in the axial velocity between the central region and the right and left sides of the computational domain at radial positions $r = R_i + 0.045d$ and $r = R_i + 0.95d$ is due to the presence of the end-walls. The axial velocity profiles at $r = R_i + 0.045d$ and $r = R_i + 0.95d$ display a low amplitude high wavenumber fluctuation superimposed on the Taylor vortex driven maxima and minima. This high wavenumber fluctuation observed in Figure

6.14 near the wall of the inner and outer cylinders may be due to the stabilizing effect of an axial flow which sometimes leads to an unstable region close to the wall of the cylinders (Coney and Simmers, 1979).

On the saddle planes, the axial velocity is essentially zero. The zero crossings that mark the axial position of the saddle planes between the neighbouring toroidal Taylor vortices offer a good visual reference point to appreciate how the vortex pattern changes axially.

In Figure 6.14(a) and Figure 6.14(b), it is observed that the axial position of the maxima and minima near the wall of the inner cylinder is not exactly the same as the corresponding axial position of the minima and maxima near the wall of the outer cylinder. This feature may be attributed to the vortical structures in which the vortex centres has been shifted toward the wall of the outer cylinder. Another factor may be the difference in fluid transport momentum. As the fluid with high transported momentum is been convected from the wall of the inner cylinder the fluid mixes at the meeting point of the adjacent vortex. As the fluid moves toward the outer cylinder, there is a reduction in the fluid momentum, such that the amount of fluid momentum that was coming from the inner cylinder has been significantly reduced before it gets to the axial position where the fluid near the wall of the outer cylinder displays an axial velocity peak. This results in the small axial offset of velocity maxima near the wall of the inner cylinder and minima near the wall of the outer cylinder at below and above each vortex core. The same process drives the axial offset of velocity minima near the wall of the inner cylinder and maxima near the wall of the outer cylinder around clockwise Taylor vortices. The offset is more pronounced for the test case $\Gamma = 7.81$ in Figure 6.14(b) than for the test case $\Gamma = 11.36$ in Figure 6.14(a), due to the increase in the gap width between the cylinders.

The axial velocity distributions obtained for the test cases $\Gamma = 11.36$ and $\Gamma = 7.81$ in Figure 6.14(a) and Figure 6.14(b) is in qualitative agreement with the CFD and with experimental results obtained by Zhou et al. (2007), Deng et al. (2009) and Haut et al. (2003).

Figure 6.15(a) and Figure 6.15(b) show the enlarged normalised axial velocity profile at $r = R_i + 0.5d$ (the gap mid-span of the annulus) for the test cases $\Gamma = 11.36$ and $\Gamma = 7.81$ respectively. The axial velocity maxima occur close to the cores of clockwise vortices and the axial velocity minima occur close to the cores of the anti-clockwise vortices. Had all the vortex centres been located in the gap mid-span of the annulus instead of being shifted toward the wall of the outer cylinder, as earlier observed and discussed in the context of

Figure 6.6, the axial velocity would have been zero at $r = R_i + 0.5d$. However, since the centres of the vortices do not lie on $r = R_i + 0.5d$, there is a small axial velocity induced by the Taylor vortices along $r = R_i + 0.5d$. The magnitude of the axial velocity maxima and minima at this radial position in Figure 6.15(a) and Figure 6.15(b) is relatively small compared to the axial velocity maxima and minima at $r = R_i + 0.045d$ and $r = R_i + 0.95d$.

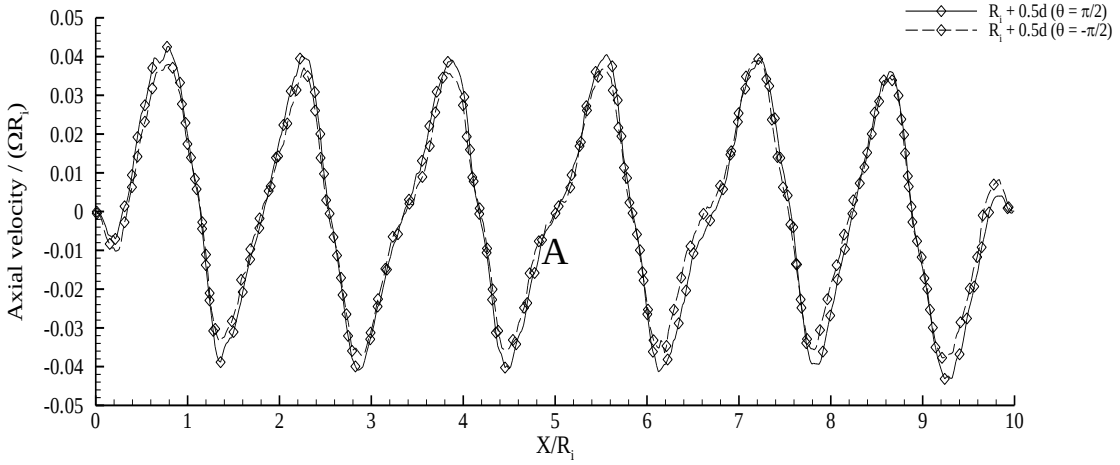

(a)

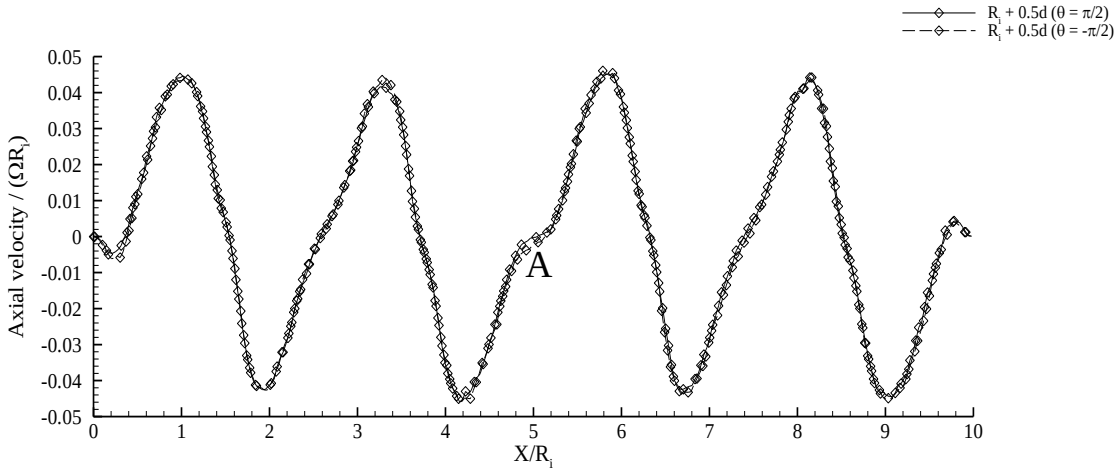

(b)

Figure 6.15: Normalised axial velocity profiles in the meridional plane at constant radial position $r = R_i + 0.5d$ for the test cases (a) $\Gamma = 11.36$ and (b) $\Gamma = 7.81$.

The profile in Figure 6.15(a) shows that the minima and the maxima in the central region over the range $1.3 \leq X/Ri \leq 8.7$ of the computational domain have almost the same axial velocity magnitude of approximately $0.04\Omega R_i$. This corresponds to approximately 4% of the speed of the inner cylinder. Similarly, the profile in Figure 6.15(b) shows that the minima and the maxima in the central region over the range $1.9 \leq X/Ri \leq 8.1$ of the computational domain have almost the same axial velocity magnitude of approximately $0.046\Omega R_i$. This corresponds to approximately 4.6% of the speed of the inner cylinder. The

position of the axial velocity minima and maxima at $r = R_i + 0.5d$ indicate the approximate location of the vortex cores. Hence, the slight difference in the maximum and minimum values between the test cases $\Gamma = 11.36$ and $\Gamma = 7.81$ may be attributed to the difference in the radial location of the vortex cores in each test cases.

The axial velocity profiles in Figure 6.15 seem to be symmetric about the cylinder mid-span $X/R_i = 5$. That is, the profiles at $0 \leq X/R_i \leq 5$ and $5 \leq X/R_i \leq 10$ seem to be mirror images of one another. A normalised axial velocity profile inflection point is shown at position A in Figure 6.15(a) and Figure 6.15(b). The inflection point at position A in both figures corresponds to the axial mid-point about which the flow is symmetric at $X/R_i = 5$. This position lies in an inflow region, where low momentum fluid near the outer wall is convected inwardly by the radial inflow. The inflection is likely to be due to a greater separation between the Taylor vortex pairs that lie either side of A.

The axial velocity at the wall is zero as expected, due to no-slip boundary condition. The zero crossings mark the axial position of the saddle planes between the neighbouring toroidal Taylor vortices.

Figure 6.16(a) and Figure 6.16(b) show respectively profiles of radial velocity at the same three radial positions along the axial direction as in Figure 6.14 for the test cases $\Gamma = 11.36$ and $\Gamma = 7.81$. The profiles of radial velocity at both the lower and upper channels exhibit the same trend, as in Figure 6.14. At the edges of the computational domain, at $X/R_i = 0$ and $X/R_i = 10$, the radial velocity is zero due to the no-slip wall boundary condition imposed. This is because the velocity of the fluid in contact with the wall moves at the same velocity as the wall, and in this case, the wall is stationary. The no-slip condition at the end-walls causes the fluid to shear resulting in shear stress. Away from the modelled solid end-walls in the central region of the computational domain, the radial velocity exhibits alternating minima and maxima. The locations of the maxima in Figure 6.16 mark the meeting points of the radial outflow between two adjacent vortices (induced downwells at $\theta = -\pi/2$ and induced upwell at $\theta = \pi/2$) on the meridional plane of Figure 6.6. Similarly, the locations of minima radial velocity mark the meeting point of the radial inward flow between two adjacent vortices (induced upwells at $\theta = -\pi/2$ and induced downwell at $\theta = \pi/2$) in the meridional plane of Figure 6.6. The locations of the zero crossing of the radial velocity mark the centres of each vortex.

The radial velocity in Figure 6.16(a) and Figure 6.16(b) exhibit a periodic trend along the axial direction. This periodic trend is more obvious in the profile at the gap mid-span

radial position $r = R_i + 0.5d$ ($\theta = \pm\pi/2$), this being the position at which the radial velocity reaches the maximum value. At this radial position ($r = R_i + 0.5d$), approximately six and four cycles of normalised radial velocity oscillation along X/R_i are shown in Figure 6.16(a) and Figure 6.16(b) for the test cases $\Gamma = 11.36$ and $\Gamma = 7.81$ respectively. Each cycle corresponds to a maximum outward flow followed by a minimum inward flow at the saddle planes between the boundaries of two adjacent Taylor vortices. The velocity profiles in Figure 6.16(a) and Figure 6.16(b) show that the radial velocity is not symmetric along the gap mid-span ($r = R_i + 0.5d$) about $u_r = 0$. The asymmetry in inflow (negative u_r) and outflow (positive u_r) regions is apparent in the radial velocity profiles at $r = R_i + 0.5d$ ($\theta = \pm\pi/2$). This feature is attributted to the vortex centres that are positioned close to each other either side of an outflow saddle plane, as shown in Figure 6.6(a) and Figure 6.6(b). The radial velocity distribution at the radial position $r = R_i + 0.5d$ along the meridional plane of the annulus is consistent and in good agreement with the experimental and computational results obtained by Wereley and Lueptow (1998) and Deng et al., (2005). The flow parameter of the coaxial cylinders investigated by Deng et al., (2005) at different Reynolds numbers is $\Gamma = 5.17$ and $\eta = 0.613$.

Figure 6.16(a) and Figure 6.16(b) show that the magnitude of the normalised radial velocity maxima is almost constant while the magnitude of the inflow radial velocity minima varies along the profiles at $r = R_i + 0.5d$ ($\theta = \pm\pi/2$). For instance, the radial velocity local minima near the boundaries at $0 \leq X/R_i \leq 0.065$ and $0 \leq X/R_i \leq 0.935$ are higher than the corresponding values in the central regions of the computational domain for the test case $\Gamma = 11.36$ in Figure 6.16(a). A similar trend is observed for the test case $\Gamma = 7.81$ in the profile of Figure 6.16(b). Specifically, the magnitude of the radial velocity minima at $X/R_i = 2.65$ and $X/R_i = 7.45$ are higher than the corresponding values at $X/R_i = 5$ at the centre of the computational domain. This flow pattern is a result from the use of side wall boundary conditions that constrained the development of the first Taylor vortex and of the last Taylor vortex thereby reducing their strength, as shown in Figure 6.6. To compensate for this increment in the axial extent of the end wall vortices, the inward flow velocity minima at $X/R_i = 2.65$ and $X/R_i = 7.45$ increase.

At the gap mid-span $r = R_i + 0.5d$, the outward radial velocity maxima are greater in magnitude than the inward radial velocity minima, which agrees with the strength of the radial inward flow between the vortices being weaker than that of the outward flow, as observed in Figure 6.6. This result is not surprising, as the Taylor vortices transport higher

tangential momentum fluid outwardly to the wall of the outer cylinder and convect fluid with lower momentum inwardly. This resulted in a powerful outward efflux of flow with tangential momentum and a weaker influx of tangential momentum, the imbalance being accounted for by viscous dissipation at the outer cylinder wall. This result is consistent with the results obtained by Snyder and Lambert (1966) and Wereley and Lueptow (1998) who obtained higher radial velocities at the outflow regions.

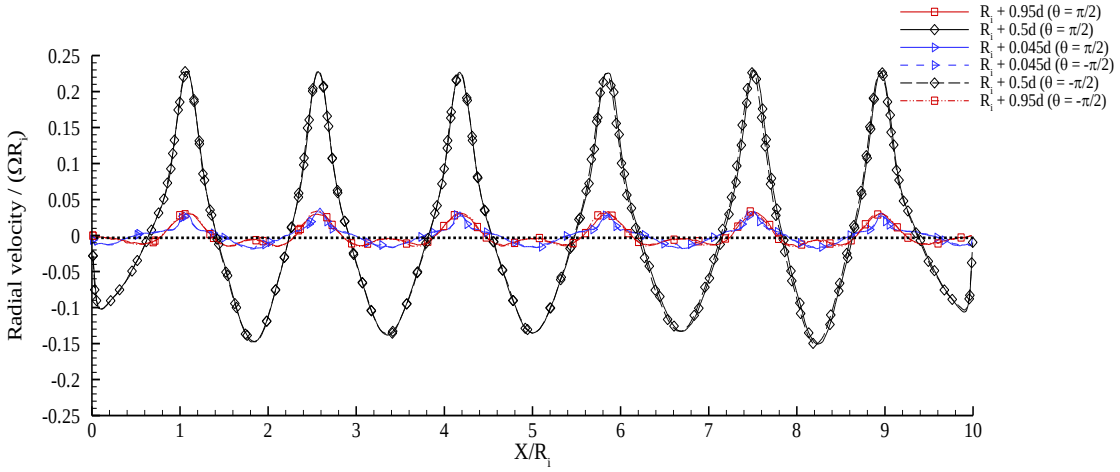

(a)

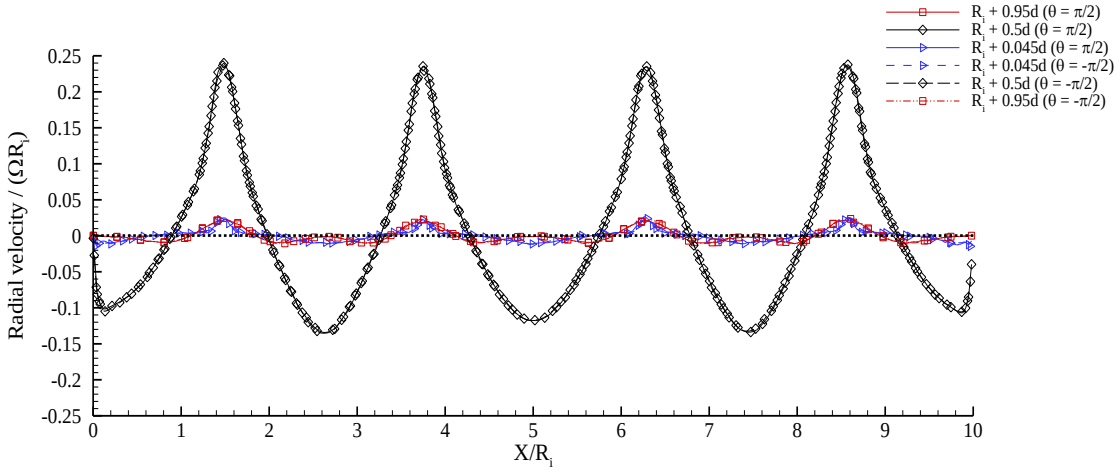

(b)

Figure 6.16: Normalised radial velocity profiles in the meridional plane at constant radial positions $r = R_i + 0.045d$, $r = R_i + 0.5d$, and $r = R_i + 0.95d$ for the test cases (a) $\Gamma = 11.36$ and (b) $\Gamma = 7.81$.

The maximum outflow velocity for test case $\Gamma = 11.36$ in Figure 6.16(a) is approximately $0.24\Omega R_i$ while the maximum inflow velocity in the central region is approximately $-0.15\Omega R_i$. Similarly, the magnitude of the maximum radial flow velocity in the outflow regions for test case $\Gamma = 7.81$ in Figure 6.16(b) is approximately $0.24\Omega R_i$ while the radial velocity minimum in the central region of the computational domain is approximately -

$0.12\Omega R_i$. For test case $\Gamma = 11.36$, at $X/R_i = 0.05$ and $X/R_i = 9.95$, the radial velocity minima are approximately $-0.10\Omega R_i$ while for test case $\Gamma = 7.81$, at $X/R_i = 2.65$ and $X/R_i = 7.45$, the radial velocity minima are approximately $-0.14\Omega R_i$.

A noticeable feature of the radial velocity in Figure 6.16(a) and Figure 6.16(b) is the shape of the velocity peak at the outflow regions. This is sharper than the velocity trough at the inflow regions. This feature is attributed to the difference in the magnitudes of the Taylor vortex induced velocity at the saddles planes between two adjacent vortices. At these planes, the magnitude of the velocity vectors of the outflow regions is stronger than the magnitude of the velocity vectors of the inflow regions, as shown in Figure 6.6. The sharper maxima (crests) in Figure 6.16(a) and Figure 6.16(b) correspond to jet-like outflows in the radial direction while the wider minima (valleys) correspond to sink-like inflows in Figure 6.6(a) and Figure 6.6(b). The width of the wider minima for the test case $\Gamma = 11.36$ in Figure 6.6(a) is almost 1.5 times that of the shaper maxima as measured between the zero crossings in Figure 6.16(a). For the test case $\Gamma = 7.81$ in Figure 6.16(b), the width of the troughs (valleys) at $X/R_i = 2.65$ and $X/R_i = 7.45$ is about 23.5% greater than that of the shaper peaks (crests), as measured between the zero crossings. Similarly, the width of the trough (valley) in the central region at $X/R_i = 5.00$ is about 53% greater than that of the shaper peaks (crests) at $X/R_i = 2.65$ and $X/R_i = 7.45$, as measured between the zero crossings. This flow feature was also observed in the literature by Wereley and Lueptow (1998) and Deng et al.(2009). In general the radial velocity distributions obtained for the test cases $\Gamma = 11.36$ and $\Gamma = 7.81$ at $r = R_i + 0.5d$ and $\theta = \pm\pi/2$ in Figure 6.16(a) and Figure 6.16(b) are in qualitative agreement with the CFD and with experimental results obtained by Deng et al. (2009) and Haut et al. (2003).

Figure 6.17(a) and Figure 6.17(b) show the enlarged view of the normalised radial velocity profiles at $r = R_i + 0.045d$ and $r = R_i + 0.95d$ for the test cases $\Gamma = 11.36$ and $\Gamma = 7.81$ respectively. The profiles show that the magnitude of the outward flow radial velocity maxima near the inner cylinder at $r = R_i + 0.045d$ is almost twice the magnitude of the inward flow radial velocity minima. The radial velocity peak of the outward flow regions is sharper than the radial velocity troughs of the inward flow regions along $r = R_i + 0.045d$ due to the strength of the induced velocity by the vortices at the either side of the saddle planes.

The normalised radial velocity profile at $r = R_i + 0.95d$ differs from the profile predicted at $r = R_i + 0.045d$. At the outward flow regions, the profiles at the two radial positions

exhibit similar trends and the respective radial velocity maxima are of almost equal magnitude. The inward flow pattern is instead quite different, as the single trough minima observed at the $r = R_i + 0.045d$ has been replaced by double trough minima at $r = R_i + 0.95d$, as shown by the two arrows labelled A in Figure 6.17(a) and Figure 6.17(b).

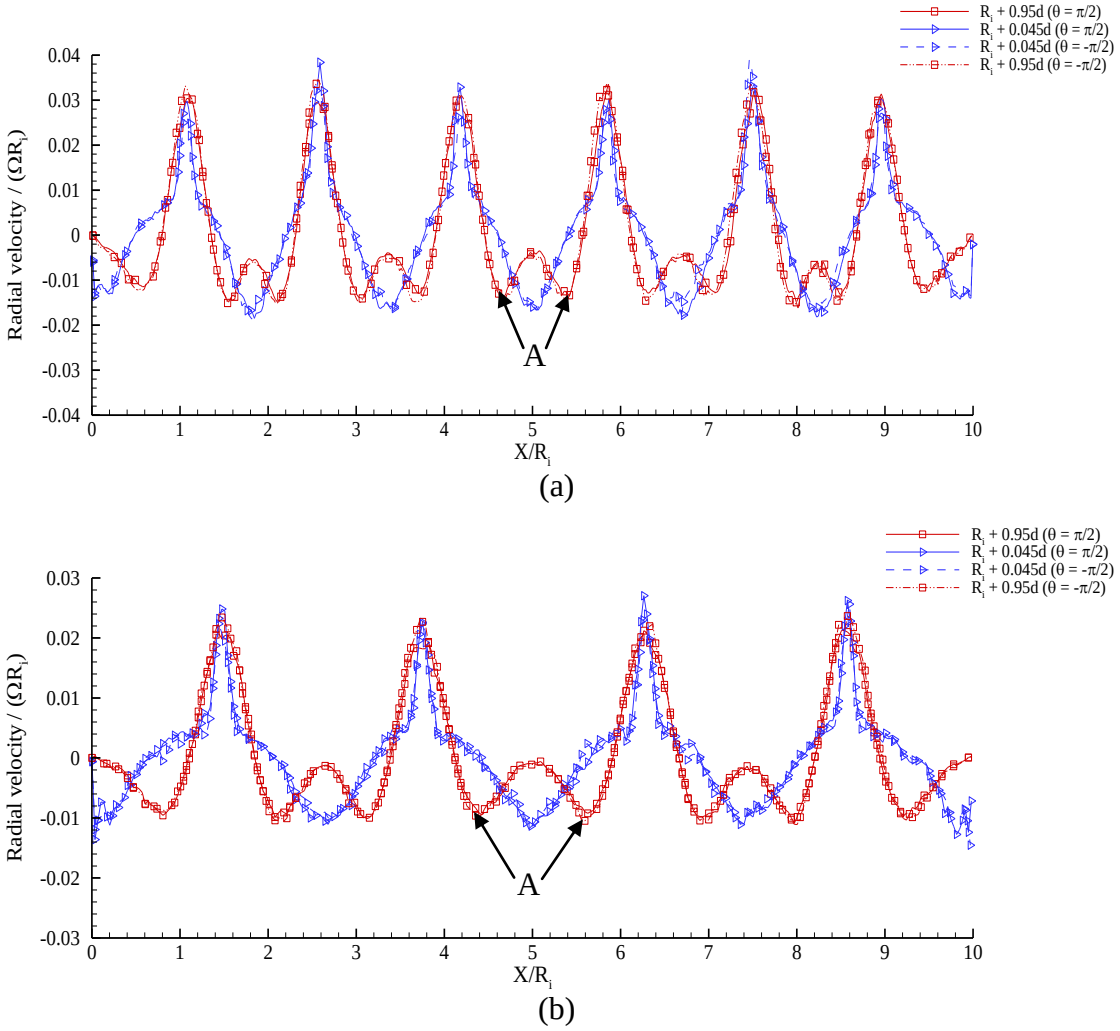

Figure 6.17: Normalised radial velocity profiles in the meridional plane at constant radial positions $r = R_i + 0.045d$ and $r = R_i + 0.95d$ for the test cases (a) $\Gamma = 11.36$ and (b) $\Gamma = 7.81$.

This may be attributed to the vortical structures in which the vortex centres are shifted towards the outer cylinder. The shifting of each vortex centre creates a variation in the boundary layer of the inward flow regions near the wall of the stationary outer cylinder. The boundary layer approaching the inward flow region is subject to an adverse streamwise pressure gradient as discussed in the context of Figure 6.11, prompting flow separation. The resulting shear layer velocity profile gives the double trough in the normalised radial velocity minima of Figure 6.17(a) and Figure 6.17(b).

The single through observed near the wall of the inner cylinder occurs in inwards flow regions. In these regions, low tangential momentum fluid is approaching the inner rotating cylinder. As the inner cylinder rotates at a constant angular speed, it imparts tangential momentum to the neighbouring fluid. This creates a thick tangential boundary layer with a dominant tangential shear at the periphery of the rotating inner cylinder. The flow is accelerating tangentially under the action of this shear stress. This acceleration sustains the confluence of the radial inflow at $r = R_i + 0.045$, such that the single peak is observed at $r = R_i + 0.045$ in Figure 6.17(a) and Figure 6.17(b). The comparison of the radial velocity distributions at the radial positions $r = R_i + 0.045d$ and $r = R_i + 0.95d$ with published work for the test cases $\Gamma = 11.36$ and $\Gamma = 7.8$ cannot be made because the radial velocity distribution at these radial positions appears not to have been reported in the open literature.

Figure 6.18(a) and Figure 6.18(b) show the profiles of normalised tangential velocity in the meridional plane of the annulus for the test cases $\Gamma = 11.36$ and $\Gamma = 7.81$ respectively. The profiles show negative tangential velocity minima near the wall of the inner cylinder and negative tangential velocity maxima near the wall of the outer cylinder. The magnitude of the tangential velocity minima is higher than that of the tangential velocity maxima. The negative values of the tangential velocity observed near the wall of the inner cylinder are due to the clockwise rotation of the inner cylinder with respect to the cylindrical reference system in Figure 6.1 as discussed in the context of Figure 6.10. The zero tangential velocity at the boundaries $X/R_i = 0$ and $X/R_i = 10$ is due to no-slip boundary conditions imposed at the end-walls of the computational domain as explained in the context of Figure 6.16.

Near the wall of the outer cylinder, at $r = R_i + 0.95d$, the positions of negative tangential velocity minima correspond to outflow regions, while the positions of negative tangential velocity maxima correspond to the inflow regions in Figure 6.6(a) and Figure 6.6(b). In Figure 6.18(a) for the test case $\Gamma = 11.36$, the negative tangential velocity minima are approximately $-0.2\Omega R_i$, while the negative tangential velocity maxima are approximately $-0.03\Omega R_i$. For the test case $\Gamma = 7.81$ shown in Figure 6.18(b), the negative tangential velocity minima are approximately $-0.16\Omega R_i$, while the negative tangential velocity maxima are approximately $-0.02\Omega R_i$. The shape of the velocity peak of the outward flow regions and the velocity trough of the inflow regions are almost the same in Figure

6.18(a), which indicate radial equilibrium in the strength of the Taylor vortices at these regions. The same feature is observed in Figure 6.18(b).

Similarly, the normalised tangential velocity profile near the wall of the inner cylinder, at r = R_i + 0.045d in Figure 6.18(a) and Figure 6.18(b), also show that the positions of negative tangential velocity minima correspond to the outflow regions, while the positions of negative tangential velocity maxima correspond to the inflow regions in Figure 6.6(a) and Figure 6.6(b). The negative tangential velocity minima are approximately -0.82ΩR_i, while the negative tangential velocity maxima are approximately -0.53ΩR_i for the test case Γ = 11.36 in Figure 6.18(a). For the test case Γ = 7.81 in Figure 6.18(b), the negative tangential velocity minima are approximately -0.82ΩR_i, while the negative tangential velocity maxima are approximately -0.56ΩR_i.

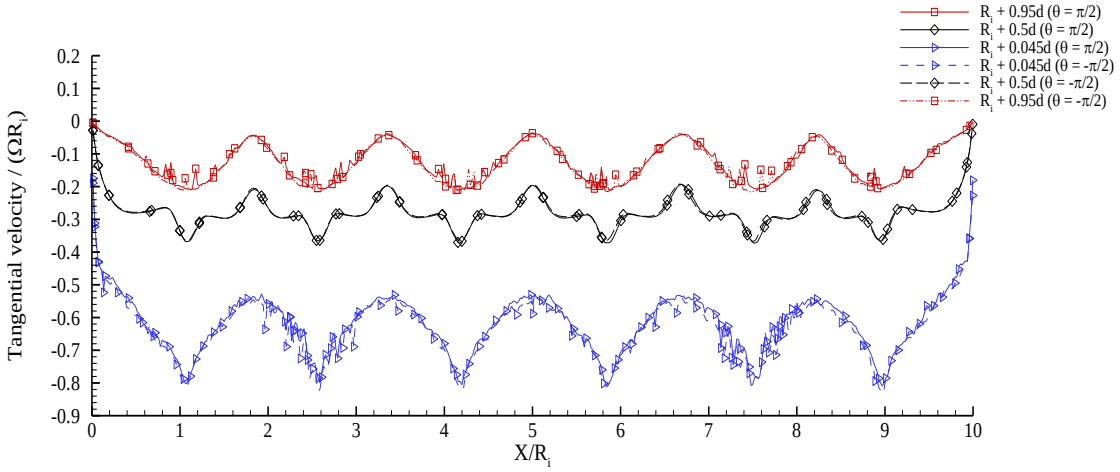

(a)

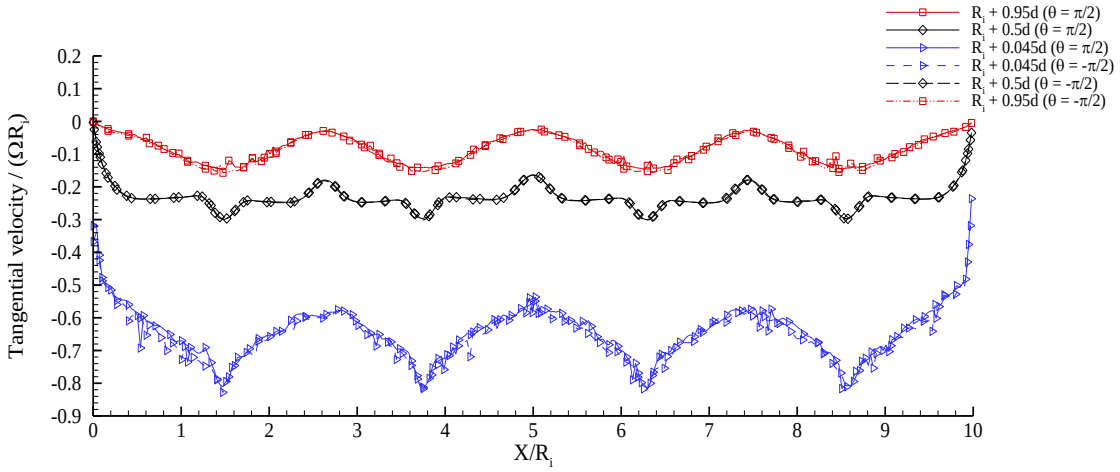

(b)

Figure 6.18: Normalised tangential velocity profiles in the meridional plane at constant radial positions r = R_i + 0.045d, r = R_i + 0.5d, and r = R_i + 0.95d for the test cases (a) Γ = 11.36 and (b) Γ = 7.81.

The shape of the velocity trough of the outward flow regions is sharper than that of the velocity peak of the inflow regions in Figure 6.18(a) and Figure 6.18(b), an indication that the transported tangential momentum by the outflow is greater than the transported tangential momentum by inflow near the wall of the inner cylinder.

The normalised tangential velocity profiles at the gap mid-span $r = R_i + 0.5d$ in Figure 6.18(a) and Figure 6.18(b) also show negative minima and maxima localised respectively at the outward and inward flow regions in Figure 6.6(a) and Figure 6.6(b). The shapes of the velocity trough of the outward flow regions and that of the velocity peak of the inflow regions are approximately the same. This indicates that the strength of the tangential momentum transport at the inward flow regions is the same as the strength of the tangential momentum transport at the outward flow regions at the gap mid-span of the annulus. The shape of the tangential velocity profiles at this radial position may be associated with the vortical structure in the mid-span of the annulus and is consistent between test cases $\Gamma = 11.36$ and $\Gamma = 7.81$.

As for the radial velocity profiles, the tangential velocity profiles in the meridional plane of the annulus along these radial positions ($r = R_i + 0.045d$, $r = R_i + 0.5d$, and $r = R_i + 0.95d$) appears not to have been reported in the open literature.

6.7.4 In-plane pressure profiles in the meridional plane

A quantitative analysis of the pressure field at the three radial positions as in Figure 6.14 is presented in this section for the test cases $\Gamma = 11.36$ and $\Gamma = 7.81$. Pressure has been normalised with respect to $0.5\rho R_i^2\Omega^2$.

Figure 6.19(a) and Figure 6.19(b) show the gauge static pressure profiles in the meridional plane of the annulus for the test cases $\Gamma = 11.36$ and $\Gamma = 7.81$ respectively. These figures show that the distributions of gauge static pressure at equal radial distance are independent of the azimuthal angle θ on the meridional plane. The profiles clearly show the gauge static pressure near the wall of the outer cylinder higher than the pressure near the wall of the inner cylinder, due to the tangential flow velocity and the requirement for radial momentum equilibrium. As the inner cylinder rotates, the centrifugal forces due to the rotation of the inner cylinder is balanced by the pressure gradient forces due to the stationary outer cylinder in order for a fluid element rotating around the cylinder axis to be in a state of radial equilibrium, as discussed in the context of Figure 6.11.

Near the wall of the inner cylinder at $r = R_i + 0.045d$ in Figure 6.19(a) and Figure 6.19(b), the negative gauge static pressure minima occur in the outward flow region, while the negative gauge static pressure maxima are present in the inward flow regions of Figure 6.6(a) and Figure 6.6(b). At this radial position, the negative gauge static pressure maxima (peaks) are observed to be sharper than the negative gauge static pressure minima (troughs). Near the wall of the outer cylinder, at $r = R_i + 0.95d$ in Figure 6.19(a) and Figure 6.19(b), the gauge static pressure maxima occur in the outward flow regions while the gauge static pressure minima are present in the inward flow regions of Figure 6.6(a) and Figure 6.6(b). At this radial position, the gauge static pressure peaks are sharper, while the gauge static pressure troughs of the minima at inward flow regions are flatter, an indication that the radial pressure gradient exerted on the outer cylinder wall at the outflow regions is greater than the radial pressure gradient at the inward flow regions. This causes the radial velocity at the outward flow regions to be higher than the radial velocity at the inward flow regions.

The difference observed between the profiles at $r = R_i + 0.045d$ and those at $r = R_i + 0.95d$ may be attributed to the action of centrifugal forces that must be balanced by the pressure gradient as a result of the stationary outer cylinder in order to maintain radial equilibrium.

At the gap mid-span $r = R_i + 0.5d$, the streamwise variation in the gauge static pressure is relatively small compared with the one near the walls of the inner and the outer cylinders. The gauge static pressure minima are close to the position of the vortex centres. This is analogous to a free vortex in classical potential flow theory, in which the static pressure is expected to be at minimum at the centre of the vortex. Since the radial position $r = R_i + 0.5d$ does not pass through the centre of the vortices, it is expected that there will be some non-uniformity in the gauge static pressure axial distribution between the centre of each Taylor vortex and the corresponding minimum at $r = R_i + 0.5d$ in Figure 6.19 as the traverse cuts below the centre of the vortices, which are locations of local pressure minima.

Another noticeable feature of the profiles at $r = R_i + 0.5d$ for test cases $\Gamma = 11.36$ and $\Gamma = 7.81$ in Figure 6.19(a) and Figure 6.19(b) is the position of the gauge static pressure maxima. It is observed that the gauge static pressure maxima are located in both the outward flow and inward flow regions, alternating one another in the positive axial direction, with the inward flow region maxima greater than the outward flow region maxima. The gauge static pressure maxima observed in the outward flow regions are

lower than the gauge static pressure maxima in the inward flow regions due to the structure of the vortices. As the axial centre (x_c) of each vortex is closer to the outward flow regions, pressure is expected to be a minimum at the vortex core, therefore the position near the vortex core (outward flow region) will experience a lower maximum gauge static pressure than the position near an inward flow region. This results in the pressure minima at either side of an outflow saddle plane in Figure 6.19.

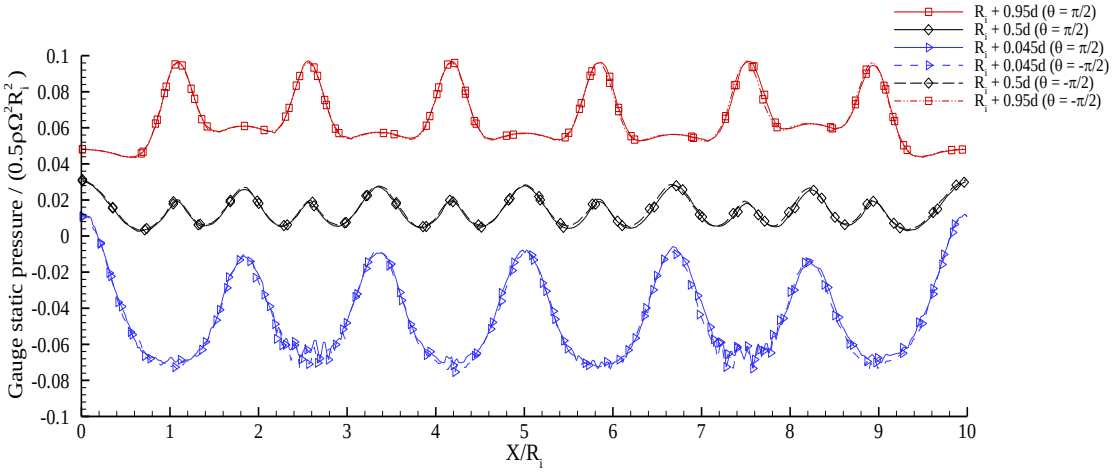

(a)

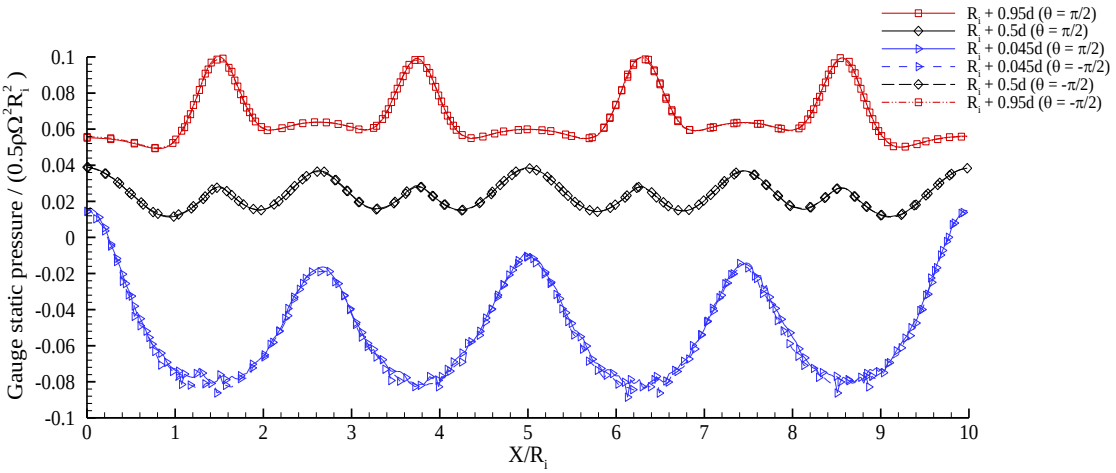

(b)

Figure 6.19: Normalized gauge static pressure profiles in the meridional plane at constant radial positions $r = R_i + 0.045d$, $r = R_i + 0.5d$, and $r = R_i + 0.95d$ for the test cases (a) Γ = 11.36 and (b) Γ = 7.81.

Figure 6.20(a) and Figure 6.20(b) show the streamwise distributions of the normalised dynamic pressure at different radial positions for the test cases Γ = 11.36 and Γ = 7.81 respectively. These profiles show that the dynamic pressure near the wall of the inner cylinder is high and that the dynamic pressure progressively decreases toward the wall of the outer cylinder. This is expected, as the fluid near the inner cylinder has a higher tangential momentum than the fluid near the wall of the outer cylinder. This results in high

dynamic pressure near the wall of the inner cylinder and in low dynamic pressure near the wall of the outer cylinder. At the three radial positions of Figure 6.20(a) and Figure 6.20(b), the dynamic pressure minima are in the inward flow regions while the dynamic pressure maxima are in the outward flow regions of Figure 6.6(a) and Figure 6.6(b). The shape of the dynamic pressure maxima (peaks) in the outward flow regions are sharper than that of the dynamic pressure minima (troughs), indicating the strength of the dynamic pressure distributions present in the flow at these regions.

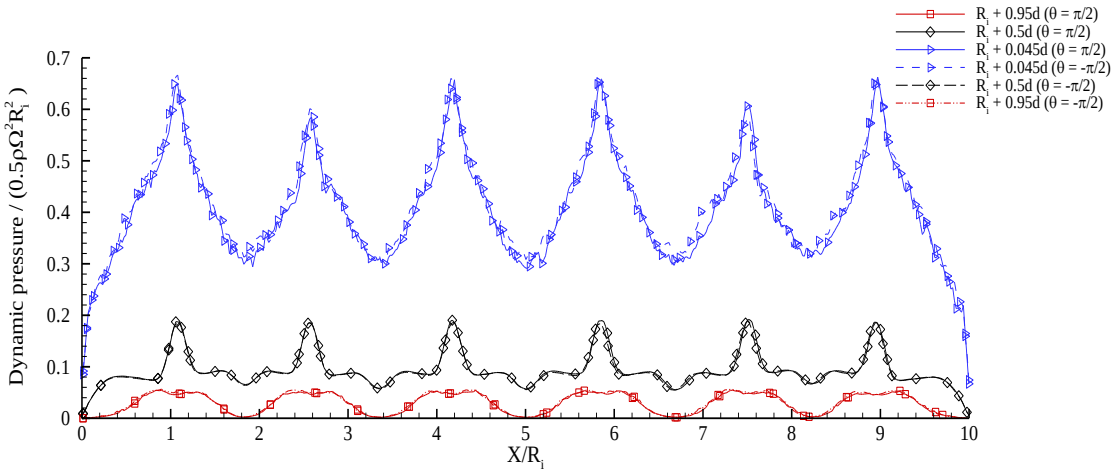

(a)

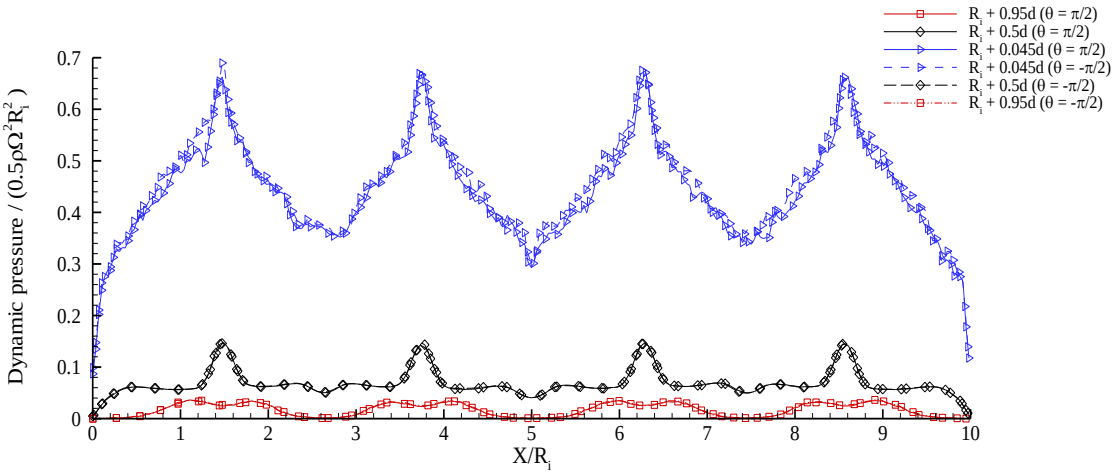

(b)

Figure 6.20: Normalised dynamic pressure profiles in the meridional plane at constant radial positions $r = R_i + 0.045d$, $r = R_i + 0.5d$, and $r = R_i + 0.95d$ for the test cases (a) $\Gamma = 11.36$ and (b) $\Gamma = 7.81$.

At the gap mid-span $r = R_i + 0.5d$, the peak of the dynamic pressure at the inward flow regions is almost flat and not well-defined. This feature is attributed to the vortical structures in this locality, since the centres of the vortices are further apart from this saddle

plane than at the saddle plane of an outflow region. This reduces the strength of the vortex induced velocity, flattening the dynamic pressure profile.

The fluid tangential momentum is at $r = R_i + 0.5d$ is lower than that of the fluid close to the wall of the inner cylinder. This gives a lower dynamic pressure at $r = R_i + 0.5d$ compared to the dynamic pressure at $r = R_i + 0.045d$. Similarly, the dynamic pressure profile near the wall of the outer cylinder is lower than the profiles at $r = R_i + 0.5d$ and $r = R_i + 0.045d$, due to low momentum of the fluid near the wall of the outer cylinder.

As for the tangential velocity distribution, profiles of gauge static pressure and of dynamic pressure in the meridional plane have not been reported in the literature along the radial positions $r = R_i + 0.045d$, $r = R_i + 0.5d$, and $r = R_i + 0.95d$. As such, no comparison is made between the results obtained in this research and previous studies.

6.7.5 Flow pattern in the azimuthal plane

One of the advantages of a three-dimensional (3D) numerical model is the ability to examine the flow details in more than one plane. A detailed analysis of the flow in the azimuthal plane for the test cases $\Gamma = 11.36$ and $\Gamma = 7.81$ is therefore documented in this section so as to complement the information obtained from the results in the meridional plane, therefore achieving a clearer understanding of the flow in the annular gap between coaxial rotating cylinders. Various cross-sections have been sliced vertically, normal to the axial direction of the coaxial cylinders, in order to obtain azimuthal planes from which various flow variables are analysed. The flow pattern at the location near the end-walls is included in order to understand the effects of the end-walls on the azimuthal plane flow. In all, six different flow patterns (including the flow pattern at the end-walls) are identified within the computational domain. Four out of the six patterns recur in the axial direction with the spatial period of one Taylor vortex pair. The sliced positions are marked with different colours and labelled alphabetically in Figure 6.21(a) and Figure 6.21(b) for the test cases $\Gamma = 11.36$ and $\Gamma = 7.81$ respectively for easy identification. These cross-sections are: (a) the left end-wall, (b) the clockwise vortex centre, (c) the downwell (outward flow) region, (d) the anti-clockwise vortex centre, (e) the upwell (inward flow) region, and (f) the right end-wall. This nomenclature is based on the flow visualisation at the lower channel of the annulus at $\theta = -\pi/2$. These sections define the azimuthal planes where the flow pattern is investigated.

Figure 6.22 and Figure 6.23 show the velocity vector maps of different flow patterns at various axial locations projected on the azimuthal plane for the test cases Γ = 11.36 and Γ = 7.81 respectively. The location of the various flow patterns shown in Figure 6.22 for the test case Γ = 11.36 corresponds to axial positions: (a) X/R_i = 0.05, (b) X/R_i = 0.65, (c) X/R_i = 1.07, (d) X/R_i = 1.41, (e) X/R_i = 1.84, and (f) X/R_i = 9.95 as illustrated in Figure 6.22(a). Similarly, the location of the various flow patterns shown in Figure 6.23 for the test case Γ = 7.81 correspond to axial positions: (a) X/R_i = 0.05, (b) X/R_i = 0.92, (c) X/R_i = 1.47, (d) X/R_i = 1.97, (e) X/R_i = 2.62, and (f) X/R_i = 9.95 as illustrated in Figure 6.21(b).

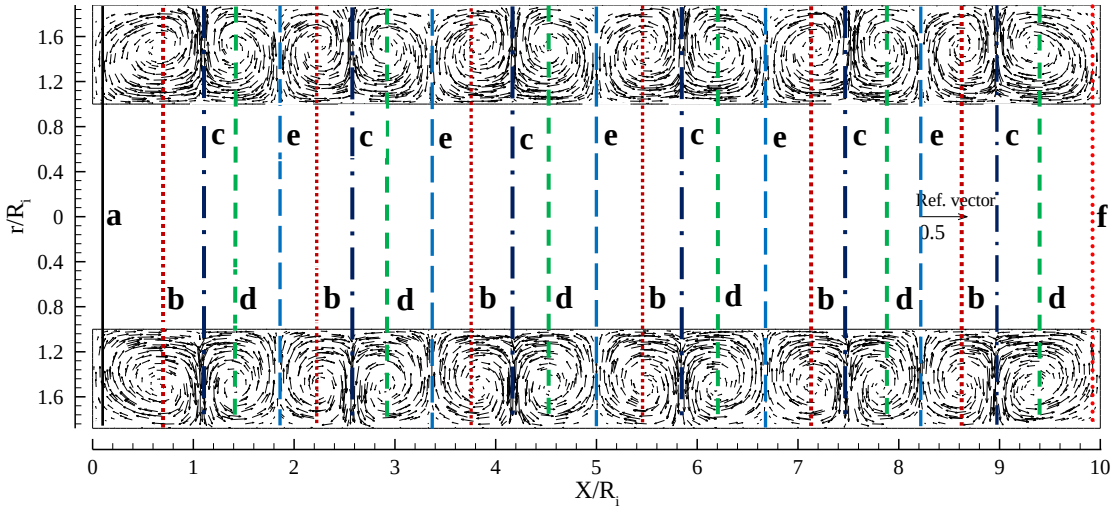

(a)

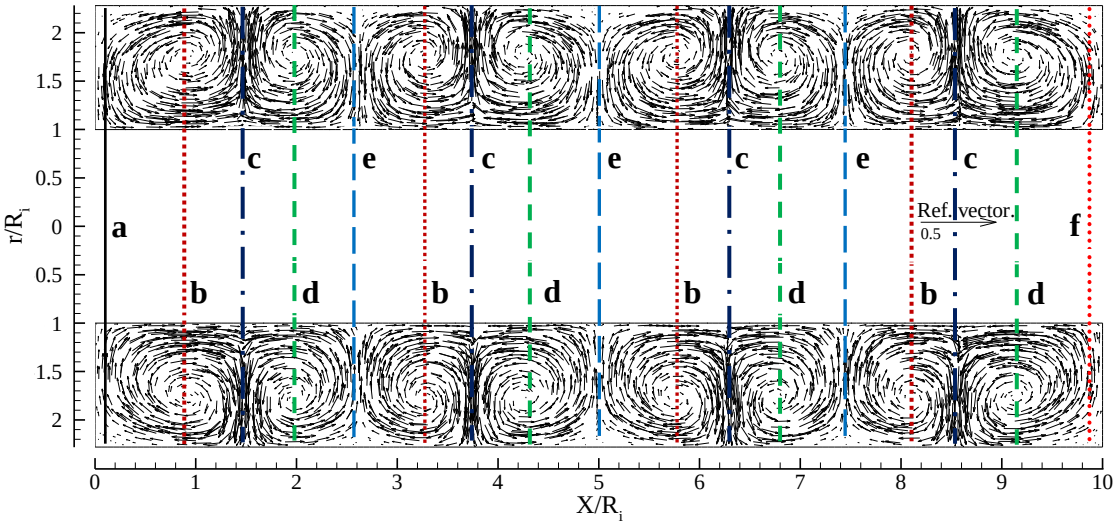

(b)

Figure 6.21: Axial locations of flow cross-sections on azimuthal planes for test cases (a) Γ = 11.36 and (b) Γ = 7.81.

The velocity vectors in Figure 6.22 and Figure 6.23 are normalised by the surface speed of the inner cylinder ΩR_i. The reference vector is shown on each velocity map so that the magnitude of the vectors can be quantified. The direction of the vectors indicates a flow driven by the clockwise rotation of the inner cylinder. These figures show that the velocity vectors near the inner cylinder display a higher tangential velocity magnitude than the vectors near the outer cylinder, consistent with Figure 6.18. The velocity at the wall of the outer stationary cylinder tends to zero, primarily to satisfy the no-slip condition imposed on the wall of the outer cylinder. These velocity vector maps indicate that the tangential velocity is the dominant velocity component, as the radial velocity is relatively weak.

Figure 6.22(a) and Figure 6.22(f) for the test case $\Gamma = 11.36$, as well as Figure 6.23(a) and Figure 6.23(f) for the test case $\Gamma = 7.81$, show the normalised velocity vector maps near the end-walls at $X/R_i = 0.05$ and $X/R_i = 9.95$ respectively. These locations correspond to the positions of radial velocity minima in Figure 6.16(a) for the test case $\Gamma = 11.36$ and in Figure 6.16(b) for the test case $\Gamma = 7.81$ at these axial locations. It is observed that the magnitudes of the velocity vectors at these locations are relatively small compared with other locations in the central region of the computational domain. This is primarily due to the no-slip boundary conditions that are imposed at the end-wall, in addition to the effects of wall shear stresses and frictional forces at these locations.

Figure 6.22(b) and Figure 6.22(d) show normalised velocity vectors at $X/R_i = 0.65$ and $X/R_i = 1.41$ for test case $\Gamma = 11.36$, while Figure 6.23(b) and Figure 6.23(d) show the normalised velocity vectors at $X/R_i = 0.92$ and $X/R_i = 1.97$ for test case $\Gamma = 7.81$. These locations correspond to the centres of a clockwise vortex and of an anti-clockwise vortex respectively in Figure 6.6(a) and Figure 6.6(b). The flow pattern in the azimuthal plane of Figure 6.22(b) and Figure 6.22(d) for the test case $\Gamma = 11.36$ are similar to each other in terms of the velocity vector magnitude, although in the meridional plane of Figure 6.21(a), the axial velocity components are opposite to one another. The velocity vectors in Figure 6.23(b) and Figure 6.23(d) for the test case $\Gamma = 7.81$ show the same trends in velocity magnitude as for test case $\Gamma = 11.36$. The axial locations $X/R_i = 0.65$ and $X/R_i = 1.41$ for the test case $\Gamma = 11.36$ and $X/R_i = 0.92$ and $X/R_i = 1.97$ for the test case $\Gamma = 7.81$ correspond to axial locations of almost zero radial velocity in Figure 6.16(a) and Figure 6.16(b). The axial locations of Figure 6.22(b) and Figure 6.22(d) correspond to axial velocity maxima and minima in the axial velocity profile of Figure 6.15(a) for the test case $\Gamma = 11.36$. Similarly, the axial locations of Figure 6.23(b) and Figure 6.23(d) correspond

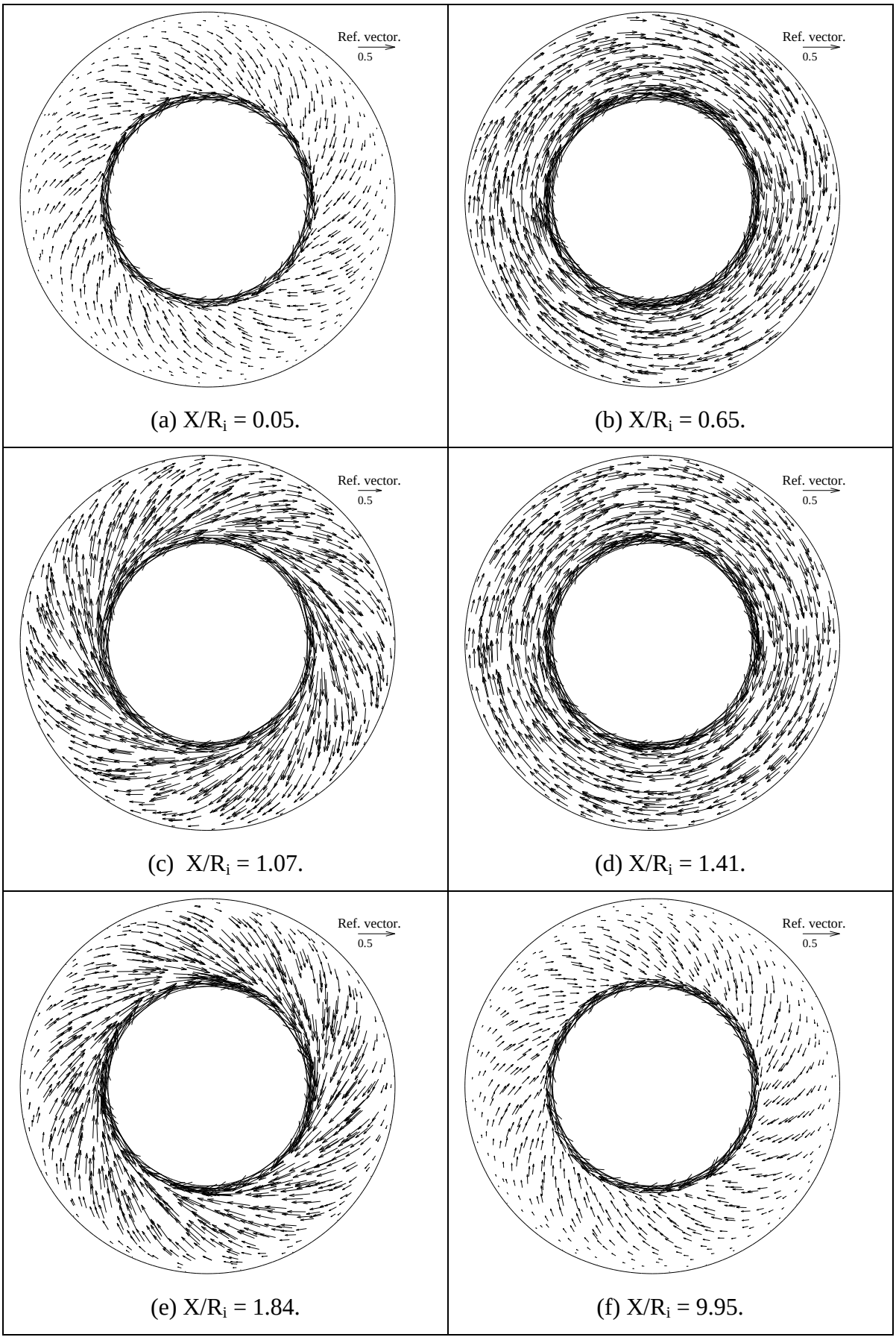

(a) $X/R_i = 0.05$. (b) $X/R_i = 0.65$.

(c) $X/R_i = 1.07$. (d) $X/R_i = 1.41$.

(e) $X/R_i = 1.84$. (f) $X/R_i = 9.95$.

Figure 6.22: Velocity vectors in the azimuthal plane normalised by ΩR_i for $\Gamma = 11.36$.

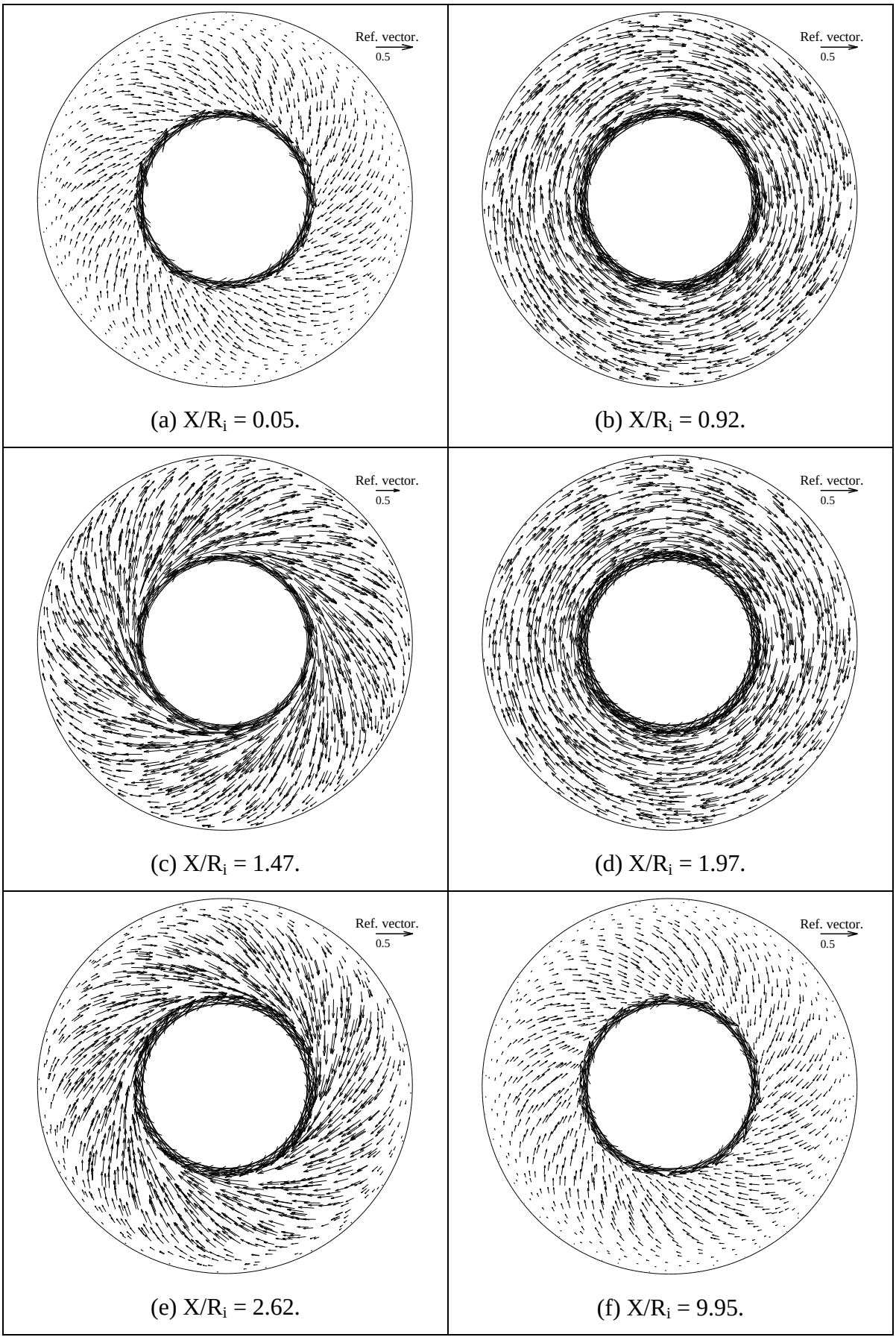

(a) $X/R_i = 0.05$. (b) $X/R_i = 0.92$.

(c) $X/R_i = 1.47$. (d) $X/R_i = 1.97$.

(e) $X/R_i = 2.62$. (f) $X/R_i = 9.95$.

Figure 6.23: Velocity vectors in the azimuthal plane normalised by ΩR_i for $\Gamma = 7.81$.

to axial velocity maxima and minima in the axial velocity profile of Figure 6.15(b) for the test case $\Gamma = 7.81$.

Figure 6.22(c) and Figure 6.23(c) show the normalised velocity vectors at $X/R_i = 1.07$ for the test case $\Gamma = 11.36$ and at $X/R_i = 1.47$ for the test case $\Gamma = 7.81$. The axial location $X/R_i = 1.07$ corresponds to the outward flow region in Figure 6.6(a) at the same axial location, while the axial location $X/R_i = 1.47$ corresponds to the outward flow region in Figure 6.6(b) at the same axial location. The flow pattern at these locations shows that the magnitude of the velocity vectors is higher compared with the magnitude of the velocity vectors at the other five locations in Figure 6.22 and Figure 6.23. These positions are where high radial momentum fluid is being carried outwardly by the Taylor vortices toward the stationary outer cylinder. These positions correspond to zero axial velocity in Figure 6.14(a) and Figure 6.14(b) and of radial velocity maxima in Figure 6.16(a) and Figure 6.16(b) at these axial locations.

Figure 6.22(e) and Figure 6.23(e) show the normalised velocity vectors at $X/R_i = 1.84$ for the test case $\Gamma = 11.36$ and at $X/R_i = 2.62$ for the test case $\Gamma = 7.81$. These locations correspond to inflow regions in Figure 6.6(a) and Figure 6.6(b) for the test cases $\Gamma = 11.36$ and $\Gamma = 7.81$ respectively at these axial locations. The magnitude of the velocity vectors at these locations is lower compared with the magnitude of the velocity vectors at $X/R_i = 1.07$ for the test case $\Gamma = 11.36$ and at $X/R_i = 1.47$ for the test case $\Gamma = 7.81$. At these locations, low tangential momentum fluid is being carried inwardly by the radial velocity induced by the Taylor vortices from the stationary outer cylinder toward the rotating inner cylinder. These positions correspond to the positions of radial velocity minimum in Figure 6.16(a) and Figure 6.16(b), and of zero axial velocity in Figure 6.14(a) and Figure 6.14(b) at these axial locations.

6.7.6 Parametric study of flow pattern in the azimuthal plane

The objective of this parametric study is to examine quantitatively various flow variables at the axial locations shown in Figure 6.21(a) and Figure 6.21(b) for the test cases $\Gamma = 11.36$ and $\Gamma = 7.81$ respectively. Figure 6.22 and Figure 6.23 show that the flow patterns exhibit similar trends on selected azimuthal planes for the test cases $\Gamma = 11.36$ and $\Gamma = 7.81$ respectively, since the inner cylinder rotates with the same angular velocity in the same direction in both test cases.

Figure 6.24 shows the contour plots of axial velocity in the azimuthal plane normalised by ΩR_i for the test case $\Gamma = 11.36$. The flow variables are examined at axial positions a, b, c, d, e, and f as defined in Figure 6.21(a). The contour plots of Figure 6.24 show that the axial velocity distribution is essentially axisymmetric.

Figure 6.24(a) and Figure 6.24(f) show respectively the normalised axial velocity contour plots near the end-walls at $X/R_i = 0.05$ and $X/R_i = 9.95$ in Figure 6.21(a). The magnitude of the axial velocity at these locations is relatively small, in agreement with the observed flow pattern of Figure 6.22. The axial velocity magnitude is of the order $0.01\Omega R_i$. The no-slip boundary conditions that are imposed at the end-walls constrain the fluid movement thereby retarding the fluid motion. The effects of wall shear stress and friction as a result of the end-walls also contribute to the low velocity observed at these locations.

Figure 6.24(b) and Figure 6.24(d) display the normalised contour plots of the axial velocity at $X/R_i = 0.65$ and $X/R_i = 1.41$, which correspond to the axial locations of the centres of the clockwise and anti-clockwise vortices respectively in Figure 6.6(a). The contours are colour coded such that the blue colour corresponds to the minimum axial velocity and the red colour corresponds to the maximum axial velocity. As observed for the meridional plane where the axial velocity distribution is axisymmetric, the distributions of the axial velocity within the annulus in the azimuthal plane in Figure 6.24(a) and Figure 6.24(b) are also essentially axisymmetric. Figure 6.24(b) also displays symmetry in the velocity magnitude about the gap mid span. In Figure 6.24(b), an axial velocity maximum of $0.15\Omega R_i$ is observed near the wall of the inner cylinder, while an axial velocity minimum of almost equal magnitude is observed near the wall of the outer cylinder, with zero axial velocity almost mid-way across the annulus at $r = R_i + 0.5d$. The first Taylor vortex induces a positive axial velocity close to the rotating inner cylinder at $X/R_i = 0.65$ and a negative axial velocity close to the stationary outer cylinder. This gives the axial velocity local maximum of $0.15\Omega R_i$ at $r \rightarrow R_i$ and an axial velocity local minimum of $-0.15\Omega R_i$ at $r \rightarrow R_o$ shown in Figure 6.24(b).

In Figure 6.24(b), a positive axial velocity maximum at $r \rightarrow R_o$ highlights the axial mass transport of fluid across the outer portion of the Taylor vortex towards the inflow region at $X/R_i = 1.07$. The negative axial velocity minimum highlights the axial mass transport of fluid close to the outer cylinder towards the left end-wall in Figure 6.6(a).

As the cylinder radius increases from R_i to R_o, the azimuthal cross-sectional area in which the axial velocity is positive tends to be larger than the cross-sectional area in which the

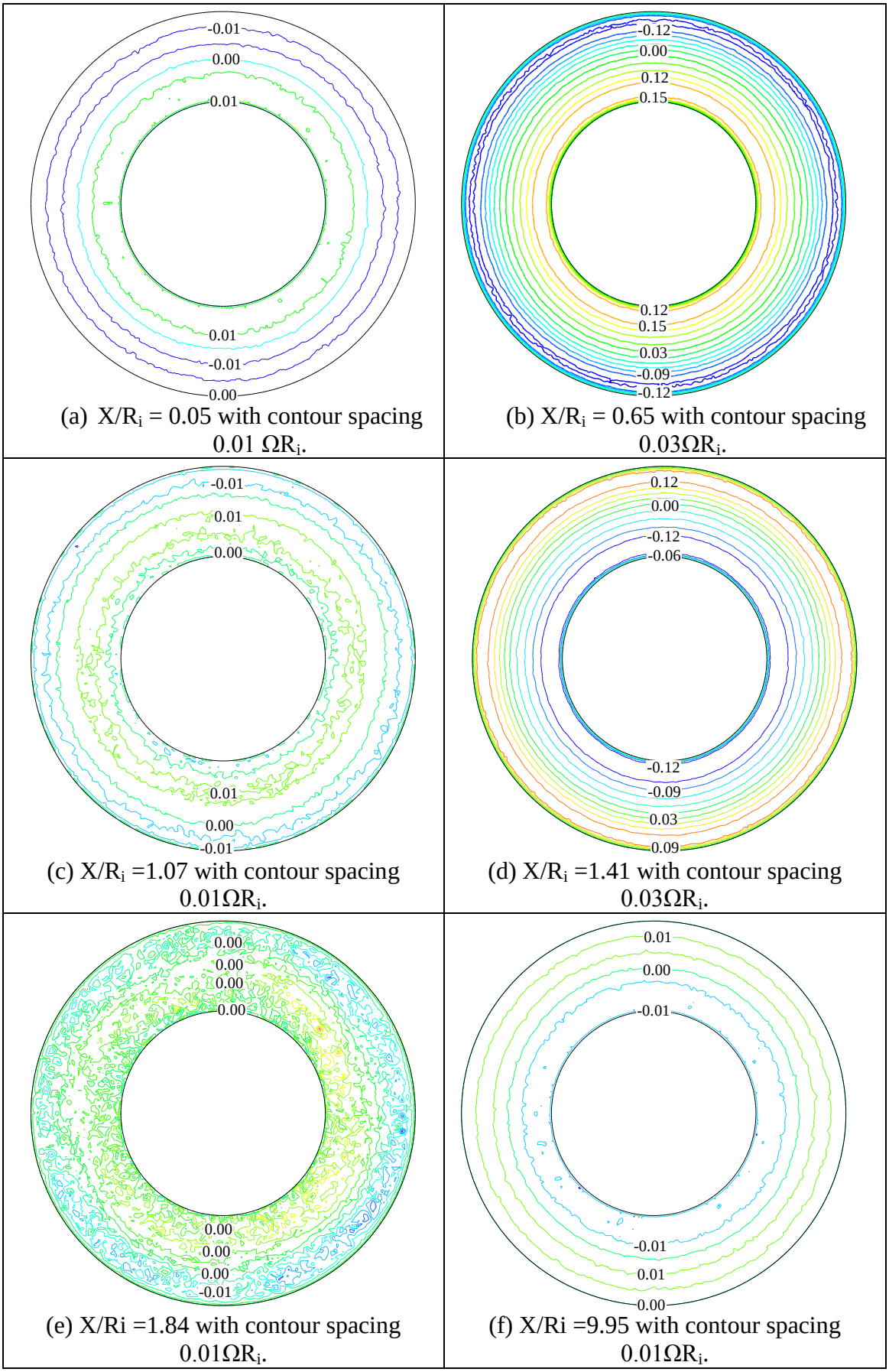

(a) X/R_i = 0.05 with contour spacing 0.01 ΩR_i.

(b) X/R_i = 0.65 with contour spacing 0.03ΩR_i.

(c) X/R_i =1.07 with contour spacing 0.01ΩR_i.

(d) X/R_i =1.41 with contour spacing 0.03ΩR_i.

(e) X/Ri =1.84 with contour spacing 0.01ΩR_i.

(f) X/Ri =9.95 with contour spacing 0.01ΩR_i.

Figure 6.24: Contour plots of axial velocity in the azimuthal plane normalised by ΩR_i for the test case Γ = 11.36.

axial velocity is negative so the net axial mass flow rate through the azimuthal plane is zero. This satisfies the conservation of mass in this enclosed system. As a result of this axial flow radial asymmetry, the centre of the vortex has been shifted toward the wall of the outer cylinder.

Figure 6.24(d) shows the opposite trend of Figure 6.24(b) with an axial velocity minimum near the wall of the inner cylinder and an axial velocity maximum near the wall of the outer cylinder. The change of sign is a result of the change in the direction of rotation of the second Taylor vortex in Figure 6.6(a) with respect to the first Taylor vortex. In the axial velocity profiles of Figure 6.15, the axial locations of Figure 6.24(b) and Figure 6.24(d) correspond to an axial velocity maximum and minimum respectively in the meridional plane.

Figure 6.24(c) shows the normalised contour plot of the axial velocity at $X/R_i = 1.07$, which corresponds to the radial outward flow region in Figure 6.6(a) at the same axial location. At this location, the axial velocity is essentially zero, as shown by the contour levels of axial velocity in the meridional plane in Figure 6.24(c). This is in agreement with the contours of axial velocity in the meridional plane at the same axial location in Figure 6.8(a). This position corresponds to the position of maximum radial velocity in Figure 6.16(a) and of a zero crossing of axial velocity in Figure 6.14(a) at the same axial location.

Figure 6.24(e) shows the normalised contour plot of the axial velocity at $X/R_i = 1.84$, which corresponds to the radial inflow region in Figure 6.6(a) at the same axial location. At this location, the axial velocity is also essentially zero as observed in Figure 6.24(c). This position corresponds to the position of minimum radial velocity in Figure 6.16(a) and of a zero crossing of axial velocity in Figure 6.14(a) at the same axial location.

Figure 6.25 shows the contour plots of tangential velocity in the azimuthal plane normalised by ΩR_i at the axial positions a, b, c, d, e, and f of Figure 6.21(a) for test case $\Gamma = 11.36$. These plots display a tangential velocity minimum close to the wall of the inner cylinder and the tangential velocity maximum close to the wall of the outer cylinder. The blue colour corresponds to the negative tangential velocity minimum and the red colour corresponds to the negative tangential velocity maximum. The magnitude of the tangential velocity minimum is higher than that of the tangential velocity maximum, as discussed in the context of Figure 6.10(a).

Figure 6.25(a) and Figure 6.25(f) show the contour plots near the end-walls at $X/R_i = 0.05$ and $X/R_i = 9.95$ respectively. At these locations, the tangential velocity has the same trends, with a negative tangential velocity local minimum near the wall of the inner

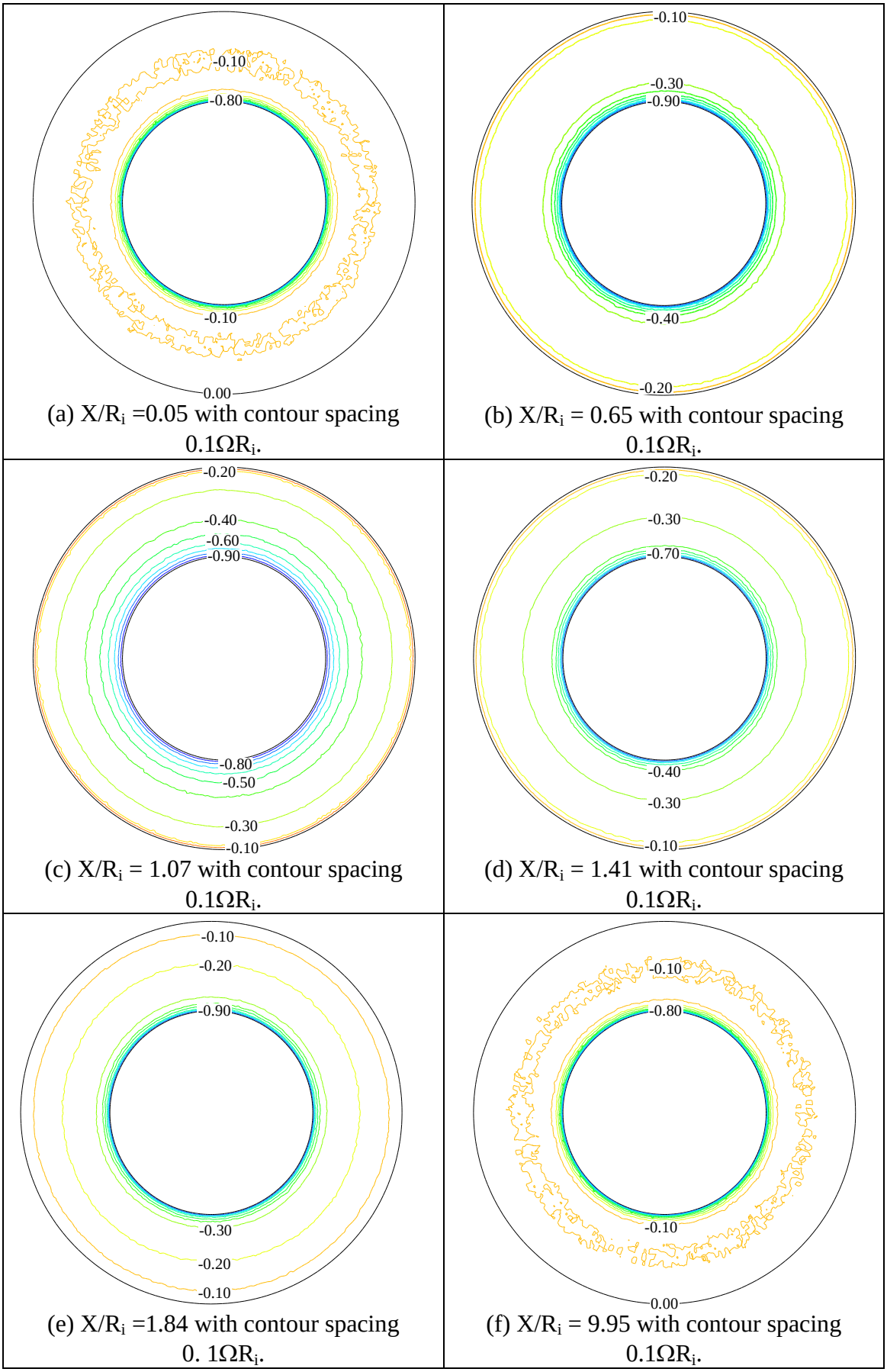

(a) X/R_i =0.05 with contour spacing $0.1\Omega R_i$.

(b) X/R_i = 0.65 with contour spacing $0.1\Omega R_i$.

(c) X/R_i = 1.07 with contour spacing $0.1\Omega R_i$.

(d) X/R_i = 1.41 with contour spacing $0.1\Omega R_i$.

(e) X/R_i =1.84 with contour spacing $0.\ 1\Omega R_i$.

(f) X/R_i = 9.95 with contour spacing $0.1\Omega R_i$.

Figure 6.25: Contour plots of tangential velocity in the azimuthal plane normalised by ΩR_i for the test case Γ = 11.36.

cylinder from where the motion of the fluid is been induced. The tangential velocity local minimum then rapidly increases toward the wall of the outer cylinder. That is, the tangential velocity magnitude decreases toward the wall of the outer cylinder. The zero velocity observed at the wall of the outer cylinder is due to the no-slip boundary condition that is imposed at $r = R_o$.

Figure 6.25(b) and Figure 6.25(d) show the contour plots of normalised tangential velocity at $X/R_i = 0.65$ and $X/R_i = 1.41$, which correspond to the centre of the clockwise and anti-clockwise vortices respectively in Figure 6.6(a) at the same axial locations. The negative tangential velocity local minimum is near the wall of the inner cylinder and the negative tangential velocity local maximum is near the wall of the outer cylinder, in agreement with Figure 6.10. The tangential velocity magnitude in both Figure 6.25(b) and Figure 6.25(d) decreases monotonically toward the wall of the outer cylinder, the decrement of tangential velocity magnitude in Figure 6.25(d) is however more rapid than the one observed in Figure 6.25(b). This is shown by the difference in contour line packing between Figure 6.25(b) and Figure 6.25(d).

Figure 6.25(c) and Figure 6.25(e) show the contour plots of the normalised tangential velocity at $X/R_i = 1.07$ and $X/R_i = 1.84$ which, respectively, correspond to the radial outward flow region and radial inward flow region in Figure 6.6(a) at the same axial locations. The decrease of tangential velocity magnitude from the inner cylinder to the outer cylinder in Figure 6.25(c) is less rapid than the decrease observed in Figure 6.25(e), as shown by the packing of the contour lines of both plots.

The equivalent of the axial velocity and tangential velocity contour plots shown in Figure 6.24 and Figure 6.25 were produced for the test case with aspect ratio 7.81. The flow pattern is substantially similar to that of the test case with aspect ratio 11.36. The contour plots for the axial velocity and the tangential velocity for the test case $\Gamma = 7.81$ are therefore not repeated in this thesis. However, the velocity and the pressure profiles for the test cases $\Gamma = 11.36$ and $\Gamma = 7.81$ in the azimuthal plane are presented and discussed in section 6.7.7.

6.7.7 Velocity profiles in the azimuthal plane

Radial profiles of flow variables at the various cross-sections of Figure 6.21(a) and Figure 6.21(b) for the test cases $\Gamma = 11.36$ and $\Gamma = 7.81$ were extracted at the azimuthal location AA illustrated in Figure 6.26.

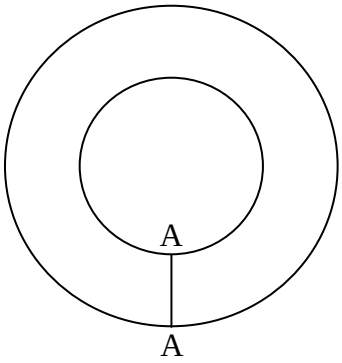

Figure 6.26: Azimuthal locations of radial profiles.

The profiles in the azimuthal plane are axisymmetric, as shown by the contour maps of Figure 6.24 and Figure 6.25. As such, the profiles at the different azimuthal positions around the annulus coincide. The profile at a single azimuthal location extracted from the azimuthal plane at the same axial locations as in Figure 6.25 is therefore presented for selected flow variables. These profiles enable to assess the radial dependence of the flow variables more readily than the meridional and cascade plane plots. The profiles, therefore, provide detailed information about the radial velocity distributions, clarifying further the trends shown by the velocity vectors in Figure 6.22 and Figure 6.23. The velocities are normalised by the inner cylinder surface velocity ΩR_i, while pressure is normalised by $0.5\rho R_i^2\Omega^2$. The abscissa in Figure 6.27(a-f) to Figure 6.33(a-f) is the radial distance from the inner cylinder surface to the outer cylinder surface, normalised by the gap width, d. It is related to the cylindrical coordinates system of Figure 6.1 by $(r - R_i)/d$.

The axial velocity profiles shown in Figure 6.27(a-f) and Figure 6.28(a-f) detail the radial distribution of axial velocity at axial positions labelled as a, b, c, d, e, and f in Figure 6.21(a) and Figure 6.21(b) for the test cases $\Gamma = 11.36$ and $\Gamma = 7.81$ respecetively with the same letter designating a recurring flow region along the axis of the cylinders. The profiles extracted from the recurring azimuthal plane flow regions along the axial span of Figure 6.21(a) and Figure 6.21(b) for the test cases $\Gamma = 11.36$ and $\Gamma = 7.81$ respectively are therefore grouped together. The radial profiles of the normalised axial velocity in Figure 6.27(a-f) and Figure 6.28(a-f), show different patterns, depending on the axial locations. These profiles show that test cases $\Gamma = 11.36$ and $\Gamma = 7.81$ exhibit similar trends. In Figure 6.27(a, c, e, and f) and Figure 6.28(a, c, e, and f), the profiles show that the axial velocity is relatively small when compared with the velocity of the rotating inner cylinder.

For the test case $\Gamma = 11.36$, the normalised axial velocity profile in Figure 6.27(a) shows an axial velocity maximum close to the wall of rotating inner cylinder. The axial velocity

then rapidly decreases from the inner cylinder wall to $(r - R_i)/d \approx 0.03$ and stabilises over the range $0.1 \leq (r - R_i)/d \leq 0.18$ from where it increases again over the range $0.18 \leq (r - R_i)/d \leq 0.24$.

For the test case $\Gamma = 7.81$, the normalised axial velocity profile in Figure 6.28(a) exhibits a similar trend as in Figure 6.27(a) with an axial velocity maximum close to the wall of rotating inner cylinder. The axial velocity rapidly decreases over the distance $0 \leq (r - R_i)/d \leq 0.08$ and plateaus between at $0.08 \leq (r - R_i)/d \leq 0.18$ from where it increases over the range $0.18 \leq (r - R_i)/d \leq 0.24$.

At approximately $(r - R_i)/d = 0.24$, the axial velocity profiles in Figure 6.27(a) and in Figure 6.28(a) start decreasing monotonically and become negative in the central region of the annulus, from where the velocity decreases to minimum close to the outer stationary cylinder at $(r - R_i)/d \approx 0.74$. The profiles thereafter increase monotonically again until the axial velocity reaches zero at the wall of the stationary outer cylinder, due to the application of the non-slip boundary conditions at the cylindrical walls in the numerical model.

Figure 6.27(f) and Figure 6.28(f) display similar axial velocity trends as in Figure 6.27(a) and Figure 6.28(a) but the velocity variations have opposite sign, due to the anti-clockwise inward flow of the Taylor vortices at these locations. The observed axial velocity common trends over the range $0.1 \leq (r - R_i)/d \leq 0.24$ in Figure 6.27(a) and Figure 6.27(f) as well as in Figure 6.28(a) and Figure 6.28(f) is attributed to the effect of the end-walls that affect the boundary layer at these locations.

Figure 6.27(b) and Figure 6.27(d) show the axial velocity profiles for the test case $\Gamma = 11.36$. The profiles show that the maximum axial velocity ($\pm 0.16\Omega R_i$) in the coaxial cylinders occurs at the azimuthal planes through the centres of the Taylor vortices. The two plots through the centres of clockwise vortices and the centres of anti-clockwise vortices show similar axial velocity trends but a change in sign mirrored about the $u_r = 0$ line. This symmetry is in agreement with the direction of rotation of the adjacent vortices, as observed in Figure 6.6(a).

The normalised axial velocity profiles for the test case $\Gamma = 7.81$ in Figure 6.28(b) and Figure 6.28(d) are the plots through the centres of clockwise vortices and the centres of anti-clockwise vortices in Figure 6.21(b). The axial velocity exhibits similar trends as for the test case $\Gamma = 11.36$ discussed in the context of Figure 6.27(b) and Figure 6.27(d).

The profiles through the centres of clockwise vortices in Figure 6.27(b) and Figure 6.28(b) show that the axial velocity maximum occurs close to the wall of the rotating inner cylinder at $(r - R_i)/d \approx 0.1$ for both test cases. The axial velocity then decreases monotonically to zero near the central region of the annulus at $(r - R_i)/d \approx 0.58$ for the test case $\Gamma = 11.36$, and at $(r - R_i)/d \approx 0.60$ for the test case $\Gamma = 7.81$.

The profiles in Figure 6.27(b) and Figure 6.28(b) show an axial velocity minimum close to the wall of the outer cylinder, at $(r - R_i)/d \approx 0.90$, from which the axial velocity increases to zero at the wall of the outer cylinder. This observed trend is due to the fluid motion induced by the neighbouring Taylor vortices. The fact that the zero crossing of the plots does not lie at radial position $(r - R_i)/d = 0.50$ is an indication that the centre of the Taylor vortices are shifted from the centre of the annulus toward the wall of the outer cylinder as discussed in the context of Figure 6.6.

Consequently, the area of positive axial velocity is greater than the area of negative axial velocity in Figure 6.27(b) and Figure 6.28(b). This difference satisfies mass conservation across the azimuthal planes given the difference in flow area for the positive inner axial flow and the negative outer axial flow observed in Figure 6.24.

In the profiles through the centres of anti-clockwise vortices presented in Figure 6.27(d) and Figure 6.28(d), the axial velocity minimum occurs close to the wall of rotating inner cylinder at $(r - R_i)/d \approx 0.1$ for the test case $\Gamma = 11.36$ and $\Gamma = 7.81$. The axial velocity profiles then increase to zero near the central region of the annulus at $(r - R_i)/d \approx 0.58$ for the test case $\Gamma = 11.36$, and at $(r - R_i)/d \approx 0.60$ for the test case $\Gamma = 7.81$. The velocity further increases and reached an axial velocity maximum close to the outer stationary cylinder wall at $(r - R_i)/d \approx 0.90$ in Figure 6.27(d) and Figure 6.28(d). Similar to the observation made in Figure 6.27(b) and Figure 6.28(b), the zero crossing of the profile does not lie at radial position $(r - R_i)/d = 0.50$, due to the vortex centre being located toward the wall of the outer cylinder. The area of negative axial velocity near the inner cylinder is greater than the area of positive axial velocity near the outer cylinder. This difference is also to satisfy mass conservation on the azimuthal planes as the axial mass flux through the negative axial velocity area balances the axial mass flux through the positive axial velocity area in Figure 6.24.

The axial velocity profiles in Figure 6.27(b) and Figure 6.27(d) for the test case $\Gamma = 11.36$ as well as in Figure 6.28(b) and Figure 6.28(d) for the test case $\Gamma = 7.81$ show that the clockwise and the anti-clockwise vortices are almost symmetric about the line

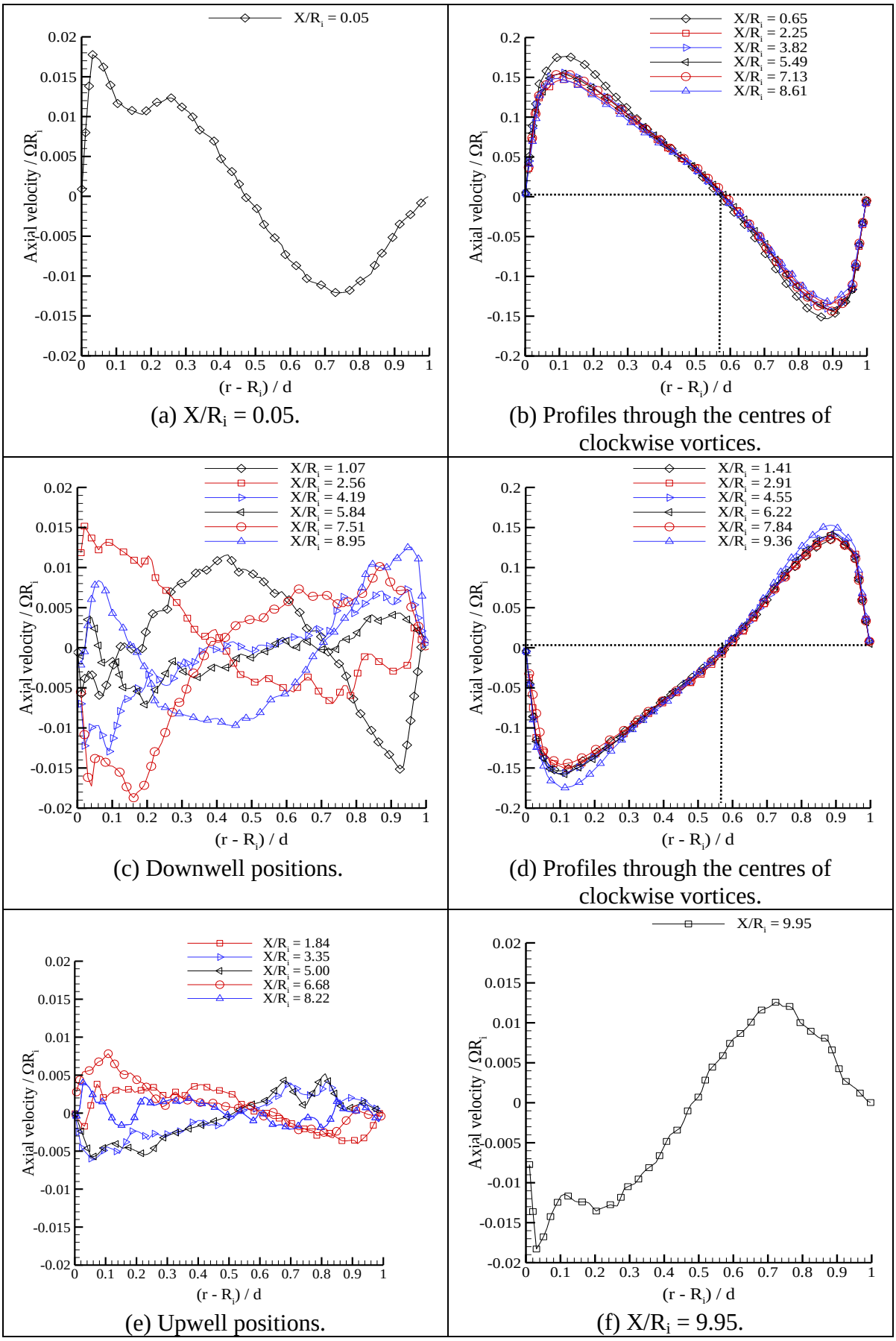

(a) $X/R_i = 0.05$.

(b) Profiles through the centres of clockwise vortices.

(c) Downwell positions.

(d) Profiles through the centres of clockwise vortices.

(e) Upwell positions.

(f) $X/R_i = 9.95$.

Figure 6.27: Normalised axial velocity profiles in the azimuthal plane at $\theta = -\pi/2$ for the test case $\Gamma = 11.36$.

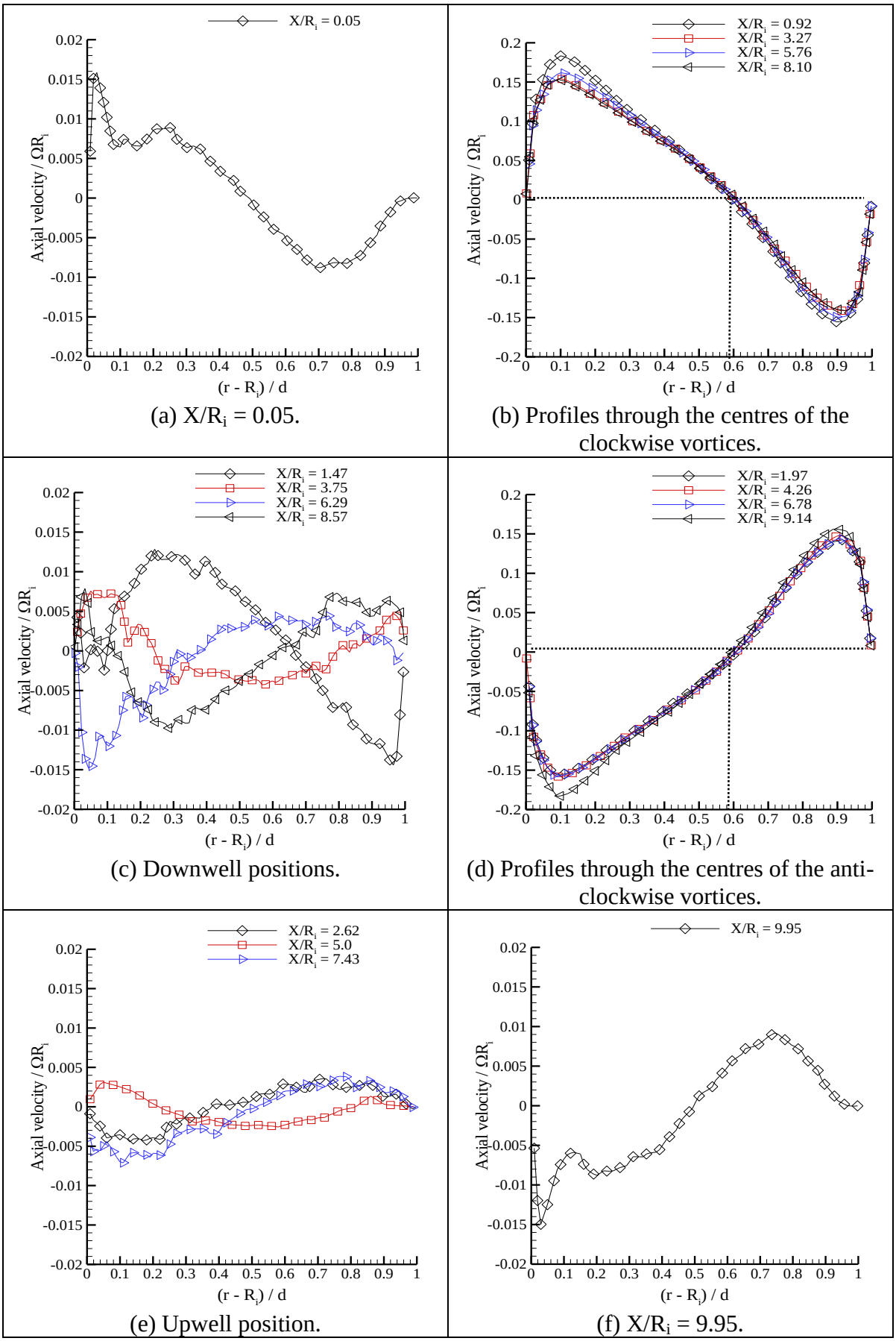

(a) $X/R_i = 0.05$.

(b) Profiles through the centres of the clockwise vortices.

(c) Downwell positions.

(d) Profiles through the centres of the anti-clockwise vortices.

(e) Upwell position.

(f) $X/R_i = 9.95$.

Figure 6.28: Normalised axial velocity profiles in the azimuthal plane at $\theta = -\pi/2$ for the test case $\Gamma = 7.81$.

corresponding to zero axial velocity. The only exception is for the profiles near the end-walls at $X/R_i \approx 0.65$ and $X/R_i \approx 9.36$ for the test case $\Gamma = 11.36$, and at $X/R_i \approx 0.92$ and $X/R_i \approx 9.14$ for the test case $\Gamma = 7.81$. At these axial locations, the profiles show a higher axial velocity maximum and a lower axial velocity minimum, compared to the axial velocity distribution in the central region. This is due to the effect of the end-walls that elongate the first and the second vortices more than the vortices at the central region. The normalised axial velocity is lowest and equal to zero at the wall of the rotating inner cylinder and at the wall of the stationary outer cylinder, due to the no-slip condition. The trends observed in Figure 6.27(b) and Figure 6.27(d) for the test case $\Gamma = 11.36$ as well as in Figure 6.28(b) and Figure 6.28(d) for the test case $\Gamma = 7.81$ is in agreement with the axial velocity profiles predicted by CFD by Deshmukh et al. (2007).

Figure 6.27(c) and Figure 6.27(e) show the axial velocity profiles in the outflow regions and in the inflow regions respectively for the test case $\Gamma = 11.36$. The profiles in Figure 6.27(c) show greater variations in the axial velocity than the profiles in Figure 6.27(e). This variation has to be considered in the context of the ordinate scale of Figure 6.27(c) and Figure 6.27(e) being ten times that of Figure 6.27(b). This makes these variations in axial velocity comparatively small. The small variation in the axial velocity observed is due to the axial locations of these profiles being that of saddle planes between two adjacent Taylor vortices.

Similarly, Figure 6.28(c) and Figure 6.28(e) show the axial velocity profiles in an outflow region and in an inflow region respectively for the test case $\Gamma = 7.81$. These profiles exhibit similar trends as for test case $\Gamma = 11.36$ discussed in the context of Figure 6.27(c) and Figure 6.27(e).

The differences in the vortex centre positions, which are reported later on in Figure 6.36, turns the saddle plane between two consecutive vortices into a curved surface, which allows a non-zero axial velocity distribution in the radial direction.

Figure 6.29(a-f) and Figure 6.30(a-f) show the radial profiles of tangential velocity in the azimuthal plane at the axial locations shown in Figure 6.21(a) and Figure 6.21(b) for the test cases $\Gamma = 11.36$ and $\Gamma = 7.81$ respectively. The predicted flow tangential velocity, normalised by the inner cylinder tangential rotational speed ΩR_i, is here plotted as clockwise negative, to be consistent with the right handed reference system of Figure 6.1. Figure 6.29 and Figure 6.30 use the same lettering (a-f) of Figure 6.21 to identify the predicted normalised tangential velocity profiles in the azimuthal plane at the same axial

locations. In Figure 6.29(a-f) and Figure 6.30(a-f), a more boundary layer-like velocity profile is obtained near the wall of the cylinders. The profiles show that the tangential velocity is the dominant component of the in-plane velocity, which has a maximum magnitude at the inner rotating wall and zero magnitude at the outer stationary wall. This confirms the dominance of the clockwise motion shown by the velocity vector maps of Figure 6.22 and Figure 6.23.

Despite the trends in the radial distribution of the tangential velocity being similar at the azimuthal planes (b-e) of Figure 6.29 and Figure 6.30 in both test cases, there are still some differences among the profiles due to the variation in flow characteristics at these axial locations.

The profiles near the end-walls shown in Figure 6.29(a) and Figure 6.29(f) for the test case $\Gamma = 11.36$ show three regions where the profiles change, one near the wall of the inner cylinder, the second at the central region of the cylinder, and the last near the wall of the outer cylinder. The tangential velocity magnitude near the wall of the inner cylinder decreases rapidly up to the radial position $(r - R_i)/d \approx 0.12$ which corresponds to a negative tangential velocity of $-0.06\Omega R_i$ and then stabilises in the central region over the range $0.12 \leq (r - R_i)/d \leq 0.60$. The tangential velocity magnitude then further decreases over the range $0.60 \leq (r - R_i)/d \leq 1.0$. For the test case $\Gamma = 7.81$, the normalised tangential velocity profiles near the end-walls shown in Figure 6.30(a) and Figure 6.30(f) exhibit similar trends as for the test case $\Gamma = 11.36$ shown in Figure 6.29(a) and Figure 6.29(f).

The profiles through the centres of the clockwise and the centres of the anti-clockwise vortices shown in Figure 6.29(b) and Figure 6.29(d) respectively for the test case $\Gamma = 11.36$, as well as in Figure 6.30(b) and Figure 6.30(d) for the test case $\Gamma = 7.81$, show the same trend. The profiles show three distinctive regions where the profiles change. The tangential velocity magnitude near the wall of the inner cylinder decreases rapidly up to the radial position $(r - R_i)/d \approx 0.2$, which corresponds to a negative tangential velocity of $-0.3\Omega R_i$. The tangential velocity magnitude then stabilises in the central region, over the range $0.2 \leq (r - R_i)/d \leq 0.90$, and then decreases rapidly over the region $0.90 \leq (r - R_i)/d \leq 1.0$ where it reaches zero at the wall of the outer cylinder as a result of the no-slip boundary condition.

In the outflow regions in Figure 6.29(c) for the test case $\Gamma = 11.36$, the normalised tangential velocity magnitude decreases less rapidly than in Figure 6.29(b) near the wall of the inner cylinder and through the centre of the annulus. The profiles then increase more

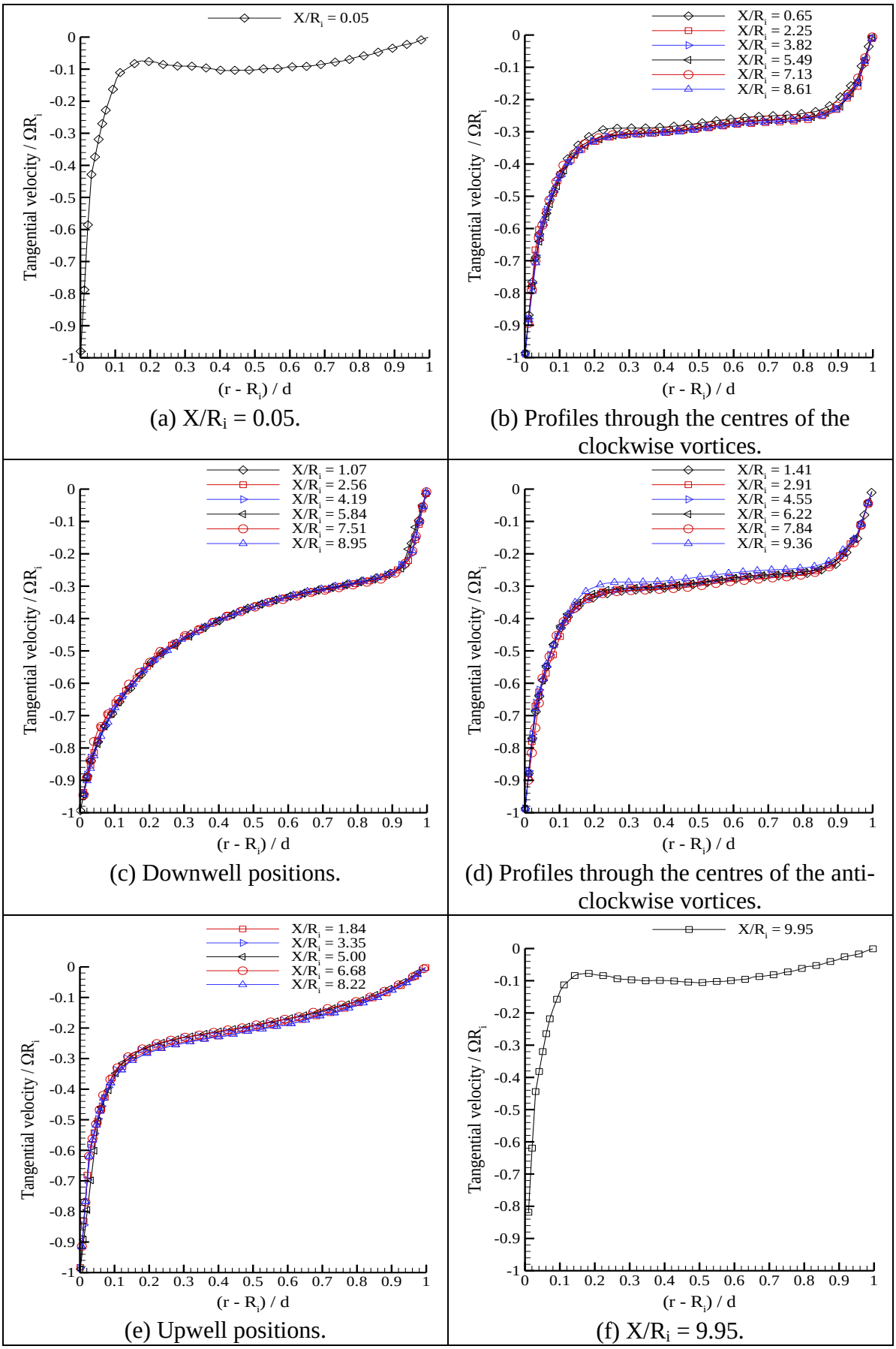

Figure 6.29: Normalised tangential velocity profiles in the azimuthal plane at $\theta = -\pi/2$ for the test case $\Gamma = 11.36$.

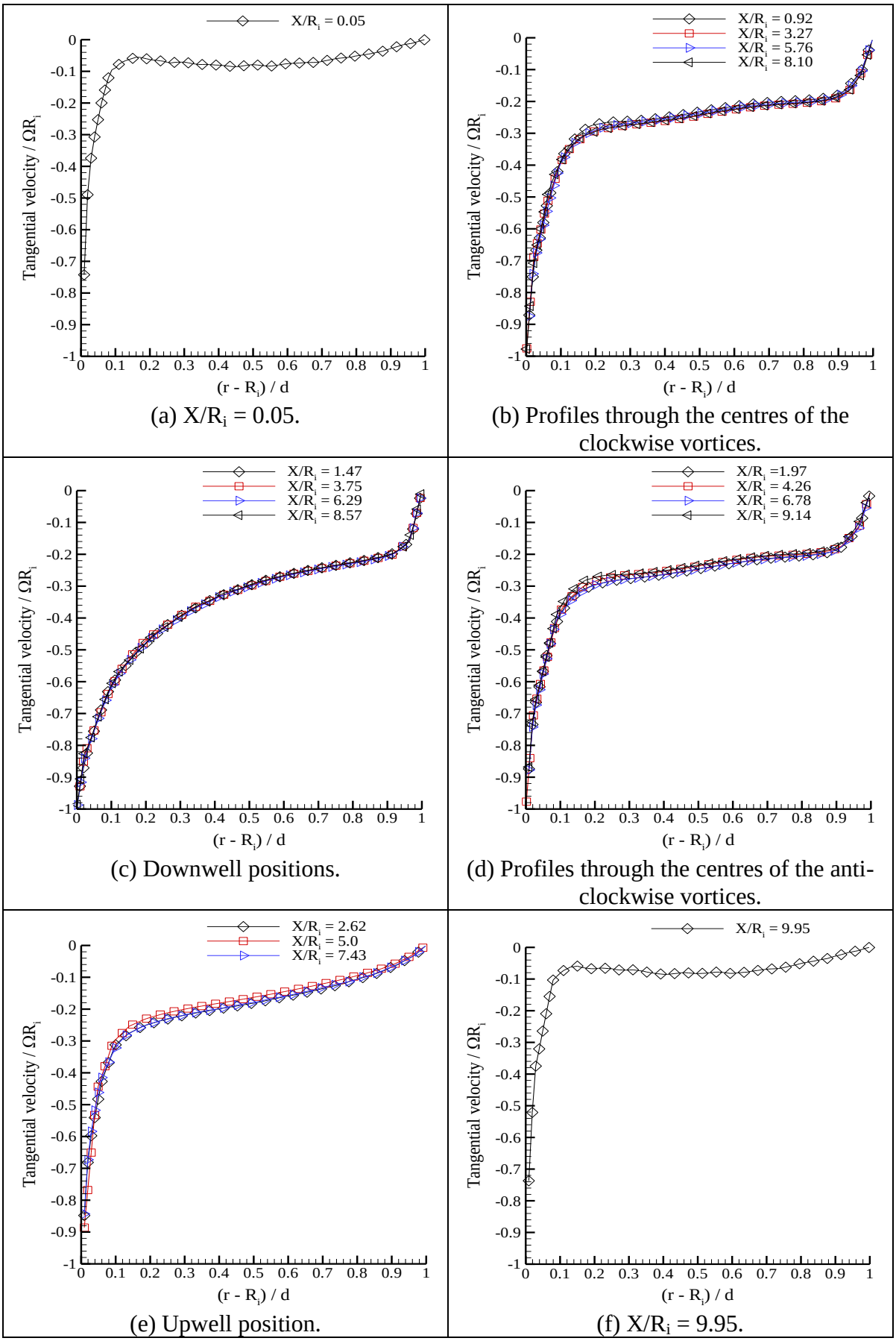

Figure 6.30: Normalised tangential velocity profiles in the azimuthal plane at $\theta = -\pi/2$ for the test case $\Gamma = 7.81$.

rapidly near the wall of the outer cylinder. The region with the lower tangential velocity magnitude decay rate is $0 \leq (r - R_i)/d \leq 0.92$, which corresponds to the tangential velocity range $-1.0\Omega R_i \leq u_\theta \leq -0.24\Omega R_i$. The region with rapid decay rate is $0.92 \leq (r - R_i)/d \leq 1.0$, which corresponds to the tangential velocity range $-0.24\Omega R_i \leq u_\theta \leq 0$. The normalised tangential velocity magnitude in Figure 6.30(c) for the test case $\Gamma = 7.81$ also decreases less rapidly than in Figure 6.30(b) and exhibits a similar trend as in Figure 6.29(c).

At the inflow regions in Figure 6.29(e) for the test case $\Gamma = 11.36$ and Figure 6.30(e) for the test case $\Gamma = 7.81$, the tangential velocity magnitude decreases monotonically in two regions. The first region is near the inner cylinder at $0 \leq (r - R_i/d) \leq 0.18$, which corresponds to the tangential velocity range $-1.0\Omega R_i \leq u_\theta \leq -0.24\Omega R_i$. The second region is in the region $0.18 \leq (r - R_i)/d \leq 1.0$, which corresponds to the tangential velocity range $-0.24\Omega R_i \leq u_\theta \leq 0$.

From the radial profiles of the in-plane normalised tangential velocity in Figure 6.29 and Figure 6.30 for the test cases $\Gamma = 11.36$ and $\Gamma = 7.81$ respectively, the tangential velocity magnitude rapidly decays from the inner rotating cylinder at all axial locations, the decay rate being more modest in the outflow region.

The normalised tangential velocity profiles in Figure 6.29 for the test case $\Gamma = 11.36$ and in Figure 6.30 for the test case $\Gamma = 7.81$ are in good qualitative agreement with a previous study by Deshmukh et al. (2007). The only difference is a change in the sign of the tangential velocity between the two studies, which is due to the clockwise rotation of the inner cylinder with respect to the cylindrical reference system in Figure 6.1.

Figure 6.31(a-f) and Figure 6.32(a-f) show respectively the radial distribution of gauge static pressure for the test cases $\Gamma = 11.36$ and $\Gamma = 7.81$ at the same axial positions as in Figure 6.29 and Figure 6.30. These radial profiles of the in-plane gauge static pressure show that the normalised gauge static pressure close to the surface of the rotating inner cylinder is minimum, while the normalised gauge static pressure close to the surface of the stationary outer cylinder is maximum. As the inner cylinder rotates, it imparts a tangential velocity to the fluid in the annulus. For the mass of the tangentially rotating fluid to be in a state of momentum equilibrium in the radial direction, the centrifugal forces must be balanced by the pressure forces. Therefore, the fluid between the rotating inner cylinder and stationary outer cylinder develops a radial pressure gradient. This opposes the centrifugal force, thereby restoring radial equilibrium in the force momentum balance. As such, the gauge static pressure at the outer stationary cylinder is greater than that at the

surface of the inner cylinder, with negative values of gauge static pressure at the wall of the inner cylinder.

The radial profiles of normalised gauge static pressure near the end-walls at $X/R_i = 0.05$ and $X/R_i = 9.95$ are shown in Figure 6.31(a) and Figure 6.31(f) for the test case $\Gamma = 11.36$, as well as in Figure 6.32(a) and Figure 6.32(f) for the test case $\Gamma = 7.81$. At these radial positions, three forces are acting on the fluid particles. These are the centrifugal forces, the pressure gradient forces, and the viscous forces. These forces affect differently the normalised gauge static pressure at these axial positions as compared with the other axial positions in the centre of the computational domain. The normalised gauge static pressure at the positions near the end-walls in Figure 6.31(a), Figure 6.31(f), Figure 6.32(a), and Figure 6.32(f) displays a lower radial gradient in the positive radial direction. This is due to the viscous forces in the boundary layer flow over the end-walls counter-balancing some of the centrifugal forces generated by the fluid rotary motion, which leads to a reduction in the radial pressure gradient required to obtain radial equilibrium in the force-momentum balance.

The radial profiles of normalised gauge static pressure in the azimuthal plane through the centre of the clockwise and the anti-clockwise Taylor vortices are shown in Figure 6.31(b) and Figure 6.31(d) respectively for the test case $\Gamma = 11.36$. The normalised gauge static pressure displays similar pressure minima of $0.05\rho R_i^2\Omega^2$ close to the rotating inner cylinder. The magnitude of the normalised gauge static pressure is lowest (minimum) close to the rotating inner cylinder. It then increases at increasing radial distance through the central region, from where the normalised gauge static pressure gradient further increases toward the stationary outer cylinder. The normalised gauge static pressure at these locations ranges from $-0.05\rho R_i^2\Omega^2$ to $0.03\rho R_i^2\Omega^2$. The normalised gauge static pressure through the centre of the clockwise and the anti-clockwise Taylor vortices for the test case $\Gamma = 7.81$ in Figure 6.32(b) and Figure 6.32(d) show similar trends as in Figure 6.31(b) and Figure 6.31(d) for the test case $\Gamma = 11.36$.

The radial profiles of normalised gauge static pressure in the outflow regions are shown in Figure 6.31(c) for the test case $\Gamma = 11.36$ and in Figure 6.32(c) for the test case $\Gamma = 7.81$. These profiles monotonically increase at increasing radial distance toward the stationary outer cylinder. The gauge static pressure gradient is highest close to the rotating inner cylinder. The gauge static pressure then plateaus in the middle of the annulus, from where

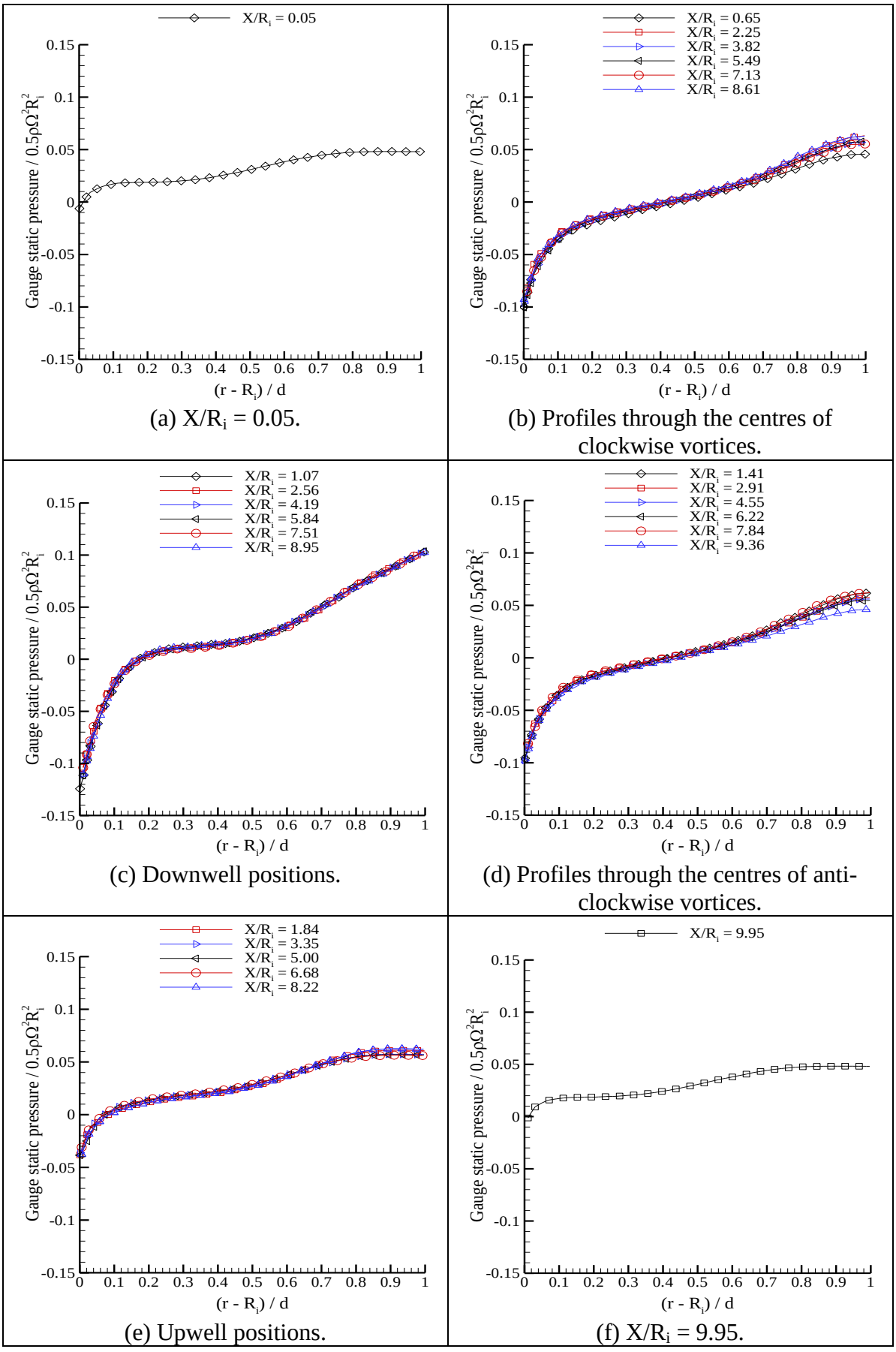

Figure 6.31: Normalised gauge static pressure profiles in the azimuthal plane at $\theta = -\pi/2$ for the test case $\Gamma = 11.36$.

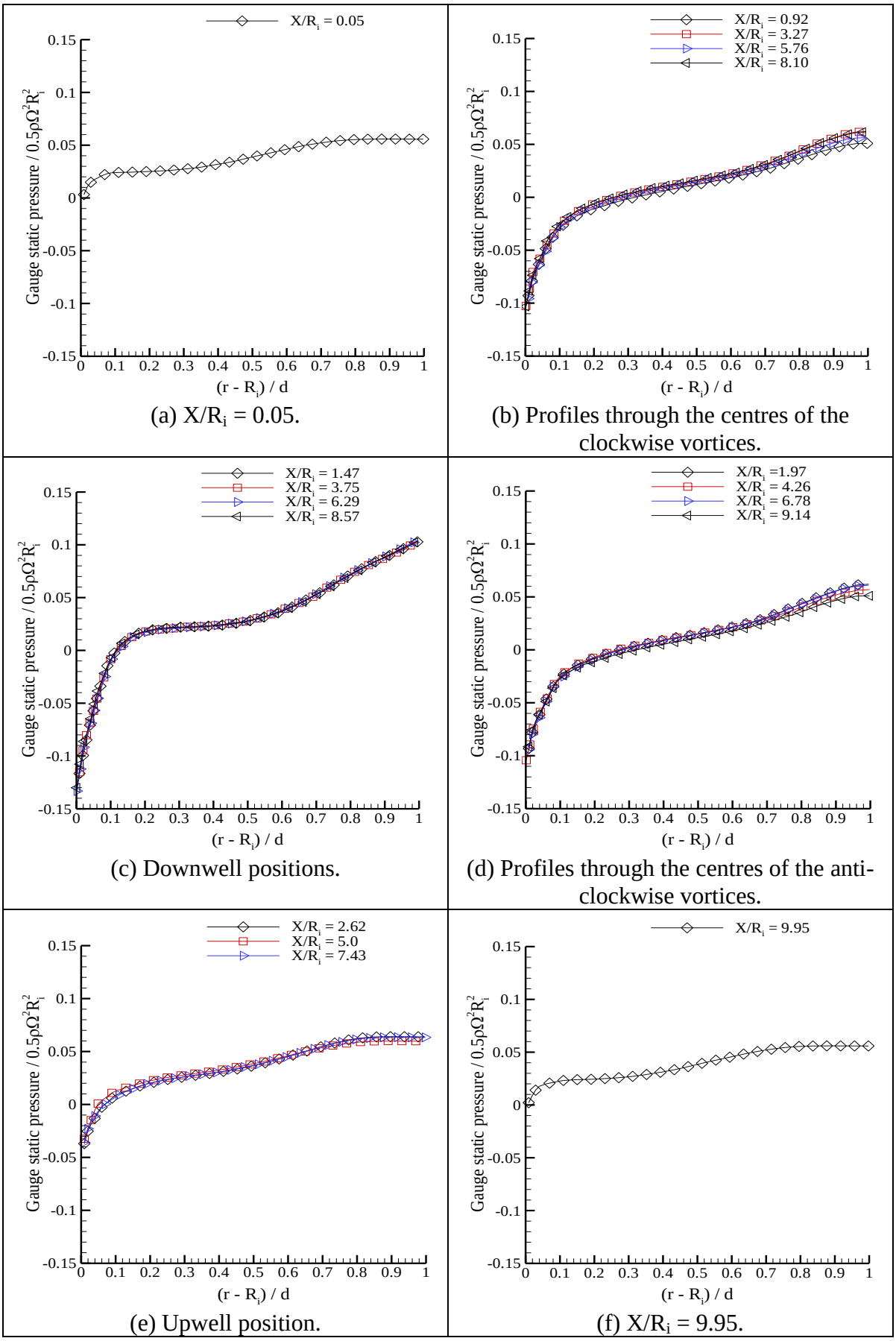

Figure 6.32: Normalised gauge static pressure profiles in the azimuthal plane at $\theta = -\pi/2$ for the test case $\Gamma = 7.81$.

the static pressure gradient increases again close to the outer cylinder. The gauge static pressure at the outer cylinder wall in the outflow regions is higher than that at any other axial plane within the computational domain. The normalised gauge static pressure in Figure 6.31(c) and Figure 6.32(c) ranges from $-0.065\rho R_i^2\Omega^2$ to $0.05\rho R_i^2\Omega^2$.

The radial profiles of normalised gauge static pressure in the inward flow regions are shown in Figure 6.31(e) for the test case $\Gamma = 11.36$ and in Figure 6.32(e) for the test case $\Gamma = 7.81$. These profiles display a gradual increase in gauge static pressure at increasing radial distance toward the stationary outer cylinder. The gauge static pressure gradient is highest close to the rotating inner cylinder as in Figure 6.31(c) and Figure 6.32(c). The gauge static pressure gradient then decreases in the central region of the annulus, from where the gradient increases again. The gauge static pressure then plateaus close to the wall of the outer cylinder. The normalised gauge static pressure at these axial positions ranges from $-0.02\rho R_i^2\Omega^2$ to $0.03\rho R_i^2\Omega^2$.

The normalised dynamic pressure profiles at the same locations as in Figure 6.31 and Figure 6.32 are shown in Figure 6.33(a-f) and Figure 6.34(a-f) for the test cases $\Gamma = 11.36$ and $\Gamma = 7.81$ respectively. All the profiles in Figure 6.33 and Figure 6.34 show similar trends with the maximum dynamic pressure close to the surface of the rotating inner cylinder that gradually decreases toward the stationary outer cylinder. This is due to the action of the rotating inner cylinder that drives the fluid motion with high angular momentum near the wall of the inner cylinder. Since the momentum of the fluid near the wall of the inner cylinder is high, the dynamic pressure near the wall of the inner cylinder is also expected to be high, as discussed in the context of Figure 6.12. The in-plane profile of dynamic pressure is lowest and equal to zero at the stationary outer cylinder, due to the no-slip boundary condition imposed.

The normalised dynamic pressure profiles near the end-walls at $X/R_i = 0.05$ and $X/R_i = 9.95$ are shown in Figure 6.33(a) and Figure 6.33(f) respectively for the test case $\Gamma = 11.36$. These profiles exhibit similar trends to one another. The dynamic pressure at these positions is small compared to that in the central region of the computational domain, due to the effects of the end-walls, as discussed in the context of Figure 6.22 and Figure 6.23. These plots show three regions where the profile changes. The first region is near the wall of the inner cylinder, the second region is in the middle of the annulus, and the last region is near the wall of the outer cylinder. The dynamic pressure near the wall of the inner cylinder decreased rapidly up to the radial position $(r - R_i)/d \approx 0.12$. The dynamic pressure

then plateaus in central region of the annulus over the radial position range $0.2 \leq (r - R_i)/d \leq 0.60$, from where the pressure further decrease over the range $0.60 \leq (r - R_i)/d \leq 1.0$ toward the wall of the outer cylinder. The normalised dynamic pressure profiles in Figure 6.34(a) and Figure 6.34(f) for the test case $\Gamma = 7.81$ exhibit similar trends as in Figure 6.33(a) and Figure 6.33(f) for the test case $\Gamma = 11.36$.

The dynamic pressure profiles across the azimuthal plane through the centres of the clockwise and anti-clockwise vortices are shown in Figure 6.33(b) and Figure 6.33(d) respectively for the test case $\Gamma = 11.36$, as well as in Figure 6.34(b) and Figure 6.34(d) for the test case $\Gamma = 7.81$. These plots exhibit similar trends to those of Figure 6.33(a), Figure 6.33(f), Figure 6.34(a), and Figure 6.34(f). These profiles show three distinctive regions where the dynamic pressure gradient changes. The dynamic pressure near the wall of the inner cylinder decreases rapidly in the positive radial direction over the range $0 \leq (r - R_i)/d \leq 0.2$. Specifically, the normalised dynamic pressure decreases from $0.325\rho R_i^2\Omega^2$ at $(r - R_i)/d = 0$ to $0.06\rho R_i^2\Omega^2$ at $(r - R_i)/d = 0.2$ for the test cases $\Gamma = 11.36$. The test case $\Gamma = 7.81$ exhibits the same trend with similar values of dynamic pressure extrema over the range $0 \leq (r - R_i)/d \leq 0.2$.

Across the remainder of the annulus, the dynamic pressure trends of test cases $\Gamma = 11.36$ and $\Gamma = 7.81$ continue to be similar. The dynamic pressure in Figure 6.33(b), Figure 6.33(d), Figure 6.34(b), and Figure 6.34(d) decreases more slowly in the middle of the annulus and further decreases at a higher rate over the radial position range $0.90 \leq (r - R_i)/d \leq 1.0$. The dynamic pressure finally reduces to zero at the wall of the outer cylinder, as a result of the no-slip boundary condition.

The radial profiles of the normalised dynamic pressure at the outflow positions in Figure 6.33(c) and in Figure 6.34(c) for the test cases $\Gamma = 11.36$ and $\Gamma = 7.81$ respectively show a modestly different trend when compared with the other plots in Figure 6.33 and Figure 6.34. At any radial location, the dynamic pressure in the outflow regions in Figure 6.33(c) and in Figure 6.34(c) is shown to be higher than in Figure 6.33(a, b, d, e, and f) and Figure 6.34(a, b, d, e, and f) at the same radial location. This is attributed to the transport of flow with high tangential momentum by the radial velocity through the outward flow region in the saddle plane between two adjacent vortices. In Figure 6.33(c) and Figure 6.34(c), the dynamic pressure decreases from the wall of the inner cylinder to the wall of the outer cylinder where it reaches a value of zero.

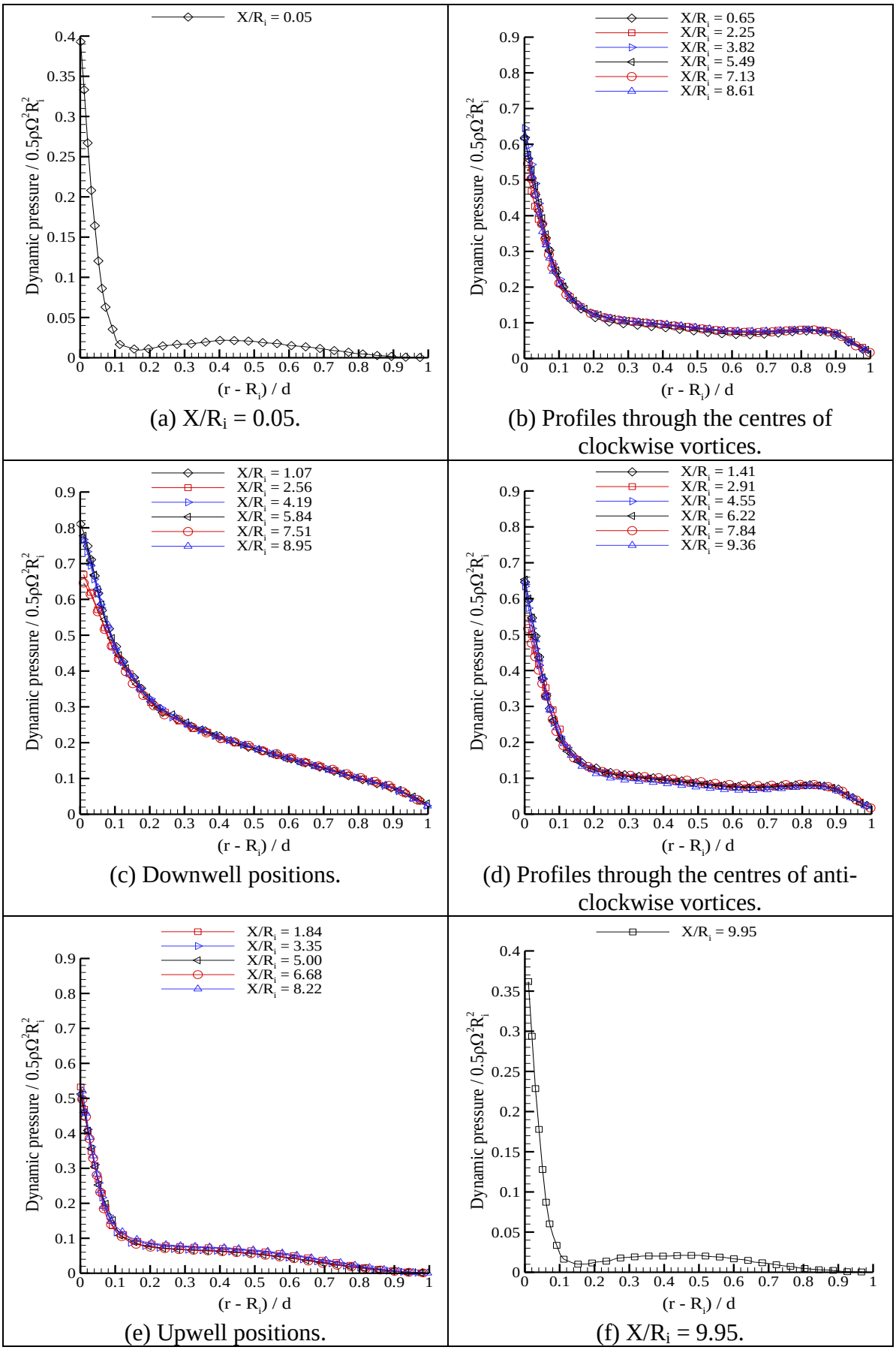

Figure 6.33: Normalised dynamic pressure profiles in the azimuthal plane at $\theta = -\pi/2$ for the test case $\Gamma = 11.36$.

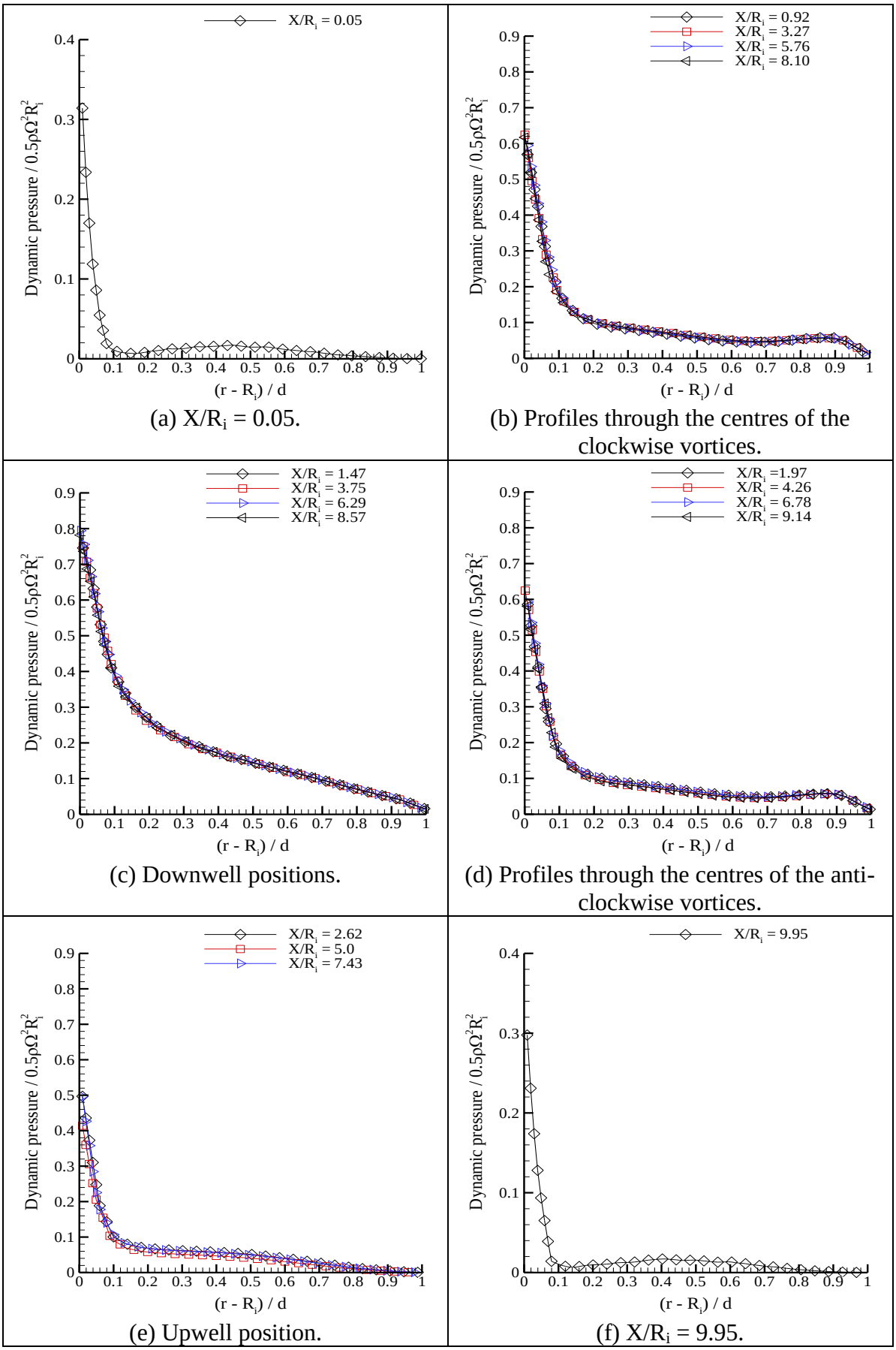

Figure 6.34: Normalised dynamic pressure profiles in the azimuthal plane at $\theta = -\pi/2$ for the test case $\Gamma = 7.81$.

On the other hand, the radial profiles of normalised dynamic pressure at the inward flow regions in Figure 6.33(e) and in Figure 6.34(e) for the test cases $\Gamma = 11.36$ and $\Gamma = 7.81$ respectively show two regions of decreasing dynamic pressure with different gradients. The first decrement occurs near the wall of the inner cylinder over the radial position range $0 \leq (r - R_i)/d \leq 0.12$. This corresponds to the normalised dynamic pressure reducing from $0.27\rho R_i^2\Omega^2$ to $0.05\rho R_i^2\Omega^2$ for the test case $\Gamma = 11.36$ and $\Gamma = 7.81$. This is followed by the second more gradual decrement in dynamic pressure which occurs through the central region of the annulus to the wall of the outer cylinder over the radial position $0.12 \leq (r - R_i)/d \leq 1$. The difference in the dynamic pressure trends at the outflow and inflow positions may be attributed to the rate of mixing of the fluid from the two adjacent vortices at their meeting point, one being an outward flow with high momentum and the other being an inward flow with low momentum.

The analysis of the gauge static pressure and of the dynamic pressure profiles in the azimuthal plane has not been documented in the open literature. As such, no comparison is made between the results obtained in this research and previous studies.

6.7.8 Parametric analysis of the Taylor vortices

The parametric analysis of the Taylor vortices formed in the region between the rotating inner cylinder and stationary outer cylinder is documented in this section. This analysis differs from the parametric analysis of the Taylor flow presented in [ref intro] as it does not aim to describe the global flow regime in the flow domain but rather to detail the geometry and the flow characteristics of the individual vortices therein.

There is no universally accepted definition of a vortex for unsteady viscous flows. However, the main parameters that characterise a vortex include location, extension, maximum circumference velocity, maximum vorticity, and strength (Vollmers, 2001). A vortex is distinguished by streamline patterns like foci and centres. According to Robinson (1991), a vortex exists when instantaneous streamlines mapped onto a plane normal to the vortex core exhibit a roughly circular or spiral pattern, when viewed from a reference frame moving with the centre of the vortex core. Other definitions have been given by researchers such as Chong et al. (1990), Robinson et al. (1989), Chakraborty et al. (2005), Haller (2005), and Jeong and Hussain (1995). Singer and Banks (1994) used both the vorticity and the pressure fields to trace vortex lines in three-dimensional transitional flow.

Vortex centre

Velocity, pressure, and vorticity can all be used to identify a vortex centre. In this study, the vortex centres are defined as the locations where the meridional plane fluid velocity equals zero in the annulus of the cylinder excluding the wall boundaries where no-slip conditions are imposed (Deng et al., 2009). The vortex centres may also be defined as the location where the local static pressure reaches a minimum (Haller, 2005). The vortex centres is also defined by Ma and Zheng (1994) as the maximum vorticity point in the region of the vortex. The vortex centre position corresponds to a local minimum of the velocity and the pressure, and the maximum of the vorticity.

Different researchers have used different methods to locate the vortex centre depending on the flow types. For example, Deng et al. (2009) used a spline interpolation method to obtain the axial and radial position of vortex centres. Agrawal and Prasad (2002) used an automated method to identify the radial and axial coordinates of the vortex centers to determine the properties of vortices in the self-similar turbulent jet. Ma and Zheng (1994) employed the tracing algorithm for identifying the vortex core using both the vorticity and velocity fields. Another method that has been used to locate the vortex centre by researchers such as Dubief and Delcayre (2000) and Lesieur et al., (2003) is the Q-criterion. The Q-criterion captures the vortex centre based on the sign of the second invariant of the velocity gradient (Alim, 2007).

In this section, the centres and the size of the Taylor vortices are estimated. As earlier observed in Figure 6.6, the vortex centres are not all located at the gap mid-span of the annulus (R_i + 0.5d) but are shifted toward the wall of the outer cylinder. This has also been confirmed by Figure 6.27(b and d) and Figure 6.28 (b and d).

In this study, the radial and axial coordinates of the Taylor vortex centres are determined by the cross-sectional lines algorithm described by Vollmers (2001), which is based on obtaining the difference between vortex induced velocity extrema. It is understood that the component of velocity perpendicular to a line cutting a vortex will exhibit a maximum difference between its extrema when the line intersects the centre of the vortex (Vollmers, 2001). Using this principle, the location of vortex centres was determined from the following six-step procedure.

1. Generate a set of parallel lines within the area of interest in the vicinity of the vortex centre, such as axial lines on the meridional plane with a constant radial stagger, as illustrated in Figure 6.35. A refinement step may be employed if the spacing between the lines is too large.

2. Obtain the absolute magnitude u of the local radial velocity at discrete points on these lines.
3. Compute for each line the maximum difference $u_{max} - u_{min}$ in u.
4. The line with the highest absolute radial velocity difference $u_{max} - u_{min}$ identifies the axial coordinate of the vortex centre X_c.
5. Generate a set of radial lines on the meridional plane with a constant axial stagger, as illustrated in Figure 6.35, analogous to step 1.
6. Repeat steps 2 to 4 to determine the radial coordinate r_c of the vortex centre, based on the line with the highest absolute axial velocity difference $u_{max} - u_{min}$, where u is the absolute magnitude of the local axial velocity at discrete points on these lines.

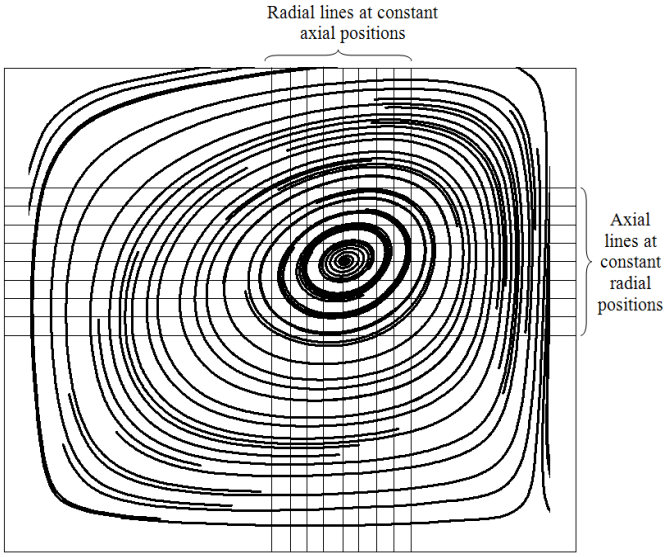

Figure 6.35: Cross-sectional lines used to locate vortex centres.

The above procedures was employed to estimate the centre of the vortices for both lower and upper channels of the annulus, starting from left to right in Figure 6.36, using the cylindrical frame of reference of Figure 6.1(a). The axial coordinate X_c and the radial coordinate r_c of each vortex were use to indicate the centres of the vortices in Figure 6.36(a) and Figure 6.36(b) for the test cases Γ = 11.36 and Γ = 7.81 respectively. The detailed coordinate values for the test cases Γ = 11.36 and Γ = 7.81 are reported in Table B 1 and Table B 2 of appendix B respectively. The vortices shown in Figure 6.36(a) and Figure 6.36(b) have been numbered starting at the left end-wall with the sequence increasing in the positive axial direction toward the right end-wall.

Figure 6.37(a) and Figure 6.37(b) show the normalised radial position of the Taylor vortex centres for the test cases Γ = 11.36 and Γ = 7.81 respectively, as a function of their

normalised axial position in the meridional plane. The axial position has been normalised by the inner cylinder radius R_i, while the radial positions has been normalised by the cylinder gap width, d. This is related to the cylindrical coordinates system of Figure 6.1 by the ordinate in Figure 6.37 being equal to $(r - R_i)/d$. Figure 6.37 uses the same open and filled circles as Figure 6.36 to identify the vortex centres at $\theta = \pm\pi/2$ for the test cases Γ = 11.36 and Γ = 7.81.

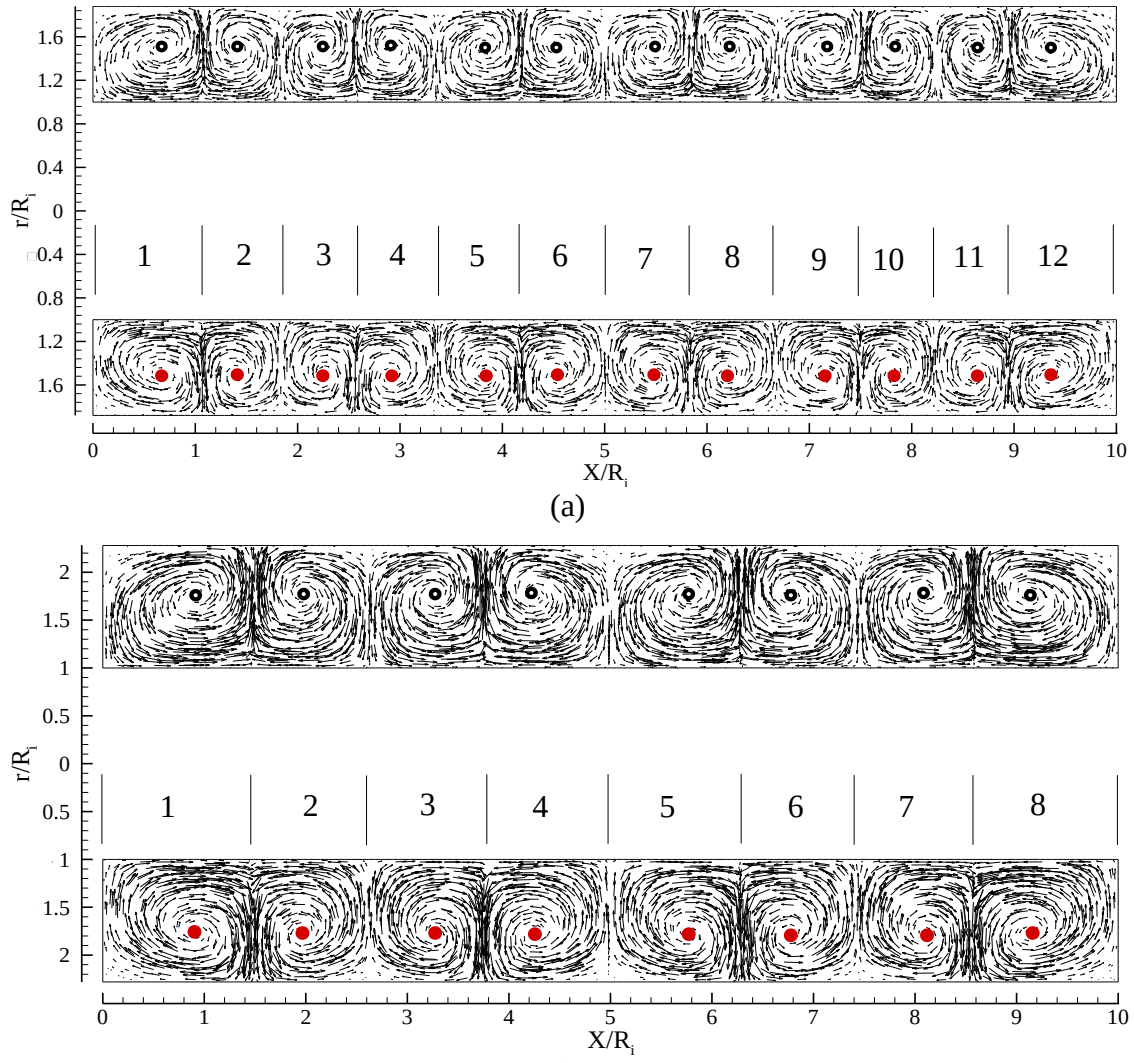

Figure 6.36: Velocity vectors showing the centre of the vortices in red and black in the meridional plane of the annulus for the test cases (a) Γ = 11.36 and (b) Γ = 7.81.

From Figure 6.36, the axial distance from the centre of each vortex to the centre of the next one to the right of it in the same plane at $\theta = \pm\pi/2$ is estimated. Figure 6.37 is used to illustrate the spread of the vortex centres in the meridional plane in both the lower and upper channels ($\theta = \pm\pi/2$) for the test cases Γ = 11.36 and Γ = 7.81. The orange dashed lines toward the top and bottom of Figure 6.37(a) and Figure 6.37(b) represent

respectively the maximum and minimum limits of the spread band about the vortex centre mean value. The standard deviation of the vortex radial positions was used to size the spread band for the two test cases, assuming a normal distribution. The standard deviation was estimated using

$$\sigma = \sqrt{\frac{1}{N-1}\sum_{i=1}^{N}(x_i - \bar{x})^2} \qquad 6.8$$

where σ is the standard deviation,

N is the number of samples,

x_i is the i^{th} data point,

$\bar{x}$ is the mean (average) of the data points.

Figure 6.36 and Figure 6.37 report a measurable change in the radial position of the vortex centres for the test cases Γ = 11.36 and Γ = 7.81, as the vortex centres in both the lower and upper channels are not all at the same radial position. However, this variation is small. When the vortex centres in the lower and upper channels (θ = ±π/2) of the annulus are compared in Figure 6.37(a) for the test case Γ = 11.36, it is evident that the flow is essentially axisymmetric, as many of the vortex centres at θ = π/2 have almost the same axial and radial positions as the corresponding ones at θ = -π/2. Figure 6.37(b) for the test case Γ = 7.81 exhibits a similar trend. In both test cases, the variation in the radial positions of the vortex centres between θ = π/2 and θ = -π/2 is more obvious than vortex centre axial variation.

The axisymmetry of the vortex centres indicates that the simulation is modelling a Conventional Taylor Vortex Flow (CVF). The use of perfectly orthogonal end walls in the model and the numerical viscosity that is intrinsic in the flow solver prevent the growth of secondary flow instabilities that the flow requires for staging to a higher Taylor mode, such as the Wavy Vortex Flow. Whilst the flow is essentially axisymmetric, Figure 6.37 shows an axial pattern of small changes in the radial position of the vortex centres. Figure 6.37 shows that the flow in the test case Γ = 7.81 is more axisymmetric than in the test case Γ = 11.36, as the variation in the radial positions of vortex centres between θ = π/2 and θ = -π/2 is comparatively lower.

In the two test cases in Figure 6.37, the radial locations of the vortex centres are anti-symmetric about the axial positon $X/R_i = 5.0$. The axial locations of the vortex centres are

instead symmetric about the axial position X/R_i = 5.0. The normalised axial spacing between the vortex centres is larger than the normalised radial spacing between the vortex centres for both test cases. The physical axial spacing is also larger than the physical radial spacing between the vortex centres. This result agrees with the conventional description of Taylor vortices of being an array of counter-rotating vortex pairs with their vortex centres approximately aligned along the gap mid-span.

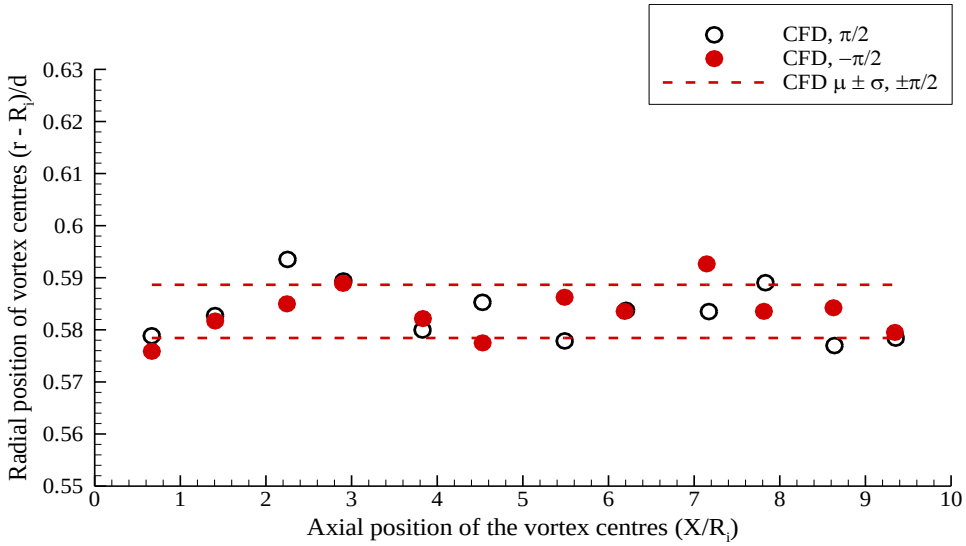

(a)

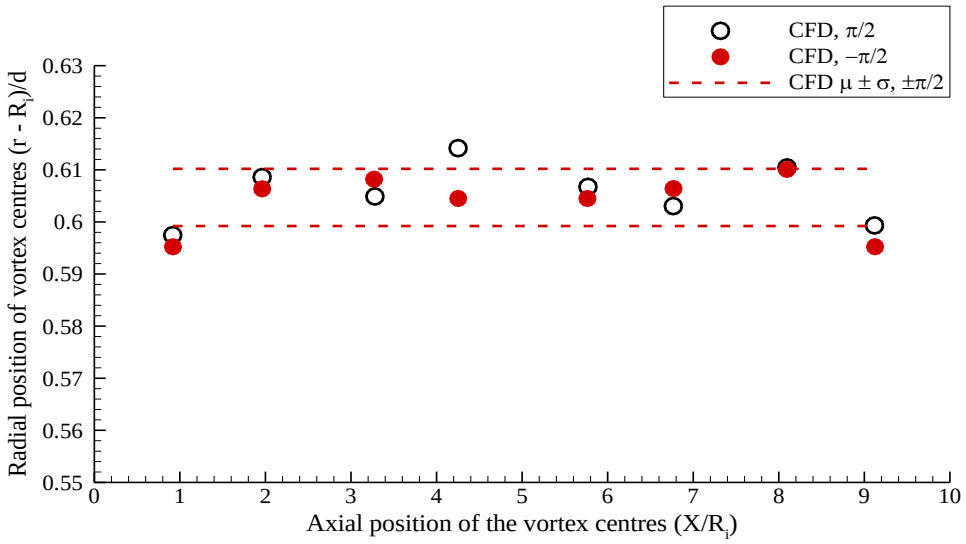

(b)

Figure 6.37: Axial and radial position of vortex centres in the meridional plane of the annulus for the test cases (a) Γ = 11.36 and (b) Γ = 7.81.

As a result of the variations in the radial positions of vortex centres and the anti-symmetry of the vortex centres about the axial positon X/R_i = 5.0, the distribution of vortex centres in Figure 6.37 is complex.

Based on the dimensions of the computational domain, the gap width between the inner and the outer cylinders ranges from $0 \leq (r - R_i)/d \leq 1$. This means the gap mid-span ($r = R_i + 0.5d$) of the annulus is located at $(r - R_i)/d = 0.5$. From Figure 6.37(a) for the test case $\Gamma = 11.36$, the area occupied by vortex centres is confined over the range $0.574 \leq (r - R_i)/d \leq 0.596$ radially. Similarly, the area occupied by vortex centres for the test case $\Gamma = 7.81$ in Figure 6.37(b) is confined over the range $0.594 \leq (r - R_i)/d \leq 0.616$ radially. This further confirms that the vortex centres are not symmetric about the gap mid-span of the annulus as the vortex centres do not coincide with the annulus gap mid-span. In fact, all the vortex centres are located more toward the wall of the stationary outer cylinder, as discussed in the contex of Figure 6.6, Figure 6.27(b, d), and Figure 6.28(b, d). As the gap width d between the cylinders increases, the vortex centres are more displaced toward the wall of the outer cylinder for the test case $\Gamma = 7.81$ than for the test case $\Gamma = 11.36$, as shown by the dashed lines in Figure 6.37(a) and Figure 6.37(b).

In Figure 6.37(a) and Figure 6.37(b), approximately 83.3% and 75% of the vortex centres is within the respective spread bands, which are delimited by the dashed orange lines, suggesting that there are a few outliers outside ±1 standard deviation bands for the two test cases.

Vortex size and end-wall effects

Taylor vortices are commonly sized by their wavelength λ, which is defined as the ratio of the axial length of a pair of vortices divided by the gap width d (Koschmieder, 1979; Xiao et al., 2002).

The wavelength λ is obtained from the average Taylor vortex pair size over the entire view area of the annulus. In this work, the half wavelength, $\lambda/2$ for each vortex was measured for the test cases $\Gamma = 11.36$ and $\Gamma = 7.81$. The half wavelength was measured as the distance between consecutive radial outflow and inflow regions which define the axial size of one vortex. The half wavelength is hereby referred to as the axial vortex size. The axial vortex size was estimated from Figure 6.36(a) and Figure 6.36(b) and reported in Table 6-7 and Table 6-8 for the test cases $\Gamma = 11.36$ and $\Gamma = 7.81$ respectively. For the test case $\Gamma = 11.36$ in Table 6-7, from the left end-wall, vortex 1 and, from the right end-wall, vortex 12 are directly affected by the stationary end-walls. Similarly, for the test case $\Gamma = 7.81$ in Table 6-8, from the left end-wall, vortex 1 and, from the right end-wall, vortex 8 are directly affected by the stationary end-walls.

Table 6-7 shows how the elongated vortices 1 and 12 for the test case Γ = 11.36 affected the vortex axial length X_L of the neighbouring vortices toward the central region of the annulus, specifically vortices 2, 3, and 4 as well as vortices 9, 10, and 11. Similarly, in Table 6-8 for the test case Γ = 7.81, the elongated vortices 1 and 8 affected the vortex axial length X_L of the neighbouring vortices 2 and 3 as well as vortices 6 and 7.

Table 6-7: Variation of vortex axial length with vortex number for the test case Γ = 11.36.

Vortex number	Vortex axial length $X_L = X/R_i$	Variation $(X_L - \overline{X}_L)$
1	1.07	0.282
2	0.77	-0.018
3	0.72	-0.068
4	0.79	0.002
5	0.84	0.052
6	0.81	0.022
7	0.84	0.052
8	0.84	0.052
9	0.83	0.042
10	0.71	-0.078
11	0.73	-0.058
12	1.05	0.262
Average	$\overline{X}_L = \frac{1}{10}\sum_{i=2}^{11}(X_L)_i = 0.788$	
Variance	$S^2 = \frac{1}{9}\sum_{i=2}^{11}(X_L - \overline{X})_i^2$ = 0.002751	
Standard deviation	$\sigma = S = 0.05245$	

From Table 6-7, considering the vortices as pairs, the first pair is composed of an elongated vortex 1 and a shortened vortex 2. Vortex 2 compensates for the elongated vortex 1 by its reduction in size. Likewise, vortex 4 compensates for the reduction in the size of vortex 3 by an increase in its size. Similarly, from the right end-wall, the same trend is observed as vortex 11 compensates for the elongated vortex 12 by a reduction in

its size. Vortex 9 compensates for the reduction in the size of vortex 10 by an increase in its size. As the vortices develop toward the centre of the computational domain, the size of neighbouring vortices 5, 6, 7, and 8 become almost the same.

For the test case Γ = 7.81 in Table 6-8, the same pattern of alternating elongated and shortened vortices near the end-wall boundaries is observed as for the test case Γ = 11.36. The affected vortices are vortices 1, 2, 3 and 6, 7, 8. The vortices towards the centre of the computational domain, which are vortices 4 and 5, are comparatively less affected.

Table 6-8: Variation of vortex axial length with vortex number for the test case Γ = 7.81.

Vortex number	Vortex axial length $X_L = X/R_i$	Variation $(X_L - \overline{X}_L)$
1	1.47219	0.28923
2	1.14438	-0.03858
3	1.13153	-0.05143
4	1.25977	0.076812
5	1.28334	0.100382
6	1.13435	-0.04861
7	1.14438	-0.03858
8	1.43006	0.2471
Average	$\overline{X}_L = \frac{1}{6}\sum_{i=2}^{7}(X_L)_i = 1.18296$	
Variance	$S^2 = \frac{1}{5}\sum_{i=2}^{7}(X_L - \overline{X}_L)_i^2$ = 0.004792	
Standard deviation	$\sigma = S = 0.069225$	

From the estimated vortex axial length, an average is calculated without the first and the last vortices in Table 6-7 and Table 6-8 being included. Since vortices 1 and 12 for the test case Γ = 11.36 and and vortices 1 and 8 for the test case Γ = 7.81 are significantly longer in the axial direction than the reminder vortices in the central region of the annulus, including them in the axial vortex size average would significantly affect the vortex axial length variance. Table 6-7 and Table 6-8 show that the estimated average vortex axial size

(half wavelength) is $0.788R_i$ and $1.183R_i$ for the test cases $\Gamma = 11.36$ and $\Gamma = 7.81$ respectively.

From the vortex axial length estimates for test cases $\Gamma = 11.36$ and $\Gamma = 7.81$, the variance and the standard deviation of vortex axial size are determined and reported in Table 6-7 and Table 6-8 . The variations in vortex axial length $X_L - \overline{X}_L$ tabulated in the third column of Table 6-7 and Table 6-8 was used for producing the residual plots shown in Figure 6.38 for both test cases.

6.7.9 Residual plot

Residual plots are used herein to assess the statistical regression of the vortex axial size. A null residual plot shows that there are no obvious defects in a regression, a curved residual plot indicates non-linearity in the regressed model, whereas a double-bow or a fan shaped pattern indicates a non-constant variance (Tsai et al., 1998). The residual E is the difference between the observed value of the dependent variable Y and the predicted value Y^i. This is represented as $E = Y - Y^i$. Both the sum and the mean of the residual plots are equal to zero. The predicted value can be obtained from the general equation for a linear plot given as $Y^i = mX + b$, where X is the independent variable, m is the slope and b is the intercept. Once the predicted value is known, the residual can be calculated and plotted against the independent variable. Therefore, the residual can be estimated using the relation $E = Y - (mX + b)$. In producing the residual plot in Figure 6.38(a) and Figure 6.38(b) for the vortex axial length, $m = 0$ and $b = \overline{X}_L$.

Figure 6.38(a) and Figure 6.38(b) are therefore the residual plots of the vortex axial length in the meridional plane at $\theta = -\pi/2$ for the test cases $\Gamma = 11.36$ and $\Gamma = 7.81$ respectively. These plots show that there are no obvious defects in the model as the residual is scattered about the zero x-axis with no significant bias. Without vortices 1 and 12, the residual of the remaining ten vortices are well defined, with the minimum and maximum deviation from the zero axis estimated as $-0.08R_i$ and $0.06R_i$ respectively for the test case $\Gamma = 11.36$. Similarly, for the test case $\Gamma = 7.81$ without vortices 1 and 8, the residuals are evenly distributed about the zero x-axis with no significant bias. The residual of the six vortices in the central region of the computational domain display a minimum and maximum deviation from the zero axis of $-0.06R_i$ and $0.11R_i$ respectively.

The two outliers on the plot in Figure 6.38(a) are the residuals from vortex 1 and 12 in Figure 6.36(a) and show the direct effects of the end-walls on the axial length of these two

vortices. The outliers on the plot in Figure 6.38(b) are the variation due to the end-walls at vortex 1 and 8 in Figure 6.36(b). This is in agreement with the observation made earlier that the end-walls directly affect the vortices next to it. The residual plots in both test cases exhibit a similar pattern and are well defined as shown by the red curve in Figure 6.38(a) and Figure 6.38(b).

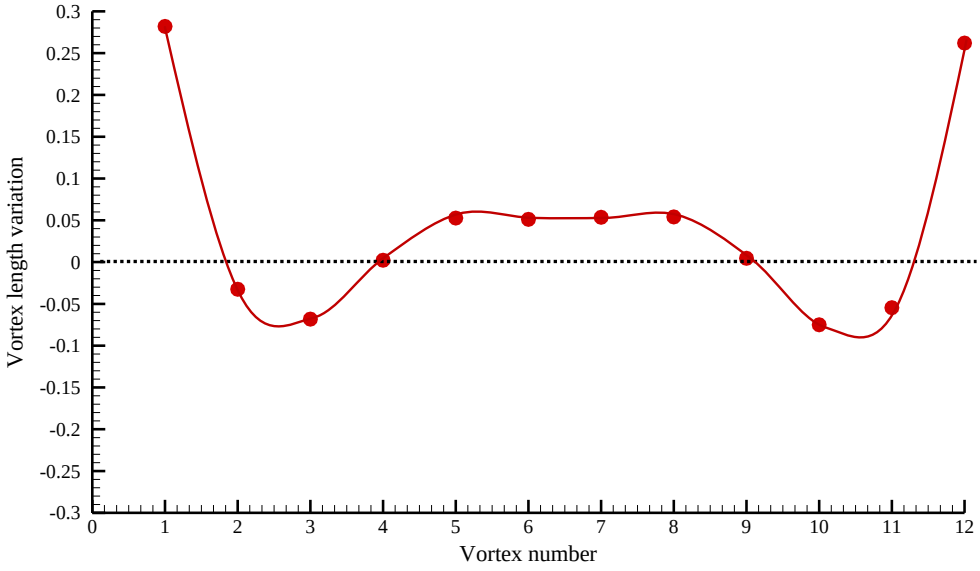

(a)

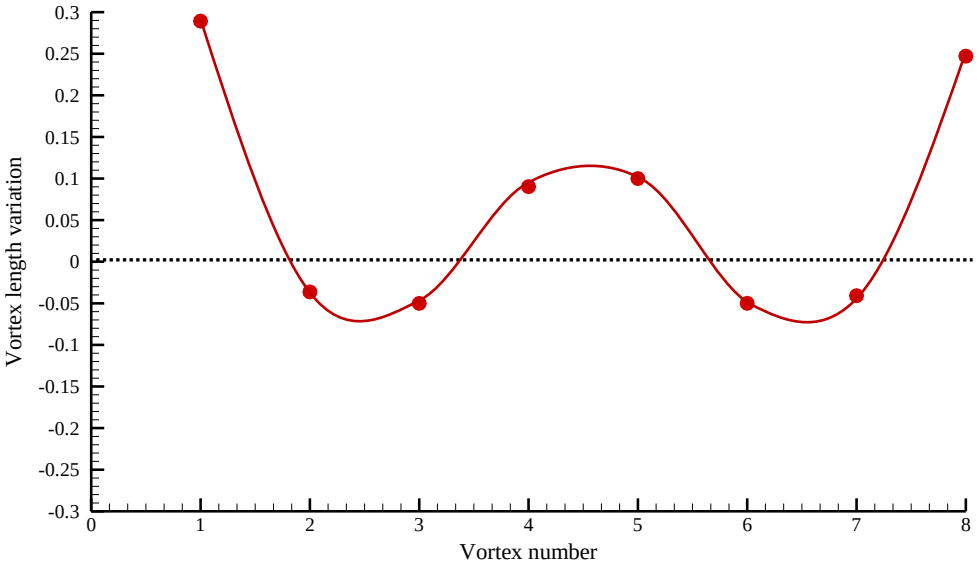

(b)

Figure 6.38: Residuals plot of vortex axial length variation in the meridional plane at $\theta = -\pi/2$ for the test cases (a) $\Gamma = 11.36$ and (b) $\Gamma = 7.81$.

Figure 6.39(a) and Figure 6.39(b) show the axial distributions of normalised radial and normalised axial velocities in the meridional plane showing the zero crossing positions for the test cases $\Gamma = 11.36$ and $\Gamma = 7.81$ respectively. The ordinates on the right and left hand

sides in Figure 6.39 are of axial velocity and of radial velocity respectively. The axial and radial velocity distributions use different ordinate scales so as to capture on each scale the full dynamic range of the respective velocity component. The abscissa is the total length of the computation domain normalised by the inner cylinder radius R_i. The horizontal dashed line on each of the two plots marks the zero value of radial and axial velocities. Vertical dashed lines across radial velocity maxima mark the maxima axial positions. These lines are a good prediction of the axial position where the axial velocity crosses the horizontal zero line. From the normalised axial velocity profile in Figure 6.39(a) and Figure 6.39(b), there is a good match between the zero crossings of the axial velocity profile and the axial location of the radial velocity maxima. This is expected because at the saddle planes, where the radial velocity is maximum, the axial velocity is expected to be zero. Also, at the vortex centres, where the radial velocity is minimum, the axial velocity is expected to be maximum. The little offset observed at point 1 and point 6 in Figure 6.39(a) and point 1 and point 4 in Figure 6.39(b) is due to the effect of the end-walls at $X/R_i = 0.0$ and $X/R_i = 10.0$ that elongated vortices 1 and 12 in Figure 6.6(a) and vortices 1 and 8 in Figure 6.6(b).

In addition, Figure 6.39 can also be used to confirm the spatial wavelength of the Taylor vortices estimated in Table 6-7 and Table 6-8. For example, for the test case $\Gamma = 11.36$ in Figure 6.39(a), the tick blue lines delimit one wavelength, which is the distance between one radial inward flow region to the next radial inward flow region to the right of it in the same plane along the positive axial direction. This delimits the axial size of one vortex pair. The spatial wavelength can also be estimated as the distance between one clockwise vortex to the next clockwise vortex to the right of it in the same plane along the positive axial direction. From Figure 6.39(a), using the former definition, the axial wavelength λ is estimated to be approximately $1.667R_i/d = 1.9$. Similarly, for the test case $\Gamma = 7.81$, the axial wavelength λ is estimated from Figure 6.39(b) to be approximately $2.5R_i/d = 1.95$.

This estimate of the wavelength λ has been checked by a simpler method used in previous work by Koschmieder (1979). By considering the vortices as pairs, the axial wavelength can be estimated from the number of vortices in the computational domain. If the two vortices at the end walls are included, the average axial wavelength using the expression $\lambda = L/Nd$ given by Koschmieder (1979) is calculated to be approximately 1.9 and 1.95 for the test cases $\Gamma = 11.36$ and $\Gamma = 7.81$ respectively, where L is the length of the cylinders, N is the number of vortex pairs, and d is the gap width. These λ estimates are in good

agreement with the theoretical value of λ = 2.0 reported in the literature by Roberts (1965).

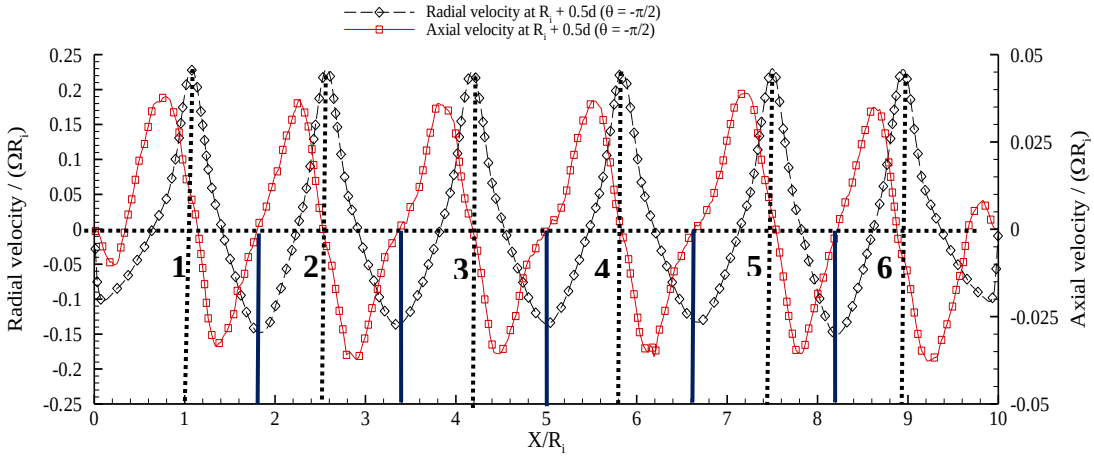

(a)

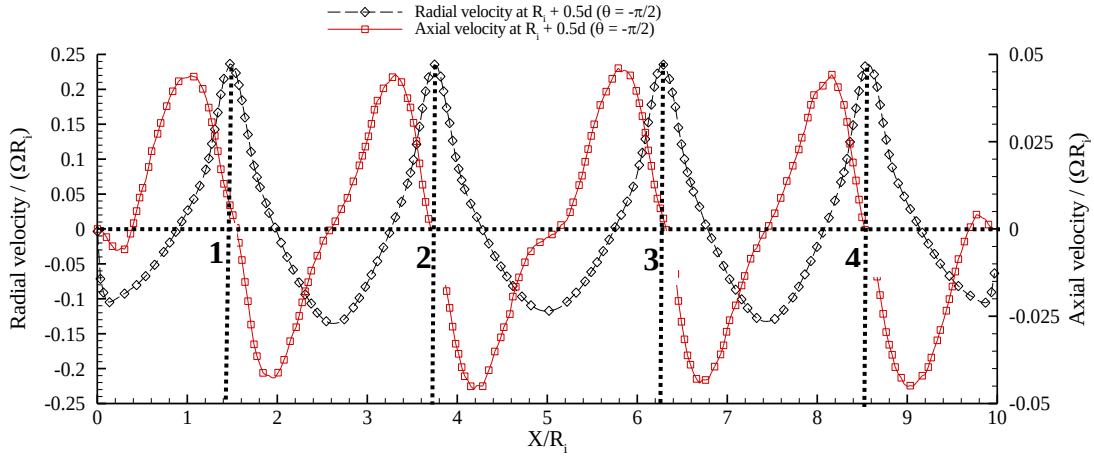

(b)

Figure 6.39: Axial distributions of radial and axial velocities in the meridional plane showing the zero crossing positions for the test cases (a) Γ = 11.36 and (b) Γ = 7.81.

Chapter Seven: Experimental investigation of flow between coaxial rotating cylinders

7.1 Introduction

This chapter is concerned with the experimental investigation of the flow regimes in the annular region between coaxial rotating cylinders. PIV has been employed for all the experimental measurements discussed in this chapter. The advantage of using PIV for flow diagnostic such as in rotating equipment is the ability to obtain instantaneous planar velocity measurements, as discussed in chapter five.

The experimental investigations reported in this chapter were focused toward two objectives. The first objective was to understand in detail through experimentation the flow in the annular region of concentric rotating cylinders of different aspect ratio when the inner cylinder is rotating and the outer cylinder is stationary. Understanding this flow will help subsequently to assess the level of intrusiveness that a cylindrical probe in the annular region has on the ensued Taylor-Couette flow. The second objective was to validate the results obtained from the CFD simulation by comparing the PIV results with those obtained from the computational prediction of the flow.

7.2 Experimental investigation parameters

The flows under consideration are generated in an apparatus with a rotating inner cylinder and a concentric stationary outer cylinder with stationary end-walls as detailed in chapter five. The detailed description of the materials and dimensions of the test, as well as the PIV arrangement, are given in chapter four and chapter five. The experimental field of view is reported in Table 5-2 and is the same as the one for the CFD in chapter six.

In this chapter, PIV measurements were obtained of the flow between concentric rotating cylinders of aspect ratios $\Gamma = 11.36$, $\Gamma = 7.81$, and $\Gamma = 5.32$. The experimental set-up and the start-up procedure were the same for all three test cases as discussed in chapter five.

7.3 PIV measurement accuracy

The accuracy of the PIV results depends on a combination of many factors ranging from the equipment set up, the recording process, to the analysis of data. In this section, the method and the criteria for verifying the convergence and accuracy of the data are discussed in details. The convergence of PIV data is assessed by testing whether a certain

number of PIV vector maps are enough to obtain an average vector map with a low statistical uncertainty. A converged PIV vector map is such that, by taking and averaging more PIV vector maps, there is no significant change in the average. If the PIV vector maps have not converged, then more PIV vector maps are needed to make them converge. From previous research by Prasad (2000) on PIV vector map averaging, it was established that the number of PIV vectors map needed to obtain a converged average ranges from 25 to 250.

For this research work, two methods have been used to determine the convergence of the PIV data. The first involves a quantitative analysis of every vector in the vector map, by estimating the average and the standard deviation of all the PIV image snapshots at every single point in the flow. The second method was based on calculating the mean of the average velocity at constant radial positions in the meridional plane. The process and the procedures for these two methods are summarised below:

Method 1

1. Acquisition of specific number of images and taking the time average of all the PIV image snapshots at every single point in the flow field.
2. Estimation of the standard deviation σ at every single point.
3. Estimation of the statistical uncertainty in the average ($\sigma/ N^{0.5}$) at every single point.
4. Estimation of the relative uncertainty in the average ($\sigma/ (\mu N^{0.5})$) at every single point.
5. Estimation of the average value of the relative uncertainty ($\sigma/ (\mu N^{0.5})$) over all points in the vector map.
6. Steps 1 to 5 were repeated with an increasing number of images.

Method 2

1. Acquiring a number $N > 25$ of image pairs to obtain an ensemble average velocity vector map of the N PIV instantaneous vector maps from the image pairs.
2. Extracting profiles at constant radial positions in the meridional plane at $\theta = - \pi/2$ along the axial direction from the ensemble average in-plane velocity magnitude distribution. The profiles are extracted at an increment radial distance of 2mm, the first and the last being 3mm away from the wall of the inner and outer cylinders.

The constant radial positions where the average was estimated are illustrated in Figure 7.1 with the black lines on the meridional plane at $\theta = -\pi/2$.

3. Estimating the average velocity magnitude of all the data points along the constant radial positions selected in step 2 and normalising the velocity magnitude by the inner cylinder tangential speed ΩR_i.
4. Steps 1 to 3 are repeated with an increasing number of image snapshots N.

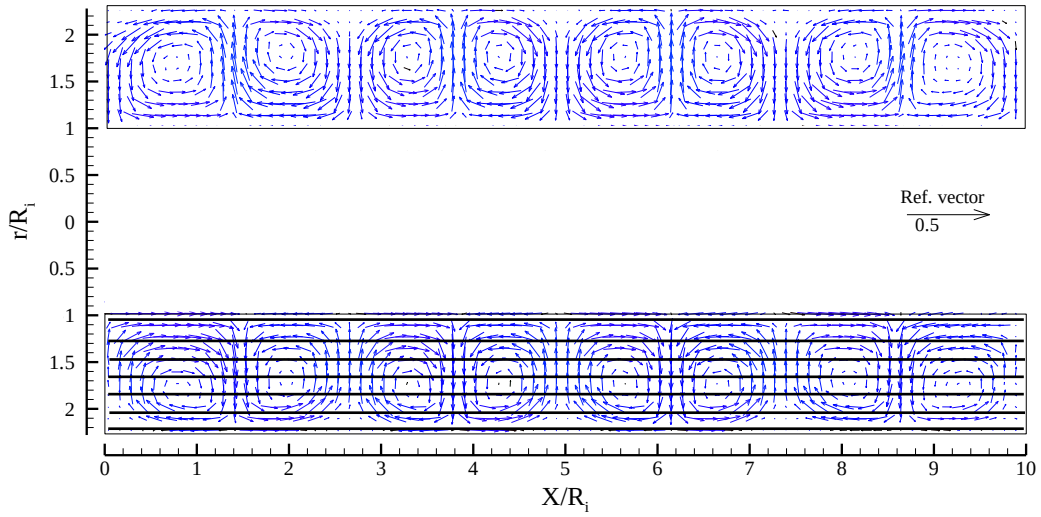

Figure 7.1: Typical velocity vectors from where velocity profiles are extracted for PIV convergence.

7.4 PIV measurement accuracy results and discussions

Figure 7.2 and Figure 7.3 show the results obtained from the two methods discussed in section 7.3. Figure 7.2 shows that the mean relative uncertainty in the ensemble averaged velocity decreases monotonically with increasing number of PIV images. For example, from the analysis of 30 images, the mean relative uncertainty of the ensemble averaged velocity is about 22%. As the number of PIV images increases to 90, this value drops to approximately 6.5%.

As the number of PIV images increases, between 100 and 120 images the mean relative uncertainty in the PIV velocity becomes nearly constant at approximately 5.5%, suggesting that taking more PIV data is not likely to change the result. This result shows that the PIV data is converged with 100 images.

Figure 7.3 shows the mean of all the data points at constant radial positions $r = R_i + 0.136d$, $r = R_i + 0.318d$, $r = R_i + 0.5d$, $r = R_i + 0.682d$, and $r = R_i + 0.864d$ in the meridional plane along the axial direction on the lower ($\theta = -\pi/2$) channel of the annulus, as illustrated in Figure 7.1 with the black lines. The mean velocity magnitude on the

ordinate of Figure 7.3 is expressed as a percentage of the inner cylinder tangential speed ΩR_i. Figure 7.3 shows a high percentage value at lower number of PIV snapshots at all the radial positions. As the number of PIV snapshots increases, the ensemble averaged of the in-plane velocity magnitude at all the radial positions reduces monotonically. Figure 7.3 shows the plot at all radial positions becoming flat at around 90 images with a near-constant value of approximately 5% in the central region of the annulus at $r = R_i + 0.318d$, $r = R_i + 0.5d$, and $r = R_i + 0.682d$.

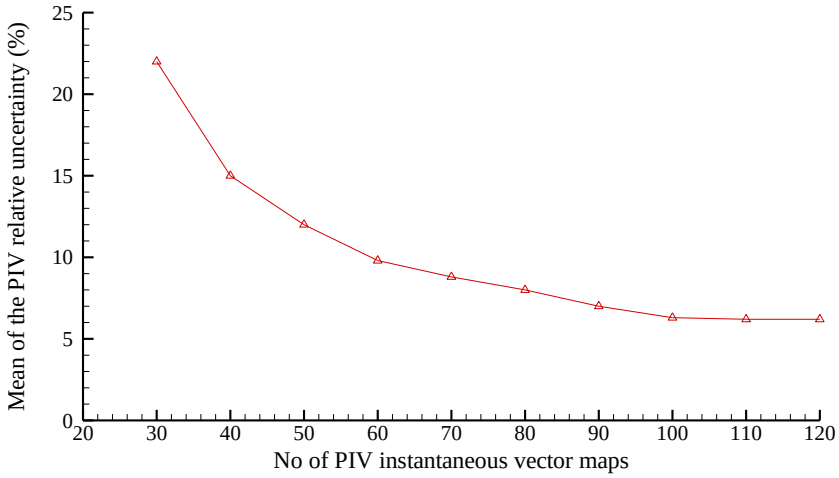

Figure 7.2: PIV data convergence based on the mean of the relative uncertainty in the velocity magnitude.

Near the walls of the inner and outer cylinders, at $r = R_i + 0.136d$ and $r = R_i + 0.864d$ in Figure 7.3, the mean relative uncertainty is slightly higher than the corresponding values in the central region of the annulus. This is because there are spurious vectors due to a reflection of the PIV light sheet near the walls. This reflection obscures the particle light scatter, giving rise to uncertainty in the velocity measurements. The reflection intensity is greater near the wall of the outer cylinder, as shown by the $r = R_i + 0.864d$ curve in Figure 7.3 being above the other ones. At these radial positions, the mean relative uncertainty of the velocity was estimated at approximately 22% with a 30 image average.

This value reduces to approximately 6.5% with a 90 image average. When more than 90 PIV images are averaged, Figure 7.3 shows no considerable change in the mean relative uncertainty of the velocity magnitude, an indication that taking more images does not improve the result. These plots confirm that the PIV results can be taken as statistically converged with about 90 images.

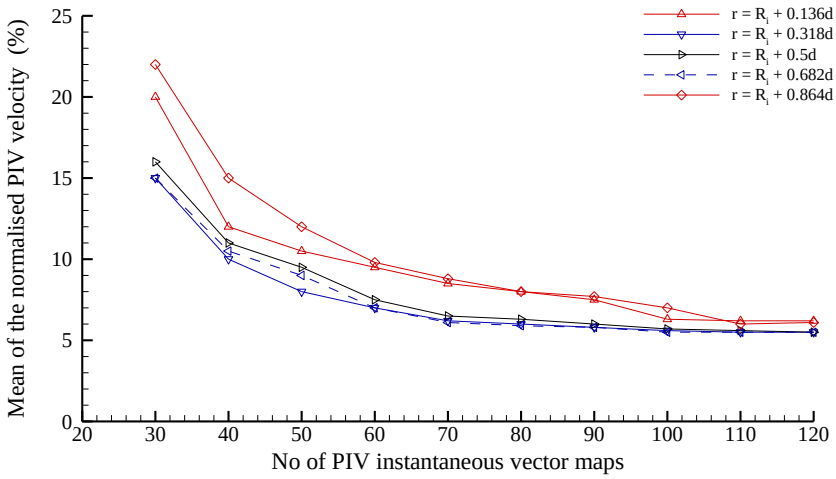

Figure 7.3: PIV data convergence based on the mean of the normalised in-plane velocity magnitude.

7.5 Experimental results and discussions for concentric cylinders Γ = 11.36 and Γ = 7.81

The flow characteristic features in the annulus of the coaxial rotating cylinders, obtained from the PIV measurements for the test case with aspect ratio Γ = 11.36 and Γ = 7.81 are discussed in this section. All the velocity fields have been normalised by the inner cylinder tangential speed, ΩR_i. The PIV measurement area for these test cases is equal to the area of the computational domain. Therefore, the PIV measurement area for all the PIV results has been normalised by the inner cylinder radius R_i consistently with the CFD results, as discussed in section 6.7.1.

7.5.1 Flow regime and pattern in the annulus of the coaxial cylinders

The geometry and the flow parameters of the apparatus used for this PIV investigation are the same as those presented in Table 6-1 for the CFD simulations. Based on these flow parameters, the Taylor number is above the first critical Taylor number. As such, Taylor-Couette instability is expected to characterise the flow. The PIV results obtained suggest that the flow regime in the test cases Γ = 11.36 and Γ = 7.81 is the wavy vortex flow.

This wavy vortex flow is characterized by travelling azimuthal waves that are superimposed on the Taylor vortices (Gollub and Swinney, 1975). The azimuthal waves rotate around the inner cylinder at some wave speed (Youd, 2005). The azimuthal waves have a defined azimuthal wave-number *m* and move at a finite wave velocity in the azimuthal direction. In the wavy vortex flow regime, the flow is characterised by vortex contraction, expansion, and undulation. There is significant cyclic exchange of fluid

between vortices. In the wavy vortex flow regime, the boundaries between adjacent vortices are dynamic, with their position and orientation changing as a function of time (Wang et al., 2005), whereas in the Taylor vortex flow regime, the boundaries between adjacent Taylor vortices are stationary and the inflow and outflow boundaries remain flat and perpendicular to the cylinder walls. This means that the wavy vortex flow is time-periodic and breaks the continuous rotational symmetry of the conventional Taylor vortex flow. A detailed description of different flow regimes was presented in chapter 2, section 2.2.4

The waves travel around the annulus at a speed that is 30% to 50% of the surface speed of the inner cylinder, depending on the Taylor number and other conditions (King et al., 1984). The whole wave pattern rotates as a rigid body about the cylinder axis, hence the pattern is at rest for an observer fixed in a reference frame that rotates with the waves. An interesting property of the waves is the absence of dispersion. The state of the system depends on the Reynolds number history and on other factors, but each state, once established, is stable over a range of Reynolds numbers (Coles, 1965). At any given Reynolds number, the wave speed is essentially independent of *m* (Shaw et al., 1982). In wavy vortex flow, the wave pattern has an *m*-fold rotational symmetry. The vortex boundaries in the wavy vortex flow are wavy and are S-shaped (Gorman and Swinney, 1982).

The travelling azimuthal waves along the boundary between two neighbouring vortices are shifted in azimuthal phase angle. As the inner cylinder rotates, the flow pattern and the travelling azimuthal waves are non-axisymmetric and unstable, such that the flow undulates and deforms in a wavy-like pattern. Because of this instability and undulation, the flow is eccentric as it travels round the axis of the cylinder, due to the azimuthal instability that develops in addition to the conventional Taylor vortex axisymmetric instability in the flow. Figure 7.4 and Figure 7.5 show schematic illustrations of the characteristic features of the resulting flow pattern. The assembly in Figure 7.4 is defined with respect to the cylindrical reference system (r, θ, x) as in Figure 6.1, where r is the distance from the inner cylinder axis, θ is the azimuthal angle about the axis, and x is the distance along the axis that coincides with the axis of rotation. Figure 7.4 shows the time-averaged vortex eccentricity by the axial and radial displacement of the vortex centres as azimuthal momentum is being transported around the axis of the rotating inner cylinder. The positions of the vortex centres are shown by the oblique ellipses in Figure 7.4. The

dots on the ellipses are the positions of the vortex centres at $\theta = \pm\pi/2$. These are arranged in an alternate pattern and do not all lie at $r = R_i + 0.5d$, which is the centre of the annulus. Figure 7.5(a) shows the variation of the vortex centre position with time. The vortex centre displaces radially with time. This is shown by the round dotted circles in Figure 7.5(a). The displacement amplitude varies with the azimuthal position θ. In Figure 7.5(a), the displacement amplitude is shown to be maximum at $\theta = 0$ and $\theta = \pi$ and zero at $\theta = \pm\pi/2$. This periodic motion can be represented by the linear superimposition of a pair of azimuthal waves, of unit circular wave-number, zero phase angle, and wave speeds of opposite sign, as shown in Figure 7.5(b) and Figure 7.5(c). The long dashed eccentric circle in Figure 7.5(b) shows the anti-clockwise $m = 1$ component of the wave pair. The wave positive maximum is indicated by a solid line at the azimuthal angle $\theta = -\pi/6$. The dash dot eccentric circle in Figure 7.5(b) shows the clockwise $m = -1$ component of the wave pair. The wave positive maximum is indicated by a second solid line at the azimuthal angle $\theta = \pi/6$. The linear interference of the two waves gives the round dotted eccentric circle, which is symmetric about $\theta = 0$ and describes one Taylor vortex centre position at a given instant in time around the inner cylinder. As the azimuthal position of the two azimuthal waves vary by the same magnitude but opposite sign over time, the radial position of the vortex centre changes as shown in Figure 7.5(c). The vortex centre new position is shown by a round dotted eccentric circle as in Figure 7.5(b).

The dotted eccentric circles from Figure 7.5(b) and Figure 7.5(c) are reproduced in Figure 7.5(a) in order to appreciate better the vortex centre motion. The eccentric square dot circle in Figure 7.5(a) denotes the time-averaged position of one of the vortex centres shown in Figure 7.4. The round dotted circles represent two instances of the time-resolved position of the vortex core at times t and $t + \Delta t$, indicating that the vortex position and orientation changes as a function of time.

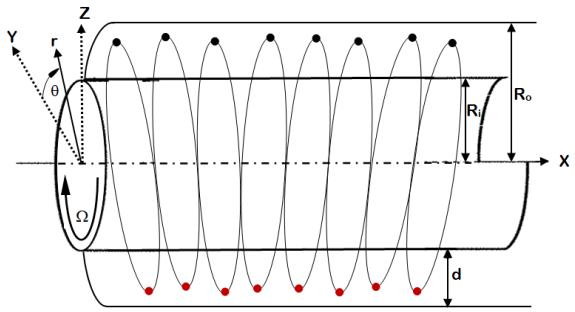

Figure 7.4: Drawing of concentric rotating cylinders showing the time-averaged eccentricity of the vortex centres as azimuthal momentum is being transported around the axis of the rotating inner cylinder.

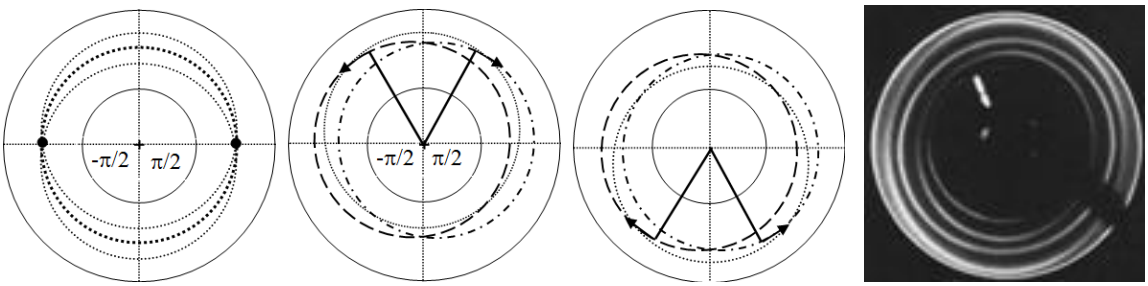

Figure 7.5: (a) Variation of radial displacement of the vortex centre with time, (b, c) linear superimposition of a pair of azimuthal waves, of unit circular wave-number, zero phase angle, and wave speeds of opposite sign, and (d) Particle Laser Induced Fluorescence flow visualisation of wavy vortex flow (Ohji and Amagai, 1988).

The two black dots represent the centre of the vortex at a nodal position for $|m| = 1$. The positions of the dotted circles show that the radial position of the vortex centre is in anti-phase on the $\theta = 0$ and $\theta = \pi$ planes because, when the vortex centre at $\theta = 0$ moves radially outward, the same vortex centre moves radially inward at $\theta = \pi$. Particle Laser Induced Fluorescence (PLIF) flow visualisation of wavy vortex by Ohji and Amagai (1988) provides independent experimental evidence of the vortex core eccentricity in the wavy vortex flow.

For an azimuthal wave pair of zero amplitude, the vortex centres become steady and concentric with the cylinders. The resulting flow is the conventional Taylor Vortex Flow (TVF), which can therefore be interpreted as a sub-class or a special case of the more general wavy vortex flow instability.

Figure 7.6 shows the schematic drawing of the time-averaged wavy vortex flow for the test case $\Gamma = 11.36$. Figure 7.6(a) shows the three-dimensional drawing of the concentric cylinder assembly with the eccentricity pattern of the vortices. Figure 7.6(a) is slightly differs from Figure 7.4 in that the axial displacement of the vortex centres is not so obvious in this test case, as shown later on in section 7.5.2. The assembly in Figure 7.6(a) is defined with respect to the cylindrical reference system (r, θ, x) of Figure 6.1. The positions of the vortex centres are shown by the eccentric circles in Figure 7.6(a). The red dots on the eccentric circles mark the positions of the vortex centres at $\theta = \pm\pi/2$. These are arranged in an alternate pattern along the positive axial direction and do not lie along $r = R_i + 0.5d$ at the centre of the annulus.

The 2D drawing in Figure 7.6(b) shows the third angle projection of the flow pattern and the azimuthal waves as viewed by a fixed observer. The inner and the outer black

concentric circles in Figure 7.6(b) are the rotating inner cylinder and the stationary outer cylinder respectively. The eccentric circles in Figure 7.6(a), represented by the square dotted eccentric circle in Figure 7.6(b), are the positions of the vortex centres that are displaced radially by the azimuthal waves as the waves travel around the rotating inner cylinder. The two solid dots in Figure 7.6(b) represent the positions of the Taylor vortex centre at $\theta = \pm\pi/2$.

The flow pattern illustrated in Figure 7.6 is assumed to involve only one azimuthal wave-number, based on the result of the experimental investigation conducted by King et al. (1984). King et al. (1984) observed that, whenever the aspect ratio is reduced below Γ = 18 (in this study Γ = 11.36), the wavy vortex flow has just one azimuthal wave-number. As the inner cylinder rotates, the travelling azimuthal waves propagate in a moving flow. Where the wave phase speed matches the tangential velocity of the oncoming flow, for instance, at the annulus mid-gap, the wave will appear stationary to a fixed observer in the frame of reference of the outer cylinder.

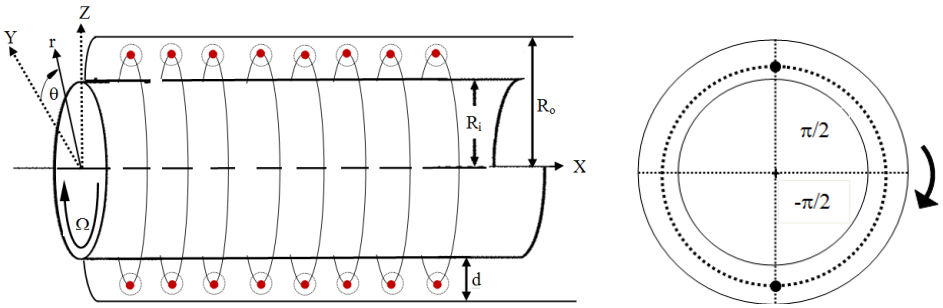

(a) (b) time averaged

Figure 7.6: Schematic drawing of concentric rotating cylinders showing the eccentricity of the Taylor vortices as observed in the experiment.

PIV ensemble averaged velocity vector maps

Figure 7.7(a) and Figure 7.7(b) display the normalised ensemble averaged velocity vector maps obtained from 100 pairs of PIV images in the meridional plane of the annulus for the test cases Γ = 11.36 and Γ = 7.81 respectively. The meridional plane is as defined in Figure 6.1. The extent of the PIV experimental view area for the test cases Γ = 11.36 and Γ = 7.81 is as given in Table 5-2. Figure 7.7(a) and Figure 7.7(b) show that the ensemble averaged flow in the annular region between the rotating inner cylinder and the concentric stationary outer cylinder is dominated by Taylor vortices in the entire measurement area. The ensemble averaged velocity vector maps in Figure 7.7(a) and Figure 7.7(b) consist of pairs of counter-rotating, toroidal vortices spaced periodically along the inner cylinder axis, modulated by the waviness of the flow. This flow pattern of pairs of counter-rotating

vortices, driven by the motion of the rotating inner cylinder, is repeated along the axial shaft with the abutting vortices in consecutive cells rotating in opposite direction at their meeting point. Along the axial direction of the PIV measurement view area, the velocity vectors of Figure 7.7(a) and Figure 7.7(b) show twelve vortices for the test case $\Gamma = 11.36$ and eight vortices for the test case $\Gamma = 7.81$ respectively. This is in both qualitative and quantative agreement with the numerical result presented in Figure 6.6.

In Figure 7.7(a) and Figure 7.7(b), the radial motion induced by the Taylor vortices convects the fluid with high azimuthal momentum near the rotating inner cylinder radially outward, in the outflow regions between two adjacent pair of vortices at $\theta = -\pi/2$. The consequent redistribution of mass flow across the annulus affects the inward flow and the outward flow velocity distribution. Thus, the radial outflow between the vortices is stronger than the radial inflow, as evidenced by the length of the velocity vectors in Figure 7.7(a) and Figure 7.7(b) in agreement with the numerical results of Figure 6.6(a) and Figure 6.6(b). The strong radial azimuthal motion at the outflow boundaries and the mixing of fluid between the adjacent vortices are responsible for the azimuthal waviness (Coughlin and Marcus, 1992; Jones, 1985; Marcus, 1984; Wereley and Lueptow, 1998).

The two vortices near the left and right end boundaries of the PIV experimental view area in Figure 7.7(a) and Figure 7.7(b) are slightly more elongated than the remaining ten vortices in the central region of the annulus, as confirmed by the vortex axial length in Table 7-1 and on pages 207 - 208 for the test cases $\Gamma = 11.36$ and $\Gamma = 7.81$ respectively. The formation of the elongated vortices near the left and right end boundaries and the compressed vortices in the central region are consistent with the numerical results of Figure 6.6. This feature is attributed to the effects of the stationary end-walls, as discussed in section 6.7.1.

In Figure 7.7(a) and Figure 7.7(b), the vortex centres are displaced toward the wall of the outer cylinder. This feature is attributed to the high Taylor number at which the investigations were conducted, as discussed in the context of the numerical results of Figure 6.6.

A distinct pattern of Figure 7.7(a) and Figure 7.7(b) is the spatial oscillation of the Taylor vortices, resulting in the radial and axial displacement of their centres. In Figure 7.7(a) and Figure 7.7(b), the radial displacement of the vortices is clearly shown by the location of the vortex centres. Comparing the vortices at $\theta = -\pi/2$ and those at $\theta = \pi/2$ with one another at the same axial position in Figure 7.7(a) and Figure 7.7(b), an axial oscillation of

the vortex centre position is not so evident in these time-averaged velocity vector maps, whereas it is more evident in the evolution of the instantaneous flow field in time discussed in Figure 7.8(a) and Figure 7.8(b), section 7.5.2.

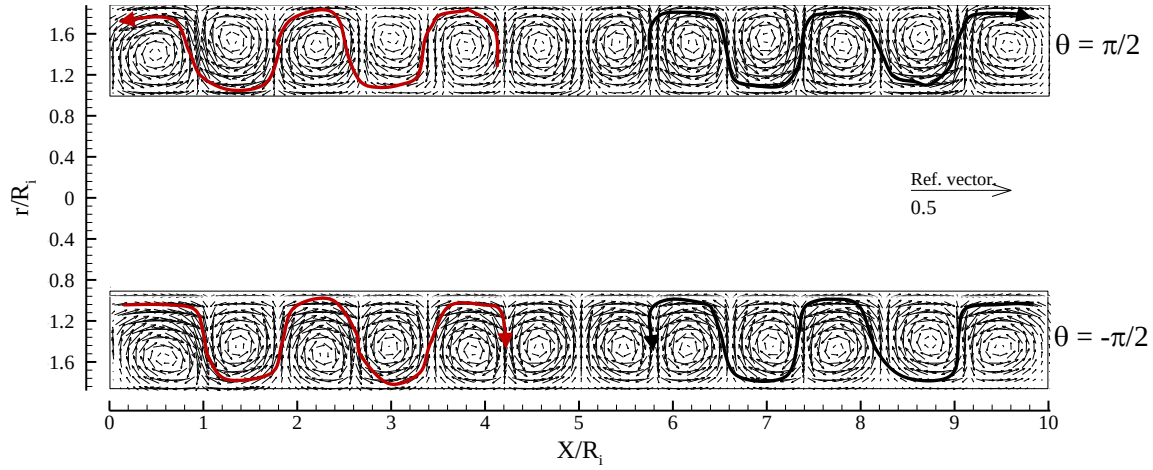

(a)

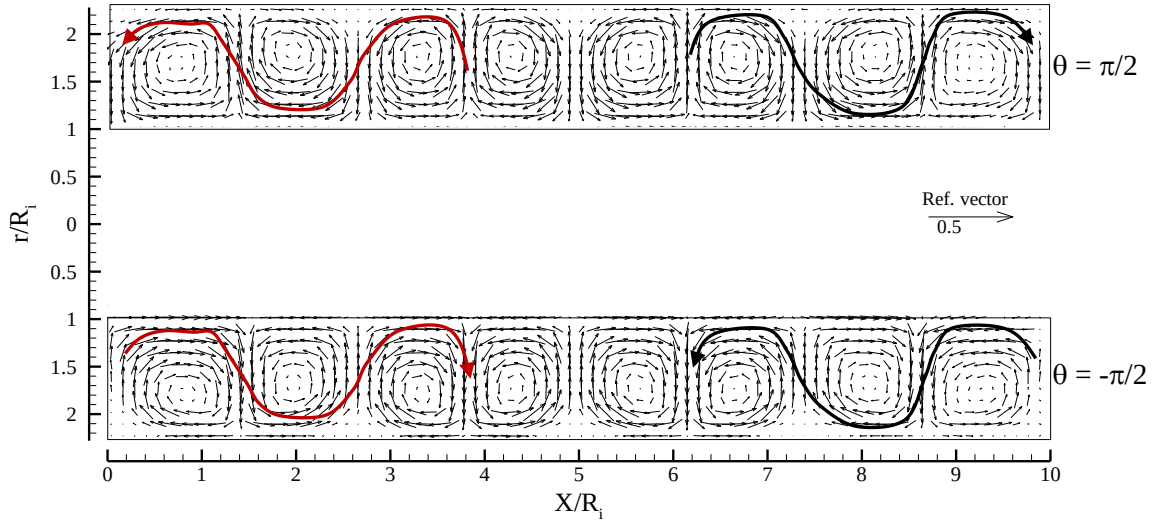

(b)

Figure 7.7: Normalised velocity vectors in the meridional plane of the annulus for the test cases (a) $\Gamma = 11.36$ and (b) $\Gamma = 7.81$. The reference vector is $0.5\Omega R_i$.

The vortices in Figure 7.7(a) and Figure 7.7(b) are organised in a definite pattern in three regions along the axial direction. The first region is toward the left end-wall, the second region is the central region along the length of the cylinders, and third region is the region near the right end-wall. For instance, in Figure 7.7(a), the first region toward the left end-wall (the region marked with red colour) ranges over $0 \leq X/R_i \leq 4.2$. The second region is the central region along the length of the cylinders and ranges over $4.2 \leq X/R_i \leq 5.8$. The third region is the region near the right end-wall (the region marked with blue colour) and ranges over $5.8 \leq X/Ri \leq 10$. The first and the third regions are organised in the same

pattern, in which the centres of a pair of vortices are displaced in an alternate manner, such that when the centre of one vortex is displaced toward the outer cylinder, the centre of the next vortex inbounds is displaced toward the wall of the inner cylinder. For example, on the lower channel of the meridional plane at $\theta = -\pi/2$, the centre of the first clockwise vortex near the left end-wall is displaced toward the wall of the outer cylinder, while the centre of the second anti-clockwise vortex is displaced toward the wall of the inner cylinder. The next pair of vortices follows the same pattern. Similarly, from the right end wall, the same pattern is observed, in which the centre of the last anti-clockwise vortex at $\theta = -\pi/2$ is displaced toward the outer cylinder and the centre of the next inbound clockwise vortex is displaced toward the wall of the inner cylinder. The instance at which the vortex centre is closest to a wall corresponds to the instance that the fluid is winding around the opposite side of the vortex. This results in an axial transport of the flow inbounds at $\theta = -\pi/2$ and outbounds at $\theta = \pi/2$, as indicated by the arrows of the coloured wavy markers in Figure 7.7(a). These two mass fluxes balance each other to satisfy the continuity of mass in this enclosed flow. The radial translation of the vortex centres may be related to the degree of axial flow. A similar flow pattern was observed by Wereley and Lueptow (1998).

In these two regions, the radial motion of the vortex centres can be described to be out of phase because where one vortex moves radially outward at $\theta = -\pi/2$, the same vortex moves radially inward at $\theta = \pi/2$. This phenomenon has been illustrated and explained in the context of Figure 7.5. In the first and the third regions of Figure 7.7(a) for the test case $\Gamma = 11.36$, there is evidence of transfer and mixing of fluid between adjacent vortices in the outflow and inflow regions, indicating that vortex cells are not independent in these regions. Also in these regions, the outflow is stronger than the inflow, consistent with previous measurements reported in the literature by Berland et al. (1986), Heinrichs et al. (1988), and Wereley and Lueptow (1994) for non-wavy and wavy Taylor vortex flows. The stronger outflow results from high azimuthal momentum being convected from the rotating inner cylinder toward the wall of the stationary outer cylinder. This high azimuthal momentum may result in a varying high axial and azimuthal shear stress at the wall of the outer cylinder.

At the centre of the vortex, the flow azimuthal wave velocity is such that its product with the distance of the vortex centre from the cylinder axis is constant for all phases in the wave, even though the position of the vortex centre is displaced radially. Akonur and

Lueptow (2003) observed that the wave speed of the travelling azimuthal wave is equal in magnitude and opposite in sign with respect to the flow azimuthal velocity at the centre of the vortex in their experimental investigation.

In the second region in Figure 7.7(a), which is the central region, the centres of the vortices are almost at the same radial position for both the lower ($\theta = -\pi/2$) and upper ($\theta = \pi/2$) channels. In this region, the inflow and outflow boundaries at $\theta = -\pi/2$ seem perpendicular to the inner and outer cylinder walls. The transfer and mixing of fluid between adjacent vortices is small and the vortex cells seem independent. This is to say that the cross-flow between the vortices in this region is small when compared with the cross-flow in the other two regions at the end boundaries. This region may be described as a region of zero net axial flow and sits between the other two regions as their common interface.

The three regions identified in Figure 7.7(a) also exhibit a unique flow pattern at the inflow and the outflow boundaries. In the first and third regions in Figure 7.7(a), the inflow and outflow boundaries are twisted along the path marked by the red and blue curves and they are not perpendicular to the inner and outer cylinder walls. These flow patterns are typical characteristics of wavy vortex flow, as detailed in the review of section 2.2.4.

The velocity vector map of Figure 7.7(b) for the test case $\Gamma = 7.81$ exhibits a similar pattern to the one of the velocity vector map for test case $\Gamma = 11.36$, with three regions along the axial direction. The first region ranges over $0 \leq X/R_i \leq 3.8$, the second region ranges over $3.8 \leq X/R_i \leq 6.2$, and the third region ranges over $6.2 \leq X/R_i \leq 10$. In the first and the third regions, the centres of a pair of vortices are displaced in the same alternate pattern as in Figure 7.7(a) for the test case $\Gamma = 11.36$. As observed for the test case $\Gamma = 11.36$ in Figure 7.7(a), transfer and mixing of fluid between adjacent vortices occurs in these two regions, especially in the outflow regions, indicating that vortex cells are not independent in these regions. Also, in these regions, the outflow is stronger than the inflow, consistent with the result for the test case $\Gamma = 11.36$.

In the second region in Figure 7.7(b), which is the central region, over the range $3.8 \leq X/R_i \leq 6.2$, the centres of the vortices do not lie on $r = R_i + 0.5d$ line. The vortex centres are displaced toward the wall of the outer cylinder and are almost at the same radial position in both the lower ($\theta = -\pi/2$) and the upper ($\theta = \pi/2$) channels. In this region, the transfer and mixing of fluid between adjacent vortices is comparably small.

As in test case $\Gamma = 11.36$ in Figure 7.7(a), in the first and third regions in Figure 7.7(b), the outflow boundaries are twisted and they are not perpendicular to the inner and outer cylinder walls. In the second region of Figure 7.7(b), the inflow and outflow boundaries at $\theta = \pm\pi/2$ are more perpendicular to the inner and outer cylinder walls. However, the radial variation of the vortex centre position along the axis approaching the end walls indicates that the flow regime is still that of a wavy vortex flow. It is more difficult to detect the waviness of the flow in the second region from the velocity field in the meridional plane shown in Figure 7.7(b) by visual observation. However, close examination of the velocity field in Figure 7.7(b) shows a radial displacement of the vortices based on the location of the vortex centres. The axial displacement of the vortex centre in the axial position at $\theta = \pm\pi/2$ is not as evident in Figure 7.7(b) as in Figure 7.7(a). However, from Figure 7.8(b), there is clear evidence of axial and radial displacement as well as of waviness in the flow at $\Gamma = 7.81$.

In Figure 7.7 for both test cases, it is also observed that (1) the interaction of the waviness with the end-walls does not result in disorder in the flow, either in the vortex near each end-wall or in those farther from the end-walls, (2) the waviness does not significantly alter the boundary layer between the vortex near the end-walls and the end-walls, and (3) the waviness penetrates through the full axial extent of the cylinders and it is not limited to the end-walls in these test cases. In Figure 7.7(a) and Figure 7.7(b), the waviness seems stronger at the end-walls compared to the central regions of the annulus. In Figure 7.7(a) for the test case $\Gamma = 11.36$, the observed waviness seems to extend more into the central region of the annulus from the end-walls than for the test case $\Gamma = 7.81$ in Figure 7.7(b). However, the instantaneous velocity vector map in Figure 7.8(b) for the test case $\Gamma = 7.81$ discussed in section 7.5.2 shows that the waviness also penetrates through the full axial extent of the cylinders.

Observations (1) and (2) in the previous paragraph are in agreement with those made by Czarny et al. (2004). However, there are some discrepancies in the flow pattern observed in this work with respect to the one modelled by CFD by Czarny et al. (2004), especially in Figure 7.7(a). Firstly, Czarny et al. (2004) observed a diminished waviness near the end-walls in their numerical predictions. They attributed this result to the flatness of the end-walls rather than a result of the no-slip condition. Secondly, they reported that the observed waviness is present just one or two vortices away from the end-walls, indicating that the effect of the end-walls on the waviness does not penetrate far from the end-walls.

These observations are different from the experimental evidence in this work. There are two likely reasons for these discrepancies. The first reason is that the study by Czarny et al. (2004) was not an experimental investigation, but rather a numerical simulation with perfectly normal and smooth end-walls and with certain assumptions being made. The second reason is that the radius ratio upon which their investigation was conducted is different from the radius ratio studied in this work. The extent of the waviness cannot be adequately quantified by a mere flow pattern visualisation and further insight is given from the analysis of the location of the vortex centres presented in section 7.5.5.

In Figure 7.7, the variation in the radial position of the vortices in the axial direction is shown by the location of the vortex centres. When the vortices at $\theta = -\pi/2$ and those at $\theta = \pi/2$ are compared with one another at the same axial position, a variation of the axial position of the vortex centres is not clearly seen. In the present study, the normalised axial spacing between the vortex centres is larger than the normalised radial spacing between the vortex centres for both test cases. The physical axial spacing is also larger than the physical radial spacing between the vortex centres. This may explains why the axial displacement of the vortex centres is not clearly seen in this study. In the experimental investigation conducted by Wereley and Lueptow (1998), they observed oscillations in both the axial and radial directions, with the former being the greatest. In their experiment, the working fluid was a mixture of water, glycerol, sodium iodide, and trace amounts of sodium thiosulfate with silver-coated hollow glass spheres of an average diameter of 14μm added as PIV seed particles in a volume concentration of about 1.0×10^{-4}. In the current work, air at ambient temperature and pressure is the working fluid. The observed difference may be ascribed to the different fluids being used in the two experiments.

Generally, it is difficult to make a direct comparison between the results obtained in this study and those reported in the literature, as the flow characteristics depend on the combination of radius ratio (η), aspect ratio (Γ), end-wall conditions, and Reynolds number/Taylor number. In this work, $\Gamma = 11.36$, $\eta = 0.53$, and $Re = 1973$ for the first test case. For the second test case, $\Gamma = 7.81$, $\eta = 0.53$, and $Re = 2870$. In both test cases, the resulting flow regime is Wavy Vortex Flow (WVF). Wereley and Lueptow (1998) first observed non-wavy vortex flow at $Re = 102$ and WVF at $Re = 131$, which persisted up to $Re = 1221$, while testing at $\Gamma = 47.7$ and $\eta = 0.830$. Walden and Donnelly (1979) observed transition to WVF at different Reynolds numbers depending on Γ. For instance, at $\Gamma = 20$ and $\Gamma = 80$, the transition to WVF occurred at $Re = 2614$ and at $Re = 3089$ respectively.

Their test range was $\Gamma \geq 20$ and $\eta = 0.875$. Walden and Donnelly (1979) stated that the re-emergence of wavy vortices above the turbulent vortex transition occurs only for a sufficiently large aspect ratio $\Gamma \geq 25$. They attribute this threshold to the influence of end effects in short devices. Takeda (1999) determined by experiment the first critical Reynolds number $Re_c = 134.57$ and observed WVF over the range $1830 \leq Re \leq 4845$ at $\Gamma = 20$ and $\eta = 0.904$. Wang et al. (2005) observed the reappearance of azimuthal waves at a high Reynolds number in cylinders at $\Gamma = 34$ and $\eta = 0.733$. Akonur and Lueptow (2003) first observed non-wavy vortex flow at Re = 97.1 and WVF at Re = 126 for $\Gamma = 47.8$ and $\eta = 0.81$. The geometry parameters used by these investigators are quite different from the ones used in this work. Lewis and Swinney (1999) acquired velocity measurements at a high Reynolds number in an apparatus with an aspect ratio Γ over the range $9.8 \leq \Gamma \leq 11.4$. The aspect ratio used in the current work falls within this range, but the radius ratio $\eta = 0.724$ is higher than in this work. They observed the presence of azimuthal waves up to a Reynolds number Re = 9375, which is higher than the Reynolds numbers Re = 1970 and Re = 2870 in this work. Therefore, some differences in the flow documented in this work with respect to the one in other investigations are to be expected, due to the differences in η, Γ, Re/Ta, and in the end-wall conditions. These four parameters have been shown by Cole (1976), Debler et al. (1968) Eagles (1971), Snyder and Lambert (1966), Snyder (1969a) to greatly influence the flow regime in Taylor-Couette system.

7.5.2 Instantaneous flow structures

The evolution of the instantaneous flow field in time was obtained in order to improve the understanding of the flow regime that develops in the annular region for test cases $\Gamma = 11.36$ and $\Gamma = 7.81$. The velocity vectors in Figure 7.8(a) and Figure 7.8(b) show a sequence of three instantaneous velocity fields in the meridional plane $\theta = -\pi/2$ for test cases $\Gamma = 11.36$ and $\Gamma = 7.81$ respectively. The velocity fields are taken in quick succession at recording times $t = t_0 + 0.0s$, $t = t_0 + 0.25s$, and $t = t_0 + 0.50s$ with the time increasing from bottom to the top, as shown by the arrows, where t_0 is the PIV image acquisition start time. PIV acquisition is started after the inner cylinder has reached the steady rotational speed ΩR_i. The instantaneous velocity vectors have been normalised by ΩR_i. In each time frame in Figure 7.8(a) and Figure 7.8(b), the wall of the rotating inner cylinder is on the top side and the wall of the stationary outer cylinder is on the bottom side. The flow patterns in Figure 7.8(a) and Figure 7.8(b) show that the vortex centres

oscillate in the radial and axial directions. The result of this oscillation is the shift in the vortex centres with time, as shown by the black arrows in Figure 7.8(a) and Figure 7.8(b). However, the shifting of the vortex centres in the axial direction is more prominent in the test case $\Gamma = 7.81$ than in the test case $\Gamma = 11.36$. The flow pattern observed for the test case $\Gamma = 7.81$ is best described schematically by the wavy vortex flow pattern sketched in Figure 7.4. At the boundaries of the inflow and outflow regions, there is a slight displacement of the radially aligned velocity vectors in the axial direction with time, though not as significant as the vortex centre motion, as indicated by the red arrows in Figure 7.8(a) and Figure 7.8(b).

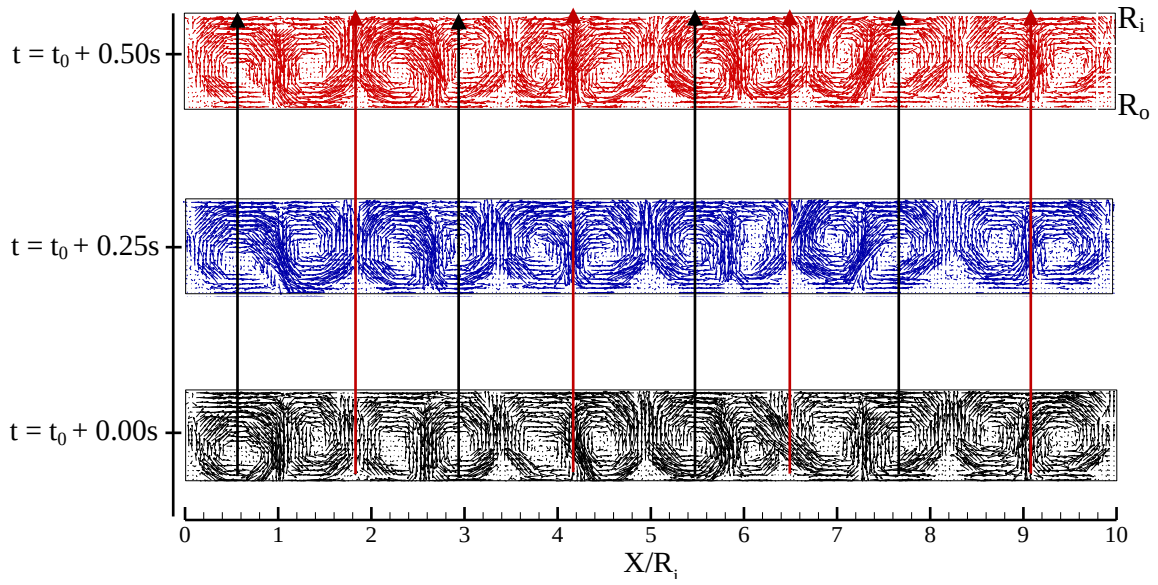

(a)

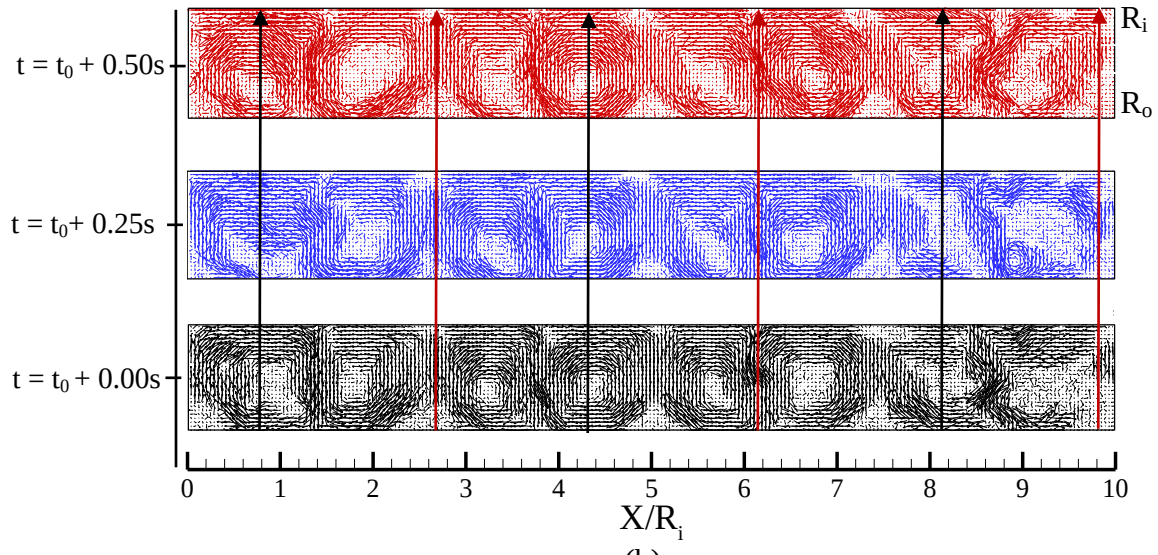

(b)

Figure 7.8: Instantaneous velocity vectors in the meridional plane ($\theta = -\pi/2$) for test cases (a) $\Gamma = 11.36$ and (b) $\Gamma = 7.81$. The time sequence $t = t_0 + 0.00s$, $t = t_0 + 0.25s$, and $t = t_0 + 0.50s$.

As earlier observed in Figure 7.7, the inflow and outflow boundaries are twisted. The observed flow features are evidence of the presence of azimuthal waves that characterise the wavy vortex flow regime. In Figure 7.8(a) and Figure 7.8(b), the magnitude of the vortex motion and of the oscillation of the inflow and outflow boundaries are not so significant as to fully disrupt the main Taylor vortex flow pattern. In Figure 7.8(b), the flow regime does not change with respect to that of Figure 7.8(a) but the instability develops across one additional degree of freedom, which is the axial motion of the instability waves. This is shown schematically in Figure 7.4.

Considering the Taylor number at which the measurements are taken, the vortex centre motion suggests that the flow regime is the wavy vortex flow that probably re-emerges at high Taylor numbers. This may be related to the re-emergence of azimuthal waves at high Taylor number and larger aspect ratios reported by Walden and Donnelly (1979), Takeda (1999), Lewis and Swinney (1999), and Wang et al. (2005). The type of fluid mixing between adjacent vortices reported by Wereley and Lueptow (1998) at a high Taylor number is evident in the instantaneous velocity vectors in Figure 7.8(a) and Figure 7.8(b). The time-averaged velocity vectors and the instantaneous velocity vector field in Figure 7.7 and Figure 7.8 show that the inflow and the outflow boundaries are not all flat and perpendicular to the cylinder wall.

Figure 7.9(a) and Figure 7.9(b) show the normalised instantaneous radial velocity profiles at a constant radial distance $r = R_i + 0.5d$ on the lower ($\theta = -\pi/2$) channels of the meridional plane for the test cases $\Gamma = 11.36$ and $\Gamma = 7.81$. The profiles are obtained from the sequence of the three velocity vector map in Figure 7.8 for both test cases. These profiles exhibit the same trend of alternating radial velocity maxima and minima. The shapes of the radial velocity maxima and minima are essentially constant in the time sequence of $0 \leq t + t_0 \leq 0.5$ seconds. The locations of the radial velocity maxima in Figure 7.9 mark the meeting points of the radial outflow between two adjacent vortices (induced downwells at $\theta = -\pi/2$ and induced upwell at $\theta = \pi/2$) on the meridional plane. Similarly, the locations of radial velocity minima mark the meeting point of the radial inward flow between two adjacent vortices (induced upwells at $\theta = -\pi/2$ and induced downwell at $\theta = \pi/2$) in the meridional plane, as discussed in the context of Figure 6.16. The locations of the zero crossing of the radial velocity mark the centres of each vortex. The radial velocity profiles in Figure 7.9 further confirm that the variation in the radial velocity distribution among the three instantaneous flow fields is quite small. The profiles in Figure 7.9(a) for

the test case Γ = 11.36 show a smaller variation in the radial velocity distribution among the three instantaneous flow fields when compared with the profiles in Figure 7.9(b) for the test case Γ = 7.81.

From the instantaneous velocity vectors of Figure 7.8 and the radial velocity profiles in Figure 7.9, there seems to be a small contribution to the unsteady radial velocity due to travelling azimuthal waves. This indicates that the travelling azimuthal waves responsible for the wavy vortex flow are present at this high Reynolds number. Some of the features of wavy vortex flow reported by previous researchers are not observed in both the mean velocity vector maps and the instantaneous velocity vectors of Figure 7.7 and Figure 7.8 respectively. However, based on the visual observation and the analysis from Figure 7.7 to Figure 7.9, the flow pattern throughout the annulus in these test cases exhibits the main characteristics of wavy vortex flow.

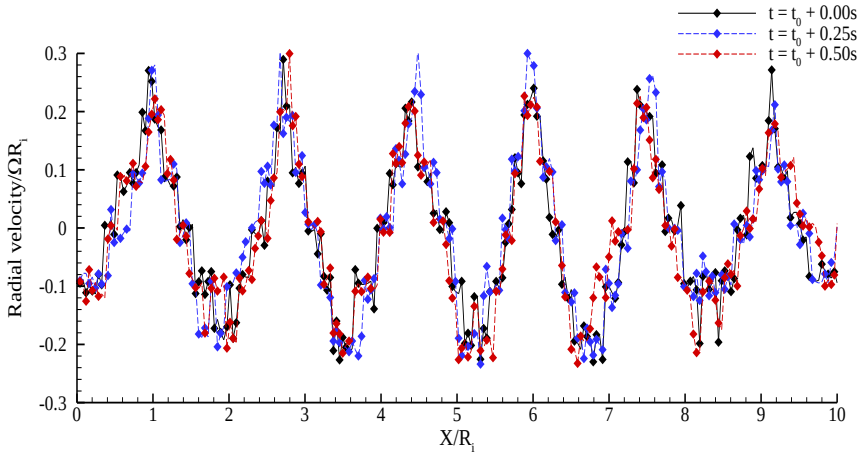

(b)

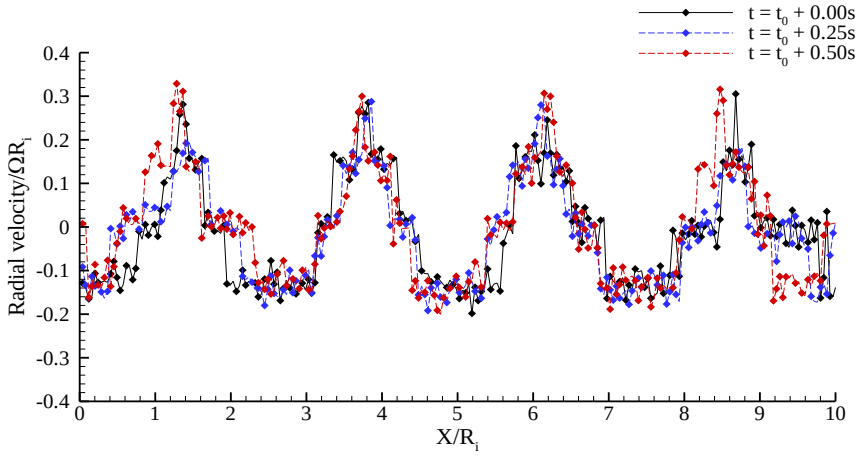

(b)

Figure 7.9: Normalised instantaneous radial velocity at constant radial position r = R_i + 0.5d on the meridional plane θ = -π/2 at times t = t_0 + 0.00s, t = t_0 + 0.25s, and t = t_0 + 0.50s for the test cases (a) Γ = 11.36 and (b) Γ =7.81.

7.5.3 Axial and radial velocity contour plots

Figure 7.10 and Figure 7.11 show the contour plots of axial and radial velocity in the meridional plane from PIV for the test cases Γ = 11.36 and Γ = 7.81. All velocities are normalised by the surface speed of the inner cylinder ΩR_i. The contour lines of the plots in Figure 7.10 and Figure 7.11 are evenly spaced with the contour spacing of $0.03\Omega R_i$, which is the same contour spacing used for the coaxial cylinder test cases Γ = 11.36 and Γ = 7.81 in the CFD simulations in chapter six.

Figure 7.10(a) and Figure 7.10(b) show the contour plots of the axial velocity for the test cases Γ = 11.36 and Γ = 7.81 respectively. The formation of an alternating pattern of axial velocity maxima and minima in the annulus in the same axial position as the vortex centres is shown in Figure 7.10 for both test cases.

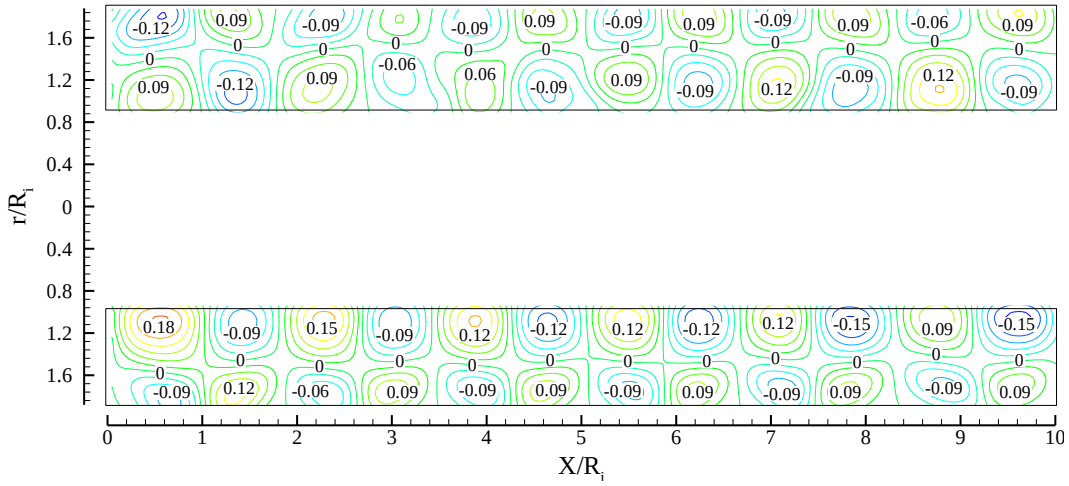

(a)

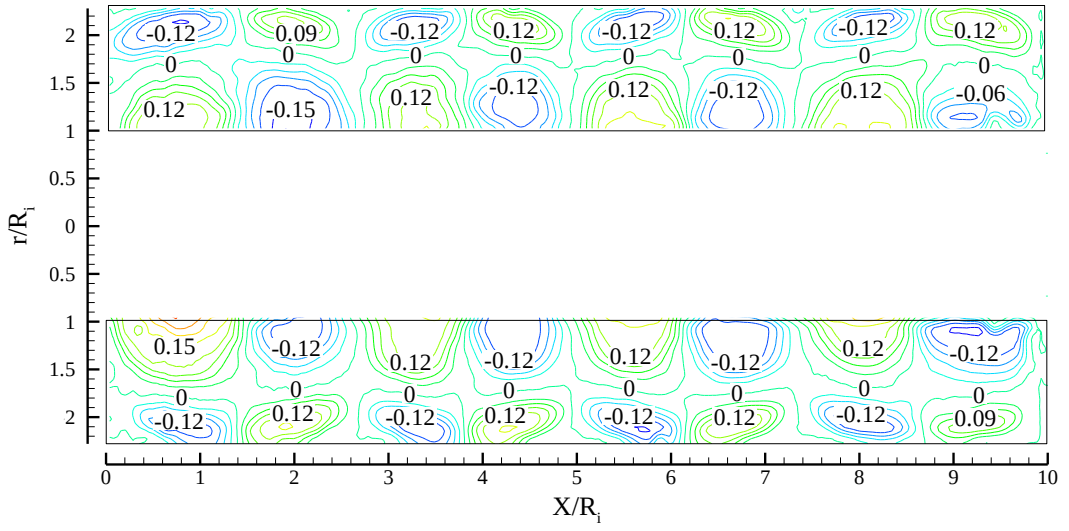

(b)

Figure 7.10: Contour plots of axial velocity in the meridional plane normalised by ΩR_i with contour spacing $\Delta u_r = 0.03\Omega R_i$ for the test cases (a) Γ = 11.36 and (b) Γ = 7.81.

The zero contour lines between the axial velocity maxima and minima in Figure 7.10(a) and Figure 7.10(b) are the radial positions of the vortex centres in Figure 7.7(a) and Figure 7.7(b). The contour plots in Figure 7.10 exhibit similar features as the contour plots obtained from the CFD simulation results discussed in details in the context of Figure 6.8. Figure 7.11(a) and Figure 7.11(b) show the normalised radial velocity contour plots for the test cases $\Gamma = 11.36$ and $\Gamma = 7.81$ respectively with an alternating pattern of radial velocity minima and maxima along the axial direction. As in the radial velocity contour plots obtained from the CFD simulations in Figure 6.9, the contour plots in Figure 7.11 are colour coded. This feature has been discussed in the context of Figure 6.9. The positive and negative values on these contour clusters indicate outward flow regions and inward flow regions respectively at $\theta = -\pi/2$ at the meeting point of two adjacent vortices in Figure 7.7.

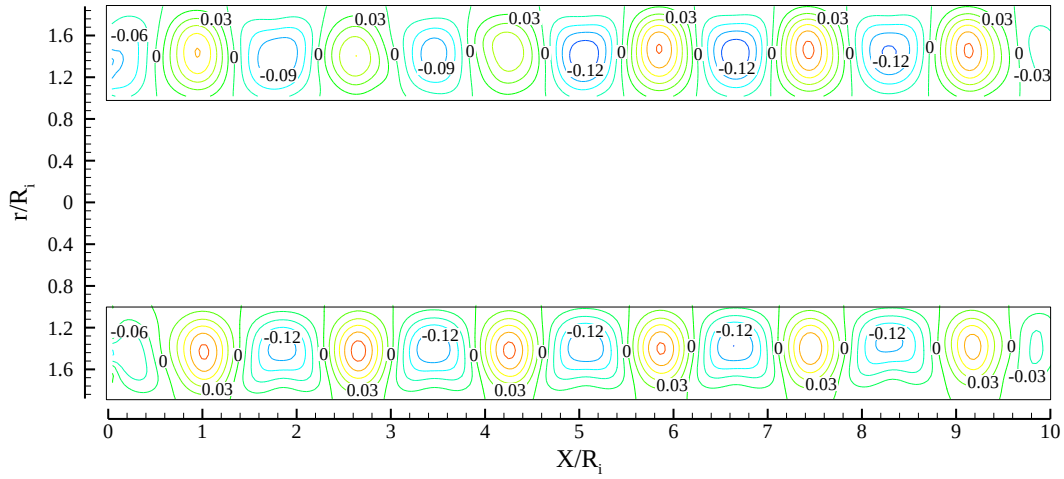

(a)

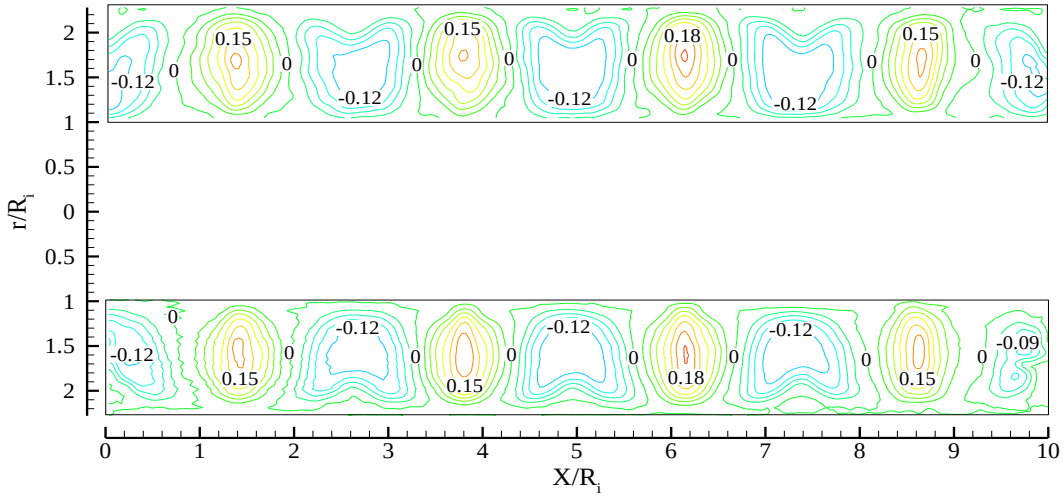

(b)

Figure 7.11: Contour plot of radial velocity in the meridional plane normalised by ΩR_i with contour spacing $\Delta u_r = 0.03\Omega R_i$ for the test cases (a) $\Gamma = 11.36$ and (b) $\Gamma = 7.81$.

The axial boundaries that show the zero velocity contours between the negative and positive values on these contour clusters run through the centres of the vortices in Figure 7.7. The radial velocity contours in Figure 7.11 show the same features and are consistent with the contour plots of Figure 6.9 for the CFD simulations. The observed twelve vortices and thirteen radial velocity extrema shown for the test case $\Gamma = 11.36$ in Figure 7.11(a), and eight vortices and nine radial velocity extrema shown for the test case $\Gamma = 7.81$ in the entire domain of Figure 7.11(b) is in quantitative agreement with the CFD simulation result in Figure 6.9. All the flow features observed in Figure 7.11(a) and Figure 7.11(b) has been discussed in details in the context of Figure 6.9 in chapter six.

7.5.4 In-plane velocity profiles in the meridional plane

This section presents a detailed quantitative analysis of the in-plane velocity profiles obtained from the velocity vectors in the meridional plane of Figure 7.7(a) and Figure 7.7(b) for the test cases $\Gamma = 11.36$ and $\Gamma = 7.81$. Velocity profiles were extracted and plotted at three constant radial positions along the axial direction on the lower ($\theta = -\pi/2$) channel of the annulus from Figure 7.7(a) and Figure 7.7(b). The radial positions along the lower channel on the meridional plane for the test case $\Gamma = 11.36$ are $r = R_i + 0.875d$ (2.75mm away from the wall of the outer cylinder), $r = R_i + 0.5d$ (the mid-span gap of the annulus), and $r = R_i + 0.125d$ (2.75mm away from the wall of the inner cylinder). The positions of the constant radial line where the profiles are extracted are 1.75mm inbounds from the walls of the inner and outer cylinders with respect to the positions shown in Figure 6.15 for the test case $\Gamma = 11.36$. These positions are chosen because the PIV interrogation areas overlap close to the wall, as such the PIV is unable to measure accurately closer than 2mm from the wall. For the test case $\Gamma = 7.81$, the positions of the constant radial line where the profiles are extracted are taken at the same percentage gap width d as for test case $\Gamma = 11.36$. The velocity profiles presented here have been normalised with respect to the inner cylinder surface speed ΩR_i.

The velocity profiles cut through the inward and outward flow regions of Figure 7.7(a) and Figure 7.7(b) for the test cases $\Gamma = 11.36$ and $\Gamma = 7.81$ respectively. In the velocity profiles of Figure 7.12 to Figure 7.17, the PIV error bands are included to document the experimental uncertainty. The experimental uncertainty is calculated based on the standard deviation, σ, computed from the measurements. The standard deviation shows how much variation or dispersion a set of data has from its average or mean value. A low standard

deviation indicates that the data points tend to be very close to the mean, whereas a high standard deviation indicates that the data points are spread out over a large range of values. Equation 6.8 has been used to compute the standard deviation values.

In Figure 7.12 and Figure 7.13, the centres of the inward and outward flows are oblique saddle planes of axial velocity separating each Taylor vortex. The axial velocity profiles display alternating maxima and minima, with zero crossings in between, which is where the $r = R_i + 0.5d$, mid-span cylindrical surface intersects the oblique saddle planes in the meridional planes. The axial velocity is observed to be relatively small compared with the surface speed of the inner cylinder, with each maximum and minimum at $r = R_i + 0.125d$ and $r = R_i + 0.875d$ indicating the axial position of a vortex core.

Figure 7.12(a) and Figure 7.12(b) show the normalised axial velocity profiles for the test cases $\Gamma = 11.36$ and $\Gamma = 7.81$ respectively along the meridional plane at constant radial positions $r = R_i + 0.125d$ and $r = R_i + 0.875d$ on the lower ($\theta = -\pi/2$) channel with the PIV experimental uncertainty σ in black and red dashed lines.

The normalised axial velocity profiles in Figure 7.12 show that the axial velocity maxima occur radially below the cores of clockwise vortices and the axial velocity minima occur radially below the cores of anti-clockwise vortices of Figure 7.7 for the profiles near the wall of the inner cylinder at $r = R_i + 0.125d$ and $\theta = -\pi/2$ for both test cases. Similarly, the profiles near the wall of the outer cylinder at $r = R_i + 0.875d$ and $\theta = -\pi/2$ show that the axial velocity maxima occur radially above the cores of the anti-clockwise vortices and the axial velocity minima occur radially above the cores of the clockwise vortices of Figure 7.7 for both test cases.

The normalised axial velocity maxima and minima at $r = R_i + 0.125d$ and $r = R_i + 0.875d$ in Figure 7.12 for both test caes occur almost at the same axial location along X/R_i. Each axial velocity maximum and minimum pair is almost radially aligned. The axial velocity is driven by the motion of the vortices. Each clockwise vortex induces an axial velocity maximum radially below its core at $r = R_i + 0.125d$ and a minimum radially above its core at $r = R_i + 0.875d$ at $\theta = -\pi/2$. Similarly, each anti-clockwise vortex induces an axial velocity minimum radially below its core at $r = R_i + 0.125d$ and a maximum radially above its core at $r = R_i + 0.875d$ and at $\theta = -\pi/2$. This flow pattern is similar and consistent with the computational results of Figure 6.8 and Figure 6.14 for both test cases.

The profiles near the inner cylinder wall at $r = R_i + 0.125d$ in Figure 7.12 show that the flow is almost centrally symmetric about the cylinder length mid-span at $X/R_i = 5$. That is,

the profile over the range $0 \leq X/R_i \leq 5$ and the one over the range $5 \leq X/R_i \leq 10$ seem to be mirror image of one another about the symmetry point $X/R_i = 5$. This is shown by the magnitude of the axial velocity maximum and minimum near the left end-wall and near the right end-wall respectively having almost the same magnitude. The profiles also show almost the same magnitude of the axial velocity maxima and minima in the central region of the annulus at $1.4 \leq X/R_i \leq 8.8$ for the test case $\Gamma = 11.36$, and at $2 \leq X/R_i \leq 8$ for the test case $\Gamma = 7.81$, about the mid-span length at $X/R_i = 5$.

For the profile near the wall of the inner cylinder at $r = R_i + 0.125d$ for the test case $\Gamma = 11.36$ in Figure 7.12(a), the axial velocity maximum and minimum near the end-wall boundaries are approximately $0.2\Omega R_i$ and $-0.2\Omega R_i$ respectively. For the same profile and the same test case, the axial velocity maxima and minima in the central region are approximately $0.17\Omega R_i$ and $-0.17\Omega R_i$ respectively. These values correspond to 20% of the speed of the inner cylinder at the boundaries and approximately 17% in the central region.

For the profile at the radial position $r = R_i + 0.125d$ for the test case $\Gamma = 7.81$ in Figure 7.12(b), the axial velocity maximum and minimum near the end-wall boundaries are approximately $0.17\Omega R_i$ and $-0.17\Omega R_i$ respectively, while the axial velocity maxima and minima in the central region are approximately $0.15\Omega R_i$ and $-0.15\Omega R_i$ respectively. These values correspond to 17% of the speed of the inner cylinder at the boundaries and 15% of the speed of the inner cylinder in the central region. At this radial position, the difference in the axial velocity between the two test cases is approximately 2%.

The profile near the wall of the outer cylinder at $r = R_i + 0.875d$ in Figure 7.12(a) for the test case $\Gamma = 11.36$ shows that the magnitude of the axial velocity minimum near the left end-wall is lower than the magnitude of the axial velocity minima in the central region of the annulus as well as near the right end-wall. The magnitude of the axial velocity minima is highest in the central region over the range $3.9 \leq X/R_i \leq 7.2$. The magnitude of axial velocity maxima for the profile at this radial position is higher near the left end-wall over the range $1.4 \leq X/R_i \leq 4.6$, from where it decreases toward the right end-wall. Over the range $1.4 \leq X/R_i \leq 4.6$ in Figure 7.12(a), the axial velocity maxima near the left end-wall are $0.17\Omega R_i$, whereas the axial velocity maximum near the right end-wall is $0.13\Omega R_i$. The difference in the magnitude of axial velocity maximum near the left and the right end-walls may be attributed to the influence of the slit at the left end wall through which the laser light sheet illuminates the flow in the PIV measurement area. The right end-wall was a complete end wall without any slit. The second factor may be due to the effect of light

reflection at the right end-wall during the experimental measurement. The difference in the end-wall conditions and the effect of light reflection gives the observed asymmetry near the wall of the outer cylinder. The axial velocity maxima over the range $4.6 \leq X/R_i \leq 7.8$ are approximately $0.15\Omega R_i$. The axial velocity minima near the left and the right end-walls at the same radial position $r = R_i + 0.875d$ are approximately $-0.12\Omega R_i$ and $-0.16\Omega R_i$ respectively, whereas the axial velocity minima at the central region of the annulus over the range $3.9 \leq X/R_i \leq 7.2$ is approximately $-0.17\Omega R_i$.

The profile near the outer cylinder wall at $r = R_i + 0.875d$ in Figure 7.12(b) for the test case $\Gamma = 7.81$ shows that the axial velocity is centrally symmetric about the mid-span $X/R_i = 5$. For instance, the magnitude of the axial velocity minimum near the left end-wall and the magnitude of the axial velocity maximum near the right end-wall are almost the same. Similarly, the axial velocity maximum at $X/R_i = 2$ is almost the same as the axial velocity minimum at $X/R_i = 8$. This trend is repeated along the central region of the annulus up to the mid-span position $4.3 \leq X/R_i \leq 5.7$ where the axial velocity maximum and minimum are almost the same. This flow pattern is similar and consistent with the axial velocity profile from the CFD simulation in Figure 6.14(b). At this radial position, the axial velocity minimum near the left end-wall at $X/R_i \approx 0.8$ is approximately $-0.14\Omega R_i$, whereas the axial velocity maximum near the right end wall at $X/R_i \approx 9.3$ is approximately $0.11\Omega R_i$. The difference in the magnitude between these two axial velocity extrema has been attributed to the effect of light reflection at the right end-wall during the experimental measurement. The axial velocity minima and maxima at this radial position in the central region of the annulus are approximately -0.15Ω and 0.15Ω respectively.

Figure 7.12(a) for the test case $\Gamma = 11.36$ shows that the PIV measurement uncertainty band is narrower near the left end-wall over the range $0 \leq X/R_i \leq 3$, whereas the measurement uncertainty band is larger over the range $3 \leq X/R_i \leq 10$, resulting in a larger spread of data points about the mean velocity profile.

In Figure 7.12(b) for the test case $\Gamma = 7.81$, the PIV measurement uncertainty band is larger near the left and the right end-walls over the ranges $0 \leq X/R_i \leq 2.6$ and $7.6 \leq X/R_i \leq 10$, whereas the measurement uncertainty band is narrower over the range $2.6 \leq X/R_i \leq 7.6$, resulting in a smaller spread of data points about the mean velocity profile in the central region of the annulus.

The negatively sloped inflection points on the profile near the wall of the outer cylinder at $r = R_i + 0.875d$ in Figure 7.12 correspond to the positions of the inflow regions in Figure

7.7 for both test cases. These positions correspond to the area where low momentum fluid near the outer wall is convected inwardly by the radial inflow. The inflections may therefore be an indication of a non-monotonic shear layer at the inflow region as a result of low radial momentum convected from the stationary outer cylinder.

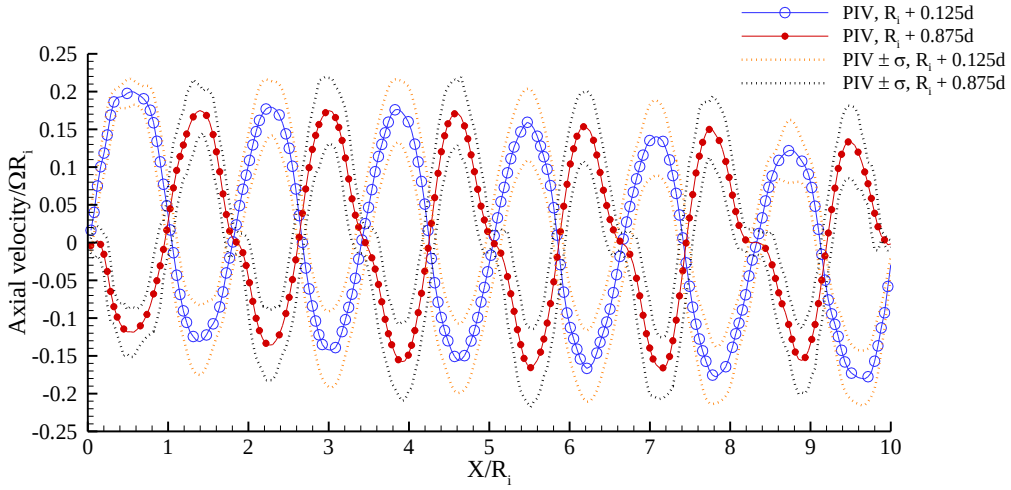

(a)

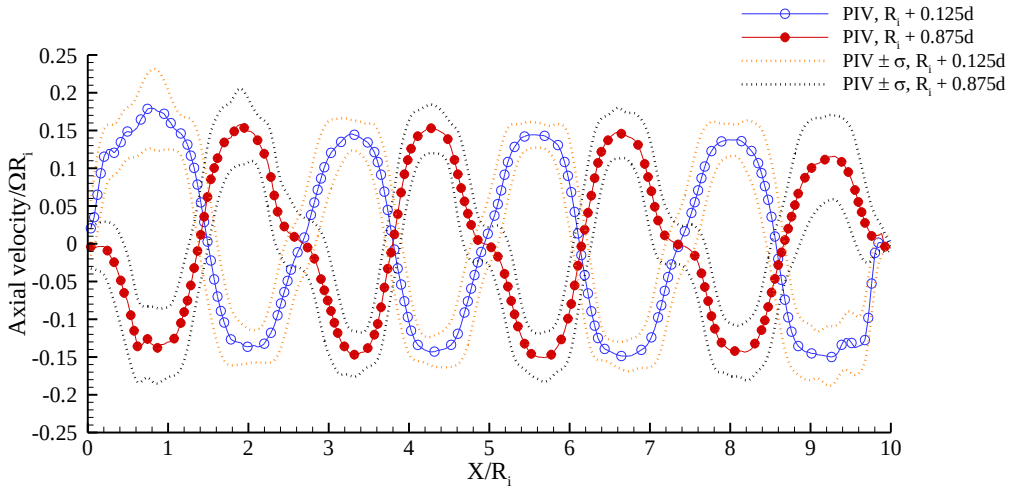

(b)

Figure 7.12: Normalised axial velocity profiles in the meridional plane at constant radial positions r = R_i + 0.125d and r = R_i + 0.875d with PIV error bands (θ = -π/2) for the test cases (a) Γ = 11.36 and (b) Γ = 7.81.

The difference in the magnitude of the axial velocity near the wall of the inner cylinder and that near the wall of the outer cylinder in Figure 7.12 for both test cases is observed to be small, indicating that there is just a small imbalance of net axial flow along both walls, due to the flow regime being that of wavy vortex flow. In Figure 7.12(a) and Figure 7.12(b), it is observed that the axial position of the maxima and minima near the wall of the inner cylinder are aligned with the corresponding axial position of the maxima and

minima near the wall of the outer cylinder. This further confirms the near zero net mass flux balance in the axial flow along both walls. As the fluid with high transported momentum is been convected from the wall of the inner cylinder, there is mixing of fluid at the confluence with the mirror stream from the adjacent vortex. As the fluid moves toward the outer cylinder, the amount of azimuthal momentum that was imparted by the inner cylinder rotation has not been significantly reduced before recirculating flow gets to the same axial position where the fluid near the wall of the outer cylinder displays an axial velocity peak, resulting in the velocity maxima near the wall of the inner cylinder and minima near the wall of the outer cylinder to almost be of similar magnitude at the same axial position. The same process applies to the axial velocity minima near the wall of the inner cylinder and maxima near the wall of the outer cylinder around clockwise Taylor vortices.

Figure 7.13(a) and Figure 7.13(b) show the normalised axial velocity profiles at $r = R_i + 0.5d$ (the gap mid-span of the annulus) at $\theta = -\pi/2$ for the test cases $\Gamma = 11.36$ and $\Gamma = 7.81$ respectively. Axial velocity maxima occur close to the cores of clockwise vortices and axial velocity minima occur close to the cores of the anti-clockwise vortices. The speed range covered by the normalised axial velocity profiles at this radial position is relatively small compared to the surface speed of the rotating inner cylinder and the speed range of the corresponding profiles at $r = R_i + 0.125d$ and $r = R_i + 0.875d$. These profiles qualitatively match the CFD trend discussed in Figure 6.15. Actually, the normalised axial velocity at this radial position should have been zero if not for the radial displacement of the vortex centres that prevents the centres from lying at $r = R_i + 0.5d$. Since the centres of the vortices do not lie along the $r = R_i + 0.5d$ line, there is a small axial velocity induced by the vortices at $R_i + 0.5d$. The normalised axial velocity profiles in Figure 7.13 show that the axial velocity maxima are higher near the left end-wall than the axial velocity maxima in the central region and near the right end-wall, with the axial velocity maxima decreasing monotonically from the left end-wall to the right end-wall. For instance, Figure 7.13(a) for the test case $\Gamma = 11.36$ shows the axial velocity maxima near the left and the right end-walls to be approximately $0.09\Omega R_i$ and $0.01\Omega R_i$ respectively. The normalised axial velocity profiles in Figure 7.13(a) shows that the axial velocity minima near the end-walls are almost the same and are higher than the axial velocity local minima in the central region. In the central region over the range $1 \leq X/R_i \leq 9$, the axial velocity minima have almost the same magnitude of $0.04\Omega R_i$. This corresponds to 4% of the surface speed of the

inner cylinder. This trend, which was also observed near the wall of the outer cylinder, has been discussed in the context of Figure 7.12. Figure 7.13(b) shows a similar trend as Figure 7.13(a). For the test case $\Gamma = 7.81$ in Figure 7.13(b), the axial velocity maxima near the left and the right end-walls are approximately $0.07\Omega R_i$ and $0.02\Omega R_i$ respectively. The axial velocity profile in Figure 7.13(b) shows that the axial velocity minimum near the left end-wall is higher than the axial velocity minima in the central central region and the axial velocity minimum near the right end-wall.

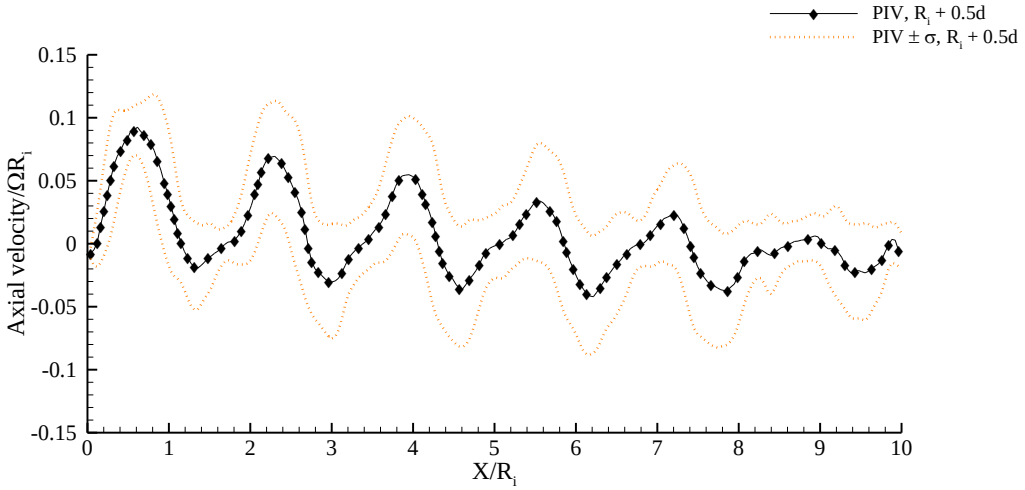

(a)

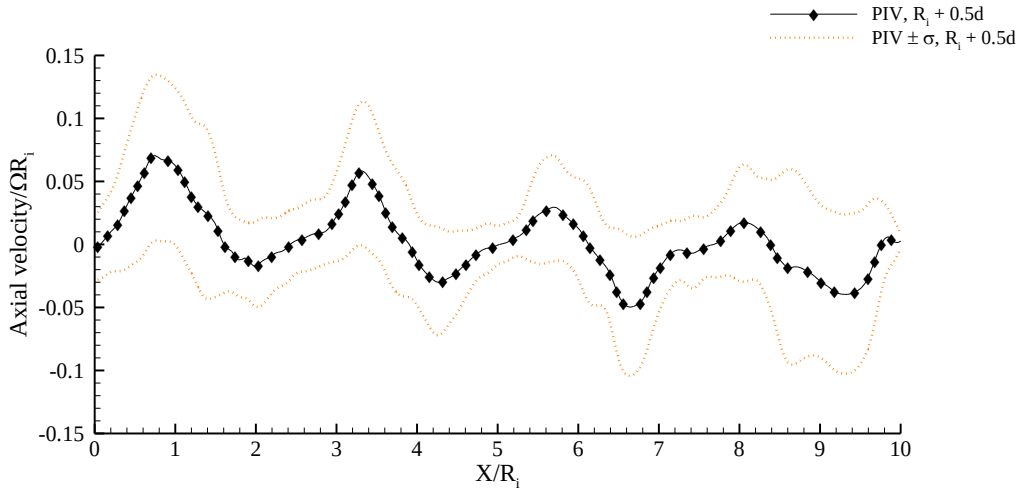

(b)

Figure 7.13: Normalised axial velocity profiles in the meridional plane at constant radial position $r = R_i + 0.5d$ ($\theta = -\pi/2$) with PIV error bands for the test cases (a) $\Gamma = 11.36$ and (b) $\Gamma = 7.81$.

It is not clear why there should be the axial decay in the magnitude of the axial velocity extrema with X/R_i along the constant radial position $R_i + 0.5d$ shown in Figure 7.13, considering the fact that all the PIV vectors in Figure 7.7 seem validated, based on the

validated result in Figure 7.2 and Figure 7.3. The trend of the axial velocity profiles at this radial position has been attributed to a combination of two factors. These are (1) the effect of light sheet reflection at the right end-wall, the PIV being unable to measure accurately close to the wall, and (2) the misalignment in the wall boundaries, that is, if the end-wall boundaries were not perfectly aligned perpendicular to the inner cylinder rotation axis, then this may have resulted in a periodic forcing of the flow. A further contributory factor may be other unavoidable mechanical perturbations of the system.

Figure 7.14(a) and Figure 7.14(b) show the normalised radial velocity profiles at the radial positions $r = R_i + 0.125d$, $r = R_i + 0.5d$, and $r = R_i + 0.875d$ in the meridional plane of the lower ($\theta = -\pi/2$) channel for the test cases $\Gamma = 11.36$ and $\Gamma = 7.81$ respectively. The radial velocity profiles in Figure 7.14 show that away from the end-wall boundaries, in the central region over the range $1 \leq X/R_i \leq 9$ for the test case $\Gamma = 11.36$ and over the range $1.4 \leq X/R_i \leq 8.56$ for the test case $\Gamma = 7.81$, the radial velocity exhibits alternating minima and maxima along the positive axial direction. The radial velocity maxima and minima correspond to the outward flow regions and inward flow regions identified in Figure 7.7. The observed trend in Figure 7.14 is the same as that of the radial velocity profiles for the CFD results in Figure 6.16. The locations of the radial velocity maxima and the radial velocity minima in Figure 7.14 mark the meeting points of the radial outflow and radial inward flow respectively, between two adjacent vortices (induced downwells at $\theta = -\pi/2$) on the meridional plane of Figure 7.7. The locations of the zero crossing of the radial velocity in Figure 7.14 mark the centres of each vortex at $\theta = -\pi/2$ on the meridional plane of Figure 7.7.

As in Figure 6.16 for the CFD, the radial velocity profiles in Figure 7.14 exhibit a periodic trend along the axial direction. This periodic trend is more obvious in the profile at the gap mid-span radial position $r = R_i + 0.5d$ ($-\pi/2$), this being the position at which the radial velocity reaches its maximum value. At this radial position, approximately six and four cycles of a periodic oscillation along X/R_i are shown in Figure 7.14(a) and Figure 7.14(b) for the test cases $\Gamma = 11.36$ and $\Gamma = 7.81$ respectively. The radial velocity profiles of Figure 7.14 also show that the radial velocity is not symmetric about $u_r = 0$ along the gap mid-span $r = R_i + 0.5d$. For instance, the magnitude of maximum radial velocity at $r = R_i + 0.5d$ ($\theta = -\pi/2$) for test case $\Gamma = 11.36$ is approximately $0.22\Omega R_i$ and the magnitude of minimum radial velocity is approximately $0.16\Omega R_i$. This feature is as result of the displacement of the vortex centres in both the axial and radial directions discussed in

details in section 7.5.1 in the context of Figure 7.7 and Figure 7.8. The asymmetry of the radial velocity profiles has also been discussed in section 6.7.3 in the context of Figure 6.16.

The profiles in Figure 7.14 are replotted in Figure 7.15 to Figure 7.17 with the PIV experimental measurement uncertainty included. The red dashed lines above and below the velocity profiles in Figure 7.15 to Figure 7.17 delimit the PIV measurement uncertainty error band, which is determined from the statistical procedure of section 6.7.3 using equation 6.8.

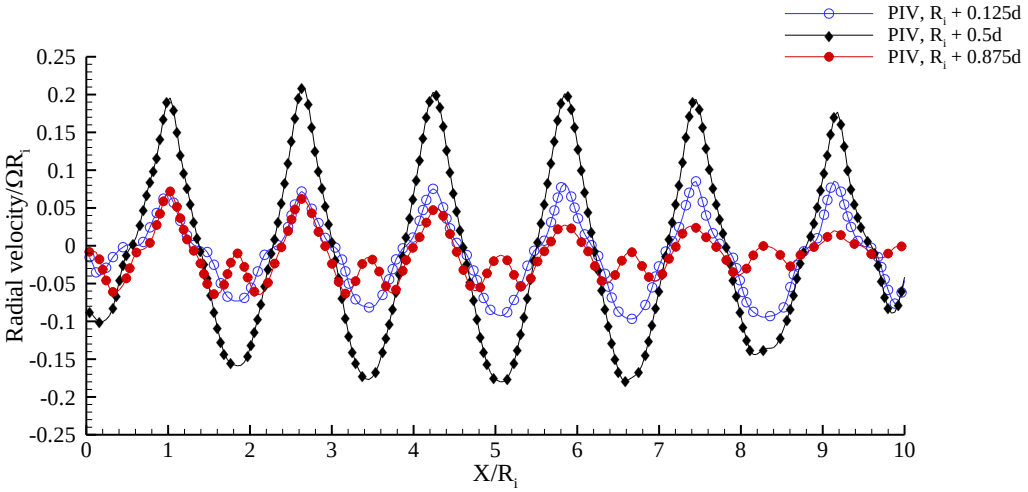

(a)

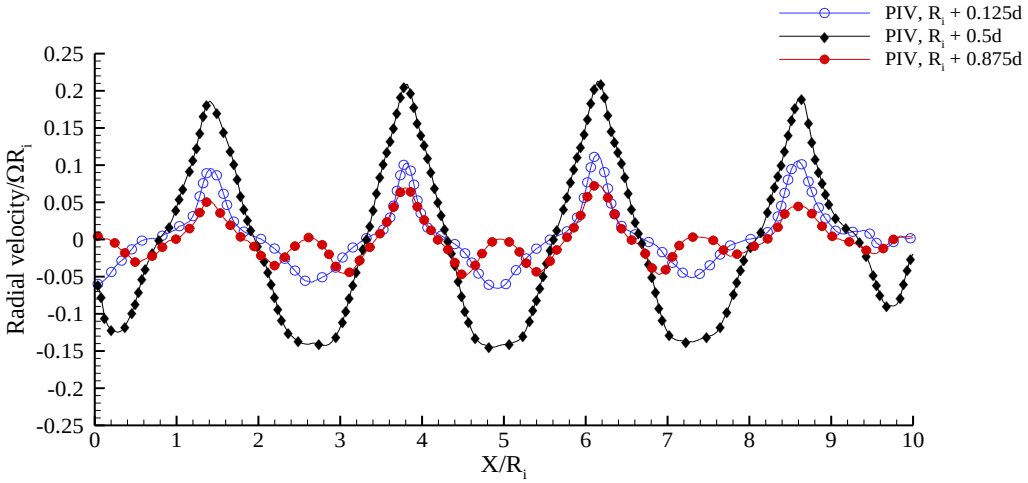

(b)

Figure 7.14: Normalised radial velocity profiles in the meridional plane at constant radial positions r = R_i + 0.125d, r = R_i + 0.5d, and r = R_i + 0.875d at θ = -π/2 for the test cases (a) Γ = 11.36 and (b) Γ = 7.81.

Figure 7.15(a) and Figure 7.15(b) show the enlarged normalised radial velocity profiles at r = R_i + 0.125d for the test cases Γ = 11.36 and Γ = 7.81 respectively. The radial velocity

maxima and minima near the left end-wall of Figure 7.15 are observed to be slightly different compared to the ones at the right end-wall. This feature is probably due to the difference in the boundary conditions at the two end-walls, as discussed in the context of Figure 7.12 and to the limitations of the PIV techniques as discussed in the context of Figure 7.13.

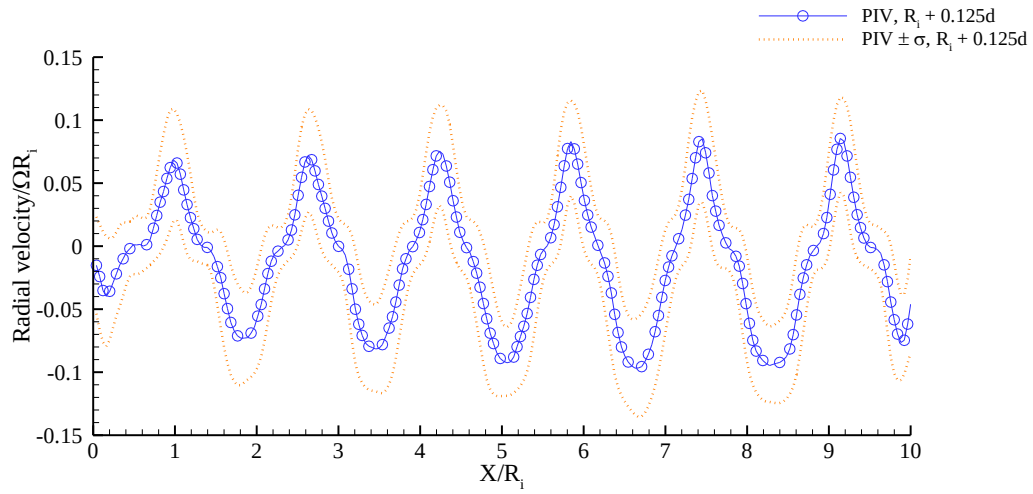

(a)

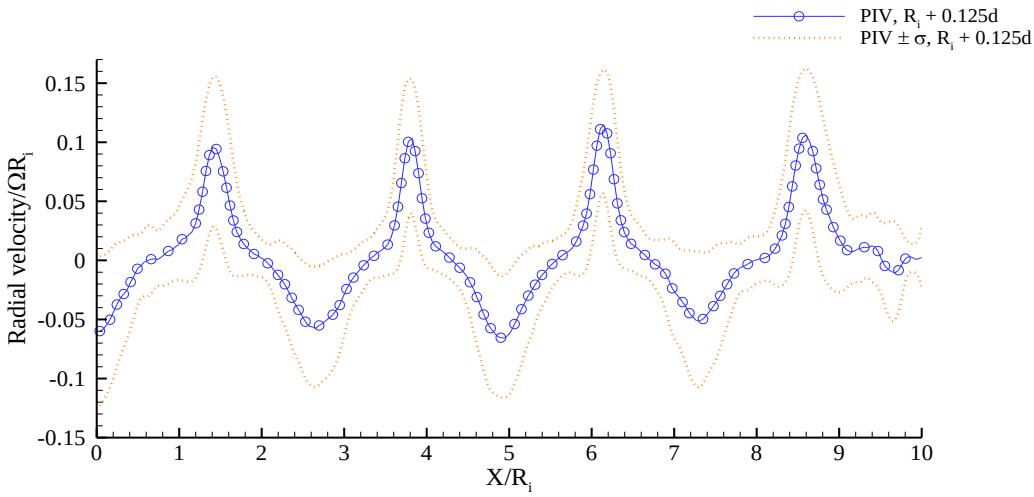

(b)

Figure 7.15: Normalised radial velocity profiles in the meridional plane at constant radial position $r = R_i + 0.125d$, $\theta = -\pi/2$ with PIV error band for the test cases (a) Γ = 11.36 and (b) Γ = 7.81.

The peak of the outward flow in Figure 7.15 is sharper than the peak of the inward flow, indicating that the strength of the induced radial velocity by the vortices is higher at the outflow regions than at the inward flow regions at either side of each oblique saddle plane. Figure 7.16(a) and Figure 7.16(b) display the normalised radial velocity profiles at the gap mid-span of the annulus at $r = R_i + 0.5d$ for the test cases Γ = 11.36 and Γ = 7.81

respectively, with the PIV uncertainty error band. The trend of the radial velocity profile in Figure 7.16 is similar to that of the CFD results discussed in the context of Figure 6.17. The radial velocity profiles in Figure 7.16 show that the radial velocity local minimum near the left end-wall is lower than the radial velocity local minimum near the right end-wall. The variation is attributed to the difference in the boundary conditions at these walls. At the central region of the annulus, the radial velocity local minima are smaller than the radial velocity local minima near the left and the right end-walls.

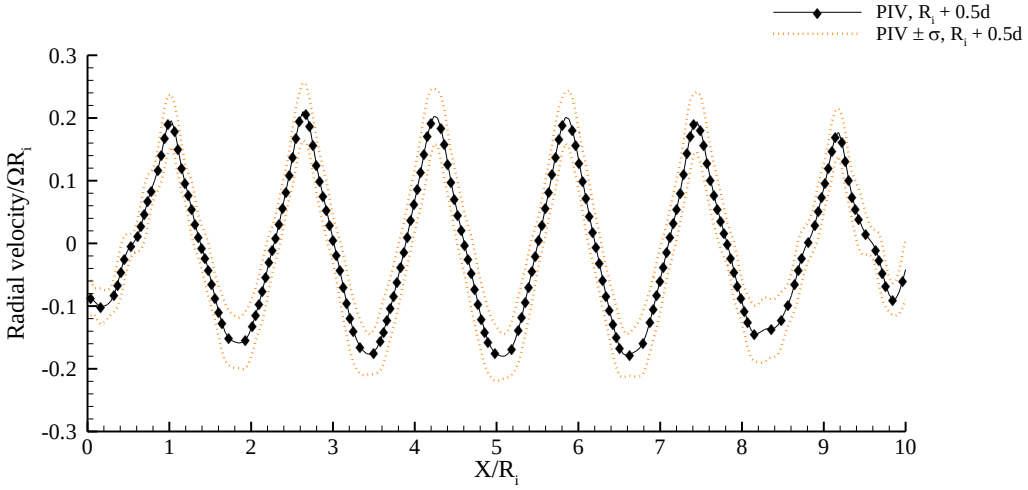

(a)

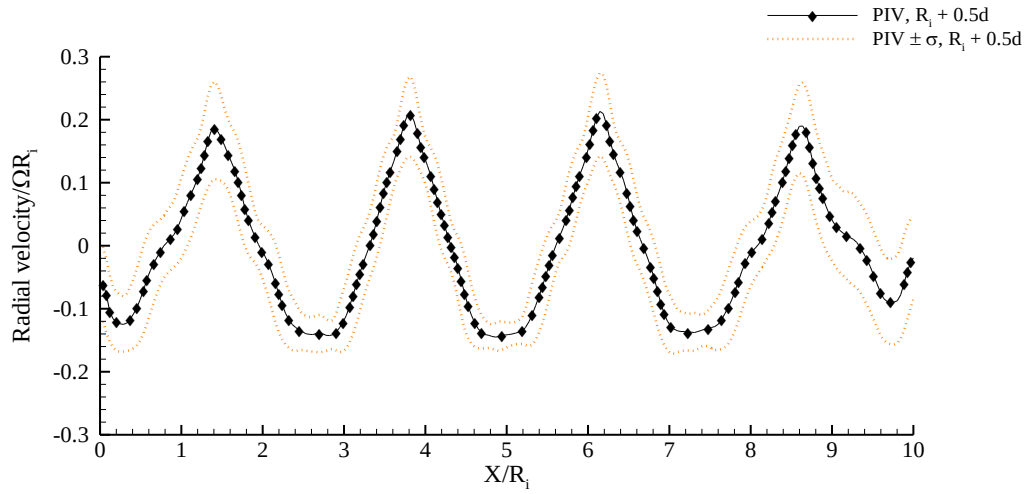

(b)

Figure 7.16: Normalised radial velocity profiles in the meridional plane at constant radial position $r = R_i + 0.5d$, $\theta = -\pi/2$ with PIV error band for the test cases (a) $\Gamma = 11.36$ and (b) $\Gamma = 7.81$.

The radial velocity maxima near the end-wall boundaries in Figure 7.16 are almost the same, with radial velocity magnitude of approximately $0.2\Omega R_i$. Near the right end-wall in Figure 7.16(a), the radial velocity maximum is slightly lower with a magnitude of

approximately $0.18\Omega R_i$. At the central region of the annulus in Figure 7.16, the radial velocity maxima are almost the same with a radial velocity magnitude of approximately $0.22\Omega R_i$.

In Figure 7.16, the PIV measurement uncertainty band is essentially uniform in the axial direction over the range $1 \leq X/R_i \leq 9.2$ for test case $\Gamma = 11.36$ and over the range $1.4 \leq X/R_i \leq 8.6$ for test case $\Gamma = 7.81$. This resulted in a narrower spread of data points about the mean velocity profile over the entire annulus compared to Figure 7.15. The peak of the outward flow in Figure 7.16 is sharper than the trough of the inward flow. This trend has been discussed in the context of Figure 7.15.

Figure 7.17(a) and Figure 7.17(b) display the normalised radial velocity profiles near the wall of the outer cylinder at $r = R_i + 0.875d$ for the test cases $\Gamma = 11.36$ and $\Gamma = 7.81$ respectively. These profiles differs from the profiles at $r = R_i + 0.125d$ shown in Figure 7.15. At the outward flow regions, the profiles at the radial positions $r = R_i + 0.125d$ and $r = R_i + 0.875d$ show one single peak. The inward flow pattern is instead quite different, as the single trough minima observed at $r = R_i + 0.125d$ in Figure 7.15 has been replaced by double trough minima at $r = R_i + 0.875d$ in the profiles of Figure 7.17. This trend was also observed in the CFD radial velocity profiles in Figure 6.17 for the same test cases. This phenomenon has been discussed in details in chapter six in the context of Figure 6.17.

The normalised radial velocity profiles in Figure 7.17(a) and Figure 7.17(b) display higher amplitude radial velocity maxima and minima near the left end-wall than at the right end-wall. In Figure 7.17(a) and and Figure 7.17(b), the magnitudes of the radial velocity maxima and minima vary from one axial location to the other in the entire annulus. This trend, which is attributed to the misalignment in the wall boundaries and other unavoidable mechanical perturbations of the system, has been discussed in the context of Figure 7.13.

In Figure 7.17(b), the normalised radial velocity profiles seem to be an approximate mirror image of one another about the annulus mid-span $X/R_i = 5$, allowing for the asymmetric end-wall boundary effects. At $X/R_i = 5$, the double trough minima have almost the same radial velocity magnitude. Similarly, the radial velocity maxima over the range $3.8 \leq X/R_i \leq 6.2$ have almost the same magnitude. The radial velocity profile to the left and right of $X/R_i = 5$ over the range $3.8 \leq X/R_i \leq 6.42$ in Figure 7.17(b) exhibits a symmetric trend. This symmetry indicates a net balance in the radial velocity mass transport along the central region of the annulus near the wall of the outer cylinder.

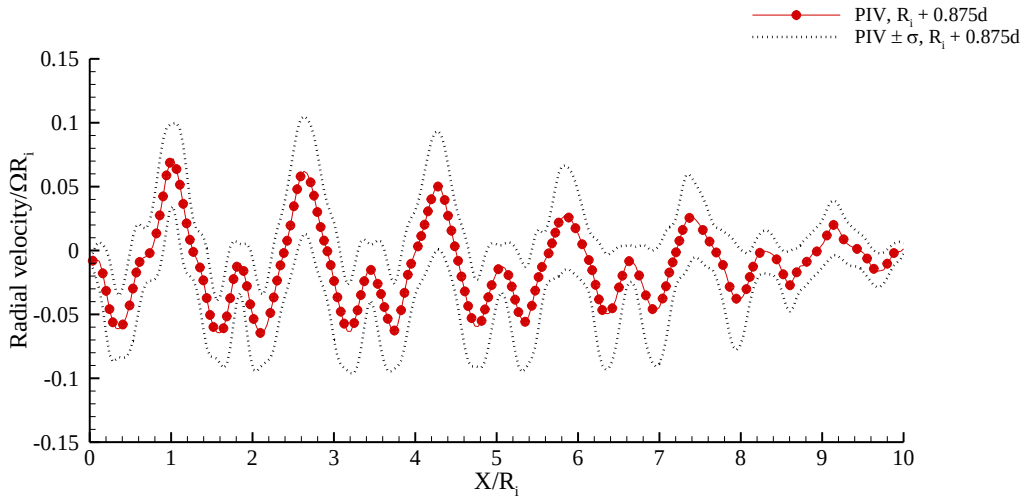

(a)

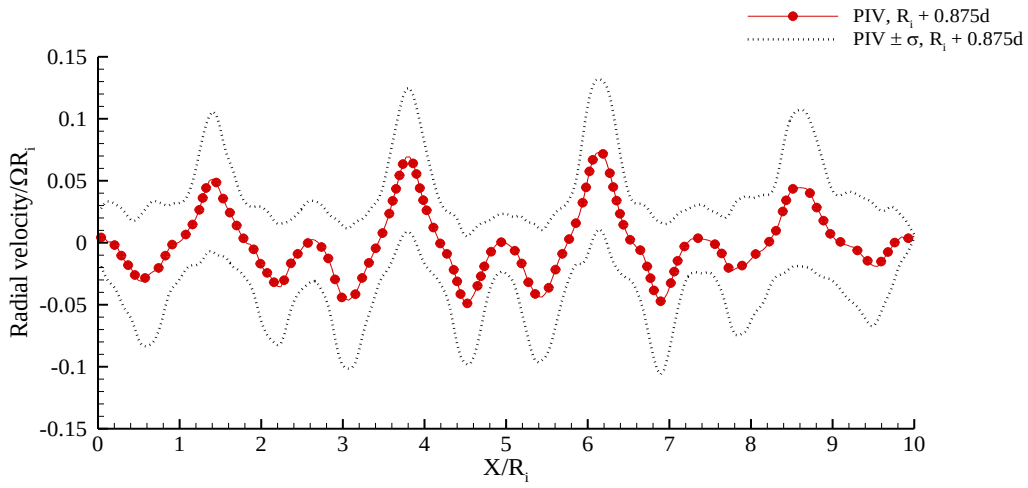

(b)

Figure 7.17: Normalised radial velocity profiles in the meridional plane at constant radial position r = R_i + 0.875d, θ = -π/2 with PIV error band for the test cases (a) Γ = 11.36 and (b) Γ = 7.81.

7.5.5 Parametric analysis of the Taylor vortices

This section documents the variation of the Tayor vortex centre and Taylor vortex size with the parameter Γ for the test cases Γ = 11.36 and Γ = 7.81.

Analysis of Taylor vortex centres

The locations of the Taylor vortex centres for the coaxial cylinders test cases Γ = 11.36 and Γ = 7.81 are estimated as in section 6.7.8. The axial coordinate X_c and the radial coordinate r_c of each of the vortex centre are used to mark the centres of the vortices in Figure 7.18. The numerical values of the vortex centre coordinates for the test cases Γ = 11.36 and Γ = 7.81 can be found in Table B 3 and Table B 4 of appendix B.

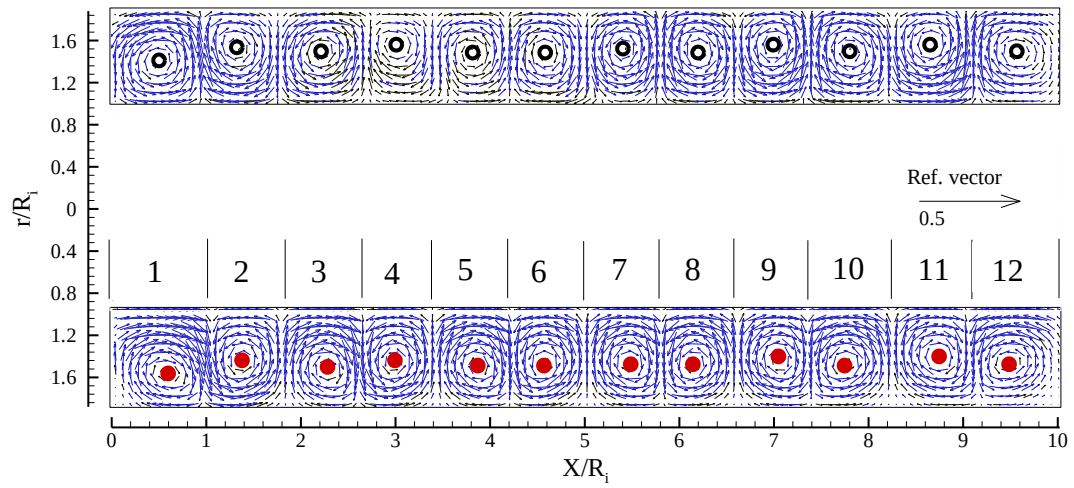

(a)

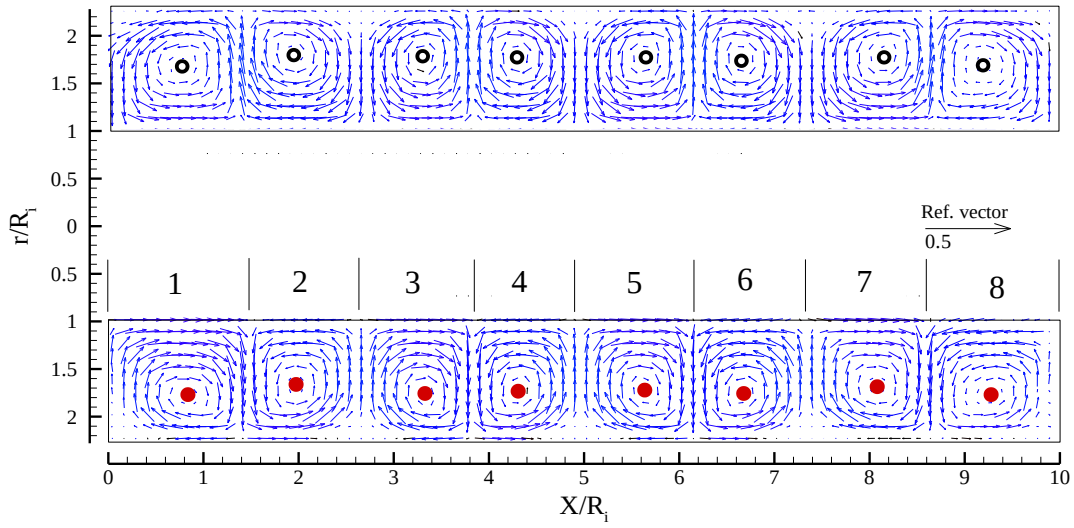

(b)

Figure 7.18: Velocity vectors showing the centre of the vortices in red and black on the meridional plane at $\theta = \pm\pi/2$ for the test cases (a) $\Gamma = 11.36$ and (b) $\Gamma = 7.81$.

The axial and radial values reported in Table B 3 and Table B 4 and the positions of red and black markers on both the lower ($\theta = -\pi/2$) and the upper ($\theta = \pi/2$) channels of Figure 7.18 further confirm that the vortex centre radial positions vary along X/R_i. The amplitude of the spatial oscillation of the vortex centres is analysed in details in the discussion of Figure 7.19 and Figure 7.20.

Figure 7.19(a) and Figure 7.19(b) show the plots of the normalised axial position of the Taylor vortex centres as a function of their normalised radial position in the meridional plane for the test cases $\Gamma = 11.36$ and $\Gamma = 7.81$ respectively. Figure 7.19 uses the same open and filled symbols as in Figure 7.18 to identify the vortex centres at $\theta = \pm\pi/2$. Figure 7.19(a) and Figure 7.19(b) are used to illustrate the radial spread of the vortex centres in

the meridional plane at $\theta = \pm\pi/2$ for both test cases. The black dashed lines toward the top and bottom of Figure 7.19 represent respectively the maximum and minimum limits of the spread band about the vortex centre mean radial position value, averaged along X/R_i. The standard deviation of the vortex radial positions was used to size the spread band using equation 6.8, assuming a normal distribution. The axial position in Figure 7.19 has been normalised by the inner cylinder radius R_i, while the radial position is normalised by the cylinder gap width d. This is related to the cylindrical coordinates system of Figure 6.1 by the ordinate in Figure 7.19 being equal to $(r - R_i)/d$. The vortices have been numbered in the sequence shown in Figure 7.18, starting at the left end-wall along the positive axial direction. From Figure 7.18, the axial distance from the centre of each vortex to the centre of the next one to the right of it in the same plane at $\theta = \pm\pi/2$ is estimated. From Figure 7.18(a), Figure 7.18(b), Figure 7.19(a), and Figure 7.19(b), a streamwise variation in the radial position of the Taylor vortex centres along the cylinders in each channel is evident.

Comparing the locations of the vortex centres between the lower and upper channels of the annulus in Figure 7.19, a small variation in the axial position of the vortex centres between $\theta = \pi/2$ and $\theta = -\pi/2$ is noticeable. In Figure 7.19, there is a larger variation in the radial location of the vortex centres at $\theta = -\pi/2$ and $\theta = \pi/2$ for many of the vortices due to the spatial oscillation of the vortices along X/R_i in the normalised radial position $(r - R_i)/d$. These observations stand whether the vortex radial and axial coordinates are stated as dimensional or non-dimensional.

The vortex centres in both the lower and the upper channels ($\theta = \pm\pi/2$) in Figure 7.18(a) and Figure 7.18(b) are displaced in a well-organised pattern, such that, when one vortex is displaced toward the wall of the stationary outer cylinder, the next vortex is displaced toward the wall of the rotating inner cylinder. This is also shown in Figure 7.19(a) and Figure 7.19(b), suggesting that this feature is independent from the aspect ratio Γ over the range tested. This pattern further confirms the inference from Figure 7.7 and Figure 7.8 that the flow regime in the coaxial cylinder test cases $\Gamma = 11.36$ and $\Gamma = 7.81$ is that of wavy vortex flow.

In Figure 7.19, it is observed that the radial displacement of the vortex centres in the lower and upper channels ($\theta = \pm\pi/2$) is highest near the end-walls over the range $0 \leq X/R_i \leq 4.5$ and $6.2 \leq X/R_i \leq 10$ for the test case $\Gamma = 11.36$, and over the range $0 \leq X/R_i \leq 3.2$ and $6.7 \leq X/R_i \leq 10$ for the test case $\Gamma = 7.81$. That is, the radial spacing of the vortex centres toward the end-wall boundaries is higher than in the central region and follows a

symmetric pattern about $X/R_i = 5$. In the central region of the annulus, the radial spacing of the vortex centres at $\theta = \pm\pi/2$ are less spread out radially, as observed and discussed in the context of Figure 7.7.

Figure 7.19(a) for the test case $\Gamma = 11.36$ shows that there is a larger radial spacing between the centres of vortices 1 and 2, 2 and 3, 3 and 4, 4 and 5, 8 and 9, 9 and 10, 10 and 11, as well as 11 and 12 in both the lower and upper channels ($\theta = \pm\pi/2$) of the annulus. These are the vortices near the end-wall boundaries. The radial spacing between vortices 1 and 2 as well as vortices 11 and 12 is directly affected by the end-wall boundaries, as discussed in section 6.7.8. The radial spacing between the centres of the vortices 5 and 6, 6 and 7, and 7 and 8 is comparatively smaller, these being the vortices in the central region of the annulus. That is, the vortices in the central region of the annulus are less scattered radially.

Similarly, the plot for the test case $\Gamma = 7.81$ in Figure 7.19(b) shows that, in both the lower and the upper channel ($\theta = \pm\pi/2$), a larger radial spacing occurs between vortices 1 and 2, 2 and 3, 6 and 7, as well as vortices 7 and 8. These are also the vortices near the end-wall boundaries. As for the test case $\Gamma = 11.36$ in Figure 7.19(a), the radial spacing between vortices 1 and 2 as well as vortices 7 and 8 are directly affected by the end-wall boundaries for the test case $\Gamma = 7.81$. The radial spacing between vortices 3 and 4, 4 and 5, and 5 and 6 is comparatively smaller. These vortices in the central region of the annulus are relatively well-organised with a lower amplitude radial oscillation at both the upper and lower channels ($\theta = \pm\pi/2$) compared to the vortices at end-walls and those nearest to it. This feature shows the effect of the end-walls on the vortex centre distribution in addition to the flow regime type for both test cases. In Figure 7.19(b), the vortices in both the lower ($\theta = -\pi/2$) and the upper ($\theta = \pi/2$) channels exhibit an approximately symmetric trend about $(r - R_i)/d = 0.59$.

Based on the dimensions of the geometry of the PIV experimental apparatus, the normalised radial position between the inner and the outer cylinders is in the range $0 \leq (r - R_i)/d \leq 1$, which means the gap mid-span ($r = R_i + 0.5d$) of the annulus is located at $(r - R_i)/d = 0.5$ for both test cases. In Figure 7.19(a) for the test case $\Gamma = 11.36$, 92% of the vortex centres lie above the mid-gap $r = R_i + 0.5d$. This clearly shows that the Taylor vortex centres are not symmetric about the gap mid-span of the annulus. Figure 7.19(a) shows that approximately 71% of the vortex centres is within the spread band delimited by

the dashed lines, an indication that there are a few outliers outside the ±1 standard deviation band.

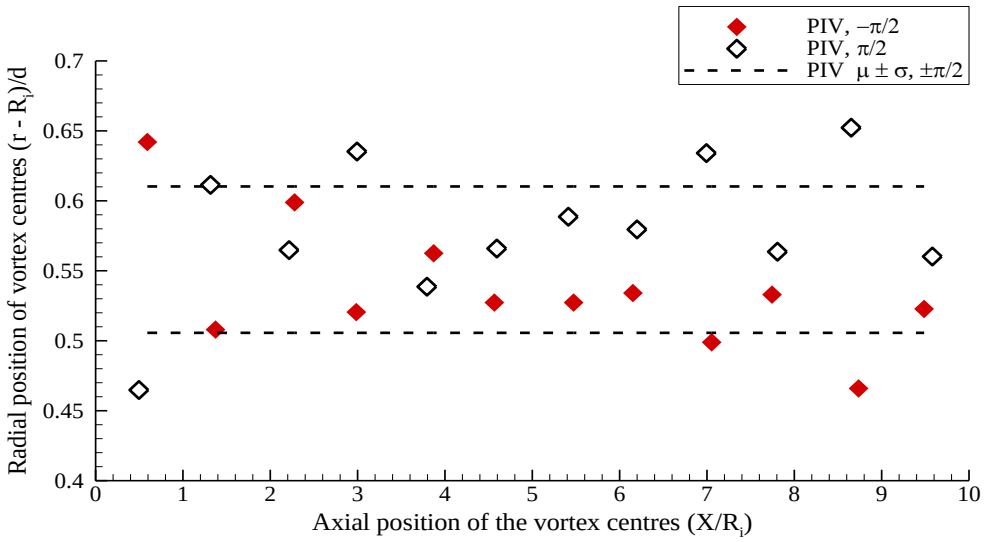

(a)

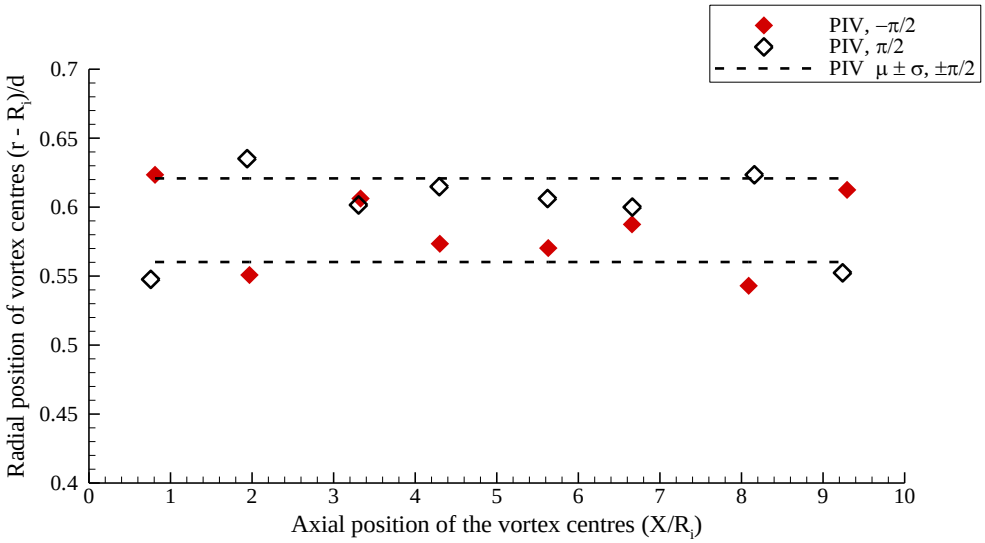

(b)

Figure 7.19: Axial and radial position of vortex centres in the meridional plane with data spread bands about the vortex centre mean value from PIV for the test cases (a) Γ = 11.36 and (b) Γ = 7.81.

Figure 7.19(b) for the test case Γ = 7.81 shows that all vortex centres lie above the mid-gap r = R_i + 0.5d. This result is consistent with the result obtained from the CFD in Figure 6.37(b), in which all the vortex centres are displaced toward the wall of the outer cylinder. This features is however different from the results obtained for the PIV test case Γ = 11.36, in which the centres of some vortices are located toward the wall of the outer

cylinder above the mid-gap $r = R_i + 0.5d$, while some are located toward the wall of the inner cylinder below the mid-gap $r = R_i + 0.5d$, as shown in Figure 7.19(a).

Despite the fact that all the vortex centres cluster toward the wall of the outer cylinder for the test case $\Gamma = 7.81$, Figure 7.19(b) shows that approximately 69% of the vortex centres is within the radial spread band, so that 31% of the vortex centres lie outside the ± 1 standard deviation band.

Comparing Figure 7.19(a) with Figure 7.19(b), it is noticeable that the vortex centres for the test case $\Gamma = 11.36$ are more scattered radially within the annulus than the vortex centres for the test case $\Gamma = 7.81$. This is evidenced by the spread bands of the vortex centres in Figure 7.19(a) and Figure 7.19(b). In fact, the area occupied by the vortex centres spreads over the range $0.46 \leq (r - R_i)/d \leq 0.65$ radially for the test case $\Gamma = 11.36$, while the area occupied by vortex centres spreads over the narrower range $0.54 \leq (r - R_i)/d \leq 0.64$ radially for the test case $\Gamma = 7.81$. This shows that the radial spread of the vortex centres in these PIV experimental test cases is affected by the change in the gap width d.

Figure 7.20(a) and Figure 7.20(b) display the spread of the vortex centre positions in the axial and radial directions in the meridional plane at the lower ($\theta = -\pi/2$) channel from Figure 7.18. The spread is estimated from the analysis of 100 instantaneous PIV vector maps, following the same procedure detailed in section 6.7.3. The vertical orange bars show the minimum and maximum radial displacement of each vortex centre at $\theta = -\pi/2$ estimated from one standard deviation of the 100 vector maps, while the horizontal blue bars represent the minimum and maximum axial displacement of each vortex centre mean value at $\theta = -\pi/2$. The standard deviation of the vortex radial and axial displacements was used to size the spread band in Figure 7.20 using equation 6.8, assuming a normal distribution. The bars in Figure 7.20 show the extent by which the vortex centres are displaced radially and axially in the annulus as azimuthal waves travel around the axis of the rotating inner cylinder. As the azimuthal waves travel around the rotating inner cylinder, the vortex centres are displaced vertically upward and downward, as well as horizontally backward and forward with time, as discussed in the context of Figure 7.5. The displacement of the vortex centres in these directions results in the spread rate about the vortex centre mean value in the axial and radial directions shown by the plots in Figure 7.20. In agreement with the observation made in Figure 7.7 and Figure 7.18, the time average positions of the vortex centres are displaced toward the inner cylinder and toward the outer cylinder in an alternating fashion, so that where the mean position at $\theta = \pi/2$ is

towards the inner rotating cylinder at a given X/R_i, the corresponding mean radial position of the vortex centre at $\theta = -\pi/2$ at the same X/R_i is towards the stationary outer cylinder. In Figure 7.20(a) and Figure 7.20(b), although the spread of vortex centres in the axial and radial positions of the meridional plane at the upper ($\theta = \pi/2$) channel was not estimated, these figures clearly indicate that there would be an overlap in the spread for both the upper and lower channels.

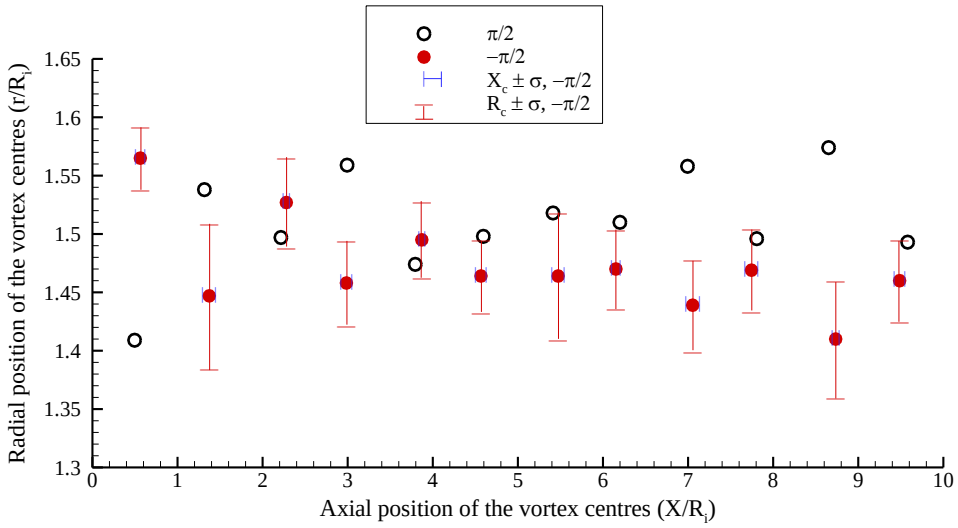

(a)

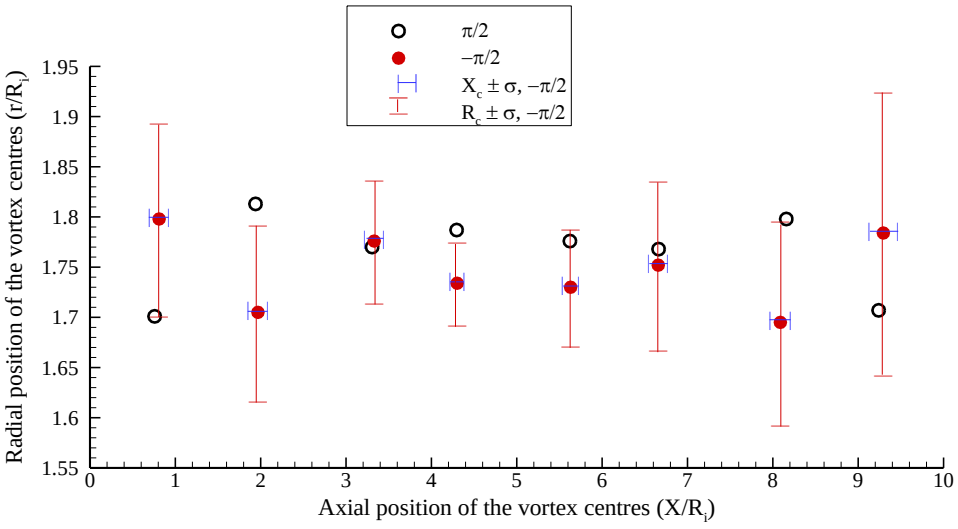

(b)

Figure 7.20: Statistical data spread rate of vortex centre in the axial and radial positions in the meridional plane at $\theta = -\pi/2$ for the test cases (a) $\Gamma = 11.36$ and (b) $\Gamma = 7.81$.

The axial displacement of the vortex centres cannot be compared directly with the radial displacement of the vortex centres in Figure 7.20, as both axes are not on the same scale. The axial variation of the vortex centre appears to be small compared to the axial spacing of the vortices.

Vortex size and end-wall effects

The half wavelength, $\lambda/2$, as defined in the analysis of the vortex size in section 6.7.8, was estimated from Figure 7.18 for each vortex using the same procedure discussed in chapter six. The axial vortex size estimated from Figure 7.18 is tabulated in Table 7-1 and for the test cases $\Gamma = 11.36$ and $\Gamma = 7.81$ respectively. From Table 7-1 and Table 7-2, the effect of end-wall boundaries and of the flow waviness on the axial distribution of the vortex centres is apparent. For the test case $\Gamma = 11.36$ in Table 7-1, from the left end-wall, vortex 1 and, from the right end-wall, vortex 12 are directly affected by the stationary end-walls. Similarly, for the test case $\Gamma = 7.81$ in Table 7-2, from the left end-wall, vortex 1 and, from the right end-wall, vortex 8 are directly affected by the stationary end-walls.

From Table 7-1 for the test case $\Gamma = 11.36$, it is observed that the elongated vortices 1 and 12 and the flow waviness affect the vortex axial length X_L of the neighbouring vortices toward the central region of the annulus. Specifically, vortices 2, 3, and 4, as well as vortices 9, 10, and 11 are affected by these end-wall vortices. Similarly, from Table 7-2 for the test case $\Gamma = 7.81$, the elongated vortices 1 and 8 and the flow waviness affect the vortex axial length X_L of the neighbouring vortices 2 and 3 as well as vortices 6 and 7. This trend matches that from the CFD predictions in 6.7.8.

From Table 7-1 and Table 7-2, the axial half wavelength of the vortices shows a definite pattern. Specifically, the axial spacing between consecutive vortices varies in an alternate manner for the test case $\Gamma = 11.36$ and varies in a symmetric manner for the test case $\Gamma = 7.81$. For test case $\Gamma = 11.36$ in Table 7-1, considering the vortices as pairs, the first set is composed of an elongated vortex 1 and an axially shortened vortex 2. Vortex 2 compensates for the elongated vortex 1 by a reduction in its axial length. Likewise, vortex 4 compensates for elongated axial size of vortex 3 by a decrease in its axial length. From the right end-wall, the same trend is observed with the axial length of vortex 11 reduced to compensate for the elongated vortex 12. Vortex 9 is reduced to compensate for the elongated in the axial length of vortex 10. As the vortices develop toward the centre of the computational domain, the vortices become more equi-spaced with the axial length of the vortices 5, 6, 7 and 8 being almost the same.

For the test case $\Gamma = 7.81$ in Table 7-2, considering the first three vortices from the left end-wall, their axial length reduces monotonically in the positive axial direction. A symmetric trend is observed at the right end-wall, in which the vortical axial length reduces monotonically in the negative axial direction. In the central region, vortices 3 and

4 form a shorter vortex pair than vortices 1 and 2, compensating for the elongation of vortices 1 and 2, due to the end-wall effects. Similarly, vortices 5 and 6 are a shorter pair compared to the end-wall vortex pair 7 and 8. This trend is different with respect to the alternating pattern of vortex lengths predicted by the CFD simulations in chapter six and results from the wavy vortex flow regime of the PIV experiment.

From the estimated vortex axial length, an average is computed for both test cases without the first and the last vortices being included in the average, as their axial length is more affected by the end-walls than that of the vortices in the central region, as in the CFD prediction in chapter six.

Table 7-1: Variation of vortex axial length with vortex number for test case Γ = 11.36.

Vortex number	Vortex axial length $X_L = X/R_i$	Variation $(X_L - \bar{X}_L)$
1	1.033	0.236
2	0.793	-0.004
3	0.82	0.023
4	0.751	-0.046
5	0.807	0.01
6	0.806	0.009
7	0.793	-0.004
8	0.807	0.01
9	0.751	-0.046
10	0.830	0.033
11	0.811	0.014
12	0.998	0.201
Average	$\bar{X}_L = \frac{1}{10}\sum_{i=2}^{11}(X_L)_i = 0.797$	
Variance	$S^2 = \frac{1}{9}\sum_{i=2}^{11}(X_L - \bar{X})_i^2$ = 0.001	
Standard deviation	$\sigma = S = 0.027$	

Table 7-2: Variation of vortex axial length with vortex number for test case Γ = 7.81.

Vortex number	Vortex axial length $X_L = X/R_i$	Variation $(X_L - \overline{X}_L)$
1	1.399	0.192
2	1.276	0.069
3	1.137	-0.07
4	1.134	-0.073
5	1.219	0.012
6	1.186	-0.021
7	1.290	0.083
8	1.358	0.151
Average	$\overline{X}_L = \frac{1}{6}\sum_{i=2}^{7}(X_L)_i = 1.207$	
Variance	$S^2 = \frac{1}{5}\sum_{i=2}^{7}(X_L - \overline{X})_i^2$ = 0.005	
Standard deviation	$\sigma = S = 0.067$	

The estimated average vortex axial size (half wavelength) is $0.797R_i$ for test case Γ = 11.36 and is $1.207R_i$ for test case Γ = 7.81.

There is an agreement in the estimated vortex mean axial size (half wavelength), variance, and standard deviation between the measured values of $0.797R_i$, $0.001R_i$, and $0.03R_i$ in Table 7-1 and the CFD estimate values of $0.788R_i$, $0.003R_i$, and $0.05R_i$ in Table 6-7 for test case Γ = 11.36. For the test case Γ = 7.81, there is also an agreement in the estimated vortex mean axial size (half wavelength), variance, and standard deviation between the measured values of $1.207R_i$, $0.005R_i$, and $0.067R_i$ in Table 7-2 and the CFD estimate values of $1.183R_i$, $0.005R_i$, and $0.069R_i$ in Table 6-8.

7.5.6 Residual plot

The variations in the vortex axial size tabulated in Table 7-1 and Table 7-2 give the axial length residual plots of Figure 7.21(a) and Figure 7.21(b). These residual plots are obtained based on the same procedure described in chapter six for Figure 6.38.

Figure 7.21(a) and Figure 7.21(b) are the residual plots of vortex axial length with respect to its mean value in the meridional plane at $\theta = -\pi/2$ for the test cases $\Gamma = 11.36$ and $\Gamma = 7.81$ respectively. The plots in Figure 7.21 show that the residuals are evenly distributed about the zero x-axis with no significant bias. The residuals from the ten vortices in the central region of the PIV domain display a minimum and maximum of $-0.06R_i$ and $0.04R_i$ respectively for the test case $\Gamma = 11.36$. Similarly, the residuals from the six vortices in the central region of Figure 7.18(b) for test case $\Gamma = 7.81$ display a minimum and maximum values of $-0.08R_i$ and $0.10R_i$ respectively.

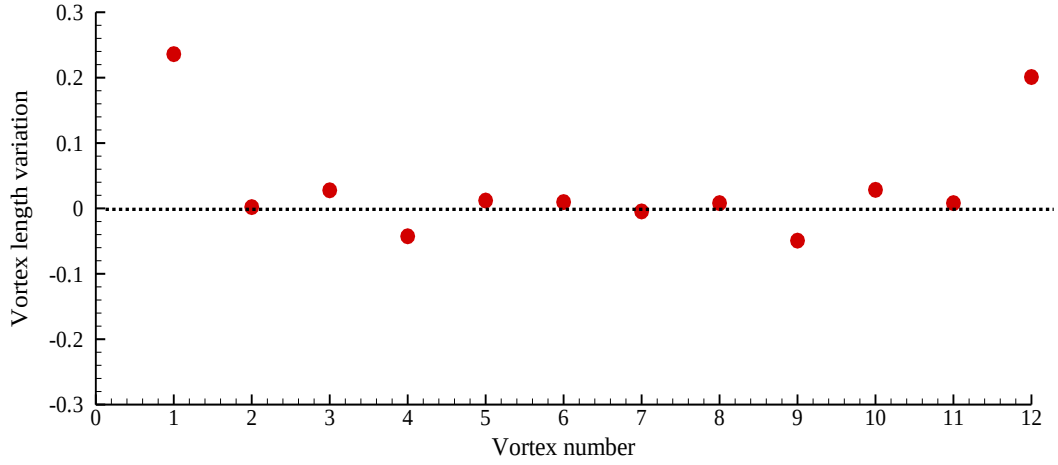

(a)

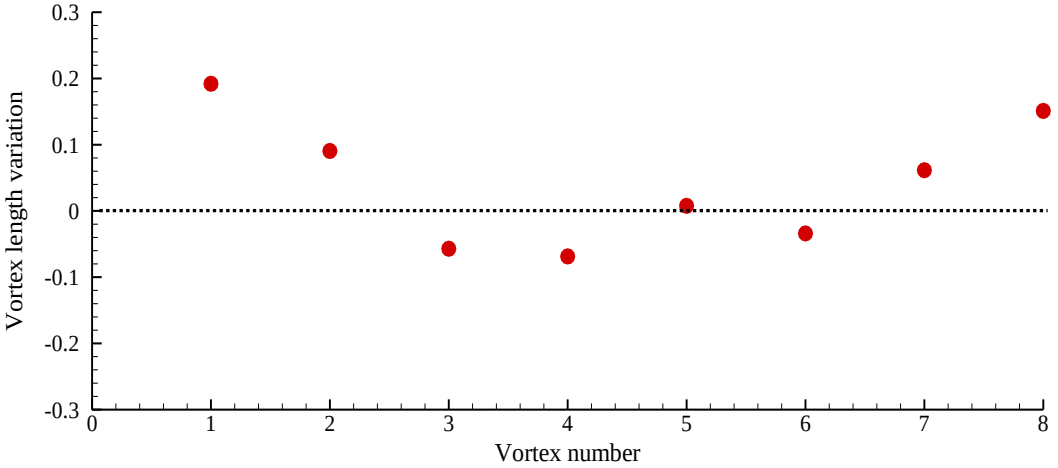

(b)

Figure 7.21: Residual plots of vortex axial length variation in the meridional plane at $\theta = -\pi/2$ for the test cases (a) $\Gamma = 11.36$ and (b) $\Gamma = 7.81$.

There is an agreement between the minimum and maximum values obtained from the PIV and the estimated CFD values of $-0.08R_i$ and $0.06R_i$ for the test case $\Gamma = 11.36$ and of $-0.06R_i$ and $0.11R_i$ for the test case $\Gamma = 7.81$ in section 6.7.9 of chapter six. The outliers on

the plot in Figure 7.21(a) and Figure 7.21(b) are the residuals from the vortex 1 and 12 in Figure 7.18(a) and Figure 7.18(b) respectively, which were excluded from the regression.

7.6 Comparison between CFD simulation and PIV results for test cases Γ = 11.36 and Γ = 7.81

Many of the modelling assumptions in the CFD simulation are necessary in order to simplify the flows that are to be modelled. In this process, errors are introduced into the simulation. Errors in the CFD simulation may be due to many factors, such as modelling, discretisation, iteration, and implementation methods. In an attempt to reduce the effect of such simplifications and approximations, selected CFD flow variables are validated against experimental data to determine their accuracy. The CFD predictions can then be used to investigate the effects of changing the experimental conditions.

Experiments are used to study flow phenomena both qualitatively and quantitatively using measurements. No measurement, however carefully made, can be completely free from uncertainty. Sources of error in the experiment are a combination of many factors, which can be classified as either systematic or residual errors. It therefore means that both CFD and experiment are affected by errors.

In this section, qualitative and quantitative comparisons of the flow features are made between the results from CFD simulations and PIV measurements for the concentric annular cylinder with aspect ratios Γ = 11.36 and Γ = 7.81 in the meridional plane of the annulus. These comparisons are presented in the context of the experimental error estimated for this flow.

7.6.1 Qualitative and quantitative analysis of the flow pattern

The flow patterns that developed in the concentric rotating cylinders with aspect ratio Γ = 11.36 and Γ = 7.81 using both CFD simulation and PIV measurement techniques are compared qualitatively and quantitatively.

Figure 6.6(a,b) and Figure 7.7(a,b) display respectively the normalised velocity vector maps obtained from the CFD simulations and the time-averaged velocity vector maps from PIV measurements, in the meridional plane of the annulus for the test cases Γ = 11.36 and Γ = 7.81. Figure 6.6(a,b) and Figure 7.79(a,b) show that the flow pattern from the steady CFD simulations and the time-averaged flow from the PIV measurements is similar in the entire annulus for test cases Γ = 11.36 and Γ = 7.81. The detailed features of

this flow pattern are discussed in the context of Figure 6.6(a,b) and Figure 7.7(a,b). Both CFD and PIV results show counter-rotating of pairs of Taylor vortices, a stronger radial outflow between the vortices, elongated vortices near the left and the right end boundaries, and the same number of the Taylor vortices. This shows that the flow patterns from CFD and PIV are in general agreement for the test cases $\Gamma = 11.36$ and $\Gamma = 7.81$.

7.6.2 Qualitative and quantitative analysis of the in-plane velocity

A detailed qualitative and quantitative comparison of the in-plane velocity profiles between the CFD simulations and the PIV experimental measurements in the meridional plane is presented in this section. The velocity profiles in Figure 7.22 to Figure 7.27 for the CFD and the PIV are obtained from the velocity vectors in the meridional plane of Figure 6.6 and Figure 7.7 respectively. The velocity profiles presented here have been normalised with respect to the inner cylinder surface speed ΩR_i.

Figure 7.22(a) and Figure 7.22(b) show the normalised axial velocity profiles from the CFD simulations and the PIV experiments at a constant radial position $r = R_i + 0.125d$ along the axial direction on the lower ($\theta = -\pi/2$) channel of the annulus for the test cases $\Gamma = 11.36$ and $\Gamma = 7.81$ respectively. The PIV error bands delimited by the orange dashed lines are included in the profiles of Figure 7.22(a) and Figure 7.22(b) to document the experimental uncertainty. The experimental uncertainty shows how much variation the PIV data has from the PIV mean value and can therefore be used to judge the accuracy of both the CFD and PIV results in test cases $\Gamma = 11.36$ and $\Gamma = 7.81$. The profiles from both the CFD and the PIV results at the constant radial position $r = R_i + 0.125d$ and at $\theta = -\pi/2$ in Figure 7.22(a) and Figure 7.22(b) show that the axial velocity maxima occur radially below the cores of clockwise vortices and the axial velocity minima occur radially below the cores of the anti-clockwise vortices. The axial velocity profiles in Figure 7.22(a) and Figure 7.22(b) show that each clockwise vortex from the CFD and PIV results induces an axial velocity maximum radially below its core at $\theta = -\pi/2$ plane. The axial velocity profiles from both CFD and PIV at the radial position $r = R_i + 0.125d$ show that the flow is almost centrally symmetric about the cylinder length mid-span at $X/R_i = 5$. This is shown by the magnitude of the axial velocity maximum and minimum near the left end-wall and near the right end-wall respectively, having almost the same magnitude. Although the axial velocity local minimum from the CFD near the right end-wall in Figure 7.22(b) for the test case $\Gamma = 7.81$ is slightly lower than the radial velocity local minimum from the

PIV at the same axial position, the CFD profile is still within the PIV measurement uncertainty band. The profiles in Figure 7.22(a) and Figure 7.22(b) also show almost the same maxima and minima axial velocity magnitudes in the central region of the annulus over the range $1 \leq X/R_i \leq 9$ for the test case $\Gamma = 11.36$ and over the range $1 \leq X/R_i \leq 8$ for the test case $\Gamma = 7.81$.

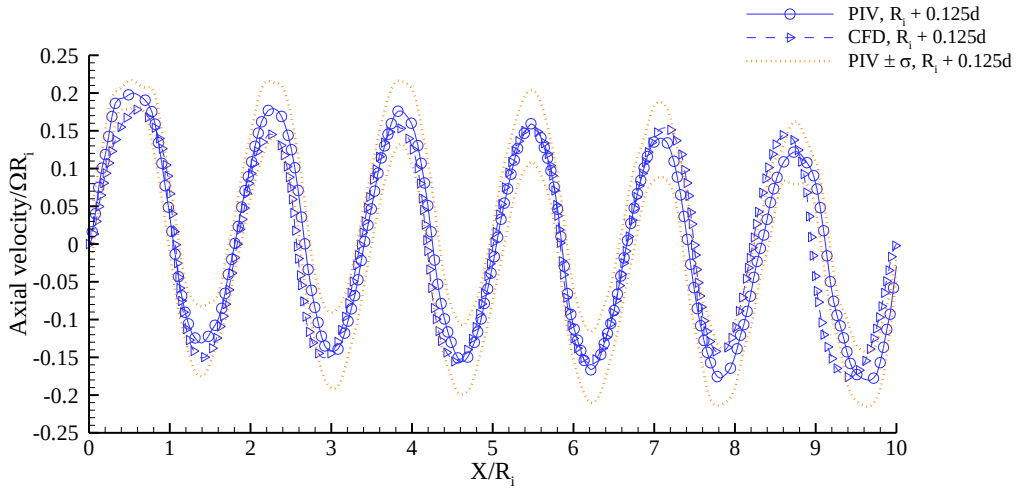

(a)

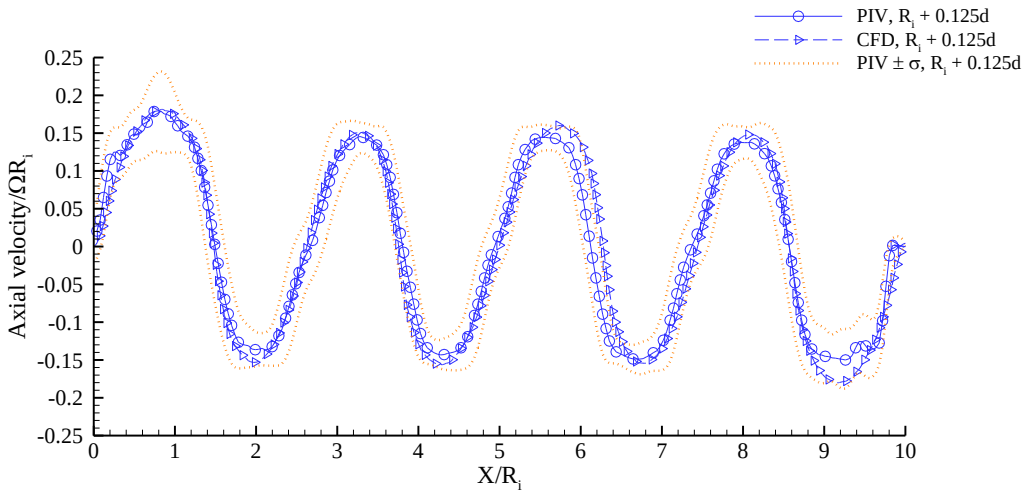

(b)

Figure 7.22: Normalised axial velocity profiles in the meridional plane at the constant radial position $r = R_i + 0.125d$ at $\theta = -\pi/2$ from PIV and CFD, with the PIV error band for the test cases (a) $\Gamma = 11.36$ and (b) $\Gamma = 7.81$.

The magnitude of the axial velocity maxima near the left end-wall and the magnitude of the axial velocity minima near the right end-wall from the PIV results for the test cases $\Gamma = 11.36$ and $\Gamma = 7.81$ has been discussed in details in the context of Figure 7.12. For the CFD, the magnitude magnitude of the axial velocity maxima near the left end-wall and the magnitude of the axial velocity minima near the right end-wall are approximately $0.18\Omega R_i$

for both test cases. Over the range $0 \leq X/R_i \leq 8.8$ for the test case $\Gamma = 11.36$ in Figure 7.22(a), the axial velocity profile for the CFD is within the upper and the lower limits of the PIV experimental error band. Near the right end-wall over the range $8.8 \leq X/R_i \leq 10$, the CFD profile is phase lagging behind the PIV profile and the CFD profile is slightly outside the experimental uncertainty band. This observation may be attributed to the misalignment of the right end-wall in the experiment, which may have been not orthogonal to the cylinder axis.

For the test case $\Gamma = 7.81$ in Figure 7.22(b), the axial velocity profile from the CFD is phase leading that of the PIV over the range $5.7 \leq X/R_i \leq 6.6$. Along the entire annulus, the axial velocity profile from the CFD is within the upper and the lower limits of the experimental uncertainty band.

The profiles in Figure 7.22(a) and Figure 7.22(b) show that there is a good agreement between the results from the CFD simulations and the PIV measurements for the test cases $\Gamma = 11.36$ and $\Gamma = 7.81$.

Figure 7.23(a) and Figure 7.23(b) show the normalised axial velocity profile at $r = R_i + 0.5d$ (the gap mid-span of the annulus) from the CFD simulation and PIV for the test cases $\Gamma = 11.36$ and $\Gamma = 7.81$ respectively. The profiles from both the CFD and the PIV in Figure 7.23 show that the normalised axial velocity at this radial position is relatively small compared with the surface speed of the rotating inner cylinder and the speed range of the corresponding profiles at $r = R_i + 0.125d$ and $r = R_i + 0.875d$ for the test cases $\Gamma = 11.36$ and $\Gamma = 7.81$. The trend of these profiles for the CFD and the PIV are discussed in the context of Figure 6.15 and Figure 7.13 for both test cases.

The normalised axial velocity profiles in Figure 7.23 show that the axial velocity maxima from PIV are higher than the ones from CFD near the left end-wall over the range $0 \leq X/R_i \leq 4$ for the test case $\Gamma = 11.36$ and over the range $0 \leq X/R_i \leq 3.3$ for the test case $\Gamma = 7.81$.

For the test case $\Gamma = 11.36$ in Figure 7.23(a), over the range $0 \leq X/R_i \leq 4$, the axial velocity maxima from the CFD simulation are $0.04\Omega R_i$, whereas the corresponding axial velocity maxima from the PIV measurement range from $0.05\Omega R_i$ to $0.09\Omega R_i$. At the axial position $X = 5.3R_i$, the axial velocity maximum is almost the same from both the CFD and the PIV with an approximate value of $0.04\Omega R_i$. Near the right end-wall, the axial velocity maxima from the CFD are higher than the ones from the PIV over the range $7 \leq X/R_i \leq 8.4$. The axial velocity maxima from the CFD and the PIV in this range are $0.04\Omega R_i$ and

$0.025\Omega R_i$ respectively. The profiles at $r = R_i + 0.5d$ in Figure 7.23(a) show that the axial velocity minima almost overlap between CFD and PIV, with an axial velocity magnitude of $0.04\Omega R_i$. The CFD profile in Figure 7.23(a) is within the PIV error band except near the end-walls, where the CFD profile over-shoots the upper limit of the PIV error band.

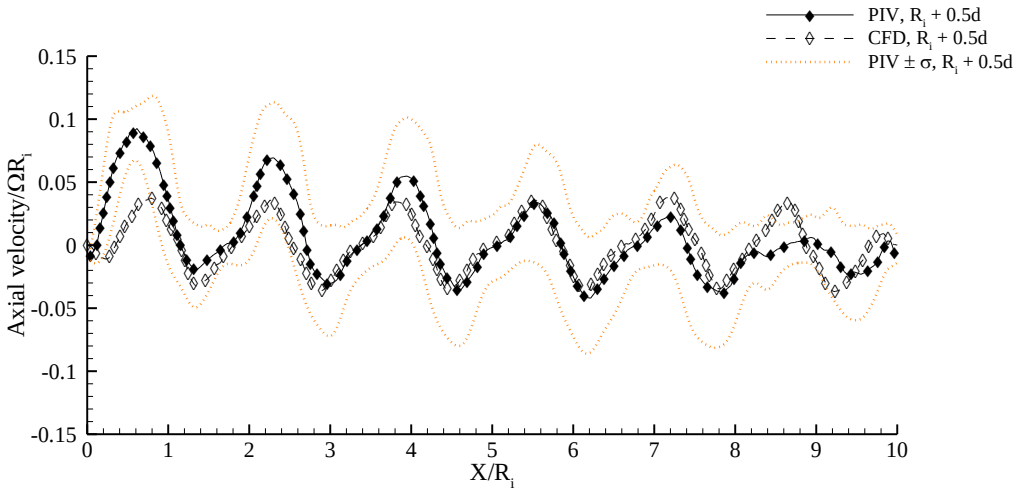

(a)

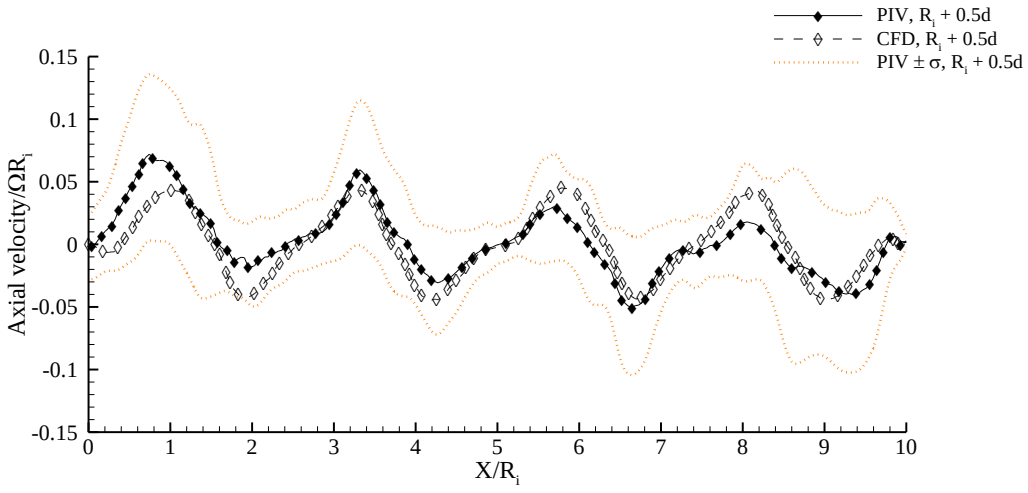

(b)

Figure 7.23: Normalised axial velocity profiles in the meridional plane at the constant radial position $r = R_i + 0.5d$ ($\theta = -\pi/2$) from PIV and CFD, with the PIV error band for the test cases (a) $\Gamma = 11.36$ and (b) $\Gamma = 7.81$.

For the test case $\Gamma = 7.81$ in Figure 7.23(b), over the range $0 \leq X/R_i \leq 3.3$, the highest magnitude of the axial velocity from the CFD and the PIV are $0.04\Omega R_i$ and $0.07\Omega R_i$ respectively. Also, the axial velocity maxima from the CFD are slightly higher than the ones from PIV over the range $5.6 \leq X/R_i \leq 8$, with the highest magnitude of the axial velocity for the CFD simulation and the PIV being approximately $0.04\Omega R_i$ and $0.03\Omega R_i$

respectively. Near the right end-wall, the axial velocity maxima from both the CFD and the PIV have almost the same magnitude of approximately $0.01\Omega R_i$.

The profiles in Figure 7.23(b) show that the axial velocity minima from the PIV are higher than the axial velocity minima from the CFD over the range $2 \leq X/R_i \leq 4.2$. Over this range, the axial velocity minima for both the CFD and the PIV are approximately $-0.04\Omega R_i$ and $-0.03\Omega R_i$ respectively. Over the range $6.6 \leq X/R_i \leq 9$, the axial velocity minima from both the CFD and the PIV are almost the same with the highest axial velocity magnitude of approximately $0.04\Omega R_i$. The profiles in Figure 7.23(a) and Figure 7.23(b) show a good agreement between the results from the CFD simulations and the PIV measurements.

The normalised axial velocity profiles near the wall of the outer cylinder at $r = R_i + 0.875d$ from CFD and PIV are shown in Figure 7.24(a) and Figure 7.24(b) for the test cases $\Gamma = 11.36$ and $\Gamma = 7.81$ respectively. The axial velocity profiles from CFD and PIV at this radial position in Figure 7.24 exhibit similar trends for both test cases. The trend of these velocity profiles has been dicussed in details in the context of Figure 6.14 and Figure 7.12.

The profiles near the outer cylinder wall at $r = R_i + 0.875d$ in Figure 7.24 show that the axial velocity local minimum near the left end-wall for the PIV is slightly higher than that of the CFD profiles, with an axial velocity of approximately $-0.15\Omega R_i$ and $-0.13\Omega R_i$ respectively in both test cases. Near the right end-wall in Figure 7.24, the axial velocity maximum from the CFD is greater than the axial velocity maximum from the PIV. The axial velocity maxima from the CFD and PIV at this axial position are approximately $0.15\Omega R_i$ and $0.11\Omega R_i$ respectively for the test case $\Gamma = 11.36$ in Figure 7.24(a) and approximately $0.16\Omega R_i$ and $0.14\Omega R_i$ for the test case $\Gamma = 7.81$ in Figure 7.24(b).

For the test case $\Gamma = 11.36$ in Figure 7.24(a), the axial velocity maxima from the PIV are greater than the axial velocity maxima from the CFD over the range $1.4 \leq X/R_i \leq 4.6$ with the magnitude of the axial velocity maxima from CFD and PIV approximately $0.13\Omega R_i$ and $0.17\Omega R_i$ respectively. The axial velocity maxima from the CFD and the PIV are almost of the same magnitude estimated to be approximately $0.16\Omega R_i$ over the range $6.2 \leq X/R_i \leq 8$.

In Figure 7.24(a), the axial velocity local minima from the CFD are higher over the range $4 \leq X/R_i \leq 9$ than the axial velocity local minima from the PIV measurement. In this region, the axial velocity minima from the CFD and the PIV are approximately $-0.13\Omega R_i$ and $-0.15\Omega R_i$ respectively.

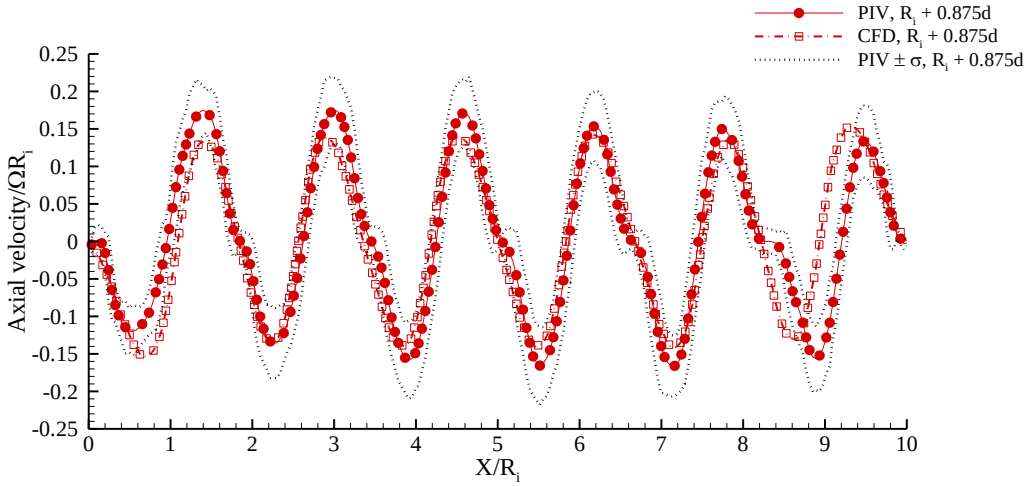

(a)

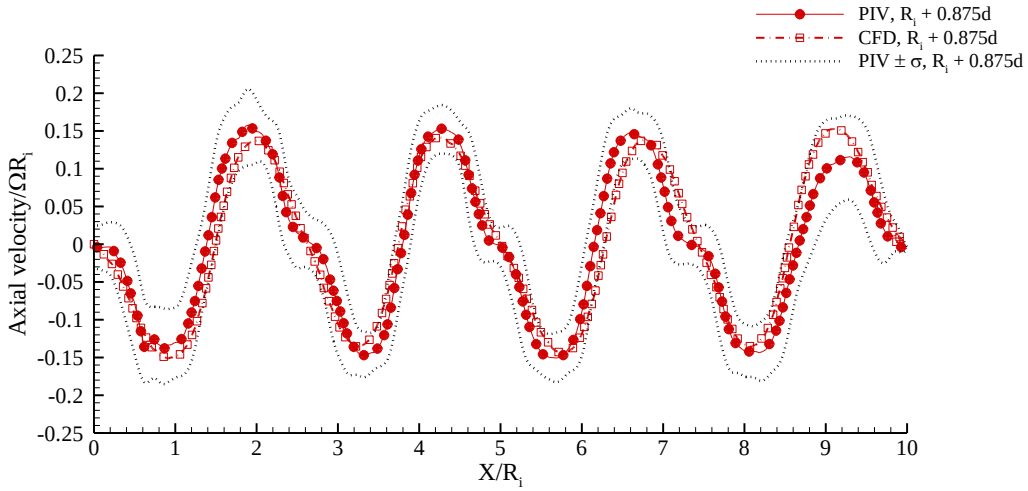

(b)

Figure 7.24: Normalised axial velocity profiles in the meridional plane at the constant radial position $r = R_i + 0.875d$ at $\theta = -\pi/2$ from PIV and CFD, with the PIV error band for the test cases (a) $\Gamma = 11.36$ and (b) $\Gamma = 7.81$.

Near the left end-wall over the range $0.6 \leq X/R_i \leq 1.4$ in Figure 7.24(a), the CFD profile is phase leading the PIV profile. In the central region over the range $1.4 \leq X/R_i \leq 8.2$ the profiles for both the CFD and the PIV are almost at the same spatial phase. Near the right end-wall, over the range $8.2 \leq X/R_i \leq 9.4$, the CFD profile is phase lagging the PIV profile. In the axial velocity profile in Figure 7.24(a), over the range $0 \leq X/R_i \leq 8.2$, the CFD profile is within the uncertainty band of the PIV measurements.

The test case $\Gamma = 7.81$ in Figure 7.24(b) displays the same trend of Figure 7.24(a) of the axial velocity maxima from the PIV being slightly higher than the axial velocity maxima from the CFD. This trend occurs over the range $2 \leq X/R_i \leq 6.6$, with the axial velocity magnitude from the CFD and the PIV being approximately $0.14\Omega R_i$ and $0.15\Omega R_i$

respectively. The axial velocity minima from both the CFD and the PIV are nearly the same over the range $0 \leq X/R_i \leq 8$. In this region, the axial velocity minima from the CFD and the PIV are approximately $-0.15\Omega R_i$.

In Figure 7.24(b), the CFD profile is phase leading the PIV profile over the ranges $0.8 \leq X/R_i \leq 2$ and $5.8 \leq X/R_i \leq 7.4$. In the central region, over the range $2 \leq X/R_i \leq 5.8$, the profiles from both the CFD and the PIV are almost at the same spatial phase. Over the range $8 \leq X/R_i \leq 9.4$, the CFD profile is phase lagging the PIV profile. The observed difference in the profiles from the CFD and the PIV near the right end-wall in Figure 7.24 for both test cases is attributed to the misalignment of the end-wall in the PIV measurements and to the effect of light reflection at the right end-wall.

The fact that most of the axial velocity profile from the CFD is within the experimental uncertainty in Figure 7.24(a) and that the axial velocity profile from the CFD in the entire annulus is within the uncertainty band of the PIV measurements in Figure 7.24(b) shows there is a good qualitative agreement between the CFD simulations and the PIV experiments for both test cases.

Figure 7.25(a) and Figure 7.25(b) show the normalised radial velocity profiles from the CFD simulations and the PIV measurements at $r = R_i + 0.125d$ for the test cases $\Gamma = 11.36$ and $\Gamma = 7.81$ respectively, with the PIV error bands included. The radial velocity profiles from CFD and PIV in Figure 7.25 exhibit the same trend, with the radial velocity maxima and minima corresponding to maximum outward flow regions and minimum inward flow regions respectively. The sharper peaks than the troughs observed in the radial velocity profiles from CFD and PIV in Figure 7.25 has been discussed in the context of Figure 6.16 and Figure 7.15. In Figure 7.25(a) and Figure 7.25(b), the radial velocity maxima from the CFD simulations are observed to be higher than the radial velocity maxima from the PIV measurements in the entire annulus for both test cases.

For the test case $\Gamma = 11.36$ in Figure 7.25(a), the magnitude of the radial velocity maxima from the CFD along the entire annulus are approximately $0.1\Omega R_i$, while the radial velocity maxima measured by PIV increase progressively in magnitude from the left end-wall to the right end-wall. The magnitude of the radial velocity maxima ranges from $0.07\Omega R_i$ near the left end-wall to $0.09\Omega R_i$ near the right end-wall.

The radial velocity minima from CFD are observed to be higher than the radial velocity minima from PIV in the entire annulus, except near the left end-wall at $X = 0.1R_i$, where the radial velocity minimum from CFD and PIV are almost the same. The radial velocity

minima from the CFD over the range $1.8 \leq X/R_i \leq 8.2$ are almost of the same value of approximately $-0.06\Omega R_i$. Near the end-walls, the CFD radial velocity minima are approximately $-0.04\Omega R_i$.

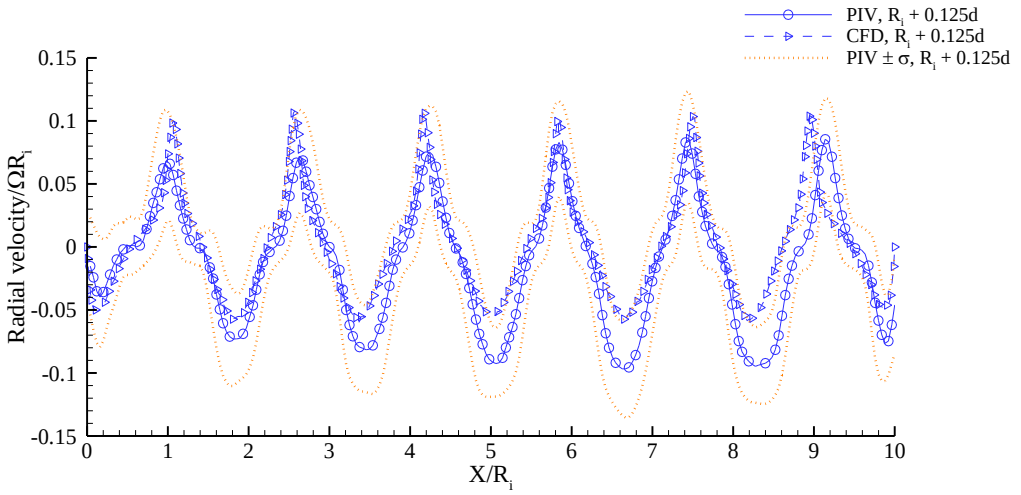

(a)

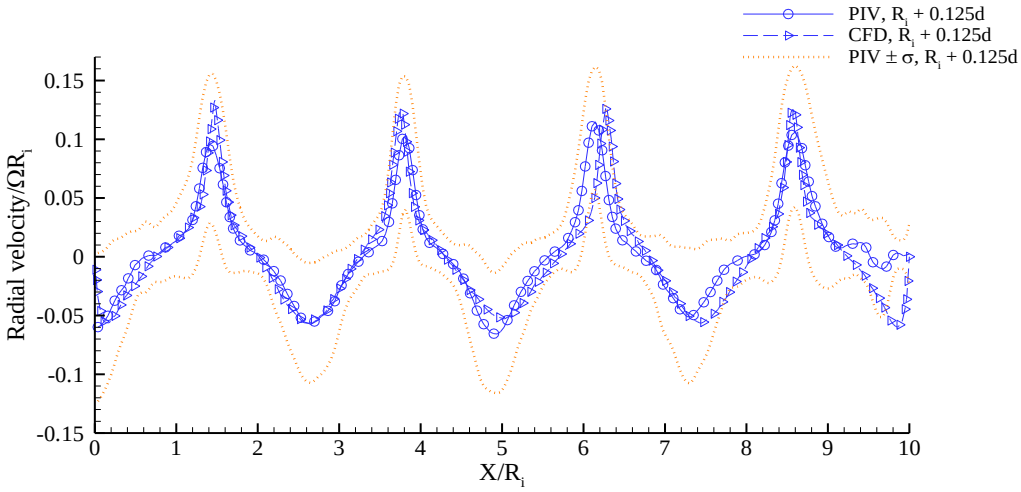

(b)

Figure 7.25: Normalised radial velocity profiles in the meridional plane at the constant radial position $r = R_i + 0.125d$ at $\theta = -\pi/2$ from PIV and CFD, with the PIV error band for the test cases (a) $\Gamma = 11.36$ and (b) $\Gamma = 7.81$.

The radial velocity local minima measured by PIV decrease progressively from the left end-wall over the range $0 \leq X/R_i \leq 6.7$. Over this region, the value of the radial velocity minima ranges from $-0.04\Omega R_i$ near the left end-wall to $-0.10\Omega R_i$ at $X/R_i = 6.7$. The radial velocity local minima from the PIV increase over the range $6.7 \leq X/R_i \leq 10$, with the magnitude of the radial velocity minima ranges from $-0.1\Omega R_i$ to $-0.08\Omega R_i$ near the right end-wall. The CFD and PIV radial velocity profiles in Figure 7.25(a) are almost at the

same spatial phase in the entire annulus, except over the range $8 \leq X/R_i \leq 9$ where the CFD profile is phase lagging.

For the test case $\Gamma = 7.81$ in Figure 7.25(b), the magnitude of the radial velocity maxima from the CFD along the entire annulus is approximately $0.13\Omega R_i$ whereas, the magnitude of the radial velocity maxima from the PIV along the entire annulus ranges from $0.10\Omega R_i$ to $0.11\Omega R_i$. The radial velocity minima from CFD and PIV are almost overlapping except toward the right end-wall where there is a significant difference. At the axial positions $X/R_i \approx 0.2$, $X/R_i \approx 2.6$, and $X/R_i \approx 7.4$, the radial velocity minima are almost the same for both the CFD and the PIV, with a radial velocity magnitude of approximately $0.06\Omega R_i$. At the axial position $X/R_i \approx 5$, the radial velocity minimum from the CFD is slightly higher than that from the PIV, with radial velocity minimum of approximately $-0.05\Omega R_i$ and $-0.06\Omega R_i$ respectively. Near the right end-wall at $X/R_i \approx 9.8$, the radial velocity minimum from the CFD is lower than that from the PIV, with values of approximately $-0.06\Omega R_i$ and $-0.01\Omega R_i$ respectively.

Over the entire annulus, the profiles from both the CFD and the PIV in Figure 7.25(b) are almost at the same spatial phase, except over the range $5.1 \leq X/R_i \leq 6.2$, where the PIV profile is phase lagging the CFD profile. Over the range $6.2 \leq X/R_i \leq 6.8$ and $7.3 \leq X/R_i \leq 8$, the CFD profile is phase leading.

Notwithstanding the observed discrepancies between the CFD and the PIV profiles of Figure 7.25(a) and Figure 7.25(b), each CFD profile is within its corresponding PIV experimental uncertainty band. This shows that there is a broad qualitative agreement between the CFD simulations and the PIV measurements.

Figure 7.26(a) and Figure 7.26(b) display the normalised radial velocity profile at the gap mid-span of the annulus at $r = R_i + 0.5d$ from CFD and PIV for the test cases $\Gamma = 11.36$ and $\Gamma = 7.81$ respectively. The PIV uncertainty error bands are included in Figure 7.26 to quantify the accuracy of the PIV experiments. The trend of the radial velocity profiles in Figure 7.26 is similar between CFD and PIV. This trend is discussed for the CFD and the PIV results in the context of Figure 6.16, Figure 7.14 and Figure 7.16 for both test cases.

As in Figure 7.25, the radial velocity maxima from the CFD are observed to be higher than the radial velocity maxima from the PIV in Figure 7.26(a) and Figure 7.26(b). At this radial position, the magnitude of the radial velocity maxima from the CFD is approximately $0.24\Omega R_i$ for both test cases in the entire annulus.

In Figure 7.26(a) and Figure 7.26(b), the two radial velocity maxima from the PIV nearer the end-wall boundaries for both test cases are almost the same, with a magnitude of approximately $0.19\Omega R_i$. This increases to $0.21\Omega R_i$ in the central region of the annulus over the range $2.6 \leq X/R_i \leq 7.5$ for the test case $\Gamma = 11.36$, and over the range $3.6 \leq X/R_i \leq 6.2$ for the test case $\Gamma = 7.81$. The difference between the radial velocity magnitude in the central region and that at the end-wall boundaries is attributed to the approximate alignment of the end-wall boundaries orthogonal to the cylinder axis in the experimental setup.

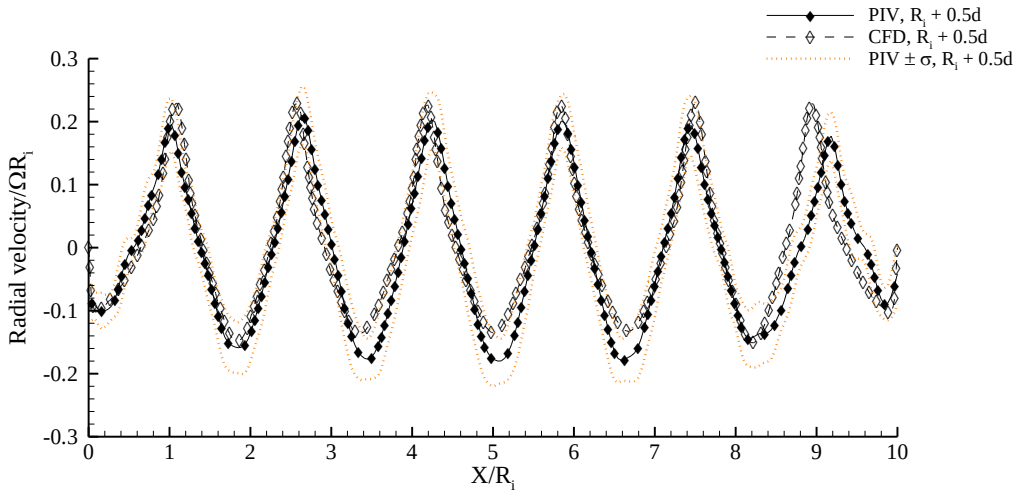

(a)

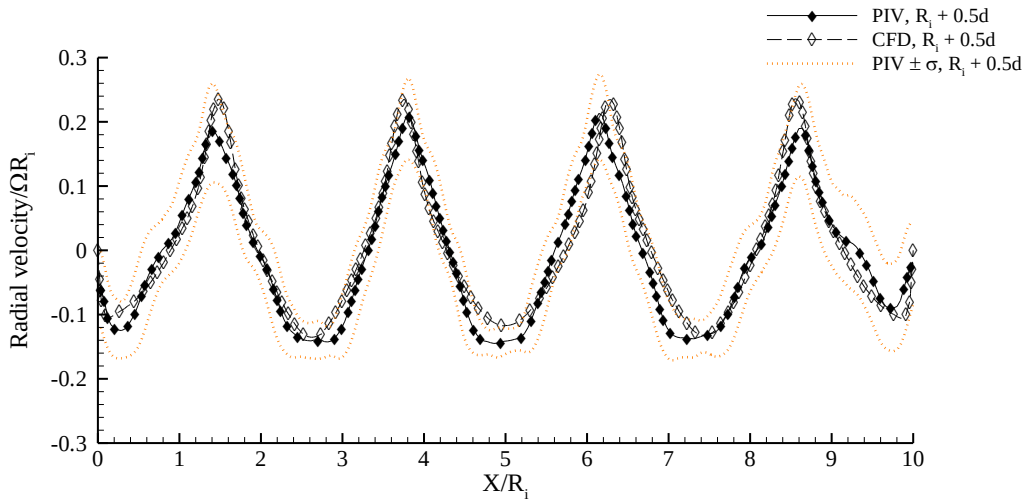

(b)

Figure 7.26: Normalised radial velocity profiles in the meridional plane at the constant radial position $r = R_i + 0.5d$ ($\theta = -\pi/2$) from PIV and CFD, with the PIV error band for the test cases (a) $\Gamma = 11.36$ and (b) $\Gamma = 7.81$.

In Figure 7.26(a) for the test case $\Gamma = 11.36$, the radial velocity minima from the CFD are observed to be higher than the radial velocity minima from the PIV measurement, except

near the left and right end-walls over the range $1 \leq X/R_i \leq 1.8$ and $8.2 \leq X/R_i \leq 10$, where the radial velocity minima from the CFD and the PIV are almost of the same magnitude. In Figure 7.26(a), the CFD radial velocity profile lies within the PIV measurement uncertainty band except near the right end-wall over the range $8.4 \leq X/R_i \leq 9.6$. In this region, the CFD radial velocity profile is phase lagging the PIV profile.

For the test case $\Gamma = 7.81$, the radial velocity minima from both the CFD and the PIV are almost of the same magnitude in the entire annulus, except at $X/R_i = 5$, where the radial velocity minimum from the CFD is slightly higher than that from the PIV, with the magnitude of the radial velocity minimum at this axial position for the CFD and the PIV being approximately $0.12\Omega R_i$ and $0.14\Omega R_i$ respectively. Near the end-wall boundaries at $X = 0.2R_i$ and $X = 9.8R_i$ in Figure 7.26(b), the radial velocity minima have almost the same magnitude of approximately $0.12\Omega R_i$.

At the central region over the range $2.6 \leq X/R_i \leq 7.4$ in Figure 7.26(b), the radial velocity minima from the PIV are the same, with a magnitude of approximately $0.14\Omega R_i$. The profiles of the normalised radial velocity from the CFD and the PIV in Figure 7.26(b) show that the CFD profile is phase leading over the range $5.4 \leq X/R_i \leq 7.4$, whereas both the CFD and the PIV profiles are almost at the same spatial phase at other axial positions along the annulus. The profiles in Figure 7.26(a) and Figure 7.26(b) show an appreciable agreement between the CFD and the PIV measurements.

Figure 7.27(a) and Figure 7.27(b) display the normalised radial velocity profiles near the wall of the outer cylinder at $r = R_i + 0.875d$ from the CFD simulations and the PIV measurements for the test cases $\Gamma = 11.36$ and $\Gamma = 7.81$ respectively. The black dashed lines represent the upper and lower limits of the PIV measurement uncertainty. The normalised radial velocity profiles from PIV and CFD exhibit a similar trend of the outward flow regions featuring one single peak, while the inward flow regions over the range $1.8 \leq X/R_i \leq 8.2$ for the test case $\Gamma = 11.36$, and over the range $2.6 \leq X/R_i \leq 7.4$ for the test case $\Gamma = 7.81$ exhibit double trough minima. This trend has been discussed in the context of Figure 6.17 and Figure 7.17.

In Figure 7.27, over the range $1 \leq X/R_i \leq 9$ for the test case $\Gamma = 11.36$ and over the range $1.4 \leq X/R_i \leq 8.6$ for the test case $\Gamma = 7.81$, the radial velocity maxima from the CFD are greater than the radial velocity maxima from the PIV. The magnitude of radial velocity maxima from the CFD is almost constant in the entire annulus and approximately equal $0.09\Omega R_i$ for both test cases. Similarly, the magnitude of the radial velocity minima from

the CFD is almost constant over the range $1.6 \leq X/R_i \leq 8.4$ for the test case $\Gamma = 11.36$ in Figure 7.27(a) and over the range $0.6 \leq X/R_i \leq 9.4$ for the test case $\Gamma = 7.81$ in Figure 7.27(b), with a magnitude of approximately $0.04\Omega R_i$ for both test cases.

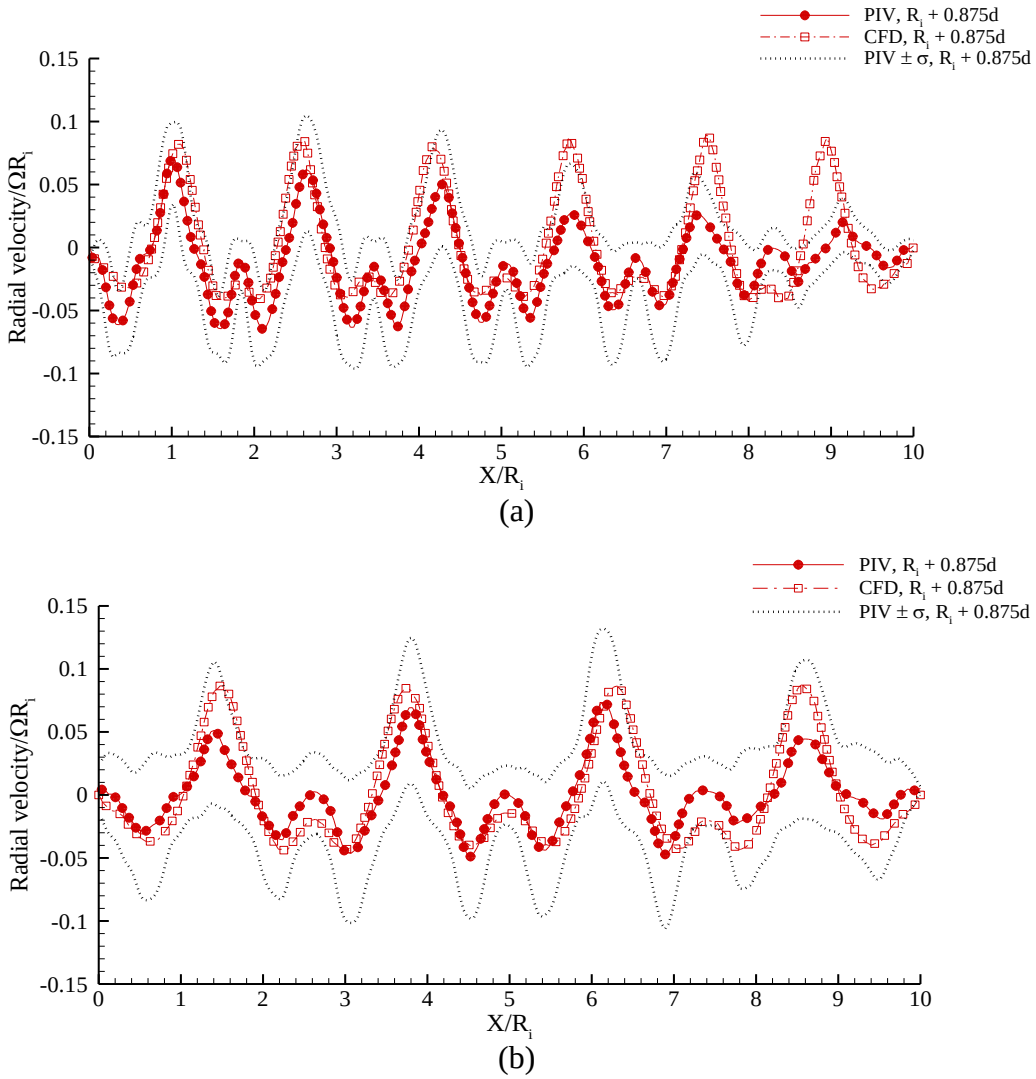

Figure 7.27: Normalised radial velocity profiles in the meridional plane at the constant radial position $r = R_i + 0.875d$ at $\theta = -\pi/2$ from PIV and CFD, with the PIV error band for the test cases (a) $\Gamma = 11.36$ and (b) $\Gamma = 7.81$.

For the test case $\Gamma = 11.36$ in Figure 7.27(a), the magnitude of the radial velocity minima from the CFD and the PIV near the left end-wall at $X/R_i = 0.4$ is approximately $0.03\Omega R_i$ and $0.06\Omega R_i$ respectively. Near the right end-wall at $X/R_i = 9.4$, the radial velocity minimum from CFD and PIV is approximately $0.03\Omega R_i$ and $0.015\Omega R_i$ respectively.

For the test case $\Gamma = 7.81$ in Figure 7.27(b), the trend of the normalised radial velocity minima from the CFD and the PIV in Figure 7.27(b) exhibit the same symmetrical trend about the axial position $X/R_i = 5$. This symmetrical trend has been discussed in the context

of Figure 7.17(b). The profile from the PIV in Figure 7.27(b) shows that the radial velocity maxima in the central region over the range $3.8 \leq X/R_i \leq 6.2$ have a radial velocity magnitude of approximately $0.07\Omega R_i$. This value is greater than the magnitude of the radial velocity maxima near the left and the right end-walls.

The trend of the normalised radial velocity profile from the PIV in Figure 7.27 has been discussed in details in the context of Figure 7.17. The radial velocity profiles from the CFD simulations and the PIV measurements in Figure 7.27 show that there is a qualitative agreement between the results from both techniques.

7.6.3 Vortex centre analysis

Figure 7.28(a) and Figure 7.28(b) show the normalised radial position of the Taylor vortex centres as a function of their normalised axial position from both the CFD simulations and the PIV measurements in the meridional plane at both the lower and the upper channels ($\theta = \pm\pi/2$) of the annulus. The radial position of the vortex centres for the CFD and the PIV are estimated from Figure 6.36(a,b) and Figure 7.18(a,b) respectively for each test case. Figure 7.28(a) and Figure 7.28(b) also show how the vortex centres spread radially in the annular region of the cylinder about their mean value in both the CFD and the PIV results by the inclusion of their respective spread bands. The spread bands are estimated using equation 6.8.

The black dashed lines toward the top and bottom of Figure 7.28 represents respectively the maximum and minimum limits of the spread band about the vortex centre mean value from the PIV measurements. The red dashed lines of Figure 7.28 represent the maximum and minimum limits of the spread band about the vortex centre mean value from the CFD simulations. Figure 7.28 show that all vortex centres from the CFD simulations lie within the PIV spread band without any outlier.

This shows that there is an agreement between the CFD and the PIV results for both test cases. The effects of the gap width on the vortex centre locations for both the CFD and the PIV are further discussed in section 7.6.4.

7.6.4 Effects of radius ratio on the vortex centres

The spread rates of the vortex centres for the test cases $\Gamma = 11.36$ and $\Gamma = 7.81$ in Figure 7.28(a) and Figure 7.28(b) can be compared directly with one another, as both the horizontal and the radial axes in both test cases are the same. Comparing Figure 7.28(a)

with Figure 7.28(b), it is noticeable that more vortex centres for the test case Γ = 11.36 are closer to the wall of the inner cylinder than those for the test case Γ = 7.81. That is, the vortex centres of the test case Γ = 7.81 are displaced more toward the wall of outer cylinder than in the test case Γ = 11.36. In addition, the PIV measured vortex centres for the test case Γ = 11.36 are more scattered radially within the annulus than the vortex centres for the test case Γ = 7.81. In order words, the measured vortex centres of the test case Γ = 7.81 are more regularly spaced than the ones of the test case Γ = 11.36.

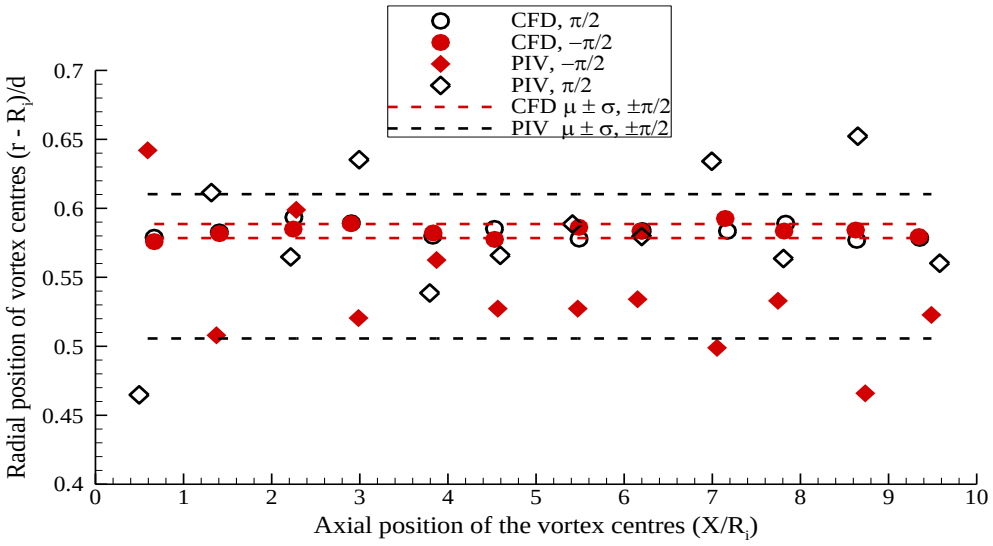

(a)

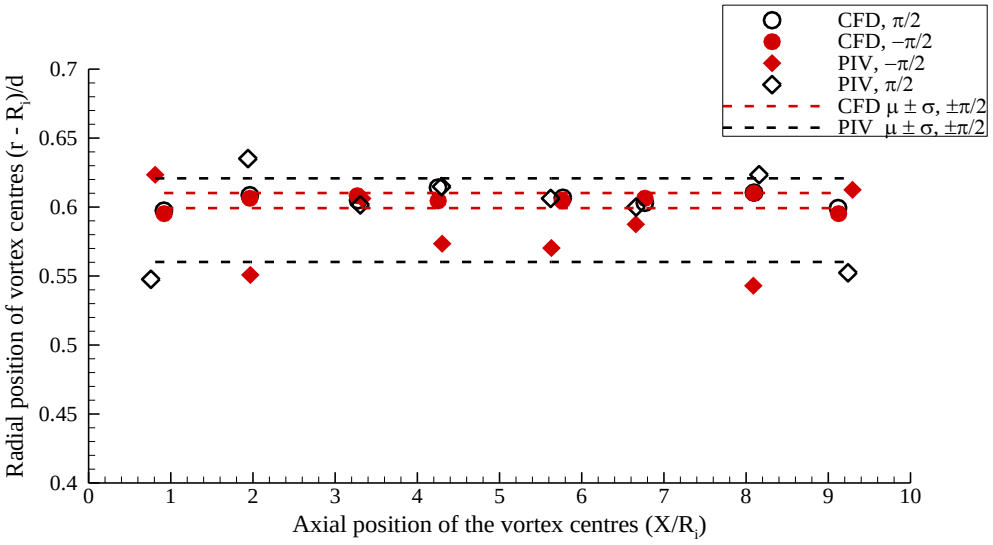

(b)

Figure 7.28: Axial and radial position of vortex centres in the meridional plane with data spread band about the vortex centre mean value from CFD and PIV for the test cases (a) Γ = 11.36 and (b) Γ = 7.81.

This is evidenced by the PIV spread bands of the vortex centres in Figure 7.28(a) and Figure 7.28(b). For instance, the area occupied by the measured vortex centres spreads

over the range $0.46 \leq (r - R_i)/d \leq 0.66$ radially for the test case $\Gamma = 11.36$, while the area occupied by measured vortex centres spreads over the narrower range $0.54 \leq (r - R_i)/d \leq 0.64$ radially for the test case $\Gamma = 7.81$.

Careful examination of Figure 7.28(a) and Figure 7.28(b) show that the spread bands from the CFD in both figures are similar. This suggests that the spread of the vortex centres in cylinder with aspect ratios $\Gamma = 7.81$ and $\Gamma = 11.36$ is almost proportional to the gap width d in the CFD, whereas in the PIV, the spread of the vortex centres are affected by a change in the flow regime and by the gap width d.

7.7 Experimental results and discussions for concentric cylinders $\Gamma = 5.32$

The PIV experimental results documented in this section are concerned the rotating concentric cylinders with aspect ratio 5.31 and radius ratio 0.35. The geometry and the flow parameters of the apparatus used for this PIV experimental investigation are the same as those presented in Table 5-2. All the velocity fields have been normalised by the inner cylinder surface speed, ΩR_i.

7.7.1 Flow regimes and patterns in the annulus of the concentric cylinders

At the aspect ratio $\Gamma = 5.32$, radius ratio $\eta = 0.35$, and at the rotational speed of the inner cylinder $\Omega = 52.36$ rad/s, the PIV flow map of Figure 7.29 shows that the flow is unsteady, suggesting a transition to a turbulent flow. This type of flow is particularly complex due to the occurrence of strong shear layers near the wall boundaries. As discussed in chapter two, turbulent Taylor vortices exist at a Taylor number greater than $Ta \approx 1000Ta_c$ (Koschmieder, 1993). In chapter two, Table 2-1 and Table 2-2 show the critical parameters for the onset of Taylor vortices for various values of radius ratio η. At the experimental conditions at which this test was conducted, using Table 2-1, the critical Taylor number Ta_c is estimated as 4775.76. Based on this value of Ta_c and on the Taylor number for the existence of turbulent Taylor vortices given by Koschmieder (1993), the Taylor number at which transition to a turbulent flow regime is expected for this test case is estimated as $Ta \approx 1000Ta_c = 4.776 \times 10^6$. Table B 6 in appendix B shows that there have been just a few studies on turbulent Taylor vortices at Taylor and Reynolds numbers similar to the ones in this work.

7.7.2 Instantaneous flow structures

The velocity vector maps in Figure 7.29 show a sequence of three instantaneous velocity fields in the meridional plane of the annulus ($\theta = \pm\pi/2$), taken in quick succession at recording times $t = t_0 + 7.25s$, $t = t_0 + 7.50s$, and $t = t_0 + 7.75s$, where t_0 is defined as in section 7.5.2.

The normalised instantaneous velocity vectors in Figure 7.29 shows there is a change in the flow regime between test case $\Gamma = 7.81$ and test case $\Gamma = 5.32$. The time sequence of velocity vector maps in Figure 7.29 shows that the flow field is characterised by randomness and it is not clear how each next flow map can be elicited from its preceding one. This is a recognisable feature of turbulent flow in which the time evolution is stochastic rather than deterministic. The flow field is changing so rapidly that it was not possible to observe undistorted regular Taylor vortices in all the three PIV snap shots in Figure 7.29 as observed for the test cases $\Gamma = 11.36$ and $\Gamma = 7.81$ in Figure 7.8(a) and Figure 7.8(b).

This flow regime is representative of the trend observed throughout a set of 100 vector maps. In some snap shots, Taylor vortices are not identifiable in the fully irregular turbulent flow and, at other times, distorted Taylor vortices are present that they cannot be easily distinguished in the background turbulent flow. This flow pattern can no longer be described by well-defined Taylor vortices, although structures associated with the Taylor vortices remain.

The instantaneous flow field in Figure 7.29 shows vortices of different sizes from larger sized vortices to smaller eddies. In Figure 7.29(a-c) there is breakdown of axial periodicity in the flow pattern. This flow pattern is in agreement with the observation made by Smith and Townsend (1982) for high Taylor number flow.

Figure 7.29 suggests that the flow field consists of large-scale motion with many small-scale vortices embedded within it. The turbulent motion is a result of variations in the increase in the Reynolds number that promotes the decay of large scale instabilities. The small-scale vortices are not so well-defined in the flow field, due to the limitation of the PIV in which the spatial resolution of the experimental apparatus used was unable to capture secondary instabilities, as the time between the pulses was too long for this PIV system to capture such features in this highly turbulent flow.

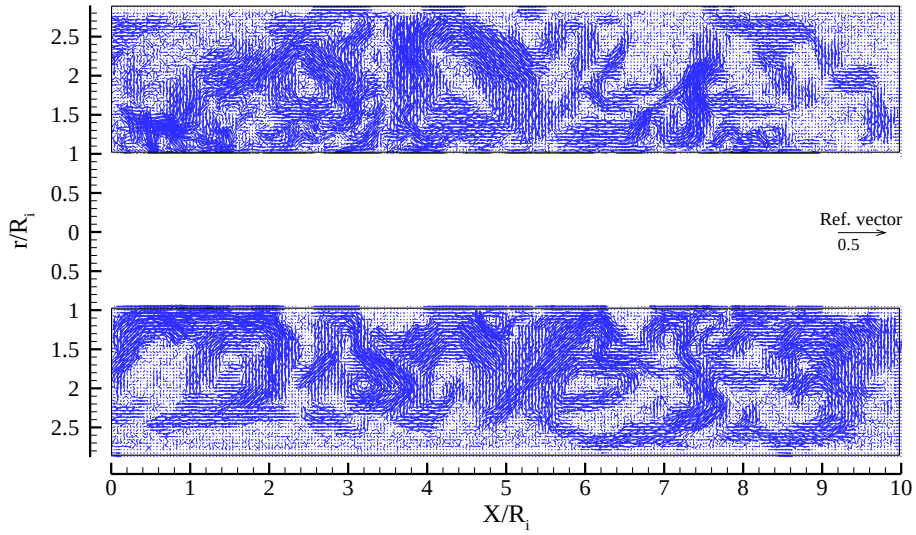

(a)

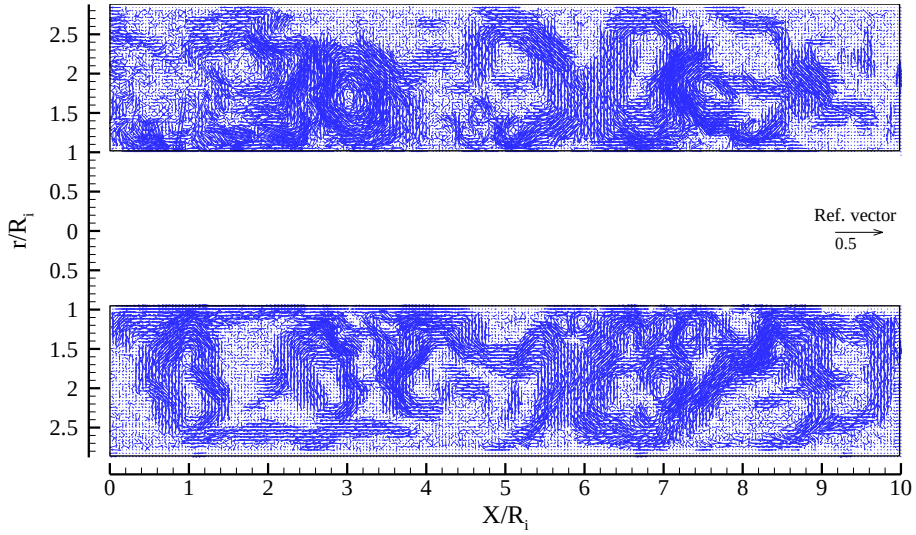

(b)

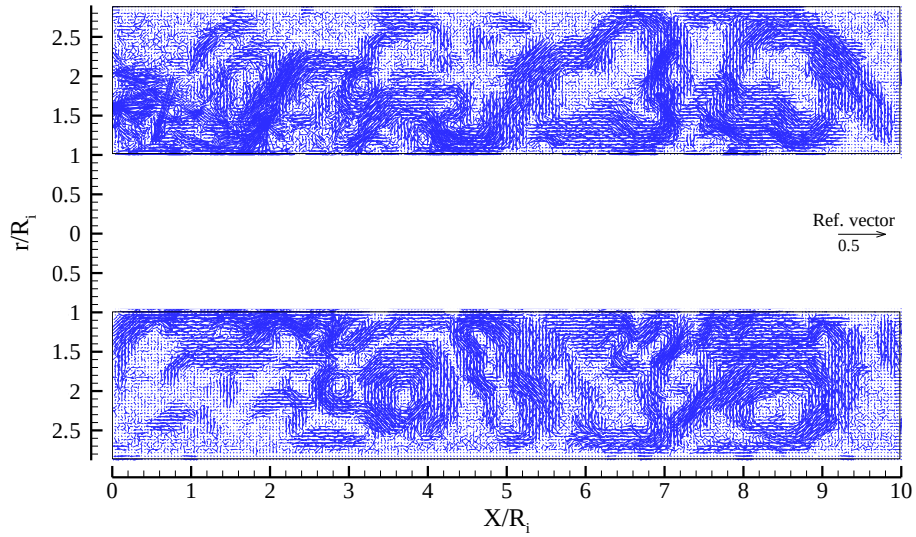

(c)

Figure 7.29: Normalised instantaneous vector maps along the meridional plane at times (a) $t = t_0 + 7.25s$, (b) $t = t_0 + 7.50s$, and (c) $t = t_0 + 7.750s$.

Figure 7.30 shows the power spectral density of the radial velocity obtained from ensemble averaging 100 Discrete Fourier Transforms (DFT) of the instantaneous axial profiles of radial velocity for the test case $\Gamma = 5.32$. Instantaneous axial profiles of radial velocity are first extracted from 100 vector maps at the constant radial position $r = R_i + 0.5d$ on the lower channel ($\theta = -\pi/2$) of the annulus of Figure 7.29. Then the Discrete Fourier Transform of each profile is obtained in Matlab R2010(a) using the DFT formulation reported in Ifeachor and Jervis (2002). The power spectral density in Figure 7.30 is plotted in logarithmic scale as a function of the axial wavenumber $k = 2\pi/\lambda$, where λ is the axial wavelength defined in section 6.7.8. The power spectral density is computed by the product of the Discrete Fourier Transform with its complex conjugate value divided by Discrete Fourier Transform vector length. The results are then ensemble averaged to reduce the noise associated with the PIV measurement technique. The power spectral density of radial velocity in Figure 7.30 shows no evidence of any sharp peak but rather the presence of a broad-band peak centred at a wavenumber of approximately $16m^{-1}$, at which E(k) approximately equals 0.17 m^3/s^2. The broad-band peak in Figure 7.30 is evidence of the onset of significant non-linearity in the kinetic energy field. This is an indication that the flow is turbulent with eddies covering a continuous broad range of length scales.

The power spectral density of a fully developed turbulent flow typically displays three regions, which are the energy producing range, the inertial sub-range, and the viscous dissipation range. The power spectral density of radial velocity in Figure 7.30 does not show all the three regions. Figure 7.30 also shows the slopes of the PIV spectrum for this study and the Kolmogrov -5/3 power law for the decay of homogeneous isotropic turbulence. Figure 7.30 shows that the decay rate for this present study is steeper than the conventional Kolmogrov -5/3 law. A roll-off rate in the inertial sub-range steeper than -5/3 was also obtained by de Jong et al. (2009) from PIV measurements of zero-mean "isotropic" turbulence in an enclosed chamber. This trend indicates that turbulence in the present study is not fully developed so that turbulence decay is influenced by intermittent large-scale structures associated to the Taylor instability. These structures have a dynamic equilibrium with the remainder of the turbulent kinetic energy spectrum different than that of a fully developed turbulent flow.

Figure 7.30 does not show a viscous dissipation range, which is a region of steeper kinetic energy roll-off at wavenumbers higher than the Kolmogrov wavenumber. In order to

explain the apparent absence of the viscous dissipation range in the PIV results, the dynamic range of the PIV measurements was determined. The dynamic range determination was based on the estimated value of the peak power spectral level, the displacement of tracer particles associated to this peak velocity fluctuation, and the assumption that the minimum spatial resolution of the PIV system is given by the size of one pixel on the CCD array.

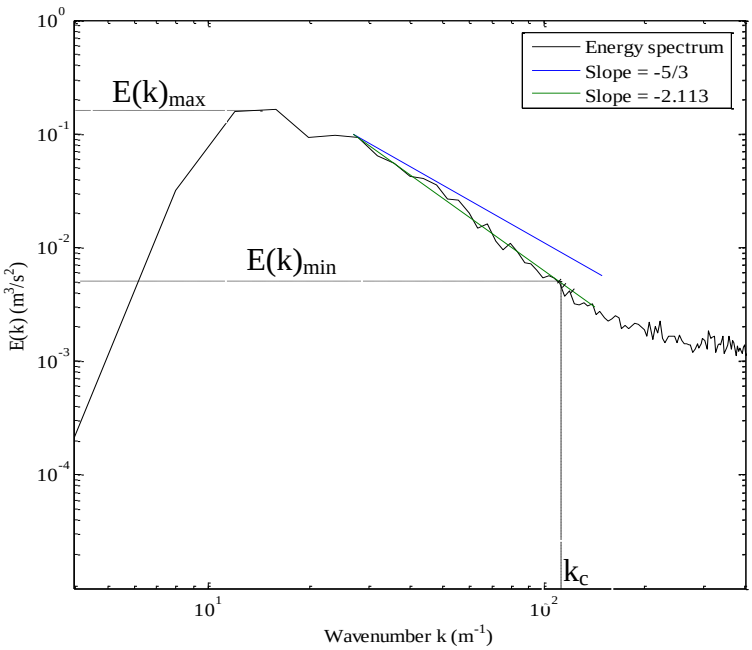

Figure 7.30: Energy spectrum of velocity component.

The estimated dynamic range of the PIV system is shown in Figure 7.30 by the dotted black lines and is $0.004 \leq E(k) \leq 0.17$. The lowest measurable value of E(k) is 0.004, which represents the measurement noise floor level. This suggests that any power spectral density value measured by PIV that is below 0.004 includes a significant component of measurement noise. This explains why the power spectral density starts to increase with increasing wavenumber above k = 100, instead of decaying due to further energy cascading and viscous dissipation. The vertical balck dashed line in Figure 7.30 shows the location of the cut-off wavenumber k_c above which the instrumentation noise in the measured power spectral density makes the measured E(k) unreliable.

The instantaneous velocity fields for the test case $\Gamma = 5.32$ in Figure 7.29 show that the flow contains some large structures of characteristic size similar to one annular gap d. This is the same characteristic size of a Taylor vortex. Four of such structures can be seen at $\theta = -\pi/2$ in Figure 7.29(b). There seems to be an approximate but not exact recurrence of Taylor vortices. The results obtained suggest that the Taylor-Couette flow is more

intermittent. This intermittency prevents the flow from developing into a fully developed turbulent state. As such, an ensemble average of all the instantaneous velocity fields in the meridional plane of the annulus was performed to obtain the mean velocity vector map shown in Figure 7.31. The PIV measurement area is normalised by the inner cylinder radius R_i, consistently with the other test cases, as shown in Table 5-2. The ensemble averaged velocity vector map in Figure 7.31 shows a typical Taylor-Couette flow pattern similar to the time averaged velocity vector maps obtained from CFD and PIV for the test cases $\Gamma = 11.36$ and $\Gamma = 7.81$ in the entire measurement area. This flow pattern has been discussed in details in the context of Figure 6.6 and Figure 7.7. Along the axial direction of the PIV measurement view area, the velocity vectors of Figure 7.31 show four vortices. The number of vortices in this test case is less than the number of vortices obtained for the test cases $\Gamma = 11.36$ and 7.81, despite the fact that the axial length and the angular speed of the inner cylinder are the same. The reduction in the number of vortices can therefore be attributed to the difference in the aspect and radius ratios of this test case when compared with the other two test cases.

The two vortices near the left and right end boundaries of the computational domain in Figure 7.31 are more elongated than the remaining two vortices in the central region of the annulus. This end-wall effect has been discussed in the context of Figure 6.6 and Figure 7.7. The two elongated vortices in Figure 7.31 are almost of the same length and are mirror image of one another, although the effect of light sheet reflection is noticeable near the right end-wall boundary as the velocity vectors in this region are lower in magnitude with respect to the symmetric ones near the left end-wall boundary. The inward radial direction of the velocity vectors ($\theta = -\pi/2$) at the end-walls is in agreement with CFD and PIV experimental results for test cases $\Gamma = 11.36$ and $\Gamma = 7.81$ and this has been discussed in the context of Figure 6.6 and Figure 7.7.

As in test cases $\Gamma = 11.36$ and $\Gamma = 7.81$, there is transfer and mixing of fluid between adjacent vortices in the outflow and inflow regions in Figure 7.31. At $X/R_i = 5.0$ in Figure 7.31, where the mixing of fluid between the adjacent vortices is not so obvious may be described as the region of zero net axial flow and sits between the two counter-rotating vortices as their common interface. The Taylor vortices are therefore observed to be symmetrical about the axial length of the annulus at $X/R_i = 5.0$.

In Figure 7.31, the outflow region boundaries are twisted and they are not perpendicular to the inner and outer cylinder walls. Also, the vortices are organised in a definite pattern in

that the vortex centres of the two vortices at the end-wall boundaries at $\theta = -\pi/2$ are displaced radially toward the outer cylinder and the vortex centres of the two vortices at the central region along the length of the cylinder are displaced radially toward the inner cylinder. This pattern is similar to the one observed for the test cases $\Gamma = 11.36$ and $\Gamma = 7.81$ discussed in the context of Figure 7.7.

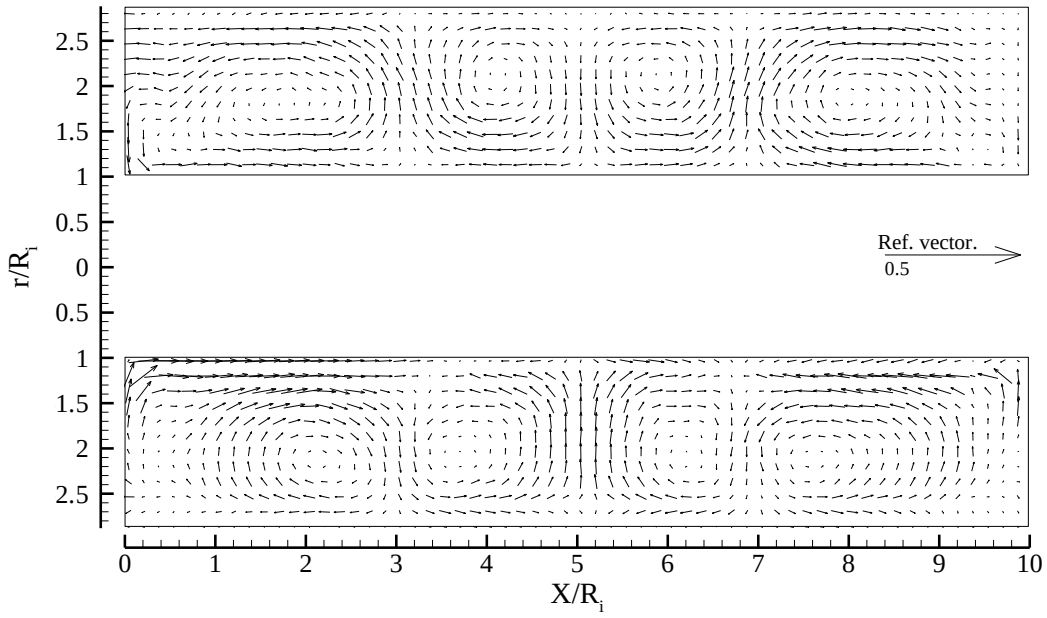

Figure 7.31: Normalised ensemble average of the velocity vector map in the meridional plane of the annulus.

7.7.3 The axial and radial velocity contour plots

The contour plots of the axial and radial velocity components in the meridional plane for the test case $\Gamma = 5.31$ are shown in Figure 7.32 and Figure 7.33 respectively. The same even contour line spacing of $0.03\Omega R_i$ is used in Figure 7.32 and Figure 7.33 as Figure 7.32. The features and structures of the normalised axial velocity contour plot in Figure 7.32 are similar to the ones obtained for test cases $\Gamma = 11.36$ and 7.81 for CFD and PIV in Figure 6.8 and Figure 7.10 respectively. However, the axial velocity magnitude both at the outward flow and inward flow regions for this test case is very small compared with the axial velocity magnitude for the test cases $\Gamma = 11.36$ and $\Gamma = 7.81$. The low axial velocity magnitude is due to the kinetic energy transfer between the large scale eddies and the smaller eddies that develop in the flow at this high Reynolds number. The velocity and time scales of these smaller eddies is therefore expected to be smaller compared to the ones of the larger eddies that characterise the test cases $\Gamma = 11.36$ and $\Gamma = 7.81$. The formation of an alternating pattern of axial velocity maxima and minima in the annulus at

the same axial positions as the vortex centres is shown in Figure 7.32. This feature has been discussed in the context of Figure 6.8 and Figure 7.10.

Figure 7.32 further shows that the centres of the vortices at the end-walls are displaced radially toward the outer cylinder at $\theta = -\pi/2$, while the centres of the vortices in the central region are displaced radially toward the inner cylinder. The reverse trend is shown at $\theta = \pi/2$. The offset of the vortex centres from the annulus radial centre is attributed to the centrifugal forces acting to throw the fluid away from the inner cylinder at high Reynolds number (Parker and Merati, 1996).

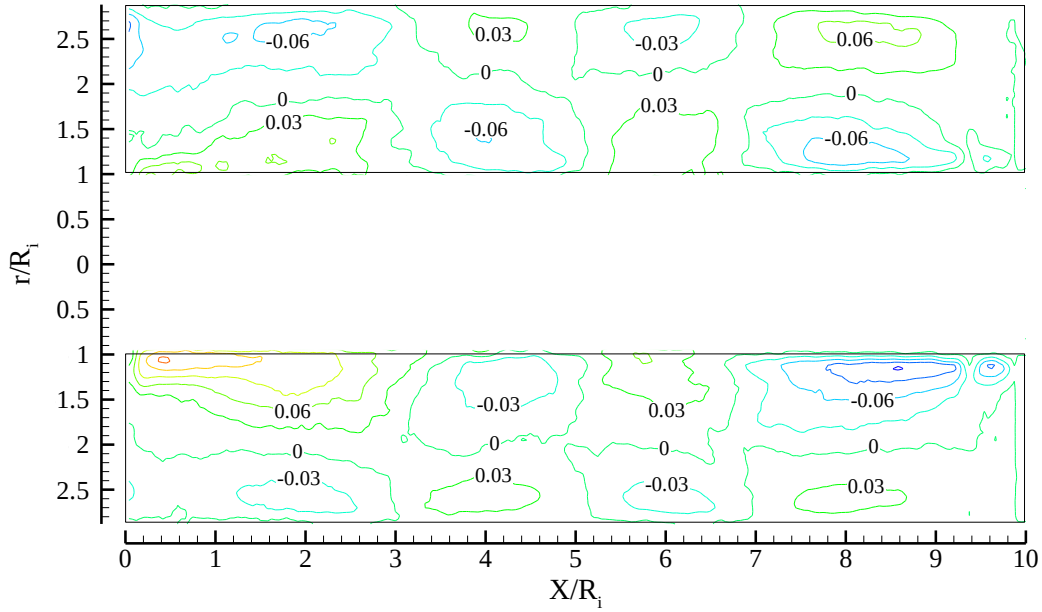

Figure 7.32: Contour plot of axial velocity in the meridional plane normalised by ΩR_i with contour spacing $\Delta u_x = 0.03\Omega R_i$.

Figure 7.32 shows that the zero axial velocity contour along the radial direction for the two vortices near the end-walls and the two vortices at the central region is located at approximately $r/R_i = 2.1$ and $r/R_i = 2.0$ respectively in the lower channel ($\theta = -\pi/2$) of the annulus. In the upper channel ($\theta = \pi/2$), the zero axial velocity along the radial direction for the two vortices near the end-walls and the two vortices at the central region is located at approximately $r/R_i = 1.9$ and $r/R_i = 2.15$ respectively. A detailed description of the axial velocity flow field is discussed in the context of CFD results in Figure 6.8 and Figure 7.10 for the test cases $\Gamma = 11.36$ and 7.81.

The normalised radial velocity contour map in Figure 7.33 shows an alternating pattern of radial velocity minima and maxima along the axial direction. The radial contour map in Figure 7.33 does not show clearly packed contour lines like the ones in Figure 7.11 for the test cases $\Gamma = 11.36$ and $\Gamma = 7.81$. However, Figure 7.33 still shows distinctive features of

Taylor vortices also observed in Figure 7.11, using the same rainbow contour colour notation. The positive (yellow) and negative (cyan) values on the contour lines indicate the direction of the vortex circulation, as in Figure 7.33.

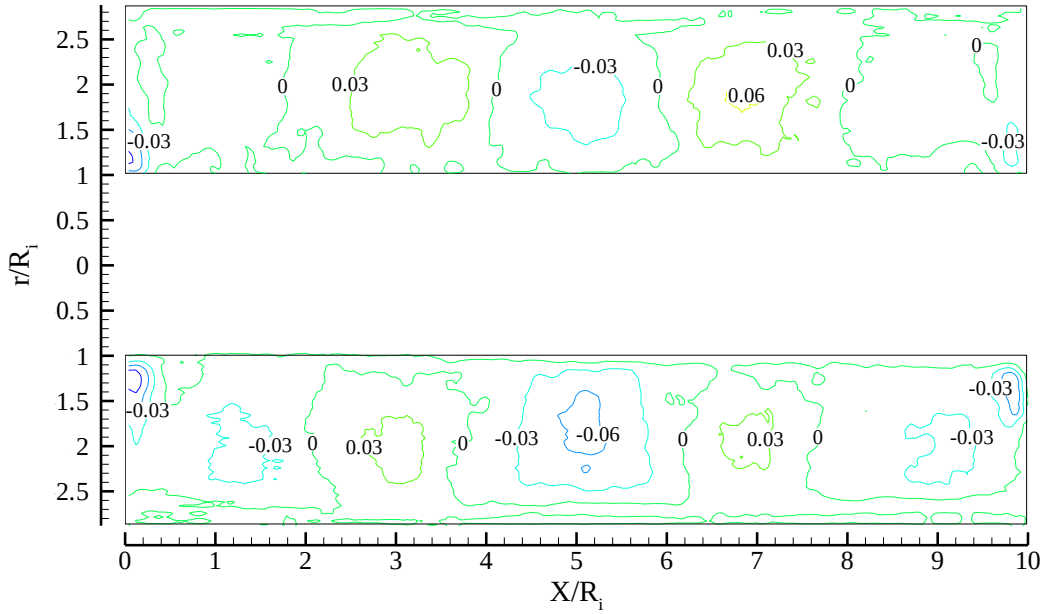

Figure 7.33: Contour plot of radial velocity in the meridional plane normalised by ΩR_i with contour spacing $\Delta u_r = 0.03\Omega R_i$.

The axial boundaries between the negative and positive values of these contour clusters delimit inward flow regions and outward flow regions at $\theta = -\pi/2$ at the meeting point of two adjacent vortices in Figure 7.33. The radial velocity maxima occur in the radial outflow regions between adjacent vortices. This is because centrifugal forces act to increase the outward radial velocity in these regions and slow down the returning flow at the inward flow region. The radial velocity magnitude for this test case is very small compared with radial velocity magnitude for the test cases Γ = 11.36 and 7.81. These features have been discussed in details in the context of Figure 6.9 and Figure 7.11.

7.7.4 RMS meridional plane velocity contours and velocity profiles

Figure 7.34 and Figure 7.35 show the contour plots of normalised Root Mean Square (RMS) of axial and radial velocity fluctuations in the meridional plane for the test case Γ = 5.32. The RMS velocity fluctuations are a measure of the flow turbulent kinetic energy in the annular region of the cylinder. The RMS was computed using equation 6.8.

The RMS levels of axial and radial velocity fluctuations are normalised by the surface speed of the inner cylinder ΩR_i. The contour levels in Figure 7.34 and Figure 7.35 are evenly spaced, with a contour spacing of $0.015\Omega R_i$. The RMS contour levels are higher

than 3% of the surface speed of the inner cylinder ΩR_i throughout the annulus, indicating that the observed flow regime in this test case at the test Taylor number is turbulent Taylor vortex flow.

The normalised axial and radial velocity RMS contours in Figure 7.34 and Figure 7.35 show that the turbulence level is high toward the wall of the rotating inner cylinder. This decreases in the positive radial direction toward the wall of the outer cylinder, where the turbulence level is lower. The high turbulence level toward the wall of the inner cylinder may be attributed to the large tangential velocity gradient in the boundary layer causing a higher shear rate in this region. In Figure 7.34 and Figure 7.35, it is observed that the RMS velocity in the meridional plane is non-uniform, which suggests that turbulence is not homogenous (uniformly distributed) and isotropic along the axial direction. This is in contrast to the Kolmogorov theory for an open free flow where turbulence can be homogenous and isotropic at a very high Reynolds number. The inhomogeneity and anisotropy may be due to fluctuations in the velocity field and the fact that the flow may not have reached a fully developed turbulent state in this test case.

In Figure 7.34 and Figure 7.35, at approximately X/R_i = 3.0 and 7.0, the turbulence intensity is higher than in any other regions in the annulus. These axial positions correspond to the outflow regions in Figure 7.31. Since more turbulence exists near the wall of the inner cylinder due to the high local shear rate, larger zones of high turbulence intensity occur at the radial outflow regions near the inner cylinder. Specifically, the radial outflow transports the turbulence generated near the rotating inner cylinder outwards towards the outer cylinder. This result further confirms that the axial and radial velocities at the outward flow regions are stronger than that at the inward flow region.

The observed dominant turbulent flow near the wall of the inner cylinder affects the RMS of axial velocity and radial velocity fluctuations as shown in the contour plots of Figure 7.34 and Figure 7.35 respectively. In Figure 7.34, larger zones of high turbulence intensity for the axial velocity component occur at the radial outflow near the wall of the inner cylinder. In Figure 7.35 on the other hand, larger zones of high turbulence intensity for the radial velocity component occur at the radial outflow regions near the mid-span gap width of the annulus. This results agrees with the observation made by Parker and Merati (1996).

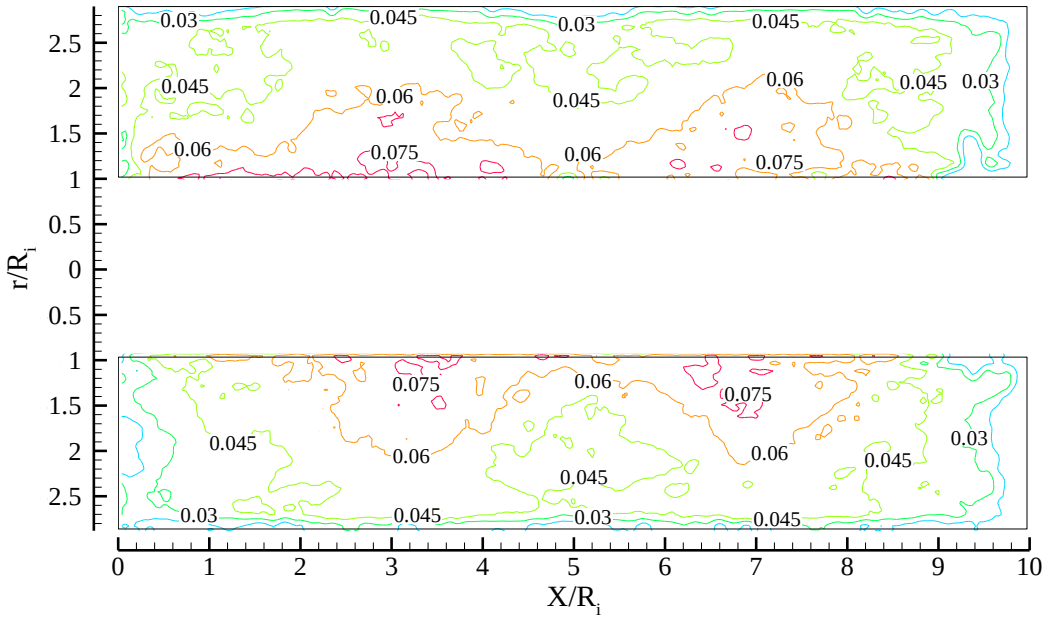

Figure 7.34: RMS axial velocity contours in the meridional plane normalised by ΩR_i with contour spacing $\Delta u_{RMS} = 0.015\Omega R_i$.

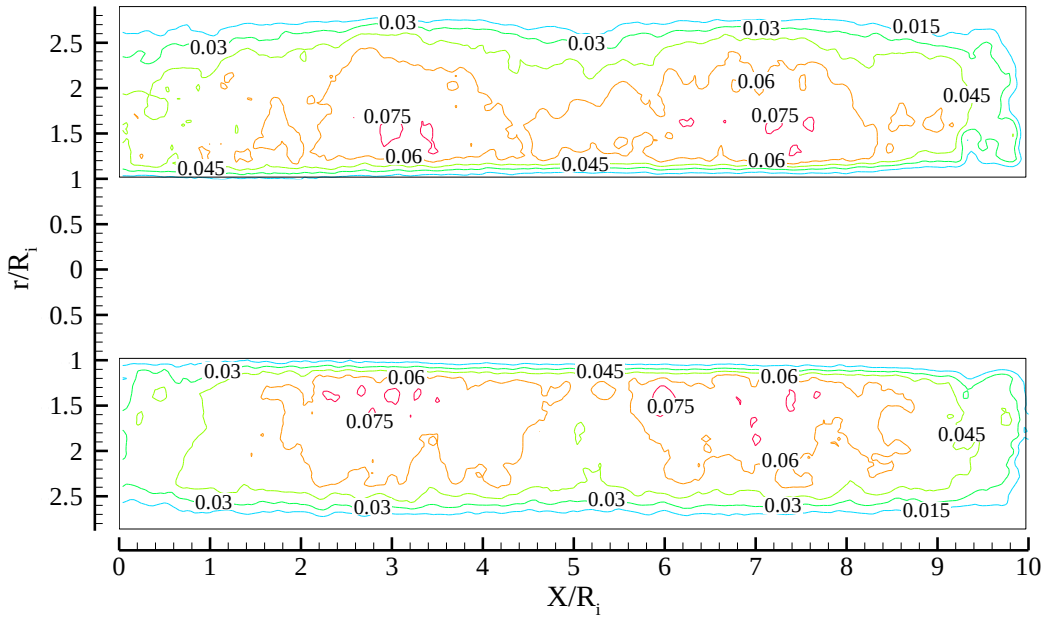

Figure 7.35: RMS radial velocity contours in the meridional plane normalised by ΩR_i with contour spacing $\Delta u_{RMS} = 0.015\Omega R_i$.

Figure 7.36 and Figure 7.37 show respectively the axial profiles of normalised RMS axial velocity and RMS radial velocity at three constant radial positions in the meridional plane on the lower ($\theta = -\pi/2$) channel of the annulus for the test case $\Gamma = 5.32$. The radial positions along the lower channel where the profiles are extracted are $r = R_i + 0.125d$ (5.875mm away from the wall of the inner cylinder), $r = R_i + 0.5d$ (the mid-span gap of the annulus), and $r = R_i + 0.875d$ (5.875mm away from the wall of the outer cylinder). The positions of the constant radial line where the profiles are extracted are taken at the same

percentage gap width d as test cases $\Gamma = 11.36$ and $\Gamma = 7.81$. The reason for extracting the velocity profiles at these positions has been discussed in the context of Figure 7.12. The RMS velocity profiles presented here have been normalised with respect to the inner cylinder surface speed ΩR_i. The normalised RMS axial velocity and RMS radial velocity profiles in Figure 7.36 and Figure 7.37 traverse through the inward and outward flow regions of Figure 7.34 and Figure 7.35 respectively.

The normalised RMS axial velocity profiles in the meridional plane at the three constant radial positions in Figure 7.36 show a progressive increase in the fluctuations amplitude of the axial velocity along the axial direction from the left end-wall boundary towards the centre of the annulus. The normalised RMS axial velocity profiles at the three radial positions show a first peak at the first outflow region near the left end-wall boundary at the axial position X/R_i of approximately 3.3, from where the profiles decrease to a local minimum along the axial direction in the range $3.4 \leq X/R_i \leq 6.6$. A second peak is observed at the second outflow region near the right end-wall boundary at approximately $X/R_i = 6.6$. From this axial position, the profiles decrease monotonically to almost zero at the right end-wall boundary. Therefore, the turbulence level is higher at the outflow regions and lower at the inflow region, in agreement with the observation made in the context of Figure 7.34 and Figure 7.35.

The normalised RMS axial velocity profiles in Figure 7.36 show that the turbulence intensity is high near the wall of the inner cylinder at $r = R_i + 0.125d$. Near the end-wall boundaries, over the ranges $0 \leq X/R_i \leq 3.4$ and $6.6 \leq X/R_i \leq 10$, the fluctuation amplitudes for the three profiles are close in magnitude to one another. The difference among the three profiles is best observed in the central region over the range $3.4 \leq X/R_i \leq 6.6$. At the radial position $r = R_i + 0.125d$, the magnitude of the normalised RMS axial velocity maxima $u_{RMS}/\Omega R_i$ at the outflow regions are approximately 0.08, while the magnitude of the RMS axial velocity minimum $u_{RMS}/\Omega R_i$ at the inflow region is approximately 0.054.

For the profile at the mid-span gap $r = R_i + 0.5d$, the magnitude of the RMS axial velocity maxima $u_{RMS}/\Omega R_i$ at the outflow regions is approximately 0.068, while the magnitude of the RMS axial velocity minimum $u_{RMS}/\Omega R_i$ at the inflow region is approximately 0.04. Similarly, for the profile near the wall of the outer cylinder at $r = R_i + 0.875d$, Figure 7.36 shows that the magnitudes of the RMS axial velocity maxima and minimum $u_{RMS}/\Omega R_i$ at the outflow and inflow regions are approximately 0.058 and 0.04 respectively. In the central region of Figure 7.36, the RMS axial velocity minima $u_{RMS}/\Omega R_i$ for the profile at

the mid-span gap at r = R_i + 0.5d and for the profile near the wall of the outer cylinder at r = R_i + 0.875d have nearly the same value.

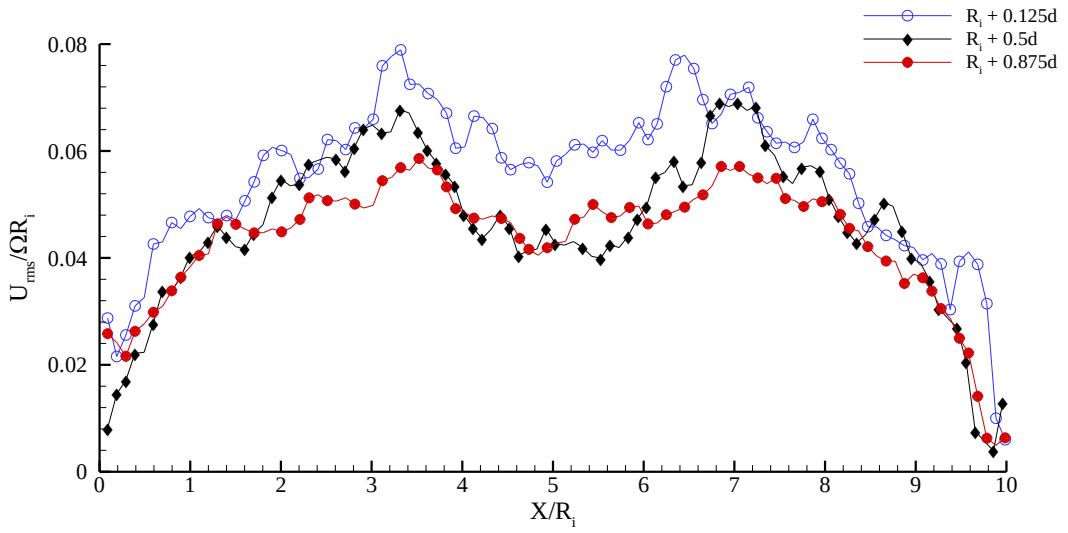

Figure 7.36: Normalised RMS axial velocity profiles in the meridional plane at constant radial positions r = R_i + 0.125d, r = R_i + 0. 5d, and r = R_i + 0.875d (θ = -π/2) from PIV for the test case Γ = 5.32.

The normalised RMS radial velocity profiles in the meridional plane at the three constant radial positions in Figure 7.37 exhibit similar trends as the ones in Figure 7.36. The normalised RMS radial velocity profiles in Figure 7.37 show that the turbulence level near the wall of the inner cylinder at r = R_i + 0.125d and at the centre of the annulus, which is at the gap mid-span r = R_i + 0.5d, is higher than the turbulence near the wall of the outer cylinder.

The normalised RMS radial velocity at r = R_i + 0.5d is slightly higher than the normalised RMS radial velocity at r = R_i + 0.125d, except at the inflow region. For instance, the magnitude of the normalised RMS radial velocity $u_{RMS}/\Omega R_i$ at r = R_i + 0.5d in the outflow region close to the right end-wall is approximately 0.074, while the magnitude of the normalised RMS radial velocity $u_{RMS}/\Omega R_i$ at the inflow region is approximately 0.046.

For the profile at r = R_i + 0.125d, the maximum and minimum magnitudes of the normalised RMS radial velocity $u_{RMS}/\Omega R_i$ at the outflow and inflow regions are approximately 0.07 and 0.052 respectively. For the profile near the wall of the outer cylinder, the maximum and minimum magnitude of the normalised RMS radial velocity $u_{RMS}/\Omega R_i$ at the outflow and the inflow regions are approximately 0.028 and 0.016 respectively. This result shows that there is a strong radial shear rate at the inner cylinder

surface and in the mid-span gap of the annulus. This shear rate is reduced approaching the wall of the outer cylinder.

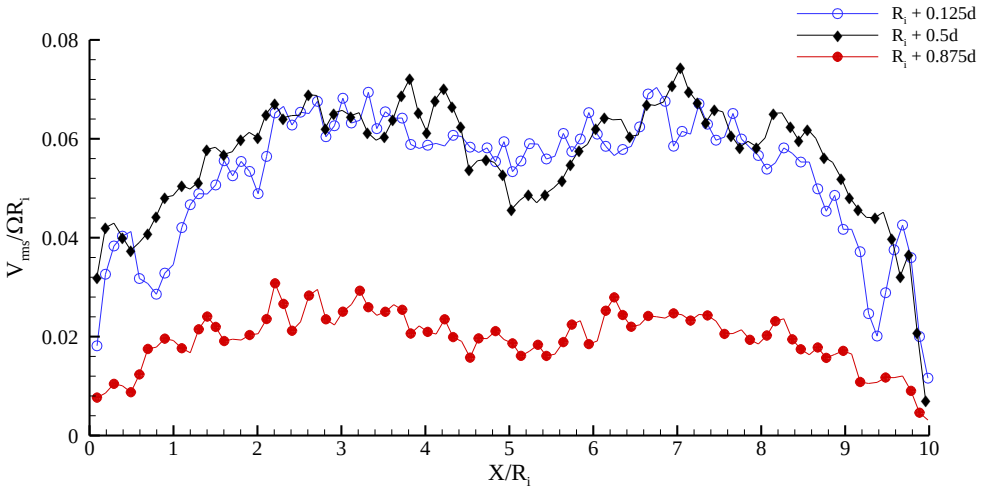

Figure 7.37: Normalised RMS radial velocity profiles in the meridional plane at constant radial positions r = R_i + 0.125d, r = R_i + 0. 5d, and r = R_i + 0.875d (θ = -π/2) from PIV for the test case Γ = 5.32.

7.7.5 Convergence of the RMS velocity

As discussed in section 7.3, convergence in PIV statistical data is obtained when taking and averaging more PIV vector maps does not affect the result. As such, the convergence of the RMS velocity was tested at selected radial positions along the axial direction of the annulus. This was determined by extracting RMS axial velocity $u_{RMS}/\Omega R_i$ profiles at three constant radial positions r = R_i + 0.125d, r = R_i + 0.5d, and r = R_i + 0.875d in the meridional plane along the axial direction on the lower (θ = - π/2) channel of the annulus. The RMS axial velocity $u_{RMS}/\Omega R_i$ was estimated from fifty and one hundred instantaneous images taken in succession. U_{50} is the RMS velocity computed from 50 images and U_{100} is the RMS velocity computed from 100 images. For the estimation of the convergence, the L_∞ and L_2 norms were computed. L_∞ is a measure of the ratio of the maximum absolute difference between two data sets to the average of the same sets of data. L_2 is a measure of the ratio of the mean absolute difference between two data sets to their average value. The L_∞ and L_2 are given respectively by equation 7.1 and 7.2.

$$L_\infty = \frac{max|U_{100} - U_{50}|_i}{\sum_{i=1}^{N}(U_{100} + U_{50})_i} \text{ x } 2N \qquad 7.1$$

$$L_2 = \frac{\sum_{i=1}^{N}|U_{100} - U_{50}|_i}{\sum_{i=1}^{N}(U_{100} + U_{50})_i} \text{ x } 2 \qquad 7.2$$

where *i* is the i^{th} data point and N is the number of data points in the X-direction.

Figure 7.38 shows the RMS axial velocity $u_{RMS}/\Omega R_i$ at the three constant radial positions for each data set. Using equations 7.1 and 7.2, the values of L_∞ and L_2 obtained for the profiles near the wall of the inner cylinder at $r = R_i + 0.125d$ are approximately 0.19 and 0.055 or 19% and 6% of the inner cylinder rotational speed, respectively. For the profiles at the mid-span gap $r = R_i + 0.5d$ of the annulus, the values of L_∞ and L_2 are estimated as 33% and 8% respectively. The values of L_∞ and L_2 are approximately 20% and 6% respectively for the profiles near the wall of the outer cylinder at $r = R_i + 0.875d$.

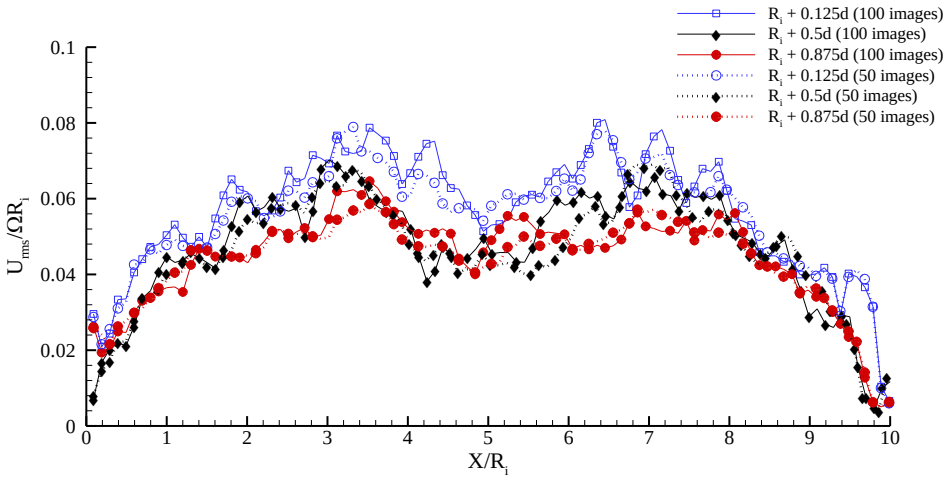

Figure 7.38: Normalised RMS of axial velocity profiles in the meridional plane at constant radial positions $r = R_i + 0.125d$, $r = R_i + 0.5d$, and $r = R_i + 0.875d$ ($\theta = -\pi/2$) from PIV for the test case $\Gamma = 5.32$.

The results show that the L_∞ norm gives a high value with the L_2 maximum occurring at the mid-span gap of the annulus. However, the L_2 norm gives a reasonably low value along the entire annulus, with a maximum of 8% at the mid-span gap $r = R_i + 0.5d$. This result suggests that the RMS velocity estimates are, on average, converged to within 8%. There are areas where the flow statistics seems to be changing over time. This may result from a form of Taylor mode staging in the flow with a greater number of transitions between a turbulent flow with embedded strong Taylor vortices and more random motion in the set of 100 images than in the set of 50 images. Direct observation of the two image sets did not provide further supportive evidence towards this hypothesis, partly due to the difficulty of identifying the variation in the outflow regions where the L_∞ maxima occur in Figure 7.38.

Chapter Eight: Effects of a cylindrical probe on the annular flow

8.1 Introduction

This chapter is concerned with the experimental investigation on the intrusive effect of a cylindrical probe representing a PIV endoscope inserted in the annular gap between two concentric rotating cylinders. The effects of a cylindrical probe on the Taylor vortex flow pattern that develops in the annular region of concentric rotating cylinders are examined by means of PIV. The objective is to examine the degree of intrusiveness that a cylindrical probe configuration inserted in the annular region of the coaxial cylinders has on the flow field. It is also of interest to determine any change in the flow regime that takes place in the annular region of concentric cylinders due to the insertion of the cylindrical probe by comparing the flow pattern with the ones presented in chapter seven. The results obtained from this study will help the understanding to what extent the insertion of a PIV endoscopic probe alters the flow regimes and the flow pattern that exist in the annular region of a concentric rotating cylinder or similar rotating equipment. The result obtained with the cylindrical probe inserted in the annulus will serve as a benchmark upon which alternative probe geometries can be tested for lower flow disturbance in the enclosure.

8.2 Experimental apparatus and technique

The flows under consideration are generated in an apparatus similar to the one used in chapter seven, apart from the introduction of the cylindrical probe in the annular region of the concentric cylinders. As such, the geometrical parameters for the concentric rotating cylinders are the same as those used for the PIV experimental investigation with no probe in chapter seven as listed in Table 5-1 and Table 5-2. The cylindrical rod representing the probe is approximately 0.06m long into the annular region with a diameter D_p = 0.01m, giving a probe diameter to annulus gap width ratio D_p/d = 0.46 and a probe length to inner cylinder radius ratio L_p/R_i = 2.4.

Figure 8.1 shows the layout of the stationary outer cylinder and the rotating inner cylinder with the cylindrical probe inserted in the annular region of the cylinders in the meridional plane as measured in the laboratory frame of reference. In Figure 8.1, the cylinders are co-axial with the axis coinciding with the X-coordinate of the cylindrical reference system (r, θ, X).

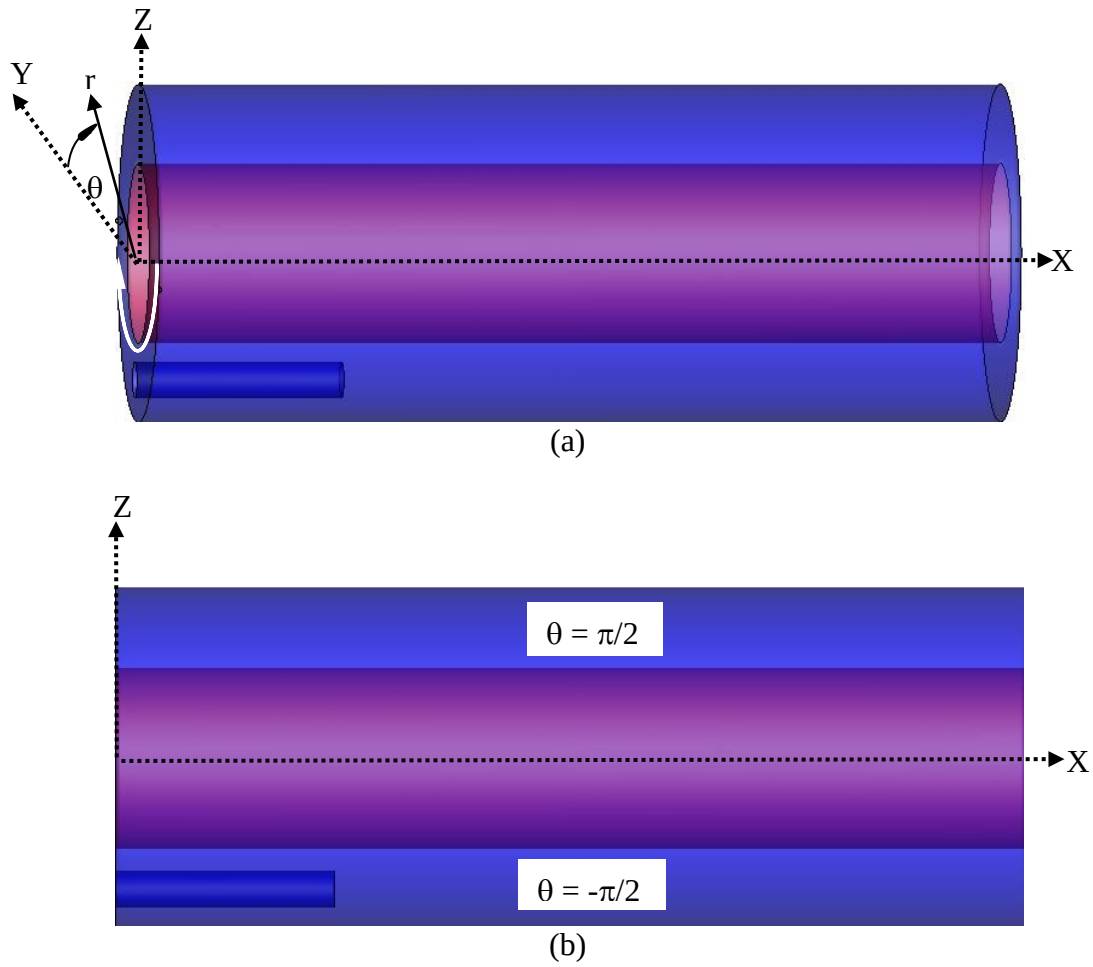

Figure 8.1: (a) Cylindrical reference system of the concentric cylinder assembly with the cylindrical probe inserted (b) Meridional plane.

A PIV experimental investigation with the cylindrical probe in the annular region was conducted for the concentric rotating cylinders test case $\Gamma = 11.36$ discussed in chapter seven. The experimental set-up for this test case is shown in Figure 8.2. The side view from the laser is as shown in Figure 4.5. The same start-up procedure was followed as in the PIV experimental test case with no probe in the annular region, in which the acceleration of the inner cylinder was started suddenly and the final speed was achieved within one second. Similarly, the same procedure for image acquisition as in the test case with no cylindrical probe in the annular region was used. The measurement procedure discussed in chapter five was followed. The two experiments without and with the cylindrical probe were conducted back to back using the same data processing. Therefore, convergence and accuracy of the results documented in chapter seven is taken to be applicable to this test case.

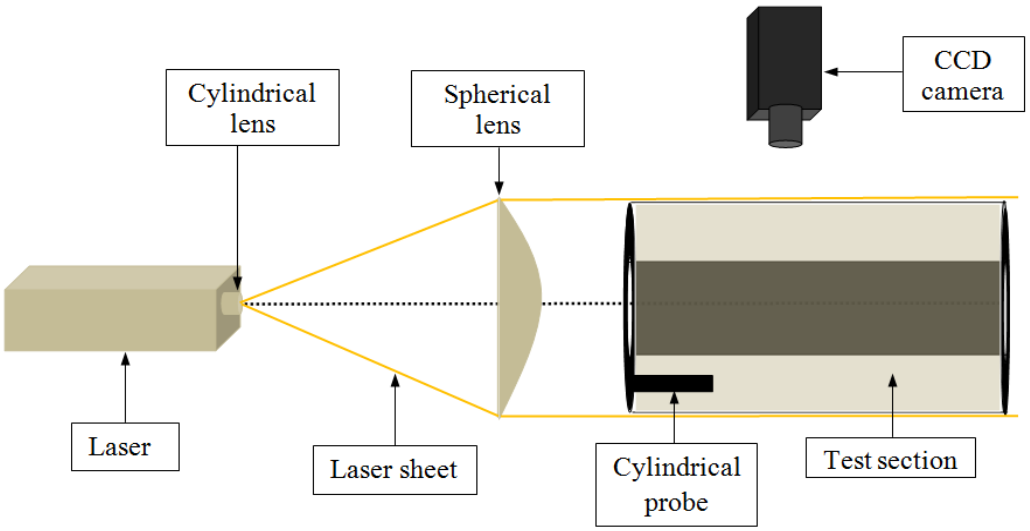

Figure 8.2: PIV experimental arrangement for the Taylor Couette flow apparatus with cylindrical probe model.

8.3 Results presentation and discussions

The PIV field of view in the annulus of the coaxial rotating cylinders in this section is the same as the one of the PIV measurements with no cylindrical probe discussed in chapter seven, section 7.5. The axial and radial length of the PIV results have been normalised by the inner cylinder radius R_i, consistent with the PIV results of chapter seven, section 7.5. All the velocity fields have been normalised by the inner cylinder angular speed ΩR_i, as in chapter seven.

8.3.1 Flow pattern in the annulus of concentric cylinders at $\Gamma = 11.36$ with a probe

The Taylor number in this test case is the same as the one for the test case with no cylindrical probe in the annulus discussed in chapter seven. The PIV results in this section suggest that the flow regime in this test case is wavy vortex flow, consistent with the PIV result without the cylindrical probe discussed in chapter seven, section 7.5.1. This type of flow regime, which is characterised by travelling azimuthal waves superimposed on the Taylor vortices, has been discussed extensively in the context of Figure 7.4 to Figure 7.6. Figure 8.3 shows the normalised time average of the velocity vector map obtained with the cylindrical probe in the annular region in the meridional plane for this test case. Figure 8.3 shows that the time average flow in the annular region between the rotating inner cylinder and the concentric stationary outer cylinder in the entire measurement area that is not occupied by the probe is similar to the flow pattern obtained for the test case with no cylindrical probe in the annulus. The features of this flow pattern have been discussed in

details in the context of Figure 7.7(a). There is qualitative agreement between the PIV results obtained without and with the cylindrical probe in the annulus.

As in Figure 7.7(a), Figure 8.3 shows that there is a slight oscillation of the Taylor vortices resulting in the radial displacement of the vortex centres. This is noticeable in both the upper and lower channels ($\theta = \pm\pi/2$) of the annulus where an axial pattern of vortices similar to that of Figure 7.7(a) is shown. In the upper channel ($\theta = \pi/2$) of the annulus, starting from the left end-wall, over the ranges $0 \leq X/R_i \leq 4.7$, the centres of a pair of vortices are displaced in the same alternate manner as described in the context of Figure 7.7(a). From the right end-wall over the range $4.8 \leq X/R_i \leq 10$, the same pattern is observed as in Figure 7.7(a). This pattern is symmetric about the axial length of the annulus at $X/R_i \approx 4.7$.

In the lower channel ($\theta = -\pi/2$) of the annulus, in the area not occupied by the probe over the range $2.4 \leq X/R_i \leq 5.8$, the centre of the clockwise vortex near the tip of the cylindrical probe is displaced toward the wall of the outer cylinder, while the centre of the next inbound anti-clockwise vortex is displaced toward the wall of the inner cylinder. The next pair of vortices follows the same pattern. Similarly, from the right end-wall over the range $5.8 \leq X/R_i \leq 10$, the same pattern is observed, in which the centre of the last anti-clockwise vortex is displaced toward the outer cylinder and the centre of the next inbound clockwise vortex is displaced toward the wall of the inner cylinder. This pattern is asymmetric about the axial length of the annulus at $X/R_i \approx 5.8$. The effect of this vortex centre radial displacement pattern on the axial flow has been discussed in the context of Figure 7.7. The alternate displacement of the vortex centres at the upper and lower channels of the annulus is in qualitative agreement with the result obtained for the PIV test case with no probe in Figure 7.7(a).

In Figure 8.3, the twisting at the inflow and the outflow boundaries between the vortices is more pronounced in this test case compared to the test case without the cylindrical probe in Figure 7.7(a), resulting in the velocity vectors of the flow field inclining at an angle of about 45^o in the outflow and inflow regions. Mass transfer of fluid from each clockwise vortex to the next anti-clockwise vortex along the positive axial direction is shown in Figure 8.3 as in the test case without the cylindrical probe in the $\theta = -\pi/2$ plane. The fluid mass flux reverses in the $\theta = -\pi/2$ plane, so that the net mass flux across the azimuthal plane is zero. These flow features are also in qualitative agreement with the result obtained for the PIV with no probe in the annulus of the cylinder in as in Figure 7.7(a).

However, the introduction of the cylindrical probe changes many aspects of the flow pattern in the annulus between the cylinders, as anticipated. For instance, the presence of the probe reduces the number of vortices in the meridional plane from twelve in as in Figure 7.7(a) to ten in Figure 8.3. In addition, the probe distorts and shifts the vortices in Figure 8.3 from their original axial position of Figure 7.7(a). This is most evident in the upper channel ($\theta = \pi/2$) of the annulus, where the presence of the probe at $\theta = -\pi/2$ affected the first, the second, and the third vortex, creating an elongated third vortex at $\theta = \pi/2$. This vortex is shown encircled by a black ellipse in Figure 8.3. At the same axial location in the lower channel ($\theta = -\pi/2$), Figure 8.3 shows that the cylindrical probe tip has constrained the third Taylor vortex toward the wall of the outer cylinder. Consequently, the centre of this vortex is shifted away from $r = R_i + 0.5d$ toward the wall of the outer cylinder. Around the probe tip, the cross-sectional area of this Taylor vortex is about 50% smaller than that of the corresponding Taylor vortex without probe in Figure 7.7(a). This result and the one obtained for the PIV test case with no probe show that, whenever there is a perturbation in the form of a wall boundary, the centre of the vortex next to the wall boundary displaces radially from the $r = R_i + 0.5d$ line. This determines an alternated pattern of vortex centre radial displacement in the central region of the annulus.

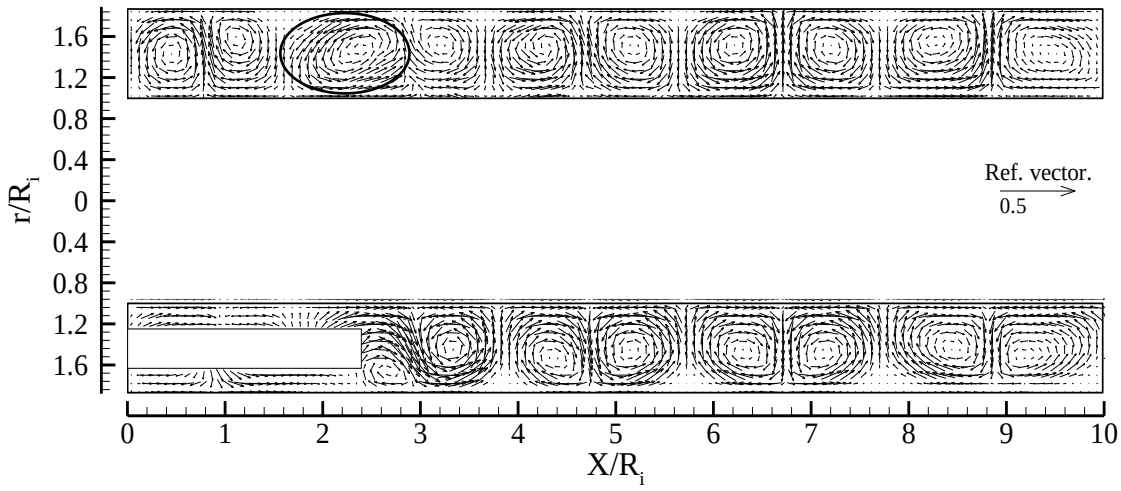

Figure 8.3: Normalised velocity vectors in the meridional plane with the cylindrical probe inserted. The reference vector is $0.5\Omega R_i$.

In Figure 8.3, the vortices near the right end-wall boundaries are more elongated than the vortices near the tip of the probe and in the central region of the annulus, as evidenced by the axial length of the vortices shown in Table 8-1. This is in contrast to the observed pattern in the flow field without the cylindrical probe in Figure 7.7(a). In that figure, the two vortices at the end-wall boundaries are elongated more than the vortices in the central

region. This difference is due to the change in the boundary condition at the left end-wall boundary in Figure 8.3 due to the presence of the cylindrical probe.

Figure 8.3 shows a radial redistribution of mass flow across the annulus similar to the one discussed in the context of Figure 7.7. The presence of the cylindrical probe in the annulus affected this redistribution of mass flow in the lower channel, as the radial outflow between the vortices near the cylindrical probe seems stronger than the radial outflow between the vortices away from the probe. This is evidenced by the length of the velocity vectors in Figure 8.3.

Figure 8.3 clearly shows that the presence of the cylindrical probe is responsible for a change in the flow pattern, especially the vortex near the tip of the cylindrical probe in the lower channel and the vortices at the upper channel in the same axial position as the area occupied by the probe in the lower channel.

8.3.2 Axial and radial velocity contour plots with a cylindrical probe

PIV contour plots of axial and radial velocity in the meridional plane of the annular region with the cylindrical probe in the annulus are shown in Figure 8.4 and Figure 8.5 respectively. To be consistent with the results obtained for the contour plots with no cylindrical probe in the annulus in chapter seven, Figure 7.10(a) and Figure 7.11(a), all velocities have been normalised by the surface speed of the inner cylinder ΩR_i. The contour lines in Figure 8.4 and Figure 8.5 have been evenly spaced with a contour spacing of $0.03\Omega R_i$, which is the same contour spacing used for all the test cases discussed in chapters six and seven.

Away from the probe, the features of the normalised axial velocity contour plot in Figure 8.4 are similar to the ones obtained for the PIV test case with no probe in Figure 7.10(a). The formation of an alternating pattern of axial velocity maxima and minima in the annulus at the same axial position as the vortex centres is evident in Figure 8.4. The velocity maxima and minima are aligned radially above and below each vortex core. The zero contour lines between the maxima and minima in Figure 8.4 are the radial positions of the centre of the vortices in Figure 8.3. The detailed description of the axial velocity flow field is discussed in the context of Figure 7.10(a).

In Figure 8.4, at approximately $X/R_i = 2.4$, corresponding to the axial location of the probe tip, the regions of high axial velocity in both the upper and lower channels of the meridional plane appear elongated in the axial direction, extending to almost 1.5 times the corresponding high velocity region at the same position in Figure 7.10(a). The same is

observed for the low axial velocity region in the upper portion of the meridional plane in Figure 8.4.

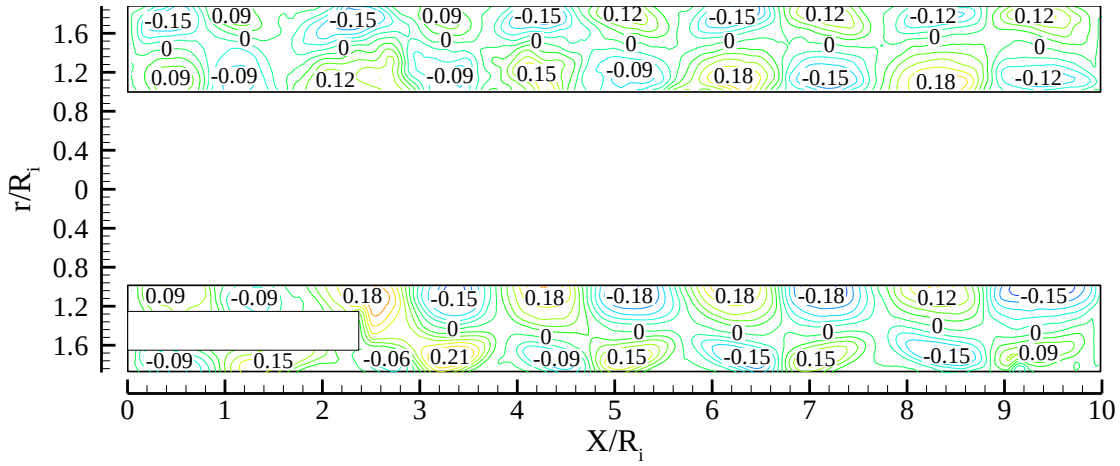

Figure 8.4: Contour plot of axial velocity in the meridional plane with cylindrical probe model. The contour spacing $\Delta u_x = 0.03\Omega R_i$.

In the contour plot of axial velocity in Figure 7.10(a), the absolute value of normalised axial velocity maxima and minima are within the range $0 \leq u_x/\Omega R_i \leq 0.15$. The presence of the probe in the annulus changes the axial velocity magnitude to within the range $0 \leq u_x/\Omega R_i \leq 0.18$, as seen in Figure 8.4. This shows that the presence of the cylindrical probe has increased the axial velocity magnitude in the annulus by about 20%. This will be discussed in details in the analysis of the in-plane velocity profiles in section 8.3.3.

Figure 8.5 shows the normalised radial velocity contour map with an alternating pattern of radial velocity minima and maxima along the axial direction. The contour plot in Figure 8.5 is colour coded as in Figure 7.11(a). The negative and positive values on these contour clusters indicate inward flow regions and outward flow regions respectively at $\theta = -\pi/2$ at the meeting point of two adjacent vortices in Figure 8.3. These features have been discussed in details in the context of Figure 7.11(a). The radial velocity contours in Figure 8.5 show the number of the radial velocity extrema in the upper channel to be eleven, while the number of cells is ten, as seen in Figure 8.3. This difference of one between the number of cells and the number of vortices is also found in the velocity vector map and contour plot of Figure 7.7(a) and Figure 7.11(a), for the case with no cylindrical probe, in which twelve vortices and thirteen radial velocity extrema are shown in the upper and lower channels. The difference in the number of the vortices and in the number of extrema has been attributed to the presence of the end-walls.

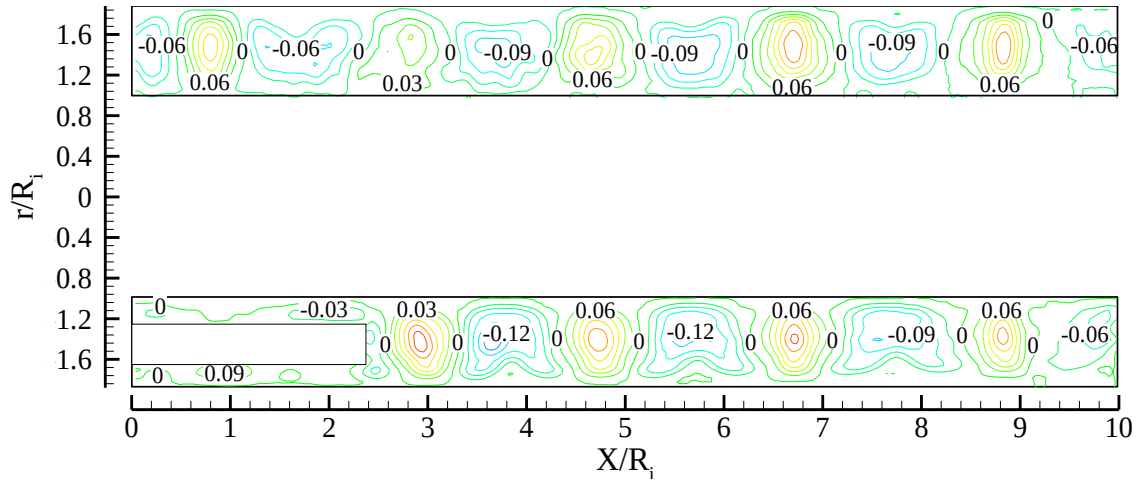

Figure 8.5: Contour plot of radial velocity in the meridional plane with cylindrical probe model. The contour spacing $\Delta u_r = 0.03\Omega R_i$.

In the contour plot of radial velocity for the PIV test case with no cylindrical probe in the annular region in Figure 7.11(a), the absolute values of the normalised radial velocity maxima and minima are within the range $0 \leq u_r/\Omega R_i \leq 0.18$. The presence of the probe in the annulus has changed the radial velocity magnitude to within the range $0 \leq u_r/\Omega R_i \leq 0.21$. This shows that the presence of the cylindrical probe has increased the radial velocity magnitude in the annulus by about 17%. This will be discussed in details in the analysis of the in-plane velocity profiles in section 8.3.3. It is interesting to observe that both the axial and radial velocity increased by the same magnitude of $0.03\Omega R_i$ as result of the cylindrical probe in the annulus.

8.3.3 Analysis of the in-plane velocity profiles in the meridional plane

A detailed quantitative analysis of the in-plane velocity profiles obtained from the velocity vectors in the meridional plane of Figure 8.3 and Figure 7.7(a) is discussed in this section. The in-plane velocity profiles for the PIV test case with cylindrical probe are extracted at $\theta = -\pi/2$ at the same radial positions along the axial direction as those of the profiles without the cylindrical probe discussed in section 7.5.4. The velocity profiles presented here have been normalised with respect to the inner cylinder surface speed ΩR_i for consistency.

Figure 8.6 shows the combined normalised axial velocity profiles in the meridional plane at constant radial positions $r = R_i + 0.125d$, $r = R_i + 0.5d$, and $r = R_i + 0.875d$ on the lower ($\theta = -\pi/2$) channel for the PIV test case with cylindrical probe in the annular region. As in the PIV test case with no cylindrical probe in the annular region, the axial velocity profiles

in Figure 8.6 traverse through the inward and outward flow regions of Figure 8.3. The zero crossings that mark the axial position of the saddle planes between the neighbouring toroidal Taylor vortices offer a good visual reference point for appreciating how the vortex pattern changes axially with the introduction of the cylindrical probe.

As in the PIV test case with no cylindrical probe in the annular region, the axial velocity is observed to be relatively small compared with the surface speed of the inner cylinder, as shown by the values of the maxima and minima in Figure 8.6. Many of the features of the axial velocity profiles in Figure 8.6 are similar to the corresponding ones in the axial velocity profiles for the PIV test case with no cylindrical probe discussed in details in section 7.5.4 in the context of Figure 7.12.

Near the inner cylinder wall at $r = R_i + 0.125d$ in Figure 8.6, the profile shows that the magnitude of the axial velocity minima and maxima near the left end-wall over the region $0 \leq X/R_i \leq 2.4$ are smaller compared to the magnitude of the axial velocity minima and maxima along the entire annulus over the range $2.4 \leq X/R_i \leq 10$. As this region ($0 \leq X/R_i \leq 2.4$) is occupied by the cylindrical probe in the gap mid-span of the annulus, the flow is obstructed by the probe blockage that reduces the in-plane flow velocity magnitude. The magnitude of the axial velocity maxima and minima near the left end-wall in the region occupied by the probe in Figure 8.6 is approximately $0.1\Omega R_i$ and $-0.08\Omega R_i$ respectively. The normalised axial velocity profile near the wall of the inner cylinder at $r = R_i + 0.125d$ in Figure 8.6 shows that the axial velocity maximum just at the tip of the cylindrical probe, at $X/R_i = 2.6$, is higher than the axial velocity maxima in the entire annulus. This is a result of the presence of the cylindrical probe in the annulus in which the probe solid blockage close to the tip causes an increase in axial velocity away from the probe boundary layer. The axial velocity magnitude at this axial position $X/R_i = 2.6$ is approximately $0.2\Omega R_i$. Along the rest of the annulus, over the range $2.6 \leq X/R_i \leq 10$, the profile shows a progressive decrease in the axial velocity maxima toward the right end-wall. Over the range $2.6 \leq X/R_i \leq 10$, the normalised axial velocity minima are almost symmetric about $X/R_i = 6.4$ with axial velocity minima at $X/R_i = 5.2$ and $X/R_i = 7.2$ approximately equal to $-0.18\Omega R_i$. Similarly, the normalised axial velocity minima at $X/R_i = 3.3$ and $X/R_i = 9.5$ are approximately equal to $-0.16\Omega R_i$, but their symmetry is adversely affected by the presence of the right end-wall.

The normalised axial velocity profile at the gap mid-span at $r = R_i + 0.5d$ in Figure 8.6 shows an axial velocity absolute maximum at the tip of the probe $X/R_i = 2.4$. This result is

given by the probe solid blockage close to the tip that causes a positive axial velocity away from the probe boundary layer. This axial velocity absolute maximum is in agreement with the strong outward flow at the tip of the probe at the same axial position in Figure 8.3. Over the range $2.4 \leq X/R_i \leq 10$, four further local maxima can be observed at $r = R_i + 0.5d$ in Figure 8.6. The axial velocity maxima decrease progressively along the positive axial direction toward the right end-wall, while the axial velocity minima reduce along the same direction. A possible explanation for the reduction in the axial velocity minima is that the low mass transport at the inflow in the positive axial direction by the Taylor vortex compensates for the increased mass transport by the induced velocity at the outflow of the vortex at the tip of the cylindrical probe. This ensures that the net mass flux balance around the azimuthal plane at $X/R_i \approx 5$ is zero, as imposed by the wall boundary conditions at the rotating cylinder ends, at $X/R_i = 0$ and $X/R_i = 10$. The low axial velocity magnitude toward the right end-wall can be attributed to the PIV laser light reflection from the right end-wall boundary, as discussed in the context of Figure 7.13.

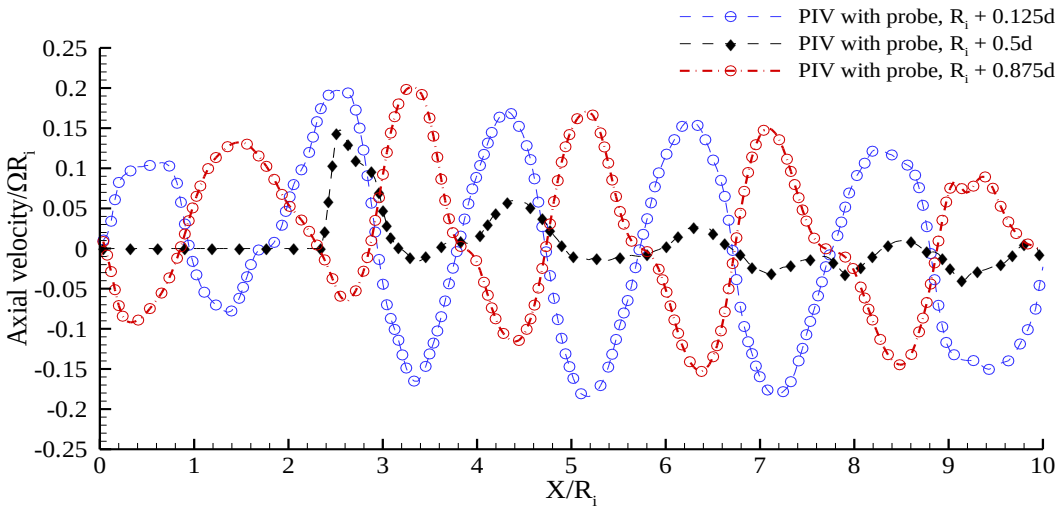

Figure 8.6: Normalised axial velocity profiles in the meridional plane of the lower channel at $\theta = -\pi/2$ at constant radial positions $r = R_i + 0.125d$, $r = R_i + 0.5d$, and $r = R_i + 0.875d$ with cylindrical probe model inserted.

The normalised axial velocity profile near the outer cylinder wall at $r = R_i + 0.875d$ in Figure 8.6 shows that the axial velocity extrema near the left end-wall over the region $0 \leq X/R_i \leq 2.4$ are smaller than the axial velocity extrema along the reminder of the annulus except near the right end-wall at $X/R_i = 9.3$. This result has been discussed in the context of the profile at $r = R_i + 0.125d$. Over the range $2.4 \leq X/R_i \leq 10$, the axial velocity maxima decrease progressively toward the right end-wall. This agrees with the results observed in Figure 8.3 in which the velocity vectors at the outflow regions near the tip of the

cylindrical probe are longer than at the outflow regions near the right end-wall boundary. Near the right end-wall boundary, the axial velocity local minimum is higher than at X/R_i = 6.8, due to the effects of wall boundary and the PIV light reflection from the wall.

The axial velocity maxima and minima near the left end-wall in the region occupied by the probe in Figure 8.6 are approximately $0.13\Omega R_i$ and $-0.09\Omega R_i$ respectively, for the profile near the wall of outer cylinder at $r = R_i + 0.875d$. For the same profile, the axial velocity absolute maximum along the entire annulus occurs at $X/R_i = 3.4$ with an axial velocity magnitude of approximately $0.2\Omega R_i$, whereas the axial velocity absolute minimum along the entire annulus occurs at $X/R_i = 6.4$ with an axial velocity of approximately $-0.16\Omega R_i$. Near the right end wall, the axial velocity maximum and minimum are approximately $0.08\Omega R_i$ and $-0.14\Omega R_i$, respectively.

The inflection points on this profile in Figure 8.6 correspond to the position of the inflow regions in Figure 8.3. These positions correspond to the area where low momentum fluid near the outer wall is convected inwardly by the radial inflow. The presence of the inflections has been discussed in details in the context of Figure 7.12.

8.3.4 Quantitative analysis of the intrusive effect of the cylindrical probe

In this section, the intrusive effects of the cylindrical probe are discussed more quantitatively. This is done by making a direct comparison between the PIV test case with and without the cylindrical probe in the annular region. The axial velocity profiles have been normalised with respect to the inner cylinder surface speed ΩR_i.

Figure 8.7 shows the normalised axial velocity profiles with and without the probe in the annular region of the annulus at a constant radial position $r = R_i + 0.125d$. Figure 8.7 shows that the profiles with and without a probe are similar in trend in the sense that the axial velocity profiles display alternating maxima and minima, with zero crossings in between, which is where the $r = R_i + 0.5d$ gap mid-span cylindrical surface intersects the saddle planes in the meridional planes. In the profiles with and without a probe, the centres of the inward and outward flows are saddle planes of axial velocity separating each Taylor vortex. These features have been discussed in the details in the context of Figure 7.12. The profiles show that the axial velocity maxima for the profile with and without a probe are almost the same in magnitude, except in the region occupied by the probe. However, there are discrepancies in the magnitude of the axial velocity minima between the test case with and without a probe in the region occupied by the probe and in the

central region of the annulus, over the range $0 \leq X/R_i \leq 6.7$. Toward the right end-wall boundary, over the range $6.7 \leq X/R_i \leq 8.6$, the axial velocity minima of the profiles with and without a probe are almost the same in magnitude. At the right end-wall boundary, the axial velocity local minimum with the probe is higher than the axial velocity local minimum with no probe.

Near the left end-wall at $X/R_i = 0.5$, the magnitude of the axial velocity maxima with and without a probe are approximately $0.1\Omega R_i$ and $0.2\Omega R_i$ respectively. In this region, the presence of the cylindrical probe has reduced the axial velocity magnitude by almost 50%. At the tip of the cylindrical probe, at the axial position $X/R_i = 2.4$, the magnitude of the axial velocity maxima with and without a probe are approximately $0.2\Omega R_i$ and $0.18\Omega R_i$ respectively, indicating an increase of almost 11% in the axial velocity maximum due to the presence of the cylindrical probe. Beyond this position, the effect of the probe on the magnitude of the axial velocity maxima is almost negligible.

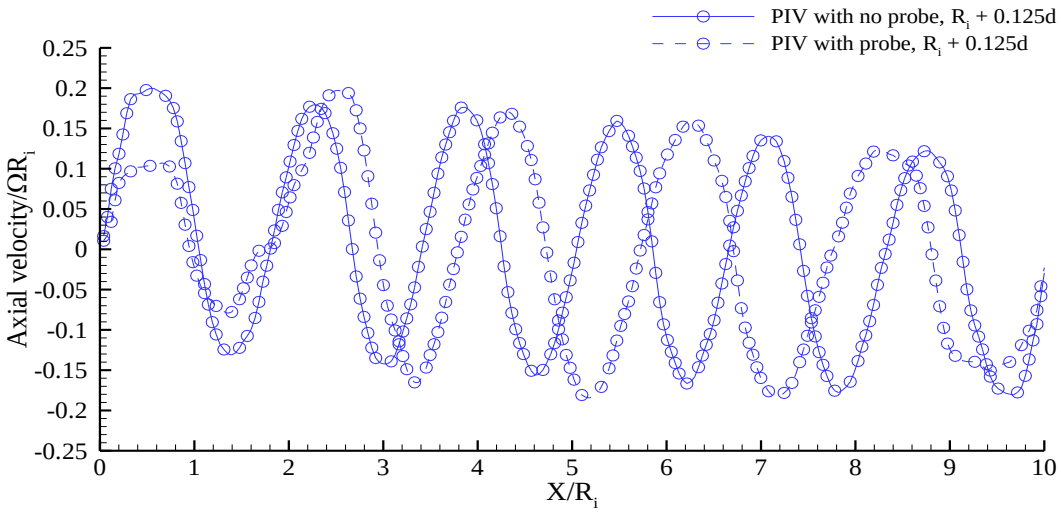

Figure 8.7: Normalised axial velocity profiles in the meridional plane of the lower channel at $\theta = -\pi/2$ at constant radial position $r = R_i + 0.125d$ with and without a probe in the annulus.

As far as the axial velocity minimum at $X/R_i = 1.4$ is concerned, which falls within the region occupied by the cylindrical probe, the axial velocity minimum with and without a probe is approximately $-0.08\Omega R_i$ and $-0.13\Omega R_i$ respectively. This result shows that the presence of the probe has increased the axial velocity local minimum by almost 38.5%. Between the region occupied by the probe and the central region of the annulus, over the range $2.4 \leq X/R_i \leq 5.8$, the presence of the probe has increased the magnitude of the axial velocity minima by almost 13.9%.

In Figure 8.7, over the range $5.8 \leq X/R_i \leq 8.0$, the presence of the probe seems not to have any significant effect on the magnitude of the axial velocity minima. At the right end-wall boundary, the presence of the probe increases the magnitude of the local axial velocity minimum by approximately 22.2%. The difference in the magnitude of the axial velocity minima between the two test cases at this position is likely to be due to combinations of many factors, including the change in the boundary condition at the left end-wall and the effect of PIV light reflection from the wall.

It is interesting to observe that, in the region occupied by the probe over the range $0 \leq X/R_i \leq 2.4$, the spatial phase difference between the profile with and without the probe is negligibly small. However, in the reminder of the annulus, over the range $2.4 \leq X/R_i \leq 10$, there is a significant change in the spatial phase of the two profiles, with the profile with the probe phase leading the profile with no probe. The change in spatial phase between the axial velocity profiles increases progressively from the tip of the cylindrical probe toward the right end-wall boundary along the positive axial direction over the range $2.4 \leq X/R_i \leq 7.6$. Near the right end-wall boundary over the range $7.6 \leq X/R_i \leq 10$, the phase difference between the profile with and without probe reduces. Over this region, the profile with no probe is phase leading the profile with probe. The large discrepancies in the spatial phase between the axial velocity profiles with and without probe is due to the reduction in the number of vortices from twelve for the latter to ten for the former as the axial length of the two missing vortices must be compensated by an adjustment in the spatial phase since the total axial length of the two test cases remains constant.

Figure 8.8 shows the normalised axial velocity profiles with and without a probe in the annular region of the annulus at a constant radial position $r = R_i + 0.5d$. Figure 8.8 shows that the profiles at $r = R_i + 0.5d$ with and without a probe follow a similar trend especially in the region not occupied by the probe, which is characterised by a relatively small axial velocity. This trend has been discussed in the context of Figure 7.13 and Figure 8.6. The profiles also show a progressive decrease in the magnitude of the axial velocity maxima away from the cylindrical probe in the positive axial direction. In Figure 8.8, there is no axial velocity reported in the region $0 \leq X/R_i \leq 2.4$ for the axial velocity profile for the PIV test case with probe, as this region is occupied by the cylindrical probe itself. The profile at $r = R_i + 0.5d$ with a probe shows an axial velocity absolute maximum at the tip of the probe at $X/R_i = 2.4$. This feature is not present in the profile without a probe. The difference between the two profiles as been attributed to the probe solid blockage close to

the tip of the cylindrical probe that causes a positive axial velocity away from the probe boundary layer. This has been discussed in the context of Figure 8.6. At this axial position, the magnitude of the normalised axial velocity maximum for the profile with and with no probe has been estimated as 0.15 and 0.07 respectively. This suggests that there is an increase of about 114% in the magnitude of the axial velocity maximum at this axial position as a result of the probe in the annular region.

Away from the tip of the cylindrical probe, the normalised axial velocity profile of Figure 8.8 shows that the axial velocity local maxima are almost the same in magnitude for the profiles with and without a probe along the positive axial direction.

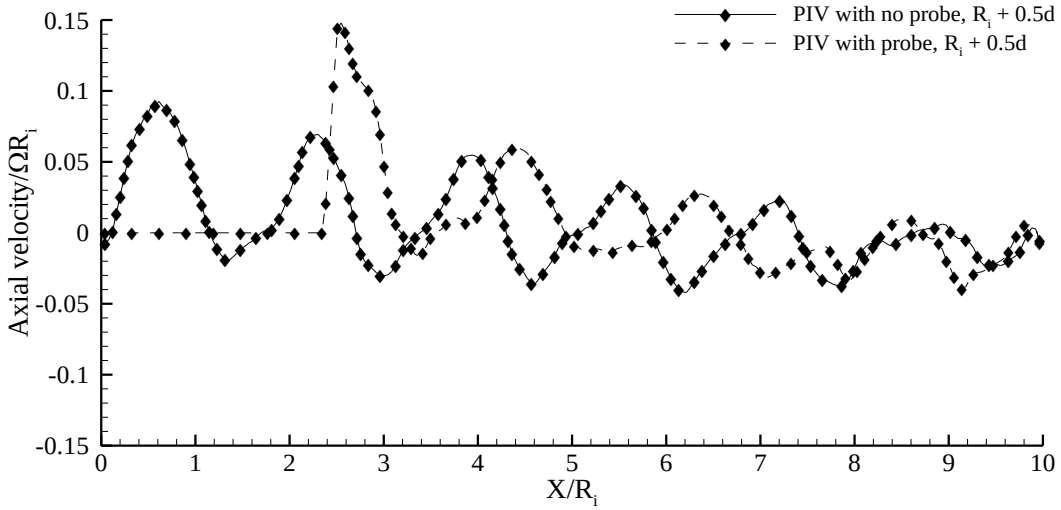

Figure 8.8: Normalised axial velocity profiles in the meridional plane of the lower channel at $\theta = -\pi/2$ at constant radial position $r = R_i + 0.5d$ with and without a probe in the annulus.

In Figure 8.8, away from the probe, the axial velocity local minima for the test case without a probe are relatively lower compared with the PIV test case with a probe, especially over the range $3.4 \leq X/R_i \leq 6.8$. Over the range $3.4 \leq X/R_i \leq 5.4$, the magnitude of the axial velocity minima with a probe are nearly constant at approximately $0.015\Omega R_i$. Over the range $7.0 \leq X/R_i \leq 8.0$, the magnitude of the axial velocity minima with probe are nearly constant at approximately $0.03\Omega R_i$. For the profile with no probe, at axial positions over the range $0 \leq X/R_i \leq 3.0$, the axial velocity minimum is approximately within the range $-0.02\Omega R_i$ to $-0.03\Omega R_i$. Over the range $4.1 \leq X/R_i \leq 8.2$, the profile without a probe shows axial velocity minima with a constant magnitude approximately equal to $0.04\Omega R_i$.

At the right end-wall boundary, the magnitude of the axial velocity minima with and without a probe is approximately $0.04\Omega R_i$ and $0.02\Omega R_i$ respectively.

There are also discrepancies in the spatial phase of the profile with and without a probe in the region beyond the tip of the probe over the range $2.4 \leq X/R_i \leq 8.0$. Over this axial length, the axial velocity with a probe is phase leading the profile with no probe. In Figure 8.8, the change in phase between the axial velocity profiles increases progressively from the tip of the cylindrical probe toward the right end-wall boundary along the positive axial direction over the range $2.4 \leq X/R_i \leq 7.6$. Near the right end-wall boundary, over the range $7.6 \leq X/R_i \leq 10$, the spatial phase difference between the profile with and without a probe reduces, with the profile without a probe phase leading the profile with a probe. This trend is also observed for the profiles near the wall of the inner cylinder at $r = R_i + 0.125d$. The discrepancies in the phase between the axial velocity profiles have been discussed in the context of Figure 8.7.

Figure 8.9 shows the normalised axial velocity profiles with and without a probe in the annular region at the constant radial position $r = R_i + 0.875d$. Figure 8.9 shows that the axial velocity profiles at $r = R_i + 0.875d$ with and without a probe display a similar trend. This trend has been discussed in the context of Figure 7.12.

The normalised axial velocity profile in Figure 8.9 shows that the axial velocity maximum for the profile with a probe is smaller than the axial velocity maximum without a probe over the range $0 \leq X/R_i \leq 2.4$, which is the region occupied by the probe. In this region, the magnitude of the axial velocity maximum for the test case with and without a probe is approximately $0.13\Omega R_i$ and $0.175\Omega R_i$ respectively. The presence of the probe has reduced the magnitude of the axial velocity maximum in this region by 25.7%.

In the region immediately after the tip of the probe, over the range $2.4 \leq X/R_i \leq 4.0$, the axial velocity maximum for the profile with a probe is greater than that for the test case without a probe. The axial velocity maximum in this region for the test case with and without a probe is approximately $0.2\Omega R_i$ and $0.175\Omega R_i$ respectively, indicating an increase of about 14.3% in the axial velocity maximum due to the presence of the probe in the annular region. In Figure 8.9, at the central region of the concentric cylinder, over the range $4.0 \leq X/R_i \leq 5.8$, the axial velocity maxima for the profiles with and without a probe are almost the same. The magnitude of the axial velocity maximum over the range $4.0 \leq X/R_i \leq 5.8$, for the PIV test case with and without a probe, is approximately $0.17\Omega R_i$. Similarly, over the range $5.8 \leq X/R_i \leq 8.7$, the axial velocity maxima for the profiles with and without a probe are almost equal and the axial velocity magnitude in this region for the PIV test case with and with no probe is approximately $0.15\Omega R_i$.

At the right end-wall boundary, the magnitude of the axial velocity maximum for the test case with probe is smaller compared with that of the test case with no probe with the former and the latter having a magnitude of $0.08\Omega R_i$ and $0.13\Omega R_i$ respectively. This shows a decrease of about 38.5% in the right most axial velocity maximum by the insertion of the probe at the left end boundary. The decrease in axial velocity at this position is due to the effects of the probe in the annular region and that of the PIV light reflection.

As far as the axial velocity minima are concerned, the profiles in Figure 8.9 show the axial velocity minima with probe to be higher than the axial velocity minima without a probe in the entire annulus. For instance, over the range $0 \leq X/R_i \leq 2.6$, which falls within the region occupied by the cylindrical probe, the profiles in Figure 8.9 show that the axial velocity minimum with a probe at $X/R_i \approx 0.4$ is approximately $-0.09\Omega R_i$, while the axial velocity minimum for the test case without a probe is approximately $-0.12\Omega R_i$. At $X/R_i = 2.6$, the axial velocity minimum with a probe is approximately $-0.06\Omega R_i$, while the axial velocity minimum for the test case without a probe at $X/R_i = 2.2$ is approximately $-0.14\Omega R_i$. These results suggest a maximum increase of about 62% in the axial velocity minimum due to the presence of the cylindrical probe over the region $0 \leq X/R_i \leq 2.6$.

In Figure 8.9, over the range $3.8 \leq X/R_i \leq 4.6$, the axial velocity minimum with a probe is higher than that without a probe, with the former being approximately $-0.12\Omega R_i$ and the latter being $-0.16\Omega R_i$ respectively. This indicates an increase of about 14.3% in axial velocity by the introduction of the cylindrical probe model. The profile of the axial velocity with a probe in Figure 8.9 shows that the magnitude of the axial velocity minima is nearly constant over the range $5.8 \leq X/R_i \leq 9$, with the axial velocity minima estimated as $-0.16\Omega R_i$. Similarly, over the same axial range of $5.8 \leq X/R_i \leq 9$, the profile of axial velocity without a probe display two axial velocity minima approximately equal to $-0.17\Omega R_i$. Over this range, the presence of the probe in the annular region causes an increase in the axial velocity minimum of about 6%.

Due to the presence of the probe near the left end-wall and due to wall boundary PIV light reflection at the right end-wall, the axial velocity maxima and minima over the range $0 \leq X/R_i \leq 10$ change their values by at least 14.3% in the test with probe as compared with the test without probe.

Figure 8.9 shows that the spatial phase of the axial velocity profiles with and without a probe is different, with the spatial phase of the axial velocity profile with a probe leading

that of the axial velocity profile without a probe over the region not occupied by the probe in the range $2.4 \leq X/R_i \leq 9.0$.

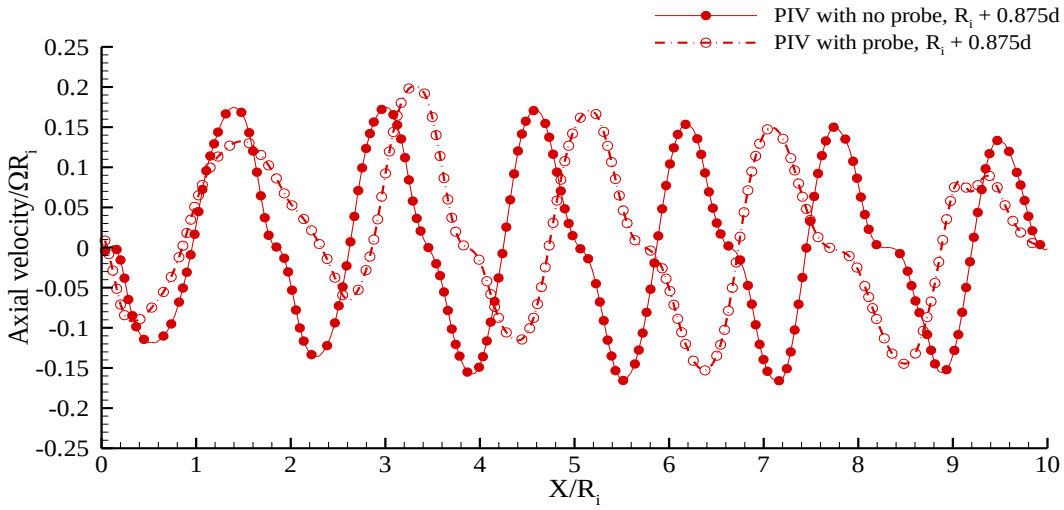

Figure 8.9: Normalised axial velocity profiles in the meridional plane of the lower channel at $\theta = -\pi/2$ at constant radial position $r = R_i + 0.875d$ with and without a probe in the annulus.

Figure 8.10 shows the normalised radial velocity profiles at the same radial positions in the meridional plane of the lower ($\theta = -\pi/2$) channel as in Figure 8.6. The radial velocity profiles in Figure 8.10 show that, away from the region occupied by the probe, in the region $2.4 \leq X/R_i \leq 9.0$, the radial velocity exhibits alternating maxima and minima. This trend is the same as that of the radial velocity profiles for the test case with no probe in Figure 7.14.

The radial velocity profile in Figure 8.10 exhibits a spatially periodic trend away from the region occupied by the probe along the positive axial direction. This periodic trend is more obvious in the profile at the gap mid-span radial position $r = R_i + 0.5d$ ($-\pi/2$), this being the position at which the radial velocity reaches its maximum value. In Figure 8.10, away from the region occupied by the probe, approximately four cycles of a periodic oscillation along X/R_i are shown for the radial position $r = R_i + 0.125d$ and $r = R_i + 0.5d$. Also, the velocity profiles of Figure 8.10 show that the radial velocity is not symmetric about the gap mid-span. The asymmetry in inflow (negative u_r) and outflow (positive u_r) regions is more noticeable in the radial velocity profiles at $r = R_i + 0.5d$ ($\theta = -\pi/2$). This feature results from the displacement of the vortex centres in both the axial and radial directions discussed in section 7.5 in the context of Figure 7.7 and Figure 7.14. These trends are similar to the ones exhibited by the test case with no probe in Figure 7.14.

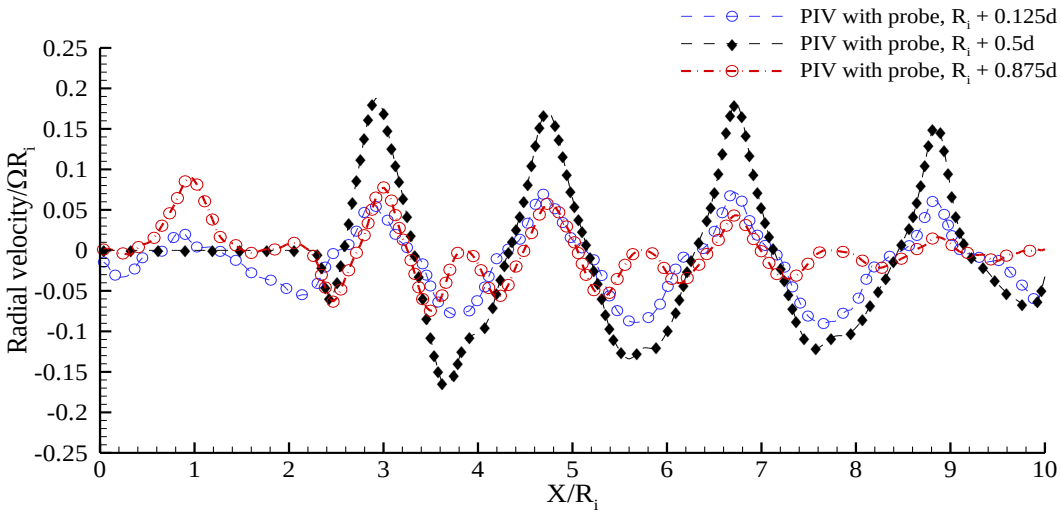

Figure 8.10: Normalised radial velocity profiles in the meridional plane of the lower channel at $\theta = -\pi/2$ at constant radial positions $r = R_i + 0.125d$, $r = R_i + 0.5d$, and $r = R_i + 0.875d$ with cylindrical probe model inserted.

Figure 8.11 displays the normalised radial velocity profiles obtained from the PIV test cases with and with no probe at $r = R_i + 0.125d$, using a smaller range for the ordinate than that of Figure 8.10. The magnitude of the radial velocity maxima and minima near the left end-wall of Figure 8.11, in the region occupied by the probe, are observed to be lower compared to the ones at the right end-wall. The radial velocity maxima and minima for the test case with no probe increase progressively in amplitude from the left end-wall to the right end-wall. Away from the region occupied by the probe over the range $2.8 \leq X/R_i \leq 9.0$, the radial velocity maxima for the test case with probe show a symmetric trend about $X/R_i = 5.6$. On the other hand, over the same region, the radial velocity minima for the PIV test case with probe increase progressively in amplitude from the left end-wall to the right end-wall.

Figure 8.11 shows that the normalised radial velocity maxima for the profile with a probe are lower than the radial velocity maxima for the profile without a probe in the entire annulus both in magnitude and in amplitude. This attributed to the presence of the cylindrical probe in annulus and it is unlikely to result from an experimental error, since both experiments were conducted back to back. Near the left end-wall in the region occupied by the probe, over the range $0 \leq X/R_i \leq 2.4$, the radial velocity maximum for the PIV test case with and without a probe is approximately $0.025\Omega R_i$ and $0.07\Omega R_i$ respectively, indicating a reduction of about 64% in the radial velocity maximum due to the presence of the probe in the annular region. In the region away from the tip of the probe, over the range $2.4 \leq X/R_i \leq 10$, the magnitude of the radial velocity maxima for the

PIV test case with and without a probe is approximately $0.07\Omega R_i$ and $0.085\Omega R_i$ respectively. The presence of the probe in the annular region has reduced the magnitude of the radial velocity maxima by 17.7% in this region.

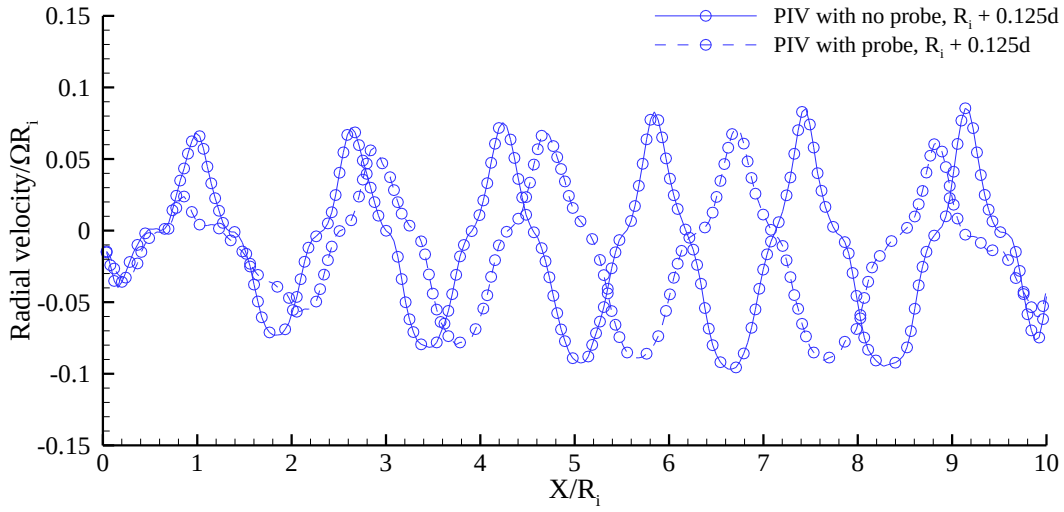

Figure 8.11: Normalised radial velocity profiles in the meridional plane of the lower channel at $\theta = -\pi/2$ at constant radial position $r = R_i + 0.125d$ with and with no probe in the annulus.

In the region occupied by the probe near the left end-wall at $X/R_i \approx 2$, the radial velocity local minimum for the PIV test case without a probe is lower than the radial velocity local minimum with the probe. In this region, the radial velocity minima with and with no probe are estimated to be approximately $-0.055\Omega R_i$ and $-0.075\Omega R_i$ respectively. This shows that the presence of the probe in this region has increased the radial velocity minimum by about 26.6%. Away from the tip of the probe, over the range $2.4 \leq X/R_i \leq 10$, the radial velocity minima for the PIV test case with and without a probe are approximately $-0.09\Omega R_i$ and $-0.095\Omega R_i$ respectively. These values show that the presence of the probe in the annular region has increased the radial velocity local minima by just 5.3% in this axial region.

From this result, it is clear that the presence of the probe in the annular region has increased the radial velocity maxima by a maximum amount of 17.7% and has increased the radial velocity local minima by 5.3% along the radial position $r = R_i + 0.125d$. In Figure 8.11, the spatial phase of the radial velocity profile with a probe is leading that of the radial velocity profile without a probe over the region not occupied by the probe in the range $2.4 \leq X/R_i \leq 9.0$.

Figure 8.12 displays the normalised radial velocity profiles at the gap mid-span of the annulus at $r = R_i + 0.5d$ for the PIV results with and without a probe. The trend of the radial velocity profiles in Figure 8.12 is similar for the PIV results with and without the probe. This is clearly noticeable in the region away from the tip of the probe boundary, over the range $2.4 \leq X/R_i \leq 10$, where the radial velocity exhibits alternating minima and maxima. The radial velocity profiles in Figure 8.12 show approximately four and five cycles of a spatially periodic oscillation respectively for the PIV results with and without a probe over the range $2.6 \leq X/R_i \leq 10$. Other features of the radial velocity profiles in Figure 8.12 have been discussed in details in the context of Figure 7.16.

The amplitude of the radial velocity maxima and minima from the PIV test case with no probe in Figure 8.12 is observed to be higher than that from the PIV test case with a probe in the entire annulus. The radial velocity maxima and minima from the PIV test case with no probe along the central region of the annulus over the range $2.6 \leq X/R_i \leq 7.5$ are almost of the same value of approximately $0.22\Omega R_i$ and $-0.18\Omega R_i$ respectively. This trend has been discussed in the context of Figure 7.16.

Over the range $2.6 \leq X/R_i \leq 7.5$, the radial velocity maxima from the PIV test case with a probe along the central region of the annulus seem symmetric about $X/R_i = 4.8$. The magnitude of the radial velocity maxima in this region at $X/R_i \approx 3$ and $X/R_i \approx 6.8$ is approximately $0.19\Omega R_i$, indicating a reduction of radial velocity magnitude of about 13.6% in this region compared to the test case without probe. On the other hand, the radial velocity minima for the PIV test case with a probe increase progressively away from the tip of the probe toward the right end-wall boundary. Over the range $2.6 \leq X/R_i \leq 7.5$, the value of the highest radial velocity minimum for the PIV result with a probe is approximately $-0.12\Omega R_i$. This results in an increase of approximately 33% in the radial velocity minimum at $X/R_i = 7.5$ due to the presence of the probe in the annular region of the cylinders.

In Figure 8.12, toward the right end-wall over the range $7.5 \leq X/R_i \leq 9.2$, the radial velocity maximum and minimum from the PIV test case without a probe are estimated as $0.18\Omega R_i$ and $-0.15\Omega R_i$ respectively. Over the same range of $7.5 \leq X/R_i \leq 9.2$, the radial velocity maximum and minimum for the PIV test case with a probe are estimated as $0.15\Omega R_i$ and $-0.12\Omega R_i$ respectively. These results suggest that the presence of the probe in the annulus decreases the radial velocity maximum by 16.7% and increases radial velocity minimum by 20% along the radial position $r = R_i + 0.5d$.

In Figure 8.12, there is no radial velocity profile in the region $0 \leq X/R_i \leq 2.4$, as this is occupied by the probe. At the tip of the probe in Figure 8.12, at $X/R_i \approx 2.4$, the magnitude of the radial velocity minimum for the PIV test case with a probe is small compared to the PIV test case without a probe in the same region. This is the result of the solid blockage of the probe that affects the boundary layer. At the right end-wall, at the axial position $X/R_i = 10$, the radial velocity minimum for the PIV test case with and without a probe have the same value which is estimated to be approximately $-0.10\Omega R_i$.

Figure 8.12 show that the spatial phases of the radial velocity profiles with and without a probe are different. Over the range $2.4 \leq X/R_i \leq 9.0$, the radial velocity profile for the test case with a probe is phase leading the radial velocity profile without a probe. Toward the right end-wall over the range $9.0 \leq X/R_i \leq 10$, the radial velocity profile without a probe is phase leading. The observed phase difference between the profiles with and without probe in the range $3.4 \leq X/R_i \leq 8.4$ is due to the axial length of the two missing vortices in the flow field of the PIV test case with a probe, as identified in Figure 8.3.

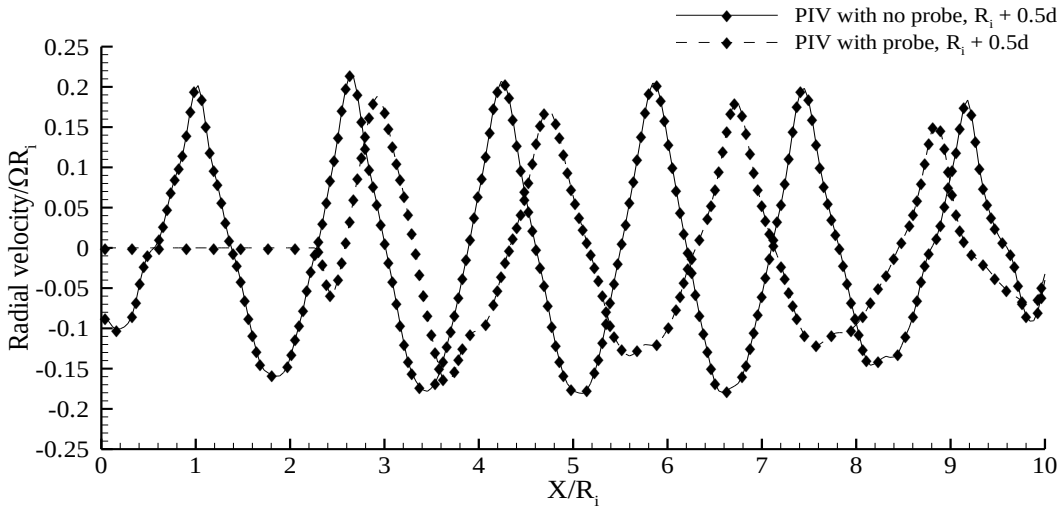

Figure 8.12: Normalised radial velocity profiles in the meridional plane of the lower channel ($\theta = -\pi/2$) at constant radial position $r = R_i + 0.5d$ with and without a probe in the annulus.

Figure 8.13 displays the normalised radial velocity profile near the wall of the outer cylinder at $r = R_i + 0.875d$ for the PIV test case with and without a probe in the annular region of the concentric cylinders. The normalised radial velocity profiles from the PIV test case with and without a probe exhibit the same trend of the outward flow regions featuring one single maximum, while the inward flow regions over the range $2.4 \leq X/R_i \leq 7.2$ exhibit double trough minima. This trend has been explained in the context of Figure

6.17 and Figure 7.17. The double trough minima for the profile without a probe are still visible till the axial position $X/R_i = 8.2$, while the ones of the profile with a probe are no longer visible over the range $7.2 \leq X/R_i \leq 10$. This may be due to combinations of changes in the boundary layer as a result of the presence of the probe in the annular region and the effect of the PIV light reflection from the walls. In the region occupied by the probe, over the range $0 \leq X/R_i \leq 2.4$, the profile with probe did not show the double trough minima. This is due to the presence of the probe in this region. However, the profiles in Figure 8.13 show some qualitative agreement between the PIV results with and without a probe in the annular region over the range $2.6 \leq X/R_i \leq 7.2$.

Apart from variation in the flow pattern observed in Figure 8.13 in the area occupied by the probe, the profiles in Figure 8.13 display higher amplitude radial velocity maxima in the entire annulus for the PIV profile with a probe than in the PIV profile without a probe, except toward the right end-wall where the radial velocity maxima of the PIV test case with and without a probe have approximately the same magnitude.

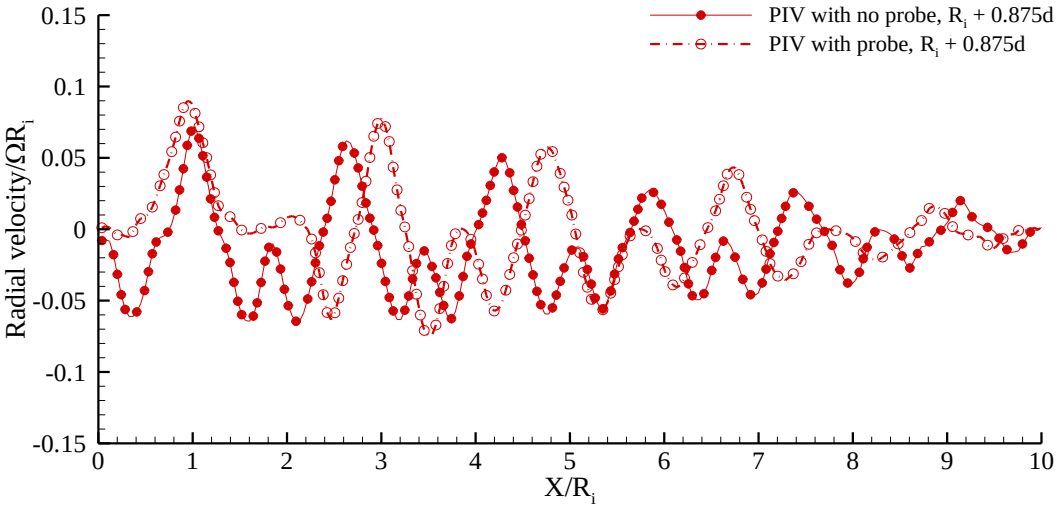

Figure 8.13: Normalised radial velocity profiles in the meridional plane of the lower channel at $\theta = -\pi/2$ at constant radial position $r = R_i + 0.875d$ with and without a probe in the annulus.

In the region occupied by the probe in the range $0 \leq X/R_i \leq 2.4$, the radial velocity maxima for the profile with and without a probe are approximately $0.09\Omega R_i$ and $0.07\Omega R_i$ respectively. This suggests that the presence of the probe in the annular region has increased the radial velocity near the wall of the outer cylinder at $r = R_i + 0.875d$ by 28.6%. At the outflow region next to the tip of the probe, over the range $2.6 \leq X/R_i \leq 3.0$, the radial velocity maxima are $0.075\Omega R_i$ and $0.06\Omega R_i$ respectively for the test cases with

and without a probe in the annulus. This is an increment of approximately 25% in the radial velocity at the radial position $r = R_i + 0.875d$. In the central region, over the range $4.2 \leq X/R_i \leq 5.0$, the radial velocity maxima for the test cases with and without a probe in the annulus are approximately $0.06\Omega R_i$ and $0.055\Omega R_i$ respectively. This result suggests that the presence of the probe in the annular region has increased the radial velocity by approximately 9.1%. In Figure 8.13, over the range $5.0 \leq X/R_i \leq 7.4$, the radial velocity maxima for the test cases with and without a probe in the annulus are approximately $0.04\Omega R_i$ and $0.03\Omega R_i$ respectively. In this region, the radial velocity has been increased by approximately 33.3% by the insertion of the cylindrical probe. Toward the right end-wall, over the range $7 \leq X/R_i \leq 10$, the radial velocity maxima for the profiles with and without a probe have almost the same value and are lower compared with the other maxima in the annulus. This variation has been attributed to the effect of light reflection from the end-wall boundary that affects the magnitude of the measured radial velocity in this region.

In Figure 8.13, over the area occupied by the probe, no radial velocity minimum for the profile with a probe is observed. Away from the tip of the probe and in the entire annulus, the profiles in Figure 8.13 show that there is no significant difference between the values of corresponding radial velocity minima with and without a probe. However, there is a significant spatial phase difference between the profiles with and without a probe and this has been discussed in the context of Figure 8.12.

8.3.5 Vortex centre analysis for $\Gamma = 11.36$ with and without a probe

This section documents the comparion between the analysis of vortex centres for the test cases with and without the cylindrical probe model in the annulus. The method discussed in section 6.7.8 in chapter six is used to estimate the axial coordinate X_c and the radial coordinate r_c of each of vortex centre for the test case with the cylindrical probe. X_c and r_c are then used to mark the centres of the vortices in Figure 8.14. The values of X_c and r_c are reported in Table B 5 of appendix B. The location of the vortex centres is analysed in details in the discussion of Figure 8.15.

Figure 8.15 displays the normalised radial position of the Taylor vortex centres from the PIV result with a probe as a function of their axial position in the meridional plane. As in Figure 7.19, Figure 8.15 is used to illustrate the radial spread of the vortex centres in the meridional plane at both the lower and upper channels ($\theta = \pm\pi/2$). The spread band was estimated using equation 6.8 and plotted in Figure 8.15 using the same notation as in

Figure 7.19. The numbering of the vortices in Figure 8.14 follows the same method as discussed in section 7.6.3 in the context of Figure 7.18.

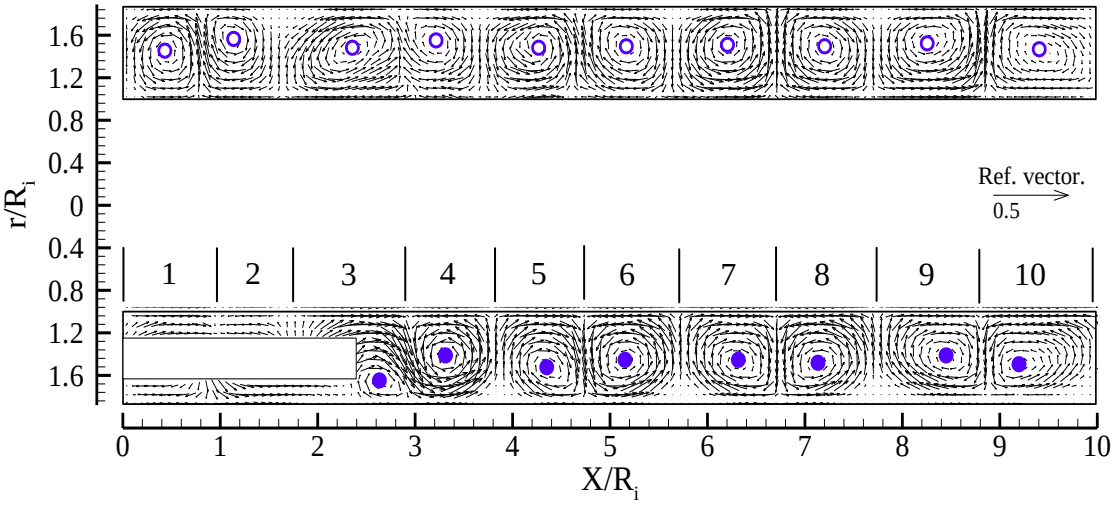

Figure 8.14: Velocity vectors showing the centre of the vortices in open and closed circles on the meridional plane.

Figure 8.15 therefore, shows the variation in both the axial and radial position of the centres among the vortices, with the radial variation being more pronounced than the axial variation, as in the test case with no probe presented in Figure 7.19(a).

The axial and radial position of the vortex centres in Figure 8.15 confirms the type of flow pattern discussed in the context of Figure 7.7 and Figure 8.3. As in Figure 7.19(a), the difference in the radial position of the vortex centres between $\theta = -\pi/2$ and $\theta = \pi/2$ in Figure 8.15 is higher near the end-wall boundaries in the range $2.4 \leq X/R_i \leq 4.2$ and $7.2 \leq X/R_i \leq 10$, but it is highest near the tip of the probe at $X/R_i = 2.4$. Also, the radial spacing of the vortex centres between one vortex and the next one in the positive axial direction is significantly higher toward the tip of the cylindrical probe than at the left and right end-wall boundaries. In the central region of the annulus, over the range $4.2 \leq X/R_i \leq 7.2$, the vortex centres at $\theta = \pm\pi/2$ are less spread out radially.

In the upper channel ($\theta = \pi/2$) in Figure 8.15, there is a higher radial spacing between the centres of vortices 1 and 2, 2 and 3, 3 and 4, 4 and 5, 8 and 9, 9 and 10. These are the vortices near the end-wall boundaries. The radial spacing between the centres of the vortices 5 and 6, 6 and 7, and 7 and 8 is comparatively smaller. At the lower channel ($\theta = -\pi/2$), vortices 1 and 2 are not detected due to the presence of the probe in this region. Therefore, the maximum radial spacing between the vortices at the lower channel ($\theta = -\pi/2$) occurs between vortices 3 and 4, 4 and 5, 5 and 6, 8 and 9, and 9 and 10. These are

also the vortices near the tip of the probe and vortices near the right end-wall boundary. At $\theta = \pm\pi/2$ the radial spacing between the vortices in the central region of the annulus is comparatively smaller than near the probe tip at $\theta = -\pi/2$. The smaller radial spacing at the central region of the annulus at $\theta = \pm\pi/2$ in Figure 8.15 is similar to the observed pattern for the test case with no probe in Figure 7.18, in which the radial spacing between vortices in the central region is smaller than near the end-walls.

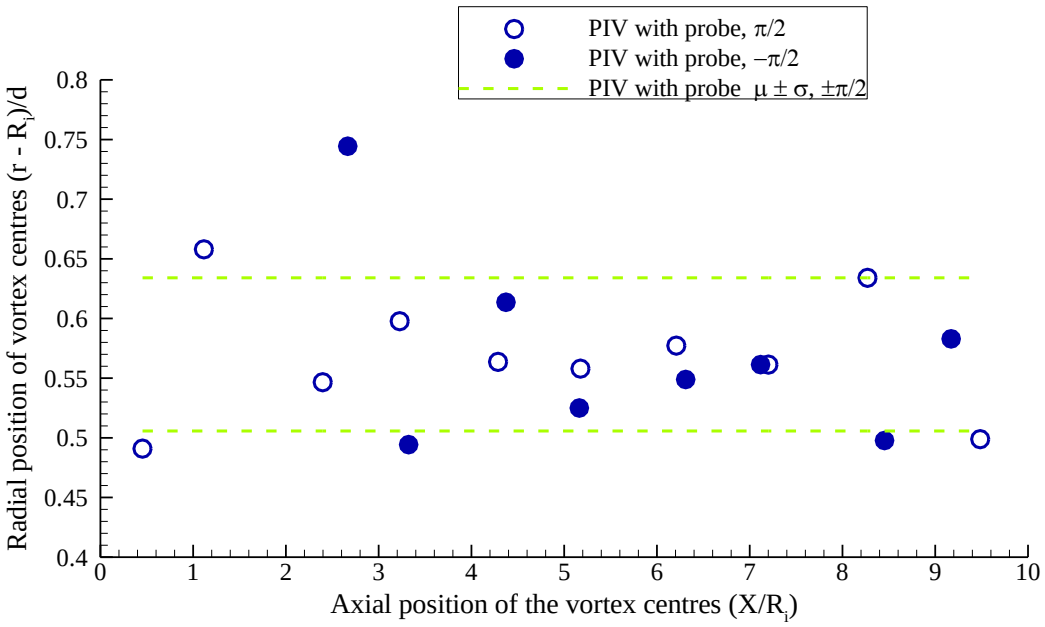

Figure 8.15: Axial and radial position of vortex centres in the meridional plane with data spread band about the PIV vortex centre mean value.

8.3.6 Effects of the probe on the vortex centre position

Figure 8.16 displays the normalised radial position of the Taylor vortex centres as a function of their axial position from the PIV measurements with and without a probe in the meridional plane of the annular region along the lower and the upper channels ($\theta = \pm\pi/2$). Figure 8.16 also shows how the vortex centres spread radially in the annular region of the cylinder in the PIV results with and without a probe by the inclusion of their respective spread bands. It is also possible to identify the missing vortices in the test case with probe in Figure 8.16. The spread bands in Figure 8.16 are estimated using equation 6.8. The black dashed lines toward the top and bottom of Figure 8.16 represent respectively the maximum and minimum limits of the spread band about the vortex centre mean value from the PIV measurement without a probe. Similarly, the orange dashed lines of Figure 8.16 represent the maximum and minimum limits of the spread band about the

vortex centre mean value from the PIV measurement with a probe. In Figure 8.16, the two band lower limits for the PIV test case with and without a probe overlap each other. In Figure 8.16, not all the vortex centres from the PIV test case with and without a probe lie within the spread bands.

Figure 8.16 shows that the presence of the probe in the annular region of the cylinder has changed both the axial and radial position of the vortex centres. This can easily be noticed by considering the vortex centres with and without a probe at the upper channel ($\theta = \pi/2$) and the lower channel ($\theta = -\pi/2$) independently. The effect of the probe in the annulus is more pronounced on the lower channel. This is not surprising because it is the plane where the probe is positioned.

At the upper channel, a significant axial and radial displacement of the vortex centres between the PIV test case with and without a probe occurs on vortices 2, 9 and 12, with vortices 5 and 10 missing. That is, there is a greater radial spacing between vortices 2, 9 and 12 from the test case with and without a probe in the annulus than between the remaining vortices.

Similarly, at the lower channel, the greater difference in axial and radial displacement of the vortex centres between the test case with and without a probe occurs near the tip of the probe where the vortex centre is displaced toward the wall of the outer cylinder, as seen in Figure 8.3 and Figure 8.14. Also, on the lower channel, a significant axial and radial displacement of the vortex centres between the test case with and without a probe occurs for vortices 3, 9 and 12, with vortices 1, 2, 5 and 10 missing. Figure 8.16 shows that the radial spacing of the vortex centres at the tip of the cylindrical probe for the PIV test case with and without a probe is more significant than for vortices 3, 9 and 12.

In the central region of the annulus, in the range $4.2 \leq X/R_i \leq 6.4$, the vortex centres for the PIV test case with and without a probe are less spread out radially and axially. In general, the PIV measured vortex centres for the test case with the probe are more scattered radially within the annulus than the vortex centres for the test case without a probe. This is evidenced by the area occupied by the measured vortex centres. For the test case with the probe, the measured vortex centres spread over the range $0.48 \leq (r - R_i)/d \leq 0.75$ radially, while the area occupied by the measured vortex centres spreads over the narrower range $0.46 \leq (r - R_i)/d \leq 0.66$ radially for the test case without a probe.

Despite the effects of the probe on the vortex centre, there are noticeable similarities in the pattern of the vortex centres for the PIV test case with and without a probe in the annulus in Figure 8.16.

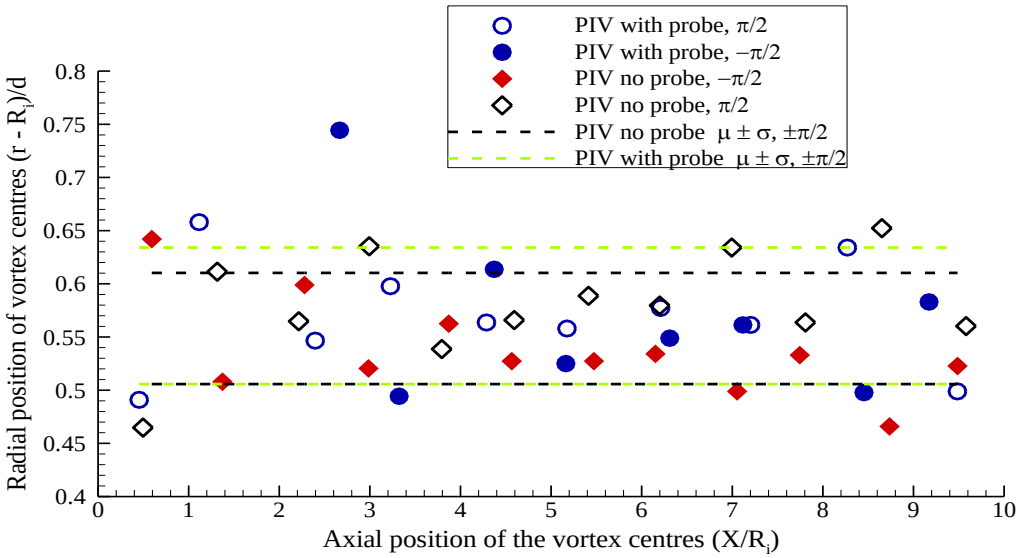

Figure 8.16: Axial and radial position of vortex centres in the meridional plane with data spread bands about the vortex centre mean value from the PIV test cases with and without a probe.

From Figure 8.14, the half wavelength, $\lambda/2$, for each vortex at $\theta = -\pi/2$ was estimated using the same procedure used for the $\Gamma = 11.36$ test case without probe in chapter six. Table 8-1 reports the axial vortex size estimated from Figure 8.14.

Table 8-1: Variation of vortex axial length with vortex number.

Vortex number	Vortex axial length $X_L = X/R_i$
1	0
2	0
3	0
4	0.889
5	0.909
6	0.990
7	0.986
8	1.058
9	1.083
10	1.147

Table 8-1 shows a progressive increase in the vortex size from the tip of the probe along positive axial direction to the right end-wall. In the central region, the axial length of the missing vortices is compensated by the increase in vortex size, while the elongated axial length of the vortex at the right end-wall is due to the boundary condition at this position.This is different from the trend reported for the test case without a probe in Table 6-7 where vortex axial length is elongated near the end-wall boundaries and shorter in the central region of the annulus.

Figure 8.17 shows the comparison of vortex axial length in the lower channel ($\theta = -\pi/2$) for the PIV test case with and without a probe in the form of a bar chart. The effect of the probe in the annulus on the vortex axial length is clearly shown by this figure in that the size of each vortex in the PIV test case with a probe is higher than the size of the corresponding vortex in the PIV test case without a probe. This is due to the axial length of the missing vortices 5 and 10 that is compensated by an increase in the axial length of the remaining vortices, since the axial length of the concentric cylinders is the same in both tests.

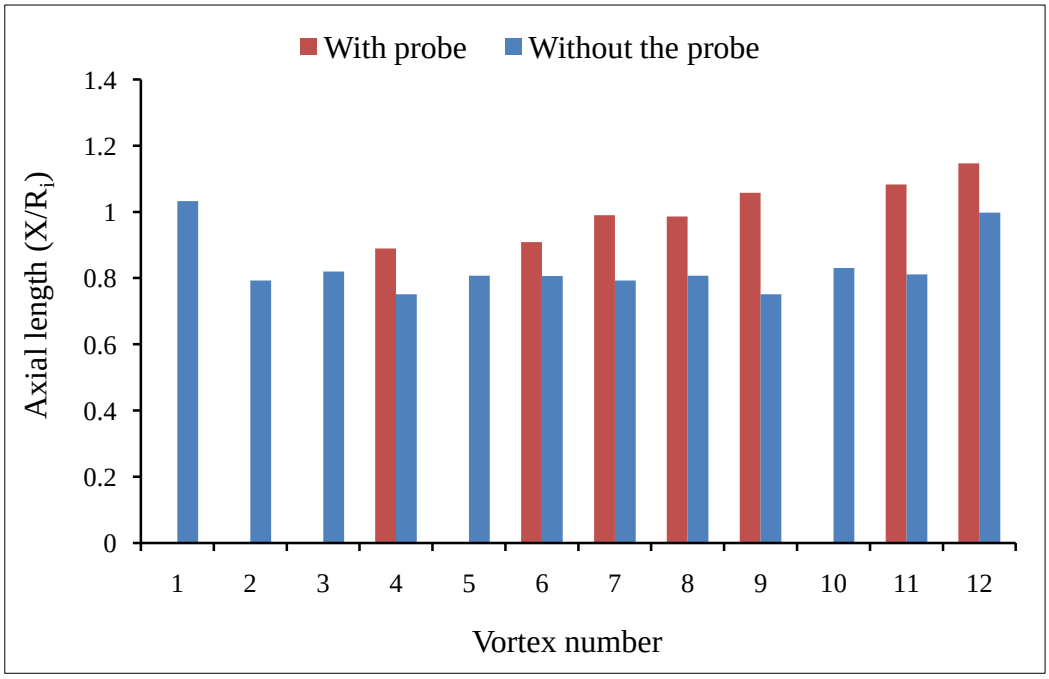

Figure 8.17: Comparison of vortex axial length in the lower channel ($\theta = -\pi/2$) for the test cases with and with no probe in the annulus.

Chapter Nine: Conclusions and recommendations for further work

9.1 Overview

This chapter gives the conclusions and recommendations for further work from the numerical modelling and experimental study on the flow pattern in concentric rotating cylinders with and without a cylindrical probe. The conclusions focus on the outcome of the computational modelling, of the experimental analysis, and on the effects of the cylindrical probe on the Taylor vortex flow.

9.2 Conclusions on the computational analysis

The elliptical windage flow in the gap between an inner rotating cylinder and an outer stationary cylinder has been modelled as an incompressible three-dimensional flow using an implicit finite-volume RANS scheme with the realisable k-ε turbulence closure model. The numerical prediction shows the formation of counter rotating axisymmetric toroidal Taylor vortices as result of the motion of the rotating inner cylinder. The radial flow in the concentric rotating cylinders is due to the imbalance between the centrifugal forces exerted on the fluid due to the rotation of the inner cylinder and radial pressure gradient restoring radial momentum equilibrium in the flow (Taylor, 1923).

This work provides more information on the velocity and pressure distributions in the meridional plane of the annulus. This is done by examining in details the axial, the radial, the tangential velocities as well as the gauge static pressure and the dynamic pressure across the full annular region. Previous results from the numerical investigations on the Taylor-Couette flow focussed mainly on the radial velocity at the gap mid-span of the annulus. To the author's best knowledge, velocity distributions near the inner and the outer cylinders in a rotating concentric cylinder assembly appears not to have been reported in the open literature. These new predictions show that the magnitude of the axial velocity reaches its maximum value near the wall of the inner and the outer cylinders and it is at a minimum at the gap mid-span. The magnitude of the radial velocity is maximum at the gap mid-span of the annulus and reduces towards the cylindrical walls.

These results also show that the radial velocity of the inward flow displays single trough minima near the inner cylinder and double trough minima near the outer cylinder, which is

a previously unreported feature of Taylor vortex flows. Its presence has been explained in terms of a pressure gradient induced boundary layer separation in this thesis.

At the gap mid-span of the annulus, this study confirms the observation by Deng et al. (2009) that the axial velocity is not zero at a high Reynolds number, since the centres of the vortices do not lie on $r = R_i + 0.5d$ line. In fact, the vortex centres are shifted towards the wall of the outer cylinder as the centrifugal forces due to the rotation of the inner cylinder is greater than the pressure gradient due to the stationary outer cylinder at a high Reynolds number.

The shifting of the vortex centres toward the wall of outer cylinder also causes the radial velocity profiles to be asymmetric along the gap mid-span.

The CFD simulation results show that, when the inner cylinder rotates clockwise, the magnitude of tangential velocity is maximum near the wall of the inner cylinder and the magnitude of the negative tangential velocity is minimum near the wall of the outer cylinder. The same pattern is observed in the PIV measurement.

Profiles of gauge static pressure and of dynamic pressure in the meridional plane near the wall of the inner cylinder, at the gap mid-span of the annulus, and near the wall of the outer cylinder have not been previously reported in the literature. The results obtained from this investigation show that the dynamic pressure near the wall of the inner cylinder is high and that the dynamic pressure progressively decreases toward the wall of the outer cylinder. This is due to the fluid near the inner cylinder having a higher tangential momentum than the fluid near the wall of the outer cylinder.

The presence of the end-walls produced elongated vortices near the end-wall boundaries and compressed vortices in the central region of the annulus as observed in the previous studied by Haut et al. (2003) and Deshmukh et al. (2007). This thesis has given an explanation for this trend, based on the balance of the inertial and viscous forces in the neighbourhood of the end-walls.

Finally, the results obtained from the CFD predictions show a good qualitative agreement with previous studies on Taylor vortex flow and documents new Taylor flow features that have not being reported in the literature.

9.3 Conclusions on the experimental analysis

Particle Image Velocimetry has been used to measure the flow between concentric cylinders with a radius ratio $0.3 \leq \eta \leq 0.6$, aspect ratio $5 \leq \Gamma \leq 12$, over the Taylor number

range $2.35 \times 10^6 \leq Ta \leq 17.5 \times 10^6$. The PIV experimental results show a wavy vortex flow regime for the test cases $\Gamma = 11.36$ and $\Gamma = 7.81$ and a turbulent vortex flow regime for the test case $\Gamma = 5.32$ displaying the formation of counter-rotating toroidal Taylor vortices, as predicted by the numerical simulations.

The experimental results show that, in the wavy vortex regime, a region of zero net axial flow is observed in the central region of the annulus, since there is no cross-flow between the vortices and vortex cells are independent. This region sits between the two regions of the end-wall boundaries where the inflow and outflow boundaries are not perpendicular to the inner and outer cylinder walls along the boundaries of two adjacent vortices.

In the wavy vortex regime, the centres of the vortices are displaced radially in an alternate manner along the axial direction in the entire annulus. The centre of the vortices near the end-walls is displaced radially toward the outer cylinder on the lower channel and toward the wall of the inner cylinder at the upper channel, irrespective of the Reynolds number value. The results obtained suggest that the centres of vortices near to the solid end-walls determine the trend of the centre positions of the remaining vortices in the central region of the annulus in the concentric cylinder geometry.

The results show that more vortex centres are closer to the wall of the inner cylinder for the test case with gap width of 0.022m than for the test case with gap width of 0.032m. That is, as the gap width increases, the vortex centres are displaced more toward the wall of the outer cylinder. In addition, the PIV measured vortex centres for the cylinders with gap width 0.022m are more scattered radially within the annulus than the vortex centres for the cylinders with gap width 0.032m, resulting in more regularly spaced vortex centres.

In addition, the wavy vortex flow shows that the interaction of the waviness with the end-wall does not result in disorder in the flow, either in the vortices near the end-walls or in those farther from the end-walls. The waviness does not significantly alter the boundary layer between the vortices near the end-walls and the end-walls. The results further revealed that the waviness near the end-walls does not reduce with increasing cylinder gap width until the flow regime changes to turbulent. The observed waviness penetrates far from the end-walls, that is, waviness is present more than one or two vortices away from the end-walls, contrary to the CFD predictions of Czarny et al. (2004).

In the turbulent flow regime, flow field is changing so rapidly that it was not possible to observe a stationary time-dependent flow regime in all the PIV snapshots. The flow

pattern can no longer be described by well-defined Taylor vortices, although structures associated with the Taylor vortices remain. The turbulent motion is a result of the increase in the Reynolds number that promotes the decay of large scale instabilities.

The experimental results of the turbulent flow regime in this study show that the instantaneous velocity field does not show a large-scale spatial periodicity, whereas a large-scale structure is observable in the corresponding time averaged flow results. The decay rate of specific turbulent kinetic energy in this flow is steeper than the conventional Kolmogrov -5/3 law and the specific turbulent kinetic energy spectrum does not show a viscous dissipation range. This is probably because the turbulent flow in the present study is not fully developed, such that turbulence decay is influenced by intermittent large-scale structures associated to the Taylor instability.

The experimental evidence provided in this research indicates that it is possible to observe wavy vortex flow for concentric cylinders with aspect ratio $\Gamma < 25$, contrary to the observation of Walden and Donnelly (1979). This present work also shows that wavy vortex flow can be maintained over a significantly larger Taylor number range, well beyond the published Taylor number for transition to turbulent flow.

Previous investigations have focussed on either qualitative flow visualisations or quantitative measurements at the cylinder annulus mid-gap. By presenting quantitative PIV measurements across the full annulus, this work documents previously unreported Taylor flow features over the selected range of geometry and flow parameters.

9.4 Conclusions on the intrusive effects of the probe on the Taylor vortex flow

A PIV investigation assessed the intrusivity that a cylindrical probe inserted in the annular region between coaxial cylinders has on the flow field and its impact on the flow regime. This investigation concerned coaxial cylinders of aspect ratio 11.36, radius ratio 0.53, tested at a Taylor number of 2.3×10^6.

The PIV results show that the flow regime with probe is the wavy vortex flow, consistent with the PIV result without the cylindrical probe. However, the introduction of the cylindrical probe changes the flow pattern in the annulus between the cylinders.

The experimental results show that the presence of the probe reduces the number of vortices in the meridional plane from twelve vortices in the test case without a probe to ten in the test case with a cylindrical probe. The introduction of the cylindrical probe constrained the Taylor vortex next to its tip toward the wall of the outer cylinder. Around

the probe tip, the cross-sectional area of this Taylor vortex is about 50% smaller than that of the corresponding Taylor vortex without a probe.

The experimental investigation further shows that the vortex immediately after the tip of the probe has its centre shifted away from $r = R_i + 0.5d$ toward the wall of the outer cylinder. This result and the one obtained from the PIV test case without a probe show that, whenever there is a perturbation in the form of a wall boundary, the centre of the vortex next to the wall boundary displaces radially from the $r = R_i + 0.5d$ line. This determines an alternated pattern of vortex centre radial displacements in the central region of the annulus.

This study also shows that the vortices near the right end-wall boundaries are more elongated than the vortices near the tip of the probe, contrary to the observed pattern in the flow field without the cylindrical probe, where the two vortices at the end-wall boundaries are elongated more than the vortices in the central region. This difference is due to the change in the boundary condition at the left end-wall. In addition, the presence of the probe in the annular region of the cylinder changed both the axial and radial position of the vortex centres.

In spite of the observed changes in the flow with the probe, the Taylor-Couette instability is not suppressed by the introduction of the cylindrical probe. The absolute magnitude of the axial and radial velocity in the regions where no cylindrical probe is positioned and in the region not affected by the PIV light reflection is within 10% to 15% between the test cases with and without probe. Therefore, a PIV endoscopic probe device can be used in experiment to produce an insight into windage flows above the critical Taylor number.

9.5 Future work

This study has shown that the flow regime in the annular region of concentric cylinders depends on the cylinder radius ratio, aspect ratio, the end-wall conditions, and on the Reynolds and Taylor numbers. As such, it was practically impossible to cover the full parameter space in this research work. Furthermore, the interaction of the annular flow regimes with a cylindrical probe has not been reported in the open literature prior to the present work. Based on the results obtained from the CFD predictions and the PIV measurements, this project can be expanded in a number of ways as follows:

(1) The present CFD work could be extended to a time-dependent simulation in which a structured mesh is employed for the discretisation of the flow field, enabling the use of Large Eddy Simulations (LES).

(2) The CFD simulations and PIV measurement were conducted at a constant angular velocity for all the test cases in this study in air. Different angular speeds and/or working fluids could be tested in future to cover a wider Reynolds number range.

(3) The intrusive effects of a cylindrical model probe have been analysed. It would be of interest to model probes of non-circular cross-section and/or with riblets or grooves, to reduce the probe drag and therefore its intrusivity in the flow.

Appendices

Appendix A

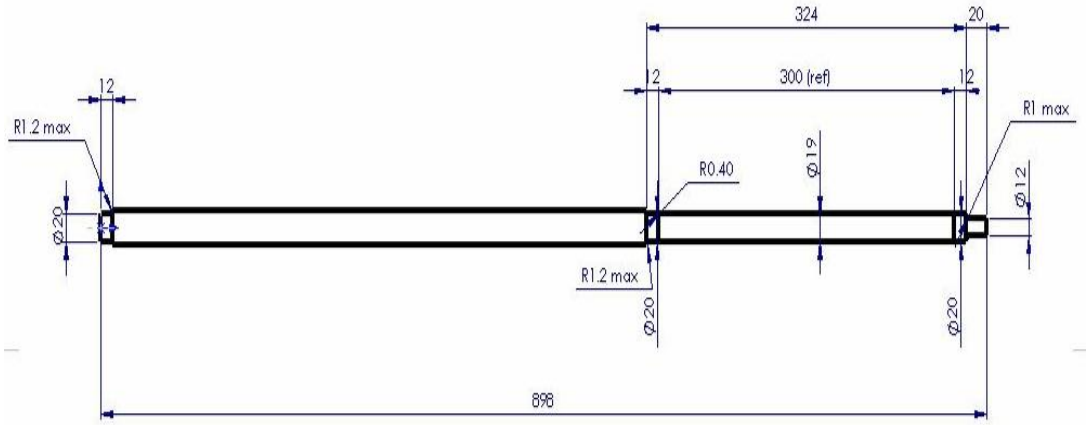

Figure A 1: The inner shaft component.

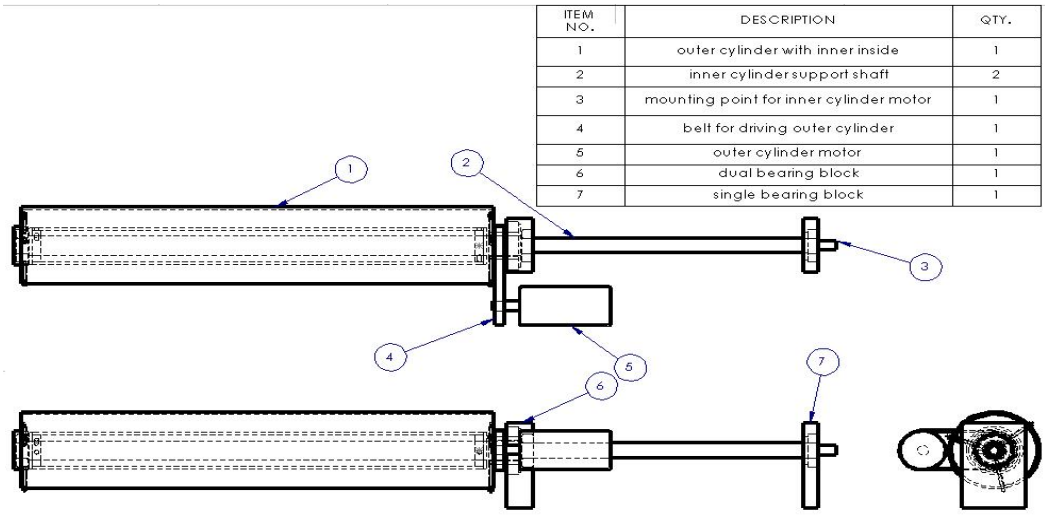

Figure A 2: The preliminary design of a concentric rotating cylinder assembly.

ITEM NO.	PART NUMBER	DESCRIPTION	QTY.
1	outer cylinder	perspex tube 100mm OD	1
2	stud captive end	main arm of motor end spider	3
3	spacer captive end	sleeve over stud at motor end	3
4	spacer free end	sleeve over stud viewing end	3
5	stud free end	main arm of viewing end spider	3
6	free end collar	mount for viewing end spider	1
7	big outer shell boss	mount for pulley, motor end spider and big bearing	1

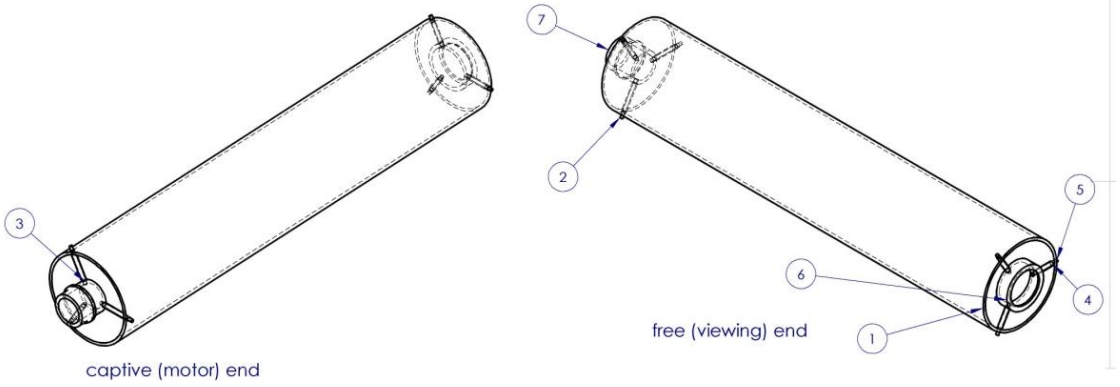

Figure A 3: Outer cylinder spiders.

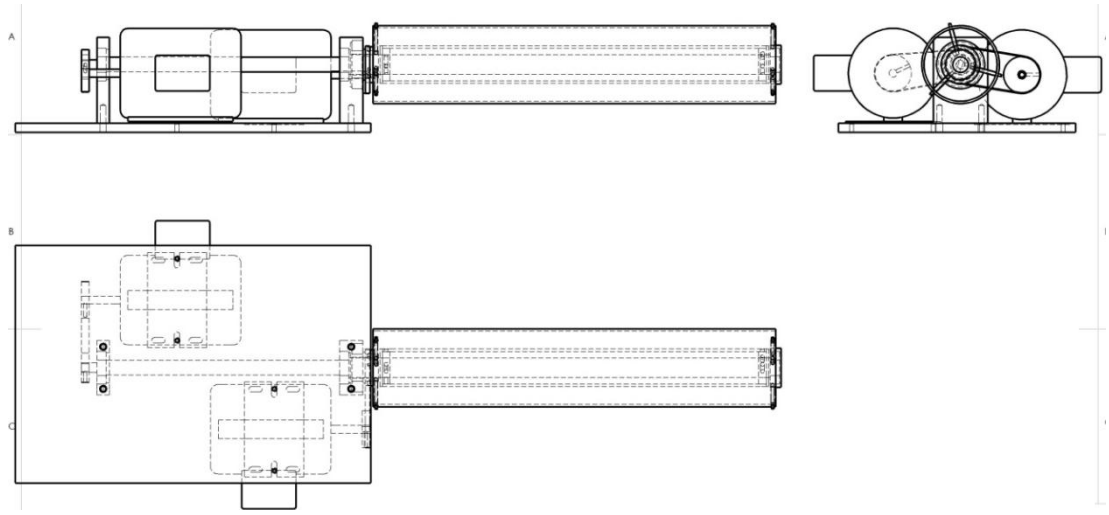

Figure A 4: Final design of concentric cylinders showing the mid bearing and the shaft.

Appendix B

Vortex number	Lower channel (-π/2)		Upper channel (π/2)	
	X_c (X/R_i)	r_c (r/R_i)	X_c (X/R_i)	r_c (r/R_i)
1	0.667269	1.50676	0.666714	1.50937
2	1.40772	1.51188	1.40613	1.51279
3	2.24531	1.51478	2.25219	1.52228
4	2.90015	1.51824	2.90465	1.51863
5	3.83247	1.51229	3.82866	1.51036
6	4.53052	1.50818	4.52843	1.51503
7	5.48747	1.51588	5.48867	1.50851
8	6.1877	1.51351	6.20533	1.51367
9	7.14693	1.52152	7.17209	1.51347
10	7.81494	1.51351	7.83274	1.51834
11	8.62709	1.51411	8.63886	1.50773
12	9.34521	1.50995	9.3538	1.50899

Table B 1: Axial and radial locations of the Taylor vortex centres for the test case Γ = 11.36, CFD without a cylindrical probe.

Vortex number	Lower channel (-π/2)		Upper channel (π/2)	
	X_c (X/R_i)	r_c (r/R_i)	X_c (X/R_i)	r_c (r/R_i)
1	0.91868	1.7619	0.916393	1.76476
2	1.96173	1.77615	1.96173	1.77901
3	3.27012	1.77852	3.27927	1.77426
4	4.2537	1.77377	4.25142	1.78613
5	5.76339	1.77377	5.77025	1.77663
6	6.76984	1.7762	6.76755	1.77189
7	8.09424	1.7809	8.09653	1.78138
8	9.12586	1.7619	9.119	1.76714

Table B 2: Axial and radial locations of the Taylor vortex centres for the test case Γ = 7.81, CFD without a cylindrical probe.

Vortex number	Lower channel (-π/2)		Upper channel (π/2)	
	X_c (X/R_i)	r_c (r/R_i)	X_c (X/R_i)	r_c (r/R_i)
1	0.582	1.587	0.500	1.362
2	1.374	1.463	1.347	1.474
3	2.277	1.538	2.222	1.449
4	2.987	1.488	3.001	1.524
5	3.876	1.513	3.794	1.424
6	4.573	1.488	4.587	1.461
7	5.475	1.488	5.434	1.474
8	6.158	1.463	6.199	1.461
9	7.047	1.463	6.992	1.511
10	7.744	1.488	7.812	1.449
11	8.742	1.438	8.660	1.524
12	9.480	1.489	9.576	1.449

Table B 3: Axial and radial locations of the Taylor vortex centres for the test case Γ = 11.36, PIV without a cylindrical probe.

Vortex number	Lower channel (-π/2)		Upper channel (π/2)	
	X_c (X/R_i)	r_c (r/R_i)	X_c (X/R_i)	r_c (r/R_i)
1	0.810	1.798	0.758	1.701
2	1.968	1.705	1.940	1.813
3	3.330	1.776	3.306	1.770
4	4.302	1.734	4.296	1.787
5	5.631	1.730	5.623	1.776
6	6.658	1.752	6.662	1.768
7	8.088	1.695	8.158	1.798
8	9.295	1.784	9.240	1.707

Table B 4: Axial and radial locations of the Taylor vortex centres for the test case Γ = 7.81, PIV without a cylindrical probe.

Vortex number	Lower channel (-π/2)		Upper channel (π/2)	
	X_c (X/R_i)	r_c (r/R_i)	X_c (X/R_i)	r_c (r/R_i)
1	0	0	0.454	1.432
2	0	0	1.116	1.579
3	2.667	1.655	2.397	1.481
4	3.323	1.435	3.227	1.526
5	4.372	1.540	4.287	1.496
6	5.163	1.462	5.176	1.491
7	6.310	1.483	6.209	1.508
8	7.117	1.494	7.202	1.494
9	8.454	1.438	8.270	1.558
10	9.172	1.513	9.485	1.439

Table B 5: Axial and radial locations of the Taylor vortex centres for the test case Γ = 11.36, PIV with cylindrical probe.

Authors	Experimental method	Aspect ratio Γ	Radius ratio η	Reynolds number	Taylor number	Flow characteristics
Lewis and Swinney, (1999)	Torque measurements	11.4, 9.8	0.724	$2 \times 10^3 \leq Re \leq 10^6$	-	WVF, TTVF
Lathrop et al. (1992)	Torque measurements and flow visualisation	11.47	0.724	$800 \leq Re \leq 1.23 \times 10^6$		TVF, WVF and TTVF.
Smith and Townsend (1982)	Hot-wire probe	23.7	0.667	$7.2 \times 10^3 \leq Re \leq 1.2 \times 10^5$		Symmetric, attached twin vortices.
Gollub and Swinney (1975)	Optical heterodyne technique	19.779	0.876			TVF, WVF and TTVF.
Parker and Merati (1996)	LDV	20 and 4	0.672	73,440	2.107×10^9	TTVF.
Fenstermacher et al. (1979)	LDV			-		-
Batten et al. (2002b)	CFD		0.734, 0.942 and 0.985.	$5 \times 10^3 \leq Re \leq 5 \times 10^4$		TTVF

Table B 6: Turbulent flow regimes in concentric rotating cylinders.

References

Achenbach, E. (1968), 'Distribution of local pressure and skin friction around a circular cylinder in cross-flow up to Re = 5 x 10^6', *Journal of Fluid Mechanics*, **34**, 625-639.

Acheson, D. J. (1995), *Elementary Fluid Dynamics: Oxford Applied Mathematics and Computing Science Series*, Oxford, Clarendon press.

Ackerman, J. R., Gostelow, J. P. and Rona, A. (2009), 'Measurements of fluctuating pressures on a circular cylinder in subsonic crossflow', *America Institute of Aeronautics and Astronautics*, **47** (9), 2121-2131.

Adaramola, M. S., Akinlade, O. G., Sumner, D., Bergstromb, D. J. and Schenstead, A. J. (2006), 'Turbulent wake of a finite circular cylinder of small aspect ratio', *Journal of Fluids and Structures*, **22**, 919-928.

Adrian, R. J. (1984), 'Scattering particle characteristics and their effect on pulsed laser measurements of fluid flow-speckle velocimetry vs. particle image velocimetry', *Applied Optics*, **23** (11), 1690–1691.

Adrian, R. J. (1988), 'Statistical properties of particle image velocimetry measurements in turbulent flow', *Laser Anemometry in Fluid Mechanics*, Instituto Superior Tecnico, Lisbon.

Adrian, R. J. (1991), 'Particle-imaging techniques for experimental fluid mechanics', *Annual Reviews of Fluid Mechanics*, **23**, 261-304.

Adrian, R. J. and Westerweel, J. (2011), *Particle Image Velocimetry*, First edition, USA, Cambridge University Press.

Agrawal, A. and Prasad, A. K. (2002), 'Properties of vortices in the self-similar turbulent jet', *Experiment in Fluids*, **33**, 565-577.

Akonur, A. and Lueptow, R. M. (2003), 'Three-dimensional velocity field for wavy Taylor-Couette flow', *Physics of Fluids*, **15** (4), 947-960.

Albrecht, H.-E., Borys, M., Damaschke, N. and Tropea, C. (2003), *Laser Doppler and Phase Doppler Measurement Techniques*, Germany, Springer-Verlag Berlin Heidelberg.

Alim, A. (2007), 'A Physical comprehensive definition of a vortex based on the lamb vector', *Algerian Journal of Applied Fluid Mechanics*, **1**, 1-5.

Andereck, C. D., Liu, S. S. and Swinney, H. L. (1986), 'Flow regimes in a circular Couette system with independently rotating cylinders', *Journal of Fluid Mechanics*, **164**, 155-183.

Anderson, J. D. (1995), *Computational fluid dynamics: the basics with applications.*, New York, McGraw-Hill.

Aroussi, A. and Menacer, M. (2003), 'Planar light sheet probes', *USA Patent number 20030133096*.

Baier, G. (1999), 'Liquid-liquid extraction based on a new flow pattern: Two-fluid Taylor-Couette flow', PhD thesis, University of Wisconsin.

Baier, G. and Graham, M. D. (1998), 'Two-fluid Taylor-Coutte flow: Experiments and linear theory for immiscible liquids between corotating cylinders.' *Physics of Fluids*, **10**, 3045-3055.

Barcilon, A. and Brindley, J. (1984), 'Organized structures in turbulent Taylor-Couette flow', *Journal of Fluid Mechanics*, **143**, 429-449.

Bates, C. J. and Banerjee, P. K. (1978), 'Laminar flow measurements in a square duct using laser Doppler anemometry', *Proceedings of the First international Conference*, Swansea, Wales, 191-199.

Batten, W. M. J., Bressloff, N. W. and Turnock, S. R. (2002a), 'Numerical simulations of the evolution of Taylor cells from a growing boundary layer on the inner cylinder of a high radius ratio Taylor-Couette system', *Physical Review E*, **66**, 066302.

Batten, W. M. J., Bressloff, N. W. and Turnock, S. R. (2002b), 'Transition from vortex to wall driven turbulence production in the Taylor-Couette system with a rotating inner cylinder', *International Journal for Numerical Methods in Fluids*, **38**, 207-226.

Batten, W. M. J., Turnock, S. R., Bressloff, N. W. and Abu-Sharkh, S. M. (2004), 'Turbulent Taylor-Couette vortex flow between large radius ratio concentric cylinders', *Experiments in Fluids*, **36**, 419-421.

Beaudan, P. and Moin, P. (1994), 'Numerical experiments on the flow past a circular cylinder at sub-critical Reynolds number', *Naval Research Technical Report TF - 62*, Stanford, Califonia, Stanford University, 1-239.

Benjamin, T. B. (1978), 'Birfurcation phenomena in steady flows of a viscous fluid. 1. Theory', *Proceedings of the Royal Society of London, Series A*, **359** (1696), 1-26.

Benjamin, T. B. and Mullin, T. (1981), 'Anomalous modes in the Taylor experiment', *Proceeding of the Royal Society of London, Series A*, **377** (1770), 221-249.

Berland, T., Jossang, T. and Feder, J. (1986), 'An experimental study of the connection between the hydrodynamic and phase-transition descriptions of the Couette-Taylor instability', *Physical Science*, **34**, 427-431.

Betchov, R. and Criminale(Jr), W. O. (1967), *Stability of parallel flows*, New York, Academic Press.

Blazek, J. (2001), *Computational Fluid Dynamics: Principles and Applications*, First edition, Oxford, UK, Elsevier Science Ltd.

Bloor, M. S. (1964), 'The transition to turbulence in the wake of a circular cylinder', *Journal of Fluid Mechanics*, **19**, 290-304.

Boussinesq, J. (1877), 'Essai sur la théorie des eaux courantes', *Mémories Présentés par Divers Savants á l'Academie des Sciences, Paris*, **23**, 1-680.

Braza, M., Perrin, R. and Hoarau, Y. (2006), 'Turbulence properties in the cylinder wake at high Reynolds numbers', *Journal of Fluids and Structures*, **22** (6-7), 757-771.

Brewster, D. B., Grosberg, P. and Nissan, A. H. (1959), 'The stability of viscous flow between horizontal concentric cylinders', *Proceedings of the Royal Society of London, Series A*, **251** (1264), 76-91.

Burkhalter, J. E. and Koschmieder, E. L. (1973), 'Steady supercritical Taylor vortex flow', *Journal of Fluid Mechanics*, **58** (3), 547-560.

Cantwell, B. J. and Coles, D. (1983), 'An experimental study of entrainment and transport in the turbulent near wake of a circular cylinder', *Journal of Fluid Mechanics*, **139**, 321-374.

Cardell, G. S. (1993), 'Flow past a circular cylinder with a permeable splitter plate', PhD thesis, Califonia Institute of Technology.

Chakraborty, P., Balachandar, S. and Adrian, R. J. (2005), 'On the relationship between local vortex identification schemes', *Journal of Fluid Mechanics*, **535**, 189-214.

Chandrasekhar, S. (1954), 'The stability of viscous flow between rotating cylinders', *Mathematika*, **1**, 5-13.

Chandrasekhar, S. (1958), 'The stability of viscous flow between rotating cylinders', *Proceedings of the Royal Society of London, Series A*, **246** (1246), 301-311.

Chandrasekhar, S. (1961), *Hydrodynamic and hydromagnetic stability*, First edition, Oxford, Oxford University press.

Choi, H., Jeon, W. P. and Kim, J. (2008), 'Control of flow over a bluff body', *Annual Review of Fluid Mechanics*, **40**, 113–139.

Chomaz, J. M., Huerre, P. and Redekopp, L. T. (1988), 'Birfurcations to local and global modes in spatially developing flows', *Physical Review Letters,* **60**, 25-28.

Chong, M. S., Perry, A. E. and Cantwell, B. J. (1990), 'A general classification of three-dimensional flow fields', *Physics of Fluids A,* **2** (5), 765–777.

Cole, J. A. (1976), 'Taylor vortex instability and annulus-length effects', *Journal of Fluid Mechanics,* **75**, 1-15.

Coles, D. (1965), 'Transition in circular Couette flow', *Journal of Fluid Mechanics,* **21**, 385-425.

Coney, J. E. R. and Simmers, D. A. (1979), 'A study of a fully-developed, laminar, axial flow and Taylor vortex flow by means of shear stress measurements', *Journal of Mechanical Engineering Science,* **21** (1), 19 - 24.

Couette, M. (1890), 'Études sur le frottement des liquides', *Ann Chim Phys,* **6**, 433-510.

Coughlin, K. T. and Marcus, P. S. (1992), 'Modulated waves in Taylor-Couette flow Part 2. Numerical simulation', *Journal of Fluid Mechanics,* **234**, 19-46.

Coutanceau, M. and Bouard, R. (1977), 'Experimental determination of the main features of the viscous flow in the wake of a circular cylinder in uniform translation. Part1. Steady flow', *Journal of Fluid Mechanics,* **79** (2), 231-256.

Criminale(Jr), W. O., Jackson, J. L. and Joslin, R. D. (2003), *Theory and Computation in Hydrodynamic Stability*, First edition, Cambridge, Cambrudge University Press.

Cumpsty, N. (2003), *Jet Propulsion*, 2nd Edition edition, Cambridge, Cambridge University Press.

Czarny, O., Serre, E., Bontoux, P. and Lueptow, R. M. (2002), 'Spiral and wavy vortex flows in short counter-rotating Taylor–Couette cells', *Theoretical and Computational Fluid Dynamics,* **16** (1), 5-15.

Czarny, O., Serre, E., Bontoux, P. and Lueptow, R. M. (2004), 'Interaction of wavy cylindrical Couette flow with endwalls', *Physics of Fluids,* **16** (4), 1140-1148.

Dantec-Dynamics (2008), 'Principles of Particle Image Velocimetry', <http://www.dantecdynamics.com/piv/Princip/Index.html.>, accessed June 2008.

Davey, A. (1962), 'The growth of Taylor vortices in flow between rotating cylinders', *Journal of Fluid Mechanics,* **14**, 336-368.

Davey, A., Di Prima, R. C. and Stuart, J. T. (1968), 'On the instability of Taylor vortices', *Journal of Fluid Mechanics,* **31**, 17-52.

de Jong, J., Cao, L., Woodward, S. H., Salazar, J. P. L. C., Collins, L. R. and Meng, H. (2009), 'Dissipation rate estimation from PIV in zero-mean isotropic turbulence', *Experiment in Fluids,* **46** (3), 499-515.

Debler, W., Funer, E. and Schaaf, B. (1968), 'Torque and flow patterns in supercritical circular Couette flow', in M. Hetenyi and W. G. Vincenti (eds.), *Proceedings of the 12th International Congress of Applied Mechanics*, Stanford University, Springer, Berlin, Heidelberg, New York, 158-178.

Delaney, K. K. and Sorensen, N. E. (1953), 'Low-speed drag of cylinders of various shapes', *National Advisory Committee for Aeronautics Technical Note 3038,* Washington, DC.

Deng, D. (2007), 'A numerical and experimental investigation of Taylor flow instabilities in narrow gaps and their relationship to turbulent flow in bearings', PhD thesis, The University of Akron.

Deng, R., Arifin, D. Y., Mak, Y. C. and Wang, C. (2009), 'Characterisation of Taylor vortex flow in a short liquid column', *Journal of American Institute of Chemical Engineers,* **55** (12), 3056-3065.

Deng, R., Yechyn, M., Wang, C. and Smith, K. A. (2005), 'Study on Taylor vortex formation in a liquid gap with significant boundary effects', *2005 AIChE Annual Meeting*, Cincinnati, OH.

Deshmukh, S. S., Joshi, J. B. and Koganti, S. B. (2008), 'Flow visualization and three-dimensional CFD simulation of the annular region of an annular centrifugal extractor', *Indutrial and Engineering Chemistry Research*, **47** (10), 3677-3686.

Deshmukh, S. S., Vedantam, S., Joshi, J. B. and Koganti, S. B. (2007), 'Computational flow modeling and visualization in the annular region of annular centrifugal extractor', *Industrial and Engineering Chemistry Research*, **46** (25), 8343-8354.

Di Prima, R. C. (1959), 'The stability of viscous flow between rotating concentric cylinders with a pressure gradient acting round the cylinders', *Journal of Fluid Mechanics*, **6**, 462-468.

Di Prima, R. C. (1960), 'The stability of a viscous fluid between rotating cylinders with an axial flow', *Journal of Fluid Mechanics*, **366**, 621-631.

Di Prima, R. C. (1961), ' Stability of non-rotationally symmetric disturbances for viscous flow between rotating cylinders ', *Phys Fluids*, **20**, 751-755.

Di Prima, R. C. and Swinney, H. L. (1981), 'Instabilities and transition in flow between concentric rotating cylinders', in H. L. Swinney and J. P. Gollub (eds.), *Hydrodynamic instabilities and the transition to turbulence*, Second edition, New York, Springer-Verlag, 139-180.

Donnelly, R. J. (1958), 'Experiments on the stability of viscous flow between rotating cylinders.1. Torque measurements', *Proceedings of the Royal Society of London, Series A*, **246** (1246), 312-325.

Donnelly, R. J. (1963), 'Experimental confirmation of the Landau law in Couette flow', *Physcal Review Letters*, **10**, 282-284.

Dou, H. S. (2006), 'Mechanism of flow instability and transition to turbulence', *International Journal of Non-linear Mechanics*, **41**, 512-517.

Dou, H. S., Khoo, B. C. and Yeo, K. S. (2008), 'Instability of Taylor–Couette flow between concentric rotating cylinders', *International Journal of Thermal Sciences*, **47** (11), 1422-1435.

Drazin, P. G. and Reid, W. H. (2004), *Hydrodynamic Stability*, Second edition, Cambridge, Cambridge University Press.

Dring, R. P. (1982), 'Sizing criteria flor laser anemometry particles', *ASME, Journal of Fluids Engineering*, **104** (1), 15-17.

Dubief, Y. and Delcayre, F. (2000), 'On coherent vortex identification in turbulence', *Journal of Turbulence*, **1** (1), 1-22.

Dyko, M. P., Vafai, K. and Mojtabi, K. A. (1999), 'A numerical and experimental investigation of stability of natural convective flows within a horizontal annulus', *Journal of Fluid Mechanics* **381**, 27-61.

Eagles, P. M. (1971), 'On stability of Taylor vortices by fifth-order amplitude expansions', *Journal of Fluid Mechanics*, **49**, 529-550.

Eagles, P. M. (1974), 'On the torque of wavy vortices', *Journal of Fluid Mechanics*, **62**, 1-9.

Fenstermacher, P. R., Swinney, H. L. and Gollub, J. P. (1979), 'Dynamical instabilities and the transition to chaotic Taylor vortex flow', *Journal of Fluid Mechanics*, **94**, 103-129.

FLUENT (2006), 'Fluent 6.3 user's manual guide', Lebanon, New Hampshire, USA, Fluent Incorporated.

Fokeer, S. (2006), 'An investigation of geometrically induced swirl applied to lean phase pneumatic flows', PhD thesis, University of Nottingham.

Fornberg, B. (1980), 'A numerical study of steady viscous flow past a circular cylinder', *Journal of Fluid Mechanics,* **98** (4), 819-855.
Fornberg, B. (1985), 'Steady viscous flow past a circular cylinder up to Reynolds number 600', *Journal of Computational Physics,* **61** (2), 297–320.
Goldstein, R. J. and Kreid, D. K. (1967), 'Measurement of Laminar Flow Development in a Square Duct Using a Laser-Doppler Flowmeter', *Journal of Applied Mechanics,* **34** (4), 813-818.
Gollub, J. P. and Swinney, H. L. (1975), 'Onset of turbulence in rotating fluid', *Physical Review Letters,* **35** (14), 927-930.
Gorman, M. and Swinney, H. L. (1982), 'Spatial and temporal characteristics of modulated waves in the circular Couette system', *Journal of Fluid Mechanics,* **117**, 123-142.
Gostelow, J. P. (1984), *Cascade Aerodynamics,* First edition, Oxford, England, Pergamon Press Ltd. 270.
Haller, G. (2005), 'An objective definition of a vortex', *Journal of Fluid Mechanics,* **525**, 1-26.
Hansford, G. and Litt, M. (1968), 'Mass transport from a rotating disk into power-law liquids', *Chemical Engineering Science,* **23**, 849-864.
Haut, B., Amor, H. B., Coulon, L., Jacquet, A. and Halloin, V. (2003), 'Hydrodynamics and mass transfer in a Couette-Taylor bioreactor for the culture of animal cells', *Chemical Engineering Science,* **58**, 774 -784.
Heinrichs, R. M., Cannell, D. S., Ahlers, G. and Jefferson, M. (1988), 'Experimental test of the perturbation expansion for the Taylor instability at various wavenumbers', *Physics of Fluids,* **31** (2), 250-255.
Hesselink, L. (1988), 'Digital image processing in flow visualisation', *Annual Review of Fluid Mechanics,* **20**, 421-485.
Higuchi, H., Sawada, H. and Kato, H. (2006), 'Separated flow field over blunt circular cylinder suspended magnetically in free stream direction', *36th American Institute of Aeronautics and Astronautics, Fluid Dynamics Conference and Exhibit,* Paper AIAA-2006-3552, San Francisco, California, USA, 1-8.
Higuchi, H., Van Langen, P., Sawada, H. and Tinney, C. E. (2006), 'Axial flow over a blunt circular cylinder with and without shear layer reattachment', *Journal of Fluids and Structures* **22**, 949–959.
Hopkins, L. M., Kelly, J. T., Wexler, A. S. and Prasad, A. K. (2000), 'Particle image velocimetry in complex geometries', *Experiments in Fluids,* **29**, 91-95.
Ifeachor, E. C. and Jervis, B. W. (2002), *Digital signal processing: A practical approach,* 2nd edition, Oxford, Prentice hall.
Jeffreys, H. (1928), 'Some cases of instability in fluid motion', *Proceedings of the Royal Society of London, Series A,* **118** (779), 195-208.
Jensen, K. D. (2004), 'Flow measurements', *Journal of the Brazilian Society of Mechanical Sciences and Engineering,* **XXVI** (4), 400-419.
Jeong, J. and Hussain, F. (1995), 'On the identification of a vortex', *Journal of Fluids Mechanics,* **285**, 69-94.
Jones, C. A. (1981), 'Nonlinear Taylor vortices and their stability', *Journal of Fluid Mechanics,* **102**, 249-261.
Jones, C. A. (1985), 'The transition to wavy Taylor vortices', *Journal of Fluid Mechanics,* **157**, 135-162.
Jones, W. M., Davies, D. M. and Thomas, M. C. (1973), 'Taylor vortices and the evaluation of material constants: a critical assessment', *Journal of Fluid Mechanics,* **60** (1), 19-41.
Joseph, D. D. (1976), *Stability of fluid motions, volumes 1 and 2,* Berlin, Springer-Verlag.

Joseph, D. D., Renardy, M. and Renardy, Y. (1984), 'Instability of the flow of two immiscible liquids with different viscosities in a pipe', *Journal of Fluid Mechanics,* **141**, 309-317.

Kalro, V. and Tezduyar, T. (1997), 'Parallel 3D computation of unsteady flows around circular cylinders', *Parallel Computing* **23**, 1235-1248.

Kawase, Y. and Ulbrecht, J. (1983), 'Heat and mass transfer in non-Newtonian fluid flow with power function velocity profiles', *Canadian Journal of Chemical Engineering,* **61** (6), 791-800.

Keane, R. D. and Adrian, R. J. (1990), 'Optimization of particle image velocimeters. Part I: Double pulsed systems', *Measuremet and Science Technology,* **1**, 1202-1215.

Keane, R. D. and Adrian, R. J. (1992), 'Theory of cross-correlation analysis of PIV images', *Applied Science Research,* **49**, 191-215.

Kim, Y. J., Yoon, C. H., Park, Y. C., Lee, D. K. and Kwon, S. K. (2007), 'Vortex flow study on non-Newtonian fluids in concentric annulus with inner cylinder rotating', *International Offshore and Polar Engineering,* **44** (5), 376-382.

King, G. P., Li, Y., Lee, W. and Marcus, P. S. (1984), 'Wave speeds in wavy Taylor-vortex flow', *Journal of Fluid Mechanics,* **141**, 365-390.

Kiya, M., Mochizuki, O., Tamura, T., Nozawa, T. and Ishikawa, R. (1991), 'Turbulence properties of axisymmetric separation and reattaching flow', *Journal of the American Institute of Aeronautics and Astronautics,* **29**, 936-941.

Koschmieder, E. L. (1979), 'Turbulent Taylor vortex flow', *Journal of Fluid Mechanics,* **93** (Part 3), 515-527.

Koschmieder, E. L. (1993), *Benard cells and Taylor vortices*, First edition, Cambridge, Cambridge University Press.

Kovasznay, L. S. G. (1949), 'Hot-wire investigation of the wake behind cylinders at low Reynolds numbers', *Proceedings of the Royal Society of London,* **198** (1053), 174-190.

Kuehn, T. H. and Goldstein, R. J. (1976), 'An experimental and theoretical study of natural convection in the annulus between horizontal concentric cylinders', *Journal of Fluid Mechanics,* **74** (4), 695-719.

Kuo, C.-H. and Chen, C.-C. (2009), 'Passive control of wake flow by two small control cylinders at Reynolds number 80', *Journal of Fluids and Structures,* **25** (6), 1021–1028.

Lad, N. (2011), 'Benchmarking a single-stem PIV endoscope in a spray', PhD thesis, University of Leicester.

Lange, C. F., Durst, F. and Breuer, M. (1998), 'Momentum and heat transfer from cylinders in laminar cross flows at $10^{-4} \leq Re \leq 200$', *International Journal of Heat and Mass Transfer,* **41**, 3409–3430.

Lathrop, D. P., Fineberg, J. and Swinney, H. L. (1992), 'Transition to shear-driven turbulence in Couette-Taylor flow', *Physical Review A,* **46** (10), 6390-6405.

Launder, B. E. and Spalding, D. B. (1972), *Mathematical models of turbulence*, London, Academic press.

Launder, B. E. and Spalding, D. B. (1974), 'The numerical computation of turbulent flows', *Computational Method in Applied Mechanical Engineering,* **3**, 269-289.

Lesieur, M., Begou, P., Briand, E., Danet, A., Delcayre, F. and Aider, J. L. (2003), 'Coherent vortex dynamics in large-eddy simulations of turbulence', *Journal of Turbulence,* **4**, 1-24.

Lewis, G. S. and Swinney, H. L. (1999), 'Velocity structure functions, scaling, and transitions in high-Reynolds number Couette-Taylor flow', *Physcal Review E,* **59** (5), 5457-5467.

Liao, C. B., Jane, S. J. and Young, D. L. (1999), 'Numerical simulation of three-dimensional Couette-Taylor flows', *International Journal for Numerical Methods in Fluids,* **29**, 827-847.

Lim, H. C. and Lee, S. J. (2003), 'PIV measurements of near wake behind a U-grooved cylinder', *Journal of Fluids and Structures,* **18** (1), 119-130.

Lin, C. C. (1955), *The theory of hydrodynamic stability*, Cambridge, Cambridge Press.

Liu, Z.-C., Landreth, C. C., Adrian, R. J. and Hanratty, T. J. (1991), 'High resolution measurement of turbulent structure in a channel with particle image velocimetry', *Experiments in Fluids,* **10**, 301-312.

Ma, K.-L. and Zheng, Z. C. (1994), '3D Visualization of unsteady 2D airplane wake vortices', *NASA Contractor Report*, Hampton, Virginia, Institute for Computer Applications in Science and Engineering, NASA Langley Research Center.

Macumber, S. (2005), 'Taylored Taylor vortices', PhD thesis, University of Colorado.

Mallock, A. (1888), 'Determination of the viscosity of water', *Proceedings of the Royal Society of London*, **45**, 126-132.

Mallock, A. (1896), 'Experiments on fluid viscosity', *Philosophical Transactions of the Royal Society of London*, Series A, **187**, 41-56.

Marcus, P. S. (1984), 'Simulation of Taylor-Couette flow. Part 2. Numerical results for wavy vortex flow with one travelling wave', *Journal of Fluid Mechanics,* **146**, 65-113.

McCluskey, D. R. (1992), 'An Optical Investigation of Air-Particle Flows', Phd thesis, University of Edinburgh.

Meinhart, C. D. and Adrian, R. J. (1995), 'On the existence of uniform momentum zones in a turbulent boundary layer', *Physics of Fluids,* **7** (4), 694-696.

Mishra, P. and Singh, P. (1978), 'Mass transfer from rotating disk to non-Newtonian fluids', *Chemical Engineering Science,* **33**, 1463-1470.

Monkewitz, P. A. (1988), 'The absolute and convective nature of instability in two-dimensional wakes at low Reynolds numbers', *Physics of Fluids,* **31**, 999-1006.

Moser, K. W., Raguin, G. L., Harris, A., Morris, D. H., Georgiadis, J., Shannonc, M. and Philpott, M. (2000), 'Visualization of Taylor–Couette and spiral Poiseuille flows using a snapshot Flash spatial tagging sequence', *Magnetic Resonance Imaging,* **18**, 199–207.

Neitzel, G. P. (1984), 'Numerical computation of time-dependent Taylor-vortex flows in finite-length geometries', *Journal of Fluid Mechanics,* **141**, 51-66.

Nishioka, M. and Sato, H. (1974), 'Measurements of velocity distributions in the wake of a circular cylinder at low Reynolds numbers', *Journal of Fluid Mechanics,* **65**, 97-112.

Nisi, H. and Porter, A. W. (1923), 'On eddies in air', *Philosophical Magazine*, **46** (6), 754-768.

Norberg, C. (1987), 'Effects of Reynolds number and a low-intensity free stream turbulence on the flow around a circular cylinder', *Publication No 87/2*, Gothenburg, Sweden, Chalmer University of Technology.

Ohji, M. and Amagai, K. (1988), 'Structure of modulated wavy vortical flows in the circular Couette system', *Fluid Dynamics Research,* **3**, 305-314.

Owen, J. M. and Rogers, R. H. (1996), *Flow and heat transfer in rotating-disc systems: Rotating cavities, Volume 2*, New York, Research Studies Press, John Wiley & Sons, Inc.

Parker, J. and Merati, P. (1996), 'An investigation of turbulent Taylor-Couette flow using Laser Doppler Velocimetry in a refractive index matched facility', *Journal of Fluid Engineering*, **118** (4), 810-818.

Pickering, C. J. D. and Halliwell, N. (1984), 'Laser speckle photography and particle image velocimetry: photographic film noise', *Applied Optics,* **23**, 2961–2969.

Prasad, A. K. (2000), 'Particle image velocimetry', *Current Science,* **79** (1), 51-60.

Raffel, M., Willert, C. E., Wereley, S. T. and Kompenhans, J. (2007), *Particle Image Velocimetry - A pratical guide*, 2nd edition, Berlin, Springer.

Rashaida, A. A. (2005), 'Flow of a non-Newtonian Bingham plastic fluid over a rotating disk', PhD thesis, University of Saskatchewan.

Rayleigh, L. (1917), 'On the dynamics of revolving fluids', *Proceedings of the Royal Society of London, Series A,* **93** (648), 148-154.

Recktenwald, A., Lucke, M. and Muller, H. W. (1993), 'Taylor vortex formation in axial through-flow: Linear and weakly nonlinear analysis', *Physical Review E,* **48** (6), 4444 - 4454.

Renardy, Y. and Joseph, D. D. (1985), 'Couette flow of two fluids between concentric cylinders', *Journal of Fluid Mechanics,* **150**, 381-394.

Roberts, P. H. (1965), 'The solution of the characteristic value problem', *Proceedings of the Royal Society of London, Series A,* **283** (1395), 550-556.

Robinson, S. K. (1991), 'Coherent motions in the turbulent boundary layer', *Annual Review of Fluid Mechanics,* **23**, 601-639.

Robinson, S. K., Kline, S. J. and Spalart, P. R. (1989), 'Quasi-coherent structures in the turbulent boundary layer. Part II: verification and new information from a numerically simulated flat-plate boundary layer. In: Kline, S. J. and Afgan, N. H. (ed) Near wall turbulence. ' *Proceedings of Zaric Memorial Conference*, New York, Hemisphere, 218-247.

Roshko, A. (1954a), 'On the development of turbulent wakes from vortex streets', *National Advisory Committee for Aeronautics Technical Note 1191*, California, California Institute of Technology.

Roshko, A. (1954b), 'On the drag and shedding frequency of two-dimensional bluff bodies', *National Aeronautics and Space Administration Technical Note 3169*, Washington, DC.

Roshko, A. (1961), 'Experiments on the flow past a circular cylinder at very high Reynolds number.' *Journal of Fluid Mechanics,* **10** (3), 345–356.

Roshko, A. and Fiszdon, W. (1969), 'On the persistence of transition in the near wake', *Problems of Hydrodynamics and Continuum Mechanics*, Philadelphia, Society for Industrial and Applied Mathematics, 606-616.

Rostami, M., Ardeshir, A., Ahmadi, G. and Thomas, P. J. (2007), 'Development of a low cost and safe PIV for mean flow velocity and Reynolds stress measurements', *International Journal of Engineering Transactions A: Basics,* **20** (2), 105-116.

Schlichting, H. (1979), *Boundary-Layer Theory*, 7th edition, New York, McGraw-Hill Science, Engineering and Mathematics.

Schmid, P. J. and Henningson, D. S. (2001), *Stability and transition in shear flows*, New York, Springer.

Schwarz, K. W., Springett, B. E. and Donnelly, R. J. (1964), 'Modes of instability in spiral flow between rotating cylinders', *Journal of Fluid Mechanics,* **20**, 281-289.

Serre, E., Crespo del Arco, E. and Bontoux, P. (2001), 'Annular and spiral patterns in flows between rotating and stationary discs', *Journal of Fluid Mechanics,* **434**, 65-100.

Serre, E., Sprague, M. A. and Lueptow, R. M. (2008), 'Stability of Taylor-Couette flow in a finite-length cavity with radial throughflow', *Physics of Fluids,* **20** (3), 034106.

Shaw, R. S., Andereck, C. D., Reith, L. A. and Swinney, H. L. (1982), 'Superposition of traveling waves in the circular Couette system', *Physical Review Letters,* **48** (17), 1172-1175.

Shih, T.-H., Liou, W. W., Shabbir, A., Yang, Z. and Zhu, J. (1995), 'A new k-epsilon eddy viscosity model for high Reynolds number turbulent flows', *Computers and Fluids,* **24** (3), 227-238.

Shih, W. C. L., Wang, C., Coles, D. and Roshko, A. (1992), 'Experiments on flow past rough circular cylinders at large Reynolds numbers', *Second International Colloquium on Bluff Body Aerodynamics and Applications,* Melbourne, Australia, December 7-10.

Shiomi, Y., Nakanishi, S. and Kutsuna, H. (2000), 'CFD calculation for two-phase flow in concentric annulus with rotating inner cylinder', *Phoenics Journal of Computational Fluid Dynamics and its Application,* **13** (1), 29-40.

Singer, B. A. and Banks, D. C. (1994), 'A predictor-corrector scheme for vortex identification. ' *NASA Technical Report*, Institute for Computer Applications in Science and Engineering.

Smieszek, M. and Egbers, C. (2005), 'Flow structures and stability in Newtonian and non-Newtonian Taylor-Couette flow', *Journal of Physics: Conference Series,* **14**, 72–77.

Smith, G. P. and Townsend, A. A. (1982), 'Turbulent Couette flow between concentric cylinders at large Taylor numbers', *Journal of Fluid Mechanics,* **123**, 187-217.

Snyder, H. A. (1969a), 'Change in waveform and mean flow associated with wavelength variations in rotating Couette flow. Part 1', *Journal of Fluid Mechanics,* **35**, 337-352.

Snyder, H. A. (1969b), 'Wave-number selection at finite amplitude in rotating Couette flow', *Journal of Fluid Mechanics,* **35**, 273-298.

Snyder, H. A. and Lambert, R. B. (1966), 'Harmonic generation in Taylor vortices between rotating cylinders', *Journal of Fluid Mechanics,* **26**, 545-562.

Sommerfeld, M. and Qiu, H.-H. (1993), 'Characterization of particle-laden, confined swirling flows by phase-doppler anemometry and numerical calculation', *International Journal of Multiphase Flow*, **19** (6), 1093-1127.

Sparrow, E. M. (1964), 'Instability of the flow between rotating cylinders: the wide gap problem', *Journal of Fluid Mechanics,* **20**, 35-46.

Stuart, J. T. (1958), 'On the non-linear mechanics of hydrodynamic stability', *Journal of Fluid Mechanics,* **4**, 1-21.

Takeda, Y. (1999), 'Quasi-periodic state and transition to turbulence in a rotating Couette system', *Journal of Fluid Mechanics,* **389**, 81-99.

Taneda, S. (1956), 'Experimental investigation of the wakes behind cylinders and plates at low Reynolds numbers', *Journal of Physical Society of Japan*, **11**, 302-307.

Taylor, G. I. (1923), 'Stability of a viscous liquid contained between two rotating cylinders', *Philosophical Transactions of the Royal Society of London, Series A,* **223**, 289-343.

Tokumaru, P. T. and Dimotakis, P. E. (1991), 'Rotary oscillation control of a cylinder wake', *Journal of Fluid Mechanics,* **224**, 77-90.

Tritton, D. J. (1959), 'Experiments on the flow past a circular cylinder at low Reynolds numbers', *Journal of Fluid Mechanics,* **6** (4), 547–567.

Tritton, D. J. (1971), 'A note on vortex streets behind circular cylinders at low Reynolds numbers', *Journal of Fluid Mechanics,* **45** (1), 203-208.

Tsai, C., Cai, Z. and Wu, X. (1998), 'The examination of residual plots', *Statistica Sinica,* **8**, 445-465.

Uberoi, M. S. and Freymuth, P. (1969), 'Spectra of turbulence in wakes behind circular cylinders', *Physics of Fluids,* **12** (7), 1359-1363.
Versteeg, H. K. and Malalasekera, W. (1995), *An introduction to computational fluid dynamics: the finite volume method*, Essex, UK, Pearson Prentice Hall.
Vollmers, H. (2001), 'Detection of vortices and quantitative evaluation of their main parameters from experimental velocity data', *Measurement Science and Technology,* **12**, 1199-1207.
Walden, R. W. (1978), 'Transition to turbulence in Couette flow between concentric cylinders', PhD thesis, University of Oregon.
Walden, R. W. and Donnelly, R. J. (1979), 'Reemergent order of chaotic circular Couette flow', *Physcal Review Letters,* **42** (5), 301-304.
Wang, L., Olsen, M. G. and Vigil, R. D. (2005), 'Reappearance of azimuthal waves in turbulent Taylor-Couette flow at large aspect ratio', *Chemical Engineering Science,* **60**, 5555-5568.
Wardle, K. E., Allen, T. R. and Swaney, R. (2006), 'Computational fluid dynamics (CFD) study of the flow in an annular centrifugal contactor', *Separation Science and Technology,* **41** (10), 2225-2244.
Wereley, S. T. and Lueptow, R. M. (1994), 'Azimuthal velocity in supercritical circular Couette flow', *Experiments in Fluids,* **18**, 1-9.
Wereley, S. T. and Lueptow, R. M. (1998), 'Spatio-temporal character of non-wavy and wavy Taylor-Couette flow', *Journal of Fluid Mechanics,* **364**, 59-80.
Wernet, M. P. (1997), 'Demonstration of PIV in a transonic compressor', *NASA Technical Memorandum -113164*, Ohio, NASA, 1-12.
Westerweel, J. (2000), 'Theoretical analysis of the measurement precision in particle image velocimetry', *Experiments in Fluids,* **29**, 3-12.
Westerweel, J., Draad, A. A., van der Hoeven, J. G. T. and van Oord, J. (1996), 'Measurement of fully developed turbulent pipe flow with digital PIV', *Experiments in Fluids,* **20**, 165 – 177.
Wild, P. M., Djilali, N. and Vickers, G. W. (1996), 'Experimental and computational assessment of windage losses in rotating machinery', *Transactions of ASME, Journal of Fluids Engineering,* **118**, 116-122.
Williamson, C. H. K. (1989), 'Oblique and parallel modes of vortex shedding in the wake of a cylinder at low Reynolds number', *Journal of Fluid Mechanics,* **206**, 579-629.
Xiao, Q., Lim, T. T. and Chew, Y. T. (2002), 'Second Taylor vortex flow: Effects of radius ratio and aspect ratio', *Physics of Fluids,* **14**, 1537-1539.
Yakhot, V. and Orszag, S. A. (1986), 'Renormalization group analysis of turbulence: I. basic theory.' *Journal of Scientific Computing,* **1** (1), 1-51.
Youd, A. J. (2005), 'Bifurcations in forced Taylor–Couette flow', PhD, University of Newcastle Upon Tyne.
Zarti, A. S. and Mobbs, F. R. (1979), 'Wavy Taylor vortex flow between eccentric rotating cylinders', *Energy conservation through fluid film lubrication technology: Frontiers in research and design*, Proceedings of the winter annual meeting, New York, American Society of Mechanical Engineers, 103-116.
Zhou, X., Pan, J., Chen, L., Shi, Y., Chen, W. and Chu, L. (2007), 'Numerical simulation of the characteristics of turbulent Taylor vortex flow', *Chemical Engineering of China,* **1** (2), 195-201.